Magnetic fields in and around galaxies

Sergio Martin
Christ Church College
University of Oxford

A thesis submitted for the degree of
Doctor of Philosophy
Hilary 2019

Abstract

Magnetic fields in and around galaxies

Sergio Martin

Christ Church college

Submitted for the degree of

Doctor of Philosophy

Hilary 2019

Magnetic fields are an ubiquitous component of our Universe. They are expected to play an important role in the evolution of many astrophysical systems, from molecular clouds to galaxy clusters. In the case of galaxies, magnetic energy is measured to be in equipartition with thermal and turbulent energies of the interstellar medium. Despite this omnipresence, the origin of cosmic magnetic fields remains an open question, and the precise influence that magnetic fields have in shaping the formation and evolution of galaxies is uncertain.

Using magnetohydrodynamical numerical simulations of both cosmological volumes and high-resolution cosmic zoom-ins on individual galaxies, I explore in this thesis the main mechanisms likely to generate galactic magnetic fields similar to those observed and the role these latter play in shaping galaxies. I present various extensions to existing numerical techniques to account for magnetism in state-of-the-art software employed to simulate galaxies. These culminate in the introduction of a new algorithm that traces magnetic fields generated by different sources separately. In particular, I simulate the formation of a Milky Way-like galaxy, magnetised either through dynamo amplification, a strong primordial magnetic field, or magnetised stellar feedback, demonstrating that each mechanism is capable of producing realistic levels of magnetisation on its own. Jointly tracing primordial and stellar generated fields, I study how they compete to produce the total magnetic field. I find a large degree of interaction, both inside galaxies, where the two components contribute significantly to the magnetic energy budget, and around galaxies, where the magnetic fields pushed out by stellar feedback pollute the primordial magnetic field. In a final set of simulations, I explore how magnetic fields modify the global properties of a galaxy, finding evidence of morphological compression and braking of the rotation of the galaxy by strong magnetisation.

Statement of Originality

I hereby declare that no part of this thesis has been accepted, or is currently being submitted, for any degree or diploma or certificate or any other qualification at the University of Oxford or elsewhere. Except where otherwise stated, the work in this thesis is entirely my own, and has been carried out under the supervision of Professor Julien Devriendt and Professor Adrianne Slyz.

My work was supported by the Oxford Hintze Centre for Astrophysical Surveys which is funded through generous support from the Hintze Family Charitable Foundation. The work in this thesis is part of the Horizon-UK project, which used the DiRAC Complexity system, operated by the University of Leicester IT Services, which forms part of the STFC DiRAC HPC Facility (www.dirac.ac.uk). This equipment is funded by BIS National E-Infrastructure capital grant ST/K000373/1 and STFC DiRAC Operations grant ST/K0003259/1. DiRAC is part of the National E-Infrastructure. This work also acknowledges the use of the University of Oxford Advanced Research Computing (ARC) facility.

Chapter 4 presents work that was accepted for publication on 14th of June 2018 by the Monthly Notices of the Royal Astronomical Society: Martin-Alvarez, S., Devriendt, J., Slyz, A., and Teyssier, R. **'A three-phase amplification of the cosmic magnetic field in galaxies'**.

Chapter 3 and part of Chapter 5 (Section 5.3.1) present work that was accepted for publication on 23rd of December 2018 by the Monthly Notices of the Royal Astronomical Society: Katz, H. & Martin-Alvarez, S., Devriendt, J., Slyz, A., and Kimm, T. **'Magnetogenesis at Cosmic Dawn: tracing the origins of cosmic magnetic fields'**. I co-first author the publication with Dr. H. Katz. The algorithm presented was co-developed by me and Dr. H. Katz based on my own original idea. I implemented the required modifications to the magnetohydrodynamical solver and the Godunov scheme. The simulations employed in Chapter 3 were run by H. Katz with my configuration files. They were co-analysed with Dr. H. Katz employing my analysis software, except for Figure 5.6.

Chapter 5 (Section 5.3.2) presents work that will be submitted to the Monthly Notices of the Royal Astronomical Society: Martin-Alvarez, S., Katz, H., Devriendt, J., Slyz, A., and Kimm, T. **'On the origin of galactic magnetic fields: primordial vs stellar'**.

Chapter 6 presents work that will be submitted to the Monthly Notices of the Royal Astronomical Society: Martin-Alvarez, S., Devriendt, J., Slyz, A., and Gomez-Guijarro, C. **'Cosmic magnetic braking: the contraction of galaxies by primordial magnetic fields'**.

Sergio Martín Álvarez, *April 2019*

Acknowledgements

First and foremost, I want to express my deep gratitude to my supervisors, Julien Devriendt and Adrianne Slyz. You have been a guiding light through this journey, and I have been extremely fortunate for all the support, effort and time that you have dedicated me. I couldn't have done it without you.

I want to thank my friends, Carlos Gomez-Guijarro, Marius Ramsøy, Miguel Pereira-Santaella, and my collaborators Yohan Dubois, Oliver Hahn, Taysun Kimm, Romain Teyssier, and Vicent Quilis. Thank you for making astrophysics so fascinating. A very special thank you goes to Harley Katz, not only for being so fantastic to work with, but also for all the guidance you have provided me. And I cannot overlook all the work done by Jonathan Patterson to ensure that the local supercomputer worked smoothly, still turns on, and has not burst in flames yet. Definitely need to also thank Matt Jarvis, for being the credit card behind my trips to half of the world. Another thank you is for the many people in the Sub-department of Astrophysics that give it its lovely atmosphere such as Christiane, Elisa, David, Lise, Rebecca, Sandor, Clotilde, Ricarda, Joe, Kearn, and Darsh. Thank you all.

To all the people that has made my time in Oxford so exceptional. The Christ Church GCR, everyone in the OU Karate Club (certainly to those who have not yet erroneously punched my face), and the incredible salsa and bachata community of Oxford. Specially thanks to Mario, Nuria, Bea, Anita, Esther, Spiros, Teresa, Jaime, and to Sheridan. A thank you to Paulina, for your support in these last hours. And to all my friends from back home, for never abandoning me from the other side of the *Canal de la Mancha*, thanks to Sara, Sheila, Olga, Rafa, Damián, Ángel, and the *Consejo de sabios*. Also to the C.M. San Juan de Ribera, to Rosario and Lorenzo, to Maura and Fernando, and to Addys and Sergio, for all your support and *por ser un pedacito de mí*.

And a devoted thank you to my housemates and friends, Sam, Catherine, Naomi, and specially to Paul. For putting up with me, and for making me feel like your country is my home. To T. and A., the beginning of this amazing adventure.
And finally, to my exceptional brother Iker, and my parents Inmaculada and Francisco:

Papá, mamá, a vosotros, gracias, porque sin vosotros, jamás se hubiese cumplido el sueño al que nunca me atreví a aspirar.

Contents

List of Figures

Chapter 1

Introduction

In this chapter, I introduce the context around the questions tackled in the thesis. Commencing with a description of the mechanisms that might have generated magnetic fields during the very early stages of the Universe (Section 1.1), I continue describing processes that have the potential to engender primordial magnetic fields as the evolution of our Universe proceeds up to its transition to the matter dominated phase. I then briefly describe the ΛCDM model paradigm, which underpins the emergence of structure in the Universe. From Large-Scale Structure down to galaxies, I outline the general aspects of their formation and evolution, with an emphasis on the generation, transformation, and impact of magnetic fields (Section 1.2). As they will be the central topics of this thesis, I set the focus specifically on galactic magnetic fields and their interrelation with the interstellar medium (Section 1.3). I conclude this chapter by describing current observational facilities, and the scientific targets and possibilities to be opened by forthcoming telescopes, indicating how numerical simulations of magnetic fields will benefit observations in their quest to uncover the magnetic Universe (Section 1.5).

1.1 Cosmogony and Magnetogenesis

The standard model for the origin of our Universe is the so-called Hot Big Bang model, supported by evidence such as the cosmic microwave background (CMB) and its anisotropies (Planck Collaboration et al. 2018) or the composition of the pristine gas predicted by Big Bang nucleosynthesis (Hinshaw et al. 2013; Coc et al. 2014). In this model, our Universe emerges from a singularity, described by complex physics outside of the scope of this thesis. I will be operating using as framework the conventional laws of physics which are recovered shortly after the epoch of inflation, occurring at $t \sim 10^{-43}$ s. After this period of exponential expansion, according to the the classical theory of electromagnetism and current constraints (Aartsen et al. 2014, 2016), it is widely assumed that magnetic fields have no magnetic monopoles and they are fully solenoidal. Thus, this should extend to magnetic fields in the large-scale structure, galaxies, and astrophysical systems below these scales. In accordance with this hypothesis, throughout this thesis I will strictly assume that magnetic fields must fulfil the solenoidal constraint

$$\vec{\nabla} \cdot \vec{B} = 0. \tag{1.1}$$

1.1.1 The Early Universe and the first magnetic fields

During the first few hundred of seconds of existence of the Universe that followed the Big Bang, various complex processes that shaped the characteristics of our Cosmos took place. Many had the potential to generate ubiquitous cosmic magnetic fields, each with their respective complex properties. The disparity of models is illustrated by several reviews (e.g. Widrow 2002; Kulsrud & Zweibel 2008; Kandus et al. 2011; Subramanian 2016). I briefly list some of them in this Section.

Inflation

It is widely believed that shortly after its beginning, our Universe underwent a period of exponential expansion known as inflation, which would be driven by e.g. the rapid initial stages of the transition of a scalar field towards an absolute minimum in its potential (Linde 1982). Through inflation, causal quantum-mechanical small-scale fluctuations are expected to expand up to scales causally disconnected, i.e. separated by distances larger than the maximal travel distance of light at a given cosmic time.

This process could have inducted magnetic field perturbations in the primordial plasma and expanded them to cosmic or super horizon lengths of coherence. The majority of non-inflationary mechanisms for generating magnetic fields struggle to reproduce magnetic fields with very large coherence lengths. However, in most simple scenarios of inflationary magnetogenesis, expansion causes both large coherence lengths for the field and extremely weak comoving primordial magnetic field strengths ($B_{\rm prim} \ll 10^{-20}$ G; Turner & Widrow 1988). More complex inflationary magnetogenesis models exist (an example are those based on Ratra 1992 models, coupling a gauge field with the inflation scalar), which have the potential to generate primordial magnetic fields of significantly higher strength (e.g. Sharma et al. 2018, $B_{\rm prim} \sim 10^{-11}$ G), with intermediate coherence lengths - on the order of 100 kpc. Other possibilities are super-adiabatic inflation resulting from non-zero curvature perturbation, which can generate strong magnetic fields coherent on cosmological scales ($B_{\rm prim} \sim 10^{-14}$ G with coherence on scales of Mpc to Gpc; Barrow & Tsagas 2011).

Reheating

Approximately 10^{-36} seconds after the Big Bang the process of inflation terminates as the scalar field reaches the true minimum for its potential. It is followed by a reheating phase during which the first particles are formed through the thermalisation of the energy remaining from inflation. While some processes could produce magnetic fields

during reheating, studies conclude that those not related with metric perturbations are of extremely weak nature and undergo non-significant amplification. Further review and literature reference can be found in Kandus et al. (2011).

QCD and electro-weak phase transitions

By the end of reheating, the Universe is radiation dominated, and most of the matter that constitutes the current baryonic component is formed. The continued expansion of the Universe reduces its temperature and it undergoes two further phase transitions at 10^{-12} s and 10^{-6} s. These are respectively the electroweak and QCD transitions.

In the first, the eletromagnetic (EM) and weak forces are separated by a symmetry breaking. During this process, various proposed mechanisms could lead to the generation of small-scale magnetic fluctuations, which cascade to magnetic fields coherent on larger scales. These mechanisms depend on the energy released by broken symmetry bubbles growth. These can create primordial magnetic fields up to $B_{\rm prim} \lesssim 10^{-21}$ G on Mpc scales, with strength depending on uncertain dissipative effects.

The QCD symmetry breaking is expected to occur at $T \sim 200$ MeV, confining quarks and gluons to atomic nuclei. While the generation of primordial magnetic fields during this process has been advocated, these are too weak to have cosmological relevance (Hollenstein et al. 2008).

Nucleosynthesis

The last of the early Universe processes is nucleosynthesis, spanning from 10^{-2} s after the Big Bang until the first few hundred seconds. While the process itself is unlikely to produce a considerable magnetic field from a cosmic perspective, the existence of significant magnetic fields during this process would alter the predicted resulting composition from Big Bang nucleosynthesis by intervening in the nuclear reaction rates and the pace of cosmic expansion (Grasso & Rubinstein 1996). Therefore, the

understanding of primordial magnetic fields is required to better constrain nucleosynthesis. Alternatively, one can use the expected properties of the Universe from this process to estimate an upper bound on the physical magnetic field during the epoch of nucleosynthesis of $B_{\rm phys}^{\rm nucleosynthesis} < 10^{11}$ G, which reflects on a limit for the comoving cosmic magnetic field of $B_0 < 10^{-6}$ G (Widrow 2002).

1.1.2 The Lambda-Cold Dark Matter cosmology

Following Big Bang nucleosynthesis a new regime commences where the effects of dark matter and dark energy start to dominate. In this era, cosmological models can be used to describe the formation and evolution of structure. The most popular and arguably successful cosmological model is the standard Λ-Cold Dark Matter (ΛCDM) model. This model is characterised by the existence of two further components to baryonic matter and radiation. CDM and Λ correspond respectively to cold dark matter and dark energy. To understand this model, we need to introduce a crucial quantity in cosmology, the scale factor a. Its particular importance for numerical cosmological simulations as the ones studied in this thesis will be illustrated in Chapter 2. This parameter describes the ratio of the Universe size at different times. If two objects were to be separated by a distance $d(t)$ and we assume the case where this distance is solely dependent on the expansion of the Universe, then we can define the scale factor as

$$\frac{a(t_1)}{a(t_0)} = \frac{d(t_1)}{d(t_0)}. \tag{1.2}$$

As commonly done, I will adopt throughout this thesis the convention that the scale factor at the current time t_0 is $a(t_0) = 1$. A useful quantity which is directly observable is the redshift

$$z = \frac{1}{a} - 1, \tag{1.3}$$

in which I have assumed that $a(t_0) = 1$. This quantity ranges from $z \to \infty$ at

the beginning of the Universe to $z = 0$ at the present. In ΛCDM cosmology, the Friedmann field equations (1.4) and (1.5) govern the expansion of the homogeneous Universe filled with an ideal fluid

$$H^2 = \left(\frac{\dot{a}}{a}\right)^2 = \frac{8\pi G}{3}\bar{\rho} - \frac{kc^2}{R^2a^2} + \frac{\Lambda}{3}, \tag{1.4}$$

$$\frac{\ddot{a}}{a} = -\frac{4\pi G}{3}\left(\bar{P} + \frac{3\bar{\rho}}{c^2}\right) + \frac{\Lambda}{3}. \tag{1.5}$$

In this work, I will use G as the gravitational constant and c as the speed of light. We can relate the radius of curvature R with the spatial curvature of the Universe $k/(R^2a^2)$, where the k factor determines whether the Universe is geometrically flat ($k = 0$), open ($k = -1$), or closed ($k = +1$). The aforementioned components of the Universe in the ΛCDM cosmological model are part of these equations and affect the evolution of the Universe. Here, $\bar{\rho}$ combines the radiation and matter density, which includes in turn dark and baryonic matter. The cold nature of dark matter implies that it is non-relativistic and assumed collision-less. As a result, dark matter does not contribute to the pressure term $\bar{P}$ in equation (1.5). Finally, the cosmological constant Λ represents the presence of dark energy. Another important quantity introduced in this set of equations is the Hubble parameter[1] $H(t)$, which describes the growth rate of the scale factor of the Universe at a given time. We can define a critical density

$$1/R^2 \to 0\,,\ \Lambda = 0 \Rightarrow \rho_C = \frac{3H^2}{8\pi G} \tag{1.6}$$

which allows us to write a more descriptive formulation of equation (1.4), in which the contribution from each component of ΛCDM Universe can be separated. For this,

[1] In this work I define $\dot{x} = \frac{\mathrm{d}x}{\mathrm{d}t}$ for a quantity x

we define relative densities per component

$$\Omega_m = \Omega_b + \Omega_{DM} = \frac{(\rho_b + \rho_{DM})}{\rho_C}, \quad \Omega_k = \frac{1}{a^2}\frac{c^2}{R^2\rho_C}, \\ \Omega_r = \frac{\rho_r}{\rho_C}, \qquad \Omega_\Lambda = \frac{1}{3}\frac{\Lambda}{\rho_C}, \tag{1.7}$$

where ρ_m, ρ_b, ρ_{DM}, and ρ_r are respectively the matter, baryonic matter, dark matter, and radiation (i.e. light and relativistic baryons) densities. Now I rewrite (1.4) as

$$H^2 = \left(\frac{\dot{a}}{a}\right)^2 = H_0^2\left[\Omega_{k,0}\left(1+z\right)^2 + \Omega_{r,0}\left(1+z\right)^4 + \Omega_{m,0}\left(1+z\right)^3 + \Omega_{\Lambda,0}\right], \tag{1.8}$$

where I take for a component that $\Omega_{x,0} = \Omega_x(z=0)$. In this expression, the contribution of each component can be appreciated explicitly, together with its scaling under expansion. Over time, the ΛCDM model has gathered significant evidence supporting it (Smoot et al. 1992; Spergel et al. 2007; Ade et al. 2016), and this thesis adopts it as the Standard Cosmological Model.

After nucleosynthesis, our Universe continued its evolution dominated by radiation - mostly in the form of relativistic particles. Given the scaling of radiation density as $\Omega_r \propto a^{-4}$ (see eq. (1.8)), a growth in the scale factor rapidly leads to domination by matter, which given the values measured for the cosmological parameters (Planck Collaboration et al. 2018), occurs approximately by redshift $z \sim 3600$. During the matter-dominated era, the ongoing formation of structure will become more relevant, emerging from the density field of primordial quantum fluctuations. These fluctuations can be fully described by a power spectrum of the form

$$\mathcal{P}_{\rm prim}(k) = Ak^{n_s-1}, \tag{1.9}$$

where k is the spatial wavenumber. The spectral index n_s will be assumed to be scale invariant, according to inflationary models ($n_s = 1$, Eisenstein & Hu 1997).

1.1.3 Post-recombination magnetogenesis

As the process of formation of structure begins, new possibilities for the generation of magnetic fields appear. The first of this series of processes is recombination.

Recombination

At redshift approximately $z \sim 1100$, the average temperature of the Universe decreases enough to allow the capturing of electrons by protons, forming hydrogen atoms and the Universe became neutral and transparent to photons: the CMB radiation is emitted. If a significant primordial magnetic field existed in our Universe generated by an early Universe mechanism, it would likely have generated no significant heating of the baryonic component prior to recombination. However, depending on the properties of the magnetic spectrum after recombination occurs, even for those fields too weak to perturb the density field, magnetic fields have the potential to generate some baryonic heating (Trivedi et al. 2018).

Magnetism after recombination

Once recombination has ended, there is a vast potential for the generation of magnetic fields that permeate our Cosmos. Many are related with plasma processes that magnetise the gas on small scales. One well-known example is the Biermann battery. This is a seeding process based on the relative displacement of electrons with respect to protons, which in turn induces a weak magnetic field $\vec{B}$ (Biermann 1950)

$$\frac{\partial \vec{B}}{\partial t} = -\frac{c}{e n_e^2} \vec{\nabla n_e} \times \vec{\nabla p_e} \tag{1.10}$$

with n_e and p_e the electron density and pressure respectively. Here e is the electron charge. This mechanism could generate from very high redshifts magnetic fields of $B_0 \sim 10^{-19} - 10^{-20}$ G (Pudritz & Silk 2002). Alternatively, Schlickeiser (2012)

suggests that an unmagnetised plasma can generate turbulent magnetic fields spontaneously, with $B_0 \sim 10^{-16}$ G in media of the typical densities for the intergalactic medium (IGM) and voids.

Other processes occurring in the early stages of structure formation are also candidates to generate ubiquitous magnetic fields. Arguably the most interesting one is reionization. Various authors have addressed how the scattering of radiation pressure and the transfer of momentum through photoionization of the IGM can separate electrons from ions, leading to the generation of an electric field that in turn induces a magnetic field in the plasma (Langer et al. 2003; Durrive & Langer 2015). The electron density and pressure gradients created would also trigger a relevant presence of the Biermann battery mechanism (Gnedin et al. 2000). These studies tend to find that the resulting magnetic field in the IGM would have an strength of $B_0 \sim 10^{-19} - 10^{-20}$ G (Doi & Susa 2011; Durrive et al. 2017).

Finally, an alternative possibility to magnetise the IGM is linked to the structure itself. Magnetised outflows from galaxies and galaxy clusters driven by supernovae (SNe) or active galactic nuclei (AGN) could fill the IGM with strong magnetic fields, polluting or replacing the primordial magnetic field of the Universe.

1.2 On structure formation in the Universe

As the competition between gravity and pressure continues, the Universe expands and the matter spectrum exhibits a scale-dependent behaviour. First, the smallest perturbations collapse, followed by larger scales. While the real picture is significantly more complicated, at first order, the formation of galaxies in the ΛCDM paradigm follows a hierarchical pattern, with the smallest galaxies forming first and then merging to yield larger systems (Press & Schechter 1974).

1.2.1 The Large-Scale Structure

On a multi-scale fashion, the Universe is an intricate ensemble conformed by a series of sheets, filaments and nodes (Bond et al. 1996), often conceived as a web, or network (Coutinho et al. 2016). The formation of these structures is driven by dark matter, and baryonic effects are non-negligible but secondary (van Daalen et al. 2011; Chisari et al. 2018). Overdense regions collapse to form bi-dimensional sheets also known as walls. In those regions where two walls cross, their one-dimensional intersection resembles a string-like structure known as a filament. Finally, points where more than two walls intersect are the nodes where these filaments meet, and they typically host massive galaxies or galaxy clusters. The forming Large-Scale Structure (LSS) is not immutable, continually evolving subject to gravity. As gravitational collapse proceeds, filaments are loaded with mass, establishing matter flows towards the nodes of the web. This consolidates the LSS, and builds-up larger and more massive structures over time.

While these often receive less attention, other important components of the LSS are the large voids formed in those regions devoid of matter which constitute most of the volume of the IGM. A strict definition of voids remains elusive, but there is agreement that voids are underdense regions created by underdense perturbations in the primordial matter spectrum and which can be identified in a 3D density representation of the cosmic web (Ricciardelli et al. 2013). While voids appear to display some substructure, studies show that all can be represented by similar density profiles regardless of their scale (Ricciardelli et al. 2014). These void regions have relatively quiet evolution when compared with overdense regions in the LSS. As a consequence, voids emerge as a particularly interesting target in the quest to probe the primordial magnetic field of our Universe. If a magnetic field was generated by any early Universe mechanism, or perhaps some of those occurring during or shortly after reionisation, it should remain unaltered and unpolluted in the most remote regions of the IGM

or deep in LSS voids. Unfortunately, due to the very low density of voids, current observations have no prospect of detecting any emission characteristic of the presence of magnetic fields. However, an alternative method exists to put a lower limit on these magnetic field. Neronov & Vovk (2010); Taylor et al. (2011) address how TeV emission from distant blazars cascades into posterior GeV emission through pair production. By reviewing the extension of the secondary GeV emission, one can deduce the strength of the intergalactic magnetic field, which would be responsible of deflecting generated particle pairs. Following this line of study, the authors obtain a lower limit to the comoving cosmic magnetic field in a range of $B_0 > 10^{-18}$ G to $B_0 > 10^{-15}$ G, pending on a set of assumptions regarding the effects of the cascade time delay. It is worth noting that a series of papers have disputed the validity of these lower limits based on, amongst others, the relevance of plasma instabilities occurring in the IGM (Broderick et al. 2012; Yan et al. 2018; Broderick et al. 2018; Vafin et al. 2019). To my best knowledge, the validity of these lower limits remains uncertain to this day, and the community presents a discordant variety of views on the issue. The most likely scenario is that these limits are subject to some degree of correction and could potentially be reduced by a handful of orders of magnitude. We can however be more optimistic when assessing the upper limit for the cosmic primordial magnetic field. Anisotropies in the CMB bound the upper cosmic magnetic field strength to be below $B_0 < 4 \cdot 10^{-9}$ G (Planck Collaboration 2015). When combining this result with results from the South Pole Telescope, the limit can be further reduced down to $B_0 < 1 \cdot 10^{-9}$ G (Pogosian & Zucca 2018). Such extremely strong primordial magnetic fields could influence structure formation in a variety of ways, as I will describe later in this manuscript. Similarly, other independent upper bounds are provided by, e.g. the arrival direction of ultra-high energy cosmic rays (UHECRs) assuming their association to specific sources, yielding $B_0 < 0.5 \cdot 10^{-9}$ G (Bray & Scaife 2018). These broad constraints on the cosmological magnetic field reflect our vast observational

ignorance on the configuration and nature of the cosmic magnetic field.

In our Universe baryonic matter is often found in a plasma state, to which I will frequently refer simply as gas. This gas closely follows the evolution of dark matter, falling into filaments and nodes of this cosmic web. The density perturbations on the small cosmological scales are able to collapse further and form galaxies. Groups of galaxies or galaxy clusters form at the largest nodes of the LSS.

These galaxy clusters are composed of large numbers of individual galaxies, submerged in a hot low-density plasma. This plasma is not a negligible component: it contributes a dominant fraction of the total mass of the galaxy cluster (Zhuravleva et al. 2014), and can be observed directly in bands such as X-rays due to its high temperature.

There is a significant body of literature addressing magnetism in the LSS and galaxy clusters. It aims to understand the origin of magnetic fields in large structures (Vazza et al. 2014, 2018), what is the typical configuration expected for their magnetic fields (Marinacci et al. 2015; Gheller et al. 2016), and what are the effects that these magnetic fields have on their properties (Yang & Reynolds 2015; Bambic et al. 2018). While no detection of large-scale magnetic fields has taken place yet, upcoming facilities spark a large amount of theoretical interest in revealing whether this will be possible, and guiding future observations (Vazza et al. 2017; Marinacci et al. 2017). A better comprehension of these magnetic fields has large implications on our understanding of magnetism in smaller astrophysical structures and on the nature of magnetic fields in our Universe. Another set of comparatively small structures in which observational detection of magnetic fields has already taken place, and which share this remarkable importance for cosmic magnetism, are galaxies. This thesis focuses on them.

1.2.2 Galaxies

Galaxies are multi-component systems comprised principally of gas, stars, dark matter, and for the purpose of this work, magnetic fields. Galaxies are found in haloes, mostly comprised of dark matter, with the majority of their volume containing also a hot and low density gas. As dark matter is collisionless and cannot cool radiatively, its collapse is halted once it virialises. On the other hand, the baryonic gas is collisional and emits energy radiatively, further dissipating support, and sinking down the gravitational potential to the centre of dark matter haloes, where it becomes a rotationally supported galaxy. There are several main types of galaxies classified according to their morphology, as dwarfs, spirals, or ellipticals. In all of them, the interstellar medium is filled with gas, structured in multiple phases (Field et al. 1969).

As previously indicated, galaxies form hierarchically. Their formation is however more complex than simple collapse. Galaxies accrue most of their mass either through cold accretion flows (Kereš et al. 2005) or for the most massive ones, through mergers with other massive galaxies (Khochfar & Silk 2009). The processes that supply baryonic mass onto these galaxies will dictate their various properties, such as their stellar mass, angular momentum (Kimm et al. 2011; Tillson et al. 2015), stability (Genel et al. 2012), or morphology (Dekel & Birnboim 2006).

In their ISM, the gas co-exists in multiple phases due to magneto-gravo thermal instabilities (e.g. Ji et al. 2018). Each of these phases is characterised by different properties and exhibits a different behaviour. The cold phase concentrates most of the gas mass, while also amounting to the least of the galaxy volume. It is in this cold phase where gas is able to further collapse, that stars eventually form. These stars then heat some of the gas in this cold phase, driving it to warmer phases. Some of the stellar processes that could do so are stellar winds (Wareing et al. 2018), radiation (Forbes et al. 2016), or supernovae explosions (Rosdahl et al. 2017). This gas also returns to the hot phase enriched with a higher proportion of metals, which in turn

accelerates the cooling rate, sustaining a complex and intricate feedback loop.

Further to these factors, the co-existence of various mass components in the galaxy also influences their evolution, e.g. the effect of the stellar component in the concentration of the ISM gas or stabilising the gas disk (Wang & Silk 1994; Elmegreen & Burkert 2010). The enormous complexity of galaxies is evident. Nevertheless, numerical simulations allow to simultaneously address a significant ensemble of the factors that provide this large complexity.

An important component of the ISM in galaxies, which is however often neglected by simulations of galaxy formation and evolution are magnetic fields. As we will demonstrate in this work, these fields co-evolve with galaxies and play various roles throughout the lifetime of galaxies, altering their properties.

1.3 Magnetic fields in galaxies

Magnetic fields account for a substantial fraction of the energy budget in galaxies. They are found in observations to be in equipartition with the turbulent and thermal energies (Beck 2015). Magnetic fields in galaxies can be separated into two main components: a field organised on galactic scales, and a small-scale turbulent component. The typical strength at which both are observed is at the level of several μG. The presence of these magnetic fields alters several properties of galaxies, e.g. the amount of gas and structure in the various ISM phases (Villagran & Gazol 2018; Ji et al. 2018). The impact of magnetic fields on the ISM is discussed in Section 1.4.1.

A comprehensive approach to understanding magnetic fields in galaxies combines direct observations of magnetic fields with theoretical studies, which are in their majority of numerical nature, as these are the most capable of capturing the large variety of factors at play in the formation and evolution of galaxies, and their interactions.

1.3.1 Observations of magnetic fields

The main aim of magnetic fields observations in galaxies has been to constrain the field configuration, determine how their structure emerges and how they interplay with the ISM. Progress is taking place at a fast pace, and observations are starting to probe magnetic fields in lower density environments, such as the circumgalactic medium (Mulcahy et al. 2017; Sobey et al. 2019). Improvements in resolution are also allowing to probe the fields on smaller scales (Roche et al. 2018). Another fundamental question tackled by state-of-the-art observations is how galactic magnetic fields evolve with redshift. Recent observations find strong and structured magnetic fields are already in place at $z \sim 2$ (Bernet et al. 2008; Mao et al. 2017), with some weaker indirect evidence of their presence at redshifts up to $z \sim 4$ (Kim et al. 2016).

Conducting observations of magnetic fields is an utterly complicated task, usually constrained to radio frequencies and with direct methods relying on complicated assumptions. I briefly introduce the most relevant methods here and refer the reader to Beck & Wielebinski (2013) for further detail.

The most widely employed procedure to observe magnetic fields to date is through the radio synchrotron emission generated by energetic particles spiralling around magnetic field lines. Synchrotron emission is polarised perpendicularly to the magnetic field component in the plane of the sky. Synchrotron observations can thus be used to measure the strength of the magnetic field in this plane, also allowing to determine the 2D structure of the field (see Fig. 1.1 for an illustrative example). Furthermore, when corrected for inclination, it allows to compute the total strength of the magnetic field in three dimensions. Synchrotron emission is still present when the local magnetic field is turbulent or unstructured. However, this turbulent magnetic component provides an unpolarised contribution to the total emission, caused by the small-scale organisation of the magnetic field in the emitting region generating light with randomly oriented polarisations. Even though extracting magnetic field infor-

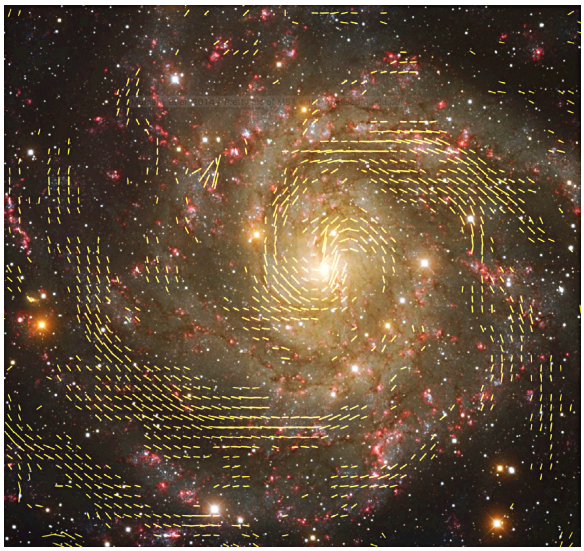

Figure 1.1: Overlay of galactic magnetic field vector orientations on the plane of the sky as yellow segments over a composite colour image taken by Kitt Peak Observatory of the galaxy IC 342. Vectors are of emission at $\lambda = 6.2$ cm, and are rotated 90^o to represent magnetic field galactic structure. This Figure is a reprint of Figure 27 by Beck (2015).

mation from synchrotron emission is ostensibly a powerful procedure, it is not free from limitations. The most significant one is that using it to measure the strength of the magnetic field requires a set of assumptions regarding the particle and energy density of the population of free electrons in the emitting region.

Moreover, the observed synchrotron polarisation is not necessarily equal to that emitted, as the presence of magnetic fields in the line-of-sight plasma column will rotate the polarisation of the emitted light. This phenomenon, known as Faraday rotation, is not necessarily always negative for synchrotron observations. The differential amount of rotation of the polarisation introduced by a parcel of gas depends linearly on the magnetic field strength along the line of sight, and thus can be used to measure the magnetic field component along this direction. It is worth noting that a small-scale turbulent component of the magnetic field does not lead to Faraday rotation, but Faraday depolarisation instead. In that case, the polarisation of the original emission is simply lost due to a incoherent rotation of polarisation vectors

over the integrated area resolved. Once again, to study magnetic fields through this Faraday rotation mechanism, we require information regarding the electron density, and for the purpose of calculating the magnetic field along the line of sight, we require measurements at different wavelengths. An example of a thorough synchrotron-based study of magnetic fields in a galaxy is given in Beck (2015). In Section 1.5 I discuss how future telescopes will push these measurements towards higher redshifts.

An alternative method to measure magnetic field strength and orientation in the plane of the sky is employing optical or far infrared (FIR) light traversing a large fraction of the ISM of a galaxy. The observed light will be polarised due to the removal of certain polarisation orientations by dust absorption. The alignment of dust grains, and the consequent orientation of the absorbed polarisations is governed by the local direction of the magnetic field, therefore allowing its measurement. Due to the required resolution and precision, these measurements are mostly restricted to employing background sources to measure fields in our own Galaxy. This method also requires a reasonable model for dust grain sizes and alignment to extract information about the magnetic field (e.g. Mao et al. 2008).

Finally, observations of the magnetic field can also be done by taking advantage of the Zeeman effect, where the wavelength of an emission line is split into two separate wavelengths depending directly on the strength of the magnetic field in the emitting region. This method is the most direct to extract information about magnetic fields in interstellar and intergalactic plasmas (Han 2017). However, Zeeman splitting is particularly complicated to observe due to the small shift in frequency produced. In galaxies other than our own, this splitting is severely contaminated by other effects such as thermal broadening. An alternative is to employ bright emission lines from masers when these are available.

Most of the observational interest in magnetic fields has focused on dwarf and spiral galaxies. The main reason is that these galaxies have a significant amount

of ongoing star formation or other processes associated with the presence of shock waves in the ISM (e.g. spiral arms). These shocks lead to the acceleration of particles capable of emitting synchrotron radiation. Amongst star forming galaxies, those undergoing starburst phases display the strongest galactic magnetic fields observed so far (Robishaw et al. 2008). While the generation of these strong magnetic fields in starburst galaxies is not well understood yet, the outflows associated with this strong star formation have the potential to launch highly magnetised winds into the IGM (Dubois & Teyssier 2010). Starburst dwarf galaxies display magnetic fields on the order of μG, but not necessarily ordered on galactic scales. Whenever dwarfs are found to host non-significant or no visible star formation, their magnetic fields are measured to be weaker or not observable at all in synchrotron emission.

In spiral galaxies, we find organised magnetic fields on galactic scales (Mulcahy et al. 2014), occasionally displaying magnetic arms located in the inter-arm space separating optical or gas spiral arms (Beck 2015). These magnetic arms are one of several interesting puzzles posed by observations to numerical simulations, discussed later. A turbulent magnetic component is also found in these galaxies, also with a typical strength of several μG (Arshakian et al. 2009). In these galaxies, the magnetic energy is in equipartition with other components (such as the thermal and turbulent) at small radii, and becomes particularly important or even dominant in the outskirts (e.g. Beck 2015). Observations also provide some evidence of interaction between galactic magnetic fields and halo magnetic fields, allegedly through galactic winds powered by SN feedback (Mulcahy et al. 2017).

Magnetic fields are more elusive in elliptical galaxies. This is largely due to the absence of significant synchrotron emission whenever they do not display AGN activity. Because star formation is quenched in these objects, they lack energetic particles which spiral around magnetic fields lines to emit synchrotron. Whenever present, most of the accelerated particles are associated with AGN, and it is difficult to disen-

tangle its synchrotron emission from any other that could be produced by the galaxy (Panessa et al. 2019). In spite of these difficulties, the expectation is that, as for previously described galaxies, ellipticals also possess magnetic fields on the order of μG. Their future study will rely on instruments with much better sensitivities or other mechanisms which instead do not depend on particle acceleration.

Magnetic fields permeate the ISM of all galaxies, observed in all the phases and found to be relevant for many sub-galactic processes. I describe these in more detail in Section 1.4, but here I illustrate the remarkable capabilities of current observations to study magnetic fields in the ISM. Examples are observations detecting interesting helical magnetic structures in cold Galactic filamentary clouds (Tahani et al. 2018), or studies of star forming regions for which their morphologies are attributed to the magnetic field (Hull et al. 2017). Magnetic fields have also been detected and studied in hot interstellar bubbles such as supernova remnants (Reynolds et al. 2012; Chen et al. 2017), where the variety of configurations of the magnetic field, either more randomised or more organised in the shell of the remnant, is not well understood yet (West et al. 2017). Observational studies even reach the very centre of our own galaxy, which is being probed with unprecedented detail (Roche et al. 2018).

1.3.2 From the theoretical side

Developing a theoretical understanding of magnetic fields is extremely challenging due to the remarkably complex origin and evolution of this component. Due to their vectorial nature, magnetic fields are intrinsically anisotropic quantities which co-exist on multiple scales and interact both locally and with larger structures of the ISM. Analytical and semi-analytical models provide invaluable insight onto which physical effects shape real systems by allowing us to reduce the latter to their most fundamental components. Consequently, there has been some work in the literature which addresses magnetic fields in galaxies analytically (e.g. Lesch & Chiba 1995), under

simplified assumptions for magnetism. However, this approach is severely hampered by the limitations indicated at the commencement of this paragraph, so that the scope of its conclusions is severely restricted. Under these circumstances, it seems natural to resort to numerical studies. Consequently, the majority of theoretical studies of magnetic fields in astrophysics, be it for LSS, galaxy clusters, galaxies, the ISM, or even small-scale turbulent boxes, are usually performed by means of magnetohydrodynamical (MHD) simulations.

Ideal MHD is the most common implementation employed for these problems, as the majority of the baryonic matter in astrophysical environments is a plasma with negligible resistivity. Performing such simulations is no easy task: they require vast amounts of computational resources (both time and memory) and their analysis is far from simple. Furthermore, the implementation of MHD in numerical codes is arduous, and it has been found on multiple occasions that different numerical schemes lead to different results, with no clear evidence of numerical convergence between different methods (Balsara & Kim 2004). I will review this last aspect in more detail in Chapter 2, where I also present the numerical implementation for solving the MHD equations employed in this thesis.

As their observational counterparts, numerical studies have addressed a wide range of environments and scales, ranging from chunks of the ISM to entire galaxies, cosmological zoom simulations of individual galaxies, or large cosmological volumes encompassing a large population of galaxies. However, there is a coupling between small-scales and large-scale magnetic fields. This implies that processes occurring at small-scales can affect large-scales magnetic fields and vice-versa. As a result, simulations need to account for both to properly model their evolution, and a combination of simulations including a large range of scales is required to properly understand magnetism. A well-known example is the turbulent dynamo, which amplifies the magnetic field at resistive scales, theoretically in the sub-viscous regime, and feeds

back strong magnetic lines to larger scales (Schekochihin et al. 2002).

These demanding conditions difficult obtaining representative models of individual galaxies, but are also a barrier when trying to compare simulations with observations, as differences caused by numerical resolution are likely to arise between the two. Another difficulty of this comparison between the theoretical and observational sides lies in the fact that magnetic fields observations do not yield directly the strength and structure of the field, but require instead a significant number of assumptions about the properties of the electron populations, dust, etc. Contrarily, simulations exactly define a magnetic field in the entirety of their volume at all times. However, in ideal MHD, quantities like the electron number density or electron temperature are still not modelled. Future simulations such as those of employing radiative transfer magnetohydrodynamics will be capable of improving our mock observations by providing ionisation fractions, which could also be coupled consistently with non-ideal MHD. It should therefore not be surprising that numerical simulations struggle to reproduce some observational results such as the existence of strong magnetic fields in the interarm region (Chamandy et al. 2014).

Arguably the most important question about magnetic fields in galaxies is what is their origin. Some of the possibilities for primordial magnetic fields were presented in Sections 1.1.1 and 1.1.3. Most of them predict an overall magnetic field strength which is extremely weak. This naturally creates a tension between theoretical scenarios and the observed magnetic fields, as one needs to explain how the gap between the two is bridged (Rees 1987). A first and appealing possibility is that primordial magnetic fields are of relatively high strength, either through one of the aforementioned magnetogenesis scenarios, or some yet-unknown process. If that is the case, the strength of magnetic fields in galaxies, galaxy clusters and the existence of an ubiquitous cosmic magnetic field can all be explained as a direct consequence of the process of structure formation, which naturally provides amplification of the field through compression

during gravitational collapse (Sharma et al. 2018). However, the only circumstantial evidence supporting this scenario is provided by observations at high redshift where galactic magnetic fields are found already at μG strengths (Bernet et al. 2008; Mao et al. 2017). These detections of magnetic fields at increasingly higher redshifts reduce the time available for other amplification or seeding mechanisms to take place and favour a primordial origin for which these fields are expected at all redshifts. Nonetheless, the most likely theoretical framework corresponds to low $B_{\rm prim}$ magnetogenesis. One alternative possibility for attaining the observed magnetic field values in that scenario is amplification by galactic dynamo mechanisms that convert kinetic energy into magnetic energy (Schekochihin et al. 2004). As I will discuss later, some dynamos are capable of amplifying very weak primordial fields to μG values even by the highest redshifts for which some evidence of strong magnetic fields has been found so far (i.e. by $z \sim 4-5$; Kim et al. 2016). An alternative scenario to the primordial origin of cosmic magnetism, stipulates that astrophysical sources amplify magnetic fields on very small scales and provide in turn strong magnetic fields through their feedback. These can range from stellar dynamos to active galactic nuclei and supernovae (Rees 1987; Vazza et al. 2017; Beck et al. 2013; Butsky et al. 2017). These will supply magnetic fields to the ISM or clusters through winds, explosions, or jets. However, this scenario faces the challenge of how to stretch spatially localised fields to galactic scales and transfer them to the intergalactic medium and LSS.

Each of these three possibilities is introduced in more detail later in this thesis, altogether with an overview of the current state of their exploration. In Chapter 4, I describe my own results in addressing how the origin of magnetic fields in galaxies could be through the amplification of a weak pre-galactic seed through a turbulent dynamo. The small-scale field produced by this dynamo later has a significant amount of time to be re-structured into a large scale component through the rotation of a galaxy. In Chapter 5, I present my work related to the potential origin of galactic

magnetic fields by either primordial or star-generated magnetic fields, discussing how a new method I have co-developed allows to study their interaction and competition to dominate the magnetic field of galaxies. Using these MHD numerical studies I also found that various properties of galaxies are shaped by galactic magnetic fields. I discuss these results in Section 1.4.

1.4 The role of magnetic fields in shaping galactic properties

As a main contributor to the energy budget of galaxies, magnetic fields are not only affected by the evolution of galaxies, but also shape their properties to a certain extent. In some extreme cases strong primordial magnetic fields might even inhibit the formation of dwarf galaxies altogether (Dubois & Teyssier 2010). In fact, some evidence of the impact of magnetic fields on the galaxy population has already been claimed by simulations (Marinacci & Vogelsberger 2016). In this Section I briefly review some well-known and other more uncertain effects of magnetic fields which could potentially alter galaxies and their formation process.

1.4.1 The ISM

As most of the magnetic energy permeates the ISM, and magnetic fields display both a large-scale and small-scale structure in this medium, a large impact from the magnetic component is expected to occur at the level of the interstellar gas. Once the magnetic energy in the ISM saturates, and the operating dynamos only sustain the field rather than amplify it, magnetic forces are expected to back-react on gas dynamics.

Indeed, the saturation of magnetic fields has been found to have an impact on the multi-phase structure of the ISM (Evirgen et al. 2017; Ji et al. 2018). Flows in the interstellar medium of galaxies are characterised by complex structuration, with

angular momentum and kinetic energy supplied by inflows on large scales (Klessen & Hennebelle 2010), turbulent forcing at intermediate scales taking place through supernova explosions (Korpi et al. 1999; Hopkins et al. 2013) and gravitational fragmentation (Krumholz & Burkhart 2016), or the strong stratification of galactic disks to name a few. In this intricate picture, magnetic fields are also crucial actors. In their presence the number of star forming regions is reduced (Hennebelle & Iffrig 2014). The number of small clumps in the ISM also decreases, with the medium becoming more filamentary (Iffrig & Hennebelle 2017). This likely depends on what is the configuration of magnetic field lines in the galaxy, with their regularity potentially altered by whichever mechanism is driving the evolution of the magnetic field (e.g increased star formation leads to lower uniformity of magnetic lines; Chyży 2008).

As the outskirts of galaxies are probed, the thermal and turbulent support seem to decrease faster than the contribution from magnetic pressure (Pakmor et al. 2017). This could lead to systematic disk flaring (Ramos-Martínez et al. 2018). Magnetic fields can also contribute to funnel gas towards the centre of galaxies undergoing ram-pressure stripping by, amongst other effects, reducing the compressibility of the gaseous disk (Ramos-Martínez et al. 2018). The gas stripped also appears smoother and more closely bound to the galaxy (Shin & Ruszkowski 2013).

At galactic scales, magnetic fields reduce the amount of gas at the highest densities (Wang & Abel 2009), altering in the process the fraction of gas mass in the cold neutral medium (Villagran & Gazol 2018). They also alter giant molecular clouds (GMCs), as for the case when accretion proceeds along magnetic field lines, in which a cloud can become supercritical more easily and undergo global collapse (Vázquez-Semadeni et al. 2011). Filamentary structures frequently form in these clouds, typically aligned with the cloud magnetic field (Hennebelle & Iffrig 2014). If these filaments are flow structures that accrete gas from their hosting clouds and direct it to star forming sites, their magnetic fields should display U-shaped patterns, in qualitative agreement with

observations from the Planck mission (Gomez et al. 2018). For most of them, the magnetic diffusion and magnetic properties of the flow in a filament will affect the gas supply to star forming regions.

1.4.2 Subgalactic - star formation and stellar feedback

Magnetic fields are renowned to be crucial for star formation, from the removal of angular momentum (Wurster et al. 2018) to the observed support against collapse in some GMCs (Kauffmann et al. 2013).

On galactic scales, the effect of magnetic fields on the stellar component appears to be secondary compared with the influence of stellar feedback (Su et al. 2017). Equally, magnetic fields do not seem to substantially affect the global stellar mass of a galaxy (Pakmor et al. 2017). However, the presence of a magnetic component significantly shapes the process of galactic star formation. Magnetic fields in galaxies delay the onset of the formation of stars (Hennebelle & Iffrig 2014), and reduce global galactic star formation rates (Iffrig & Hennebelle 2017). In turn, magnetic fields might increase the star formation rate for individual clouds, inhibiting turbulence (Zamora-Avilés et al. 2018). While these two results might appear to be in contradiction with the unobserved changes of global galaxy stellar masses in the presence of magnetic fields (Su et al. 2017), star formation could proceed for longer periods of time at a lower rate to still produce the same final stellar mass content. Alternatively, this disagreement might result from different numerical schemes. A caveat to keep in mind is that all the aforementioned studies are numerical, where the implementation of sub-grid star formation is bound to affect the results. As the resolution of simulations of galaxies improves, galactic-scale empirical laws used to reproduce the observed star formation rates commence to break down. This, and our approach to deal with this issue are discussed in Chapter 2.

Magnetic fields are also important for feedback processes. In the stellar feedback

case, magnetic fields are likely to play an important role in SN explosions (Zhang et al. 2018; Fujisawa et al. 2018). For galaxies, they might influence the supply of energy by SN remnants, and have been argued to partially motivate feedback models as delayed cooling (Stinson et al. 2006; Teyssier et al. 2013). The presence of magnetic fields in the environment of stellar feedback sources will also affect the impact that these feedback events have on the ISM (Seifried et al. 2012; Ntormousi et al. 2017). On larger scales, accounting for magnetised galactic winds allows us to explore whether strong magnetic fields are ejected from galaxies to the IGM (Dubois & Teyssier 2010) and how they propagate. A related issue is whether magnetic fields inhibit SN-driven turbulence by an analogous mechanism to that of magnetic draping of AGN bubbles (Bambic et al. 2018).

At this stage, it is worth reviewing additional pieces of physics which are generally missing in simulations and are likely to also influence star formation and stellar feedback. Interestingly, most of these require magnetic fields to be modelled to reasonable accuracy. This makes magnetic fields the next obvious component to become the norm in numerical simulations of galaxy formation and evolution.

1.4.3 Magnetic fields and other galactic physics

Significant effort has been made in the last decade to understand the importance of stellar feedback. As our comprehension improves, efforts are shifting towards including yet more complex physics, such as radiation, cosmic rays, and even dust effects. The former is particularly relevant for magnetism due to effects arising from the coupling between ions and radiation, which could generate magnetic fields during the epoch of reionisation. Cosmic rays have their dynamics directly affected by the presence of magnetic fields. Dust in turn is important to better understand our observations of magnetic fields.

Cosmic rays (CRs) have been gaining popularity as a missing feedback ingredient

in numerical simulations. These energetic particles are likely to supply important quantities of thermal energy to the ISM, but also have intricate dynamics. This is due to the two mechanisms that decouple cosmic rays from gas dynamics, namely cosmic ray diffusion and streaming. Both are dependent on the local magnetic field (Zweibel 2013). Furthermore, the main mechanisms contemplated for the acceleration of cosmic rays require the presence of magnetic fields and shock waves (Wittor et al. 2017). As a result, modelling CRs in simulations also requires the inclusion of magnetic fields (Dubois & Commerçon 2015; Pfrommer et al. 2017). One of the reasons cosmic rays have been gaining popularity in recent years is their potential capability to drive and enhance galactic winds (Salem & Bryan 2014; Samui et al. 2018), solving the current tension between numerical simulations and outflow observations. Furthermore, cosmic rays have been suggested to have other interesting effects such as the capability to alter disk structure and the ISM (Girichidis et al. 2016), modify stellar initial mass functions (IMFs, Fontanot et al. 2018), or heating the IGM (Jana & Nath 2018).

Finally, the presence of dust in the ISM will also play a role in shaping galaxies. Dust grains play a significant role in coupling radiation with the ISM gas, trapping emission or boosting the impact of radiation pressure (Rosdahl & Teyssier 2015). Further to the local orientation of dust grains, dust dynamics will also be influenced by magnetic fields (Hopkins & Squire 2018).

1.5 The window to the magnetic Universe and SKA

A vast amount of observational information about magnetic fields in galaxies is already available from current state-of-the-art observations by surveys such as LOFAR[2]. LOFAR has the potential to look for both polarised and unpolarised emission at low

[2]http://www.lofar.org/astronomy/cosmic-magnetism/measuring-cosmic-magnetic-fields/measuring-cosmic-magnetic-fields

radio frequencies. On top of this, it can also study the formation of first structures through 21cm emission, map the 3D structure of the galactic magnetic field, and its 2D structure in other galaxies (Beck 2015).

While LOFAR is a remarkable telescope currently operating, the prospects for SKA revolutionise the sample size and the depth of any present facility.

SKA will generate an all-sky survey of $\sim 10^7$ background sources, yielding information of magnetic fields through rotation measures (RM), up to redshift $z = 3$ (Gaensler et al. 2004). Advances in polarimetry will be one of the major developments brought by SKA, allowing this telescope to detect low degrees of polarisation (i.e. $\lesssim 1\%$), while also permitting detections at different frequencies. This will be particularly useful for RM studies. This is because employing RM to extract information about the magnetic field requires information about the electron population of the source. This disadvantage can be overcome by employing multi-frequency RM studies (in at least three separate bands) which break the degeneracy between the electron density and the magnetic field strength and orientation along the line of sight (Clarke 2004). More complex methods (which also require polarisation observations and small Faraday depolarisations) such as Faraday tomography allow to obtain the 3D structure of the magnetic field (Beck & Wielebinski 2013).

Through RM grid observations of local galaxies and the Milky Way, SKA will have the potential to map magnetic fields with enough precision to tackle questions such as what is the vertical structure of the field, how are magnetic reversals configured, or improving our understanding of magnetism in haloes. These measurements can also be done for clusters of galaxies, allowing the first measurements mapping the structure of magnetic fields in these systems.

SKA will increase the current number of observed sources by various orders of magnitudes just in one year of observations.

The most exciting perspective is the one for the IGM field, where SKA has the

potential to observe or constrain its strength with a significant degree of confidence, given the sample of RM is ample enough. An example of the possibilities for these constraints comes from Kolatt (2002). Their technique could lead to the detection of a $B_0 \sim 10^{-10}$ G, already below current upper observational constraints.

Other goals of SKA will also benefit from understanding cosmic magnetism, as observing diffuse synchrotron emission from baryons infalling onto the LSS, even in the presence of considerably weak magnetic fields. An example of potential detection of a filament in synchrotron emission is done by (Bagchi et al. 2002), with a magnetic field of 0.3 μG. Given its power, SKA could at low frequencies map the diffuse synchrotron from filaments in the local supercluster (Wilcots 2004). For the case of the Perseus-Pisces cluster, SKA could also observe infalling baryons into the connecting filament with the Virgo cluster at virial shocks.

With the advent of facilities such as SKA, the current disconnect between MHD simulations of galaxies and their observational counterpart complicates fully exploiting the potential that numerical studies have to help understand observations. From the numerical perspective, it emerges from the aforementioned difficulty faced in capturing the vast dynamical range of magnetic fields or to reproduce the observations in the absence of various components. Strong synergies are commencing to emerge, with simulations of individual galaxies that will help future observations, and large simulations capable of capturing galactic properties while modelling cosmological scales, such as IllustrisTNG (Pillepich et al. 2018). Thus, numerical simulations have to step up to the challenge, developing novel methods that allow accurate comparison with observations, providing them with the physical insight that simulations possess. For this task, not only mock observational methods will be required (e.g. mock synchrotron maps), but also new numerical methods to unfold the evolution and effects of the magnetic component. This thesis should be considered as a step in this direction.

Chapter 2

Methods

Modelling the formation of structure is no easy task. It involves following the evolution of various mass components (gas, stars and dark matter), governed by a non-linear set of hydrodynamical equations, and all coupled through the action of gravity. Furthermore, additional physics are crucial in shaping the structures observed in our Universe. E.g. chemistry, magnetism, radiation, or even atomic and nuclear physics taking place in stars. As we aim to study galaxy formation, we require a method capable of encapsulting this physics, or at the very least, to account for their most important effects.

This is precisely what has been done by a number of publicly available astrophysical codes specialising in solving structure formation problems. Popular examples are Ramses (Teyssier 2002), ENZO (Bryan et al. 2014), or Gadget (Springel et al. 2001). These codes are the result of many years of dedicated work. They have demonstrated extraordinary versatility to tackle structure formation. Proof is the remarkable fact that simply selecting the appropriate initial conditions, one can employ these codes to simulate structure formation from molecular clouds, to cosmic scales.

While these numerical codes are not devoid of their own limitations, when employed carefully, they are fantastic tools to study the role played by each piece of

physics intervening in the growth of structures and the effects of their combination. Through them, we can also interpret and predict existing and future observations.

All the work presented in this thesis has been done using the MHD version of the Ramses code (Teyssier 2002; Teyssier et al. 2006; Fromang et al. 2006). I review this code in this Chapter. As I have also made significant modifications and extensions to Ramsesto tailor it for the task at hand and extend its capabilities, I present some of them in this Chapter. I commence by introducing in Section 2.1 the magnetohydrodynamical equations, and their re-formulation for cosmological simulations, as well as the divergence-free constrained transport method to implement them numerically. Section 2.2 describes in some detail the physics available in the Ramses code and my implementation of a term accounting for the Universe expansion in the evolution of the magnetic field equation. In Section 2.3, I describe the stellar feedback and star formation routines, which I have extended to either account for the presence of local magnetic fields or inject them in simulations. I describe in Section 2.4 the general procedure to carry simulations of galaxies, and more specifically the zoom-in technique employed to generate cosmological simulations of their formation with high spatial resolution. Finally, in Section 2.5, I present the methods I have employed to generate optical mock images from simulations in order to compare them with observations.

2.1 Magnetohydrodynamics

The equations of magnetohydrodynamics are an extension of the hydrodynamic equations to describe the dynamics of electrically conductive fluids in the presence of magnetic fields. In an astronomical setup, these equations serve to describe the evolution of plasma in the fluid limit. Due to its high conductivity when fully ionised, plasma can be assumed to have infinite conductivity for most applications (e.g. Pakmor et al. 2011). The MHD equations in their Eulerian form describe the mass, momentum,

and energy conservation

$$\frac{\partial \rho}{\partial t} + \vec{\nabla} \cdot (\rho \vec{u}) = 0, \tag{2.1}$$

$$\rho \frac{\partial \vec{u}}{\partial t} + \rho \left(\vec{u} \cdot \vec{\nabla} \right) \vec{u} - \left(\vec{B} \cdot \vec{\nabla} \right) \vec{B} + \vec{\nabla} \left(\frac{B^2}{2} \right) + \vec{\nabla} p + \rho \vec{\nabla} \phi - \vec{\nabla} \cdot \bar{\sigma} = 0, \tag{2.2}$$

$$\frac{\partial \epsilon}{\partial t} + \vec{\nabla} \cdot \left[(\epsilon + p + p_{\rm mag}) \, \vec{u} - \vec{B} \left(\vec{B} \cdot \vec{u} \right) \right] - \vec{\nabla} \cdot (\bar{\sigma} \cdot \vec{u}) = 0, \tag{2.3}$$

respectively for a fluid. When these are applied to a volume, ρ corresponds to the density of the fluid inside it, $\vec{u}$ is the velocity of the fluid traversing the volume, $\vec{B}$ is the magnetic field permeating this volume, ϕ the gravitational potential, and $\bar{\sigma}$ the anisotropic viscous stress tensor, negligible in most astrophysical environments ($\bar{\sigma} = 0$). p and $p_{\rm mag}$ are the thermal and magnetic pressure supporting the fluid respectively, and ϵ is its internal energy density. To fully complete the description of a conducting fluid, the MHD equations include an equation of state (eq. 2.16) and the induction equation

$$\frac{\partial \vec{B}}{\partial t} - \vec{\nabla} \times \left(\vec{u} \times \vec{B} \right) - \eta \nabla^2 \vec{B} = 0 \tag{2.4}$$

to describe the evolution of the magnetic field, and the solenoidal constraint

$$\vec{\nabla} \cdot \vec{B} = 0, \tag{2.5}$$

which reflects the fact that, as explained in Chapter 1, there are no monopoles in the magnetic field. Another quantity introduced in equation (2.4) is the magnetic diffusivity η, inversely correlated with the conductivity of the fluid. Unless it is indicated otherwise, I will assume that the physical value for the magnetic diffusivity is negligible ($\eta \to 0$) for the fluid in my simulations.

To study structure formation and evolution, we solve the hyperbolic (e.g wave-like equations or time-evolving problems) MHD equations as an initial value Cauchy

problem. This is done either with a Lagrangian or Eulerian approach, depending on how the mass in the studied domain is assigned. A usual Eulerian treatment is to divide the domain in cubic cells by iterative bisection, and solve the Riemann problem for every common boundary between every two pairs of cells (i.e. cell faces). Alternatively, mass in the simulation can be represented by point-like particles, evolved with the Lagrangian form of the MHD equations. These are connected to the Eulerian representation by the Lagrangian derivative (for a tensor field a)

$$\frac{Da}{Dt} = \frac{\partial a}{\partial t} + \left(\vec{u} \cdot \vec{\nabla}\right) a. \tag{2.6}$$

Novel methods aim to improve physical accuracy while reducing computational costs by exploring sophisticated ways to divide the spatial domain (e.g. see works of Springel 2010; Hopkins 2017). A popular approach for Eulerian codes is Adaptive Mesh Refinement, the method employed by RAMSES and described in Section 2.2.1.

This concludes a general presentation of the MHD equations, but their application to a cosmological context benefits from their reformulation to a different set of coordinates.

2.1.1 Cosmological Magnetohydrodynamics

The set of equations introduced above do not account for the expansion of the Universe. To do this, it is useful to define a set of variables comoving with the expansion of space which allows us to rewrite eqs. (2.1 - 2.3) in an almost identical form. The comoving variables for numerical cosmological simulations are commonly referred to as supercomoving (SCM) coordinates. Presented by Martel & Shapiro (1998), the set implemented in RAMSES relates the comoving distance $\hat{\vec{r}}$, density $\hat{\rho}$, peculiar velocity

$\hat{\vec{v}}$, and specific internal energy $\hat{\varepsilon}$ as

$$\hat{\vec{r}} = \frac{\vec{r}}{ar_*}, \quad \hat{\vec{v}} = \frac{a\vec{v}}{v_*}, \quad \hat{\rho} = \frac{a^3\rho}{\rho_*}, \quad \hat{\varepsilon} = \frac{a^2\varepsilon}{\varepsilon_*}. \tag{2.7}$$

The peculiar velocity $\vec{v}$ is defined as

$$\vec{v} = \vec{u} - H\vec{r}, \tag{2.8}$$

We also introduced fiducial scaling factors x_* for each quantity, to scale the numerical values for each variable into a numerical regime where the computing hardware and software yield the most accurate results. Martel & Shapiro (1998) suggest definitions for all the scaling factors corresponding to each supercomoving coordinate

$$\rho_* = \frac{3H_0^2\Omega_0}{8\pi G}, \quad \vec{v}_* = \frac{r_* H_0}{2}\sqrt{\Omega_0 a_0^3}, \quad \varepsilon_* = v_*^2, \tag{2.9}$$

except r_* which hence determines the entire system. Combinations of the SCM variables give other quantities such as time $\hat{t}$, or pressure $\hat{p}$ through straightforward dimensional analysis. For example the Hubble constant is equivalent to

$$H(t) = \frac{1}{a^2 t_*}\mathcal{H} = \frac{v_*}{a^2 r_*}\mathcal{H} = \left(\frac{v_*}{a^2 r_*}\right)\left(\frac{1}{a}\frac{\partial a}{\partial \hat{t}}\right), \tag{2.10}$$

where $\mathcal{H}$ is the SCM Hubble constant. To obtain the SCM form of the MHD equations, we express in supercomoving coordinates the time derivative and spatial gradient

$$\left(\frac{\partial f}{\partial t}\right)_r = \frac{1}{a^2 t_*}\left[\left(\frac{\partial f}{\partial \hat{t}}\right)_{\hat{r}} - \mathcal{H}\hat{\vec{r}}\left(\hat{\vec{\nabla}} f\right)_{\hat{t}}\right], \tag{2.11a}$$

$$\left(\vec{\nabla} f\right)_t = \frac{1}{ar_*}\left(\hat{\vec{\nabla}} f\right)_{\hat{t}}. \tag{2.11b}$$

Under these transformations, the hydrodynamical (i.e. no magnetic fields) mass (eq. (2.1)) and momentum conservation (eq. (2.2)) equations remain unchanged. The energy conservation equation becomes

$$\frac{\partial \hat{\epsilon}}{\partial t} + \hat{\vec{\nabla}} \cdot \left[\left(\hat{\epsilon} + \hat{p} \right) \hat{\vec{u}} \right] = \mathcal{H} \left(3\gamma - 5 \right) \hat{\epsilon}, \tag{2.12}$$

where γ is the specific heat ratio. A drag term $\mathcal{H}\left(3\gamma - 5\right)\hat{\epsilon}$ appears in equation (2.12), associated with contributions to the internal energy of the fluid from rotational and vibrational modes, unchanged by expansion. Throughout this thesis my choice of γ is that of a monatomic gas (i.e. $\gamma = 5/3$). The internal energy thus only depends on the kinetic motion of individual particles. The drag term vanishes and we can treat the cosmological case using the same algorithms as for the non-cosmological case, so long as we take into account the transformation to supercomoving coordinates.

So far, my description of the hydrodynamical equations in SCM coordinates has omitted magnetic fields. To adapt Ramses to cosmological simulations with magnetic fields, I developed a SCM implementation of the magnetic field, described in more detail in Section 2.2.3, where I also present numerical tests to show its validity. It is useful to review the scheme employed to solve the magnetic part of the magneto-hydrodynamical equations in Ramses prior to describing this extension. Namely the Constrained Transport (CT) scheme which guarantees the fulfilment of the solenoidal constraint (eq. (2.5)) to machine precision.

2.1.2 Constrained Transport: a divergence-free solution

Despite of its simplicity, the solenoidal constraint for the magnetic field is remarkably problematic to implement in a numerical MHD solver. While the induction equation preserves the solenoidality of the field when solved analytically in a continuous medium, once the spatial domain is discretised and a numerical solution is sought,

this is no longer the case. One could choose to ignore this artificially generated divergence, but the magnetic monopole grows rapidly and it can dominate the magnetic field strength. Over the years, numerical astrophysical simulations have approached this issue in a variety of ways:

1. A popular approach to keep the magnetic divergence under control is to use a divergence cleaning scheme. Some of these include in the MHD equations a term proportional to $\vec{\nabla} \cdot \vec{B}$ and then either propagate this non-zero divergence outside of the computational domain or damp it (Balsara & Kim 2004). An example is the method by Powell et al. (1999) and employed by studies such as Pakmor et al. (2011). Wang & Abel (2009) use instead the Dedner et al. (2002) divergence-cleaning. Alternatively, other authors (e.g. Dolag & Stasyszyn 2009) subtract the magnetic divergence effect from the Lorentz force in their simulations, according to Borve et al. (2001). However the zero divergence of the magnetic field by these methods is never fully enforced, and still dominates the magnetic field in various regions of simulations.

2. An alternative and elegant approach is to eliminate all divergence of the magnetic field by construction. The CT method proposed by Evans & Hawley (1988) does precisely this with a remarkable robustness. This method is implemented in various codes such as Ramses (Teyssier et al. 2006), Athena (Stone et al. 2008), or Pencil (Brandenburg & Dobler 2002).

A good way to quantify the monopolar error is with local and global measurements of the relative magnetic divergence defined as the ratio of the absolute value of the magnetic divergence in a resolution element to the absolute value of the magnetic field in this element:

$$\text{relative magnetic divergence} = \frac{|\vec{\nabla} \cdot \vec{B}|}{|\vec{B}|} \Delta \mathrm{x}_{\mathrm{cell}}, \tag{2.13}$$

where $\Delta x_{\rm cell}$ is the cell size of a resolution element of a discretised grid. As this quantity approaches ~ 1, the resolution element becomes a magnetic monopole, and the $\vec{\nabla} \cdot \vec{B} \neq 0$ component can influence the evolution of the fluid both dynamically and through the induction equation. When expanding the induction term in eq. (2.4)

$$\vec{\nabla} \times \left(\vec{u} \times \vec{B}\right) = \vec{u} \overset{(1)}{\left(\vec{\nabla} \cdot \vec{B}\right)} - \vec{B} \overset{(2)}{\left(\vec{\nabla} \cdot \vec{u}\right)} + \overset{(3)}{\left(\vec{B} \cdot \vec{\nabla}\right)} \vec{u} - \overset{(4)}{\left(\vec{u} \cdot \vec{\nabla}\right)} \vec{B}, \tag{2.14}$$

it can be seen that this monopolar contribution will not only contribute to terms (2) and (3), and advect with term (4), but because term (1) will no longer be null, a magnetic field proportional to the divergence will always be generated in the direction of motion $\vec{u}$. In addition, whenever the magnetic field is dynamically important, monopolar magnetic fields will also influence the dynamics through eqs. (2.2) and (2.3). Therefore, one should aim for simulations where divergences of the magnetic field never exceed a cautiously selected threshold.

To illustrate the remarkable divergence-less capabilities of CT when compared with other schemes for the magnetic component, Figure 2.1 reproduces from Hopkins (2016) a comparison of various numerical test problems. The top part of the figure displays 2D test problems while the bottom half presents results from more realistic astrophysical applications. In the upper half, each pair of columns is a different 2D test (from left to right: field loop advection, Orszag-Tang vortex, MHD rotor, and MHD blastwave) with the fluid solution shown on the left, and the relative magnetic divergence on the right. Each row displays results from a different MHD solver. From top to bottom the solvers used are: Constrained Transport, Constrained Gradients (CG Hopkins 2016), Dedner divergence cleaning, and Powell divergence cleaning. The bottom half of this Figure gives results for two test problems. The left half displays a full physics simulation of a galaxy using the Hopkins et al. (2014) FIRE models for stellar feedback in winds and supernovae, stellar radiation pressure, and photoheating,

and the multi-phase ISM. The right half displays instead the Santa Barbara cluster (details in Hopkins 2016). For each test problem the three columns correspond from left to right to the ratio of magnetic to thermal pressure (galaxy) or density (cluster), the relative magnetic divergence, and

$$\frac{|\vec{\nabla}\cdot\vec{B}|}{\sqrt{2\left(P_{\rm mag}+P_{\rm th}\right)}}\Delta \mathrm{x}_{\rm cell}. \tag{2.15}$$

Each row again represents (from top to bottom) MHD solvers: CG, Dedner, and Powell cleaning. For Hopkins (2016) Gizmo implementation Figure 2.1 shows that divergence cleaning methods still display a significant monopolar component of the magnetic field which influences the evolution of the magnetic field and hence the dynamics, even for the simplest 2D tests. Furthermore, each MHD solver provides a significantly different solution for the galaxy simulation. A similar comparison is done by Mocz et al. (2016) for the Powell divergence cleaning and CT implementations in the Arepo code. They find a different structure for the density and magnetic fields in the galaxy. Furthermore, the magnetic energy saturates above both the thermal and turbulent components in the moving Powell simulation, while it remains approximately comparable to the turbulent energy in the CT simulation.

I remark that it is specifically relevant to ensure $\vec{\nabla}\cdot\vec{B}$ is controlled when modelling shocks and turbulent flows, as it will be in these regions where line stretching and tangling will lead to the largest divergences (Balsara & Kim 2004). The integrated quantities in Figure 2.1 reveal that depending on the MHD solver, magnetic fields can display divergences per cell $(\vec{\nabla}\cdot\vec{B})\,\Delta x_{\rm cell}$ comparable to local magnetic field values $|\vec{B}|$. For the study of dynamo amplifications presented in Chapter 4, it is fundamental to ensure that the amplification of the magnetic field is not driven by the presence of a monopolar contribution. With divergence cleaning algorithms, a rapid diffusion of the artificial magnetic divergence is not guaranteed, and therefore, the dissipation time of

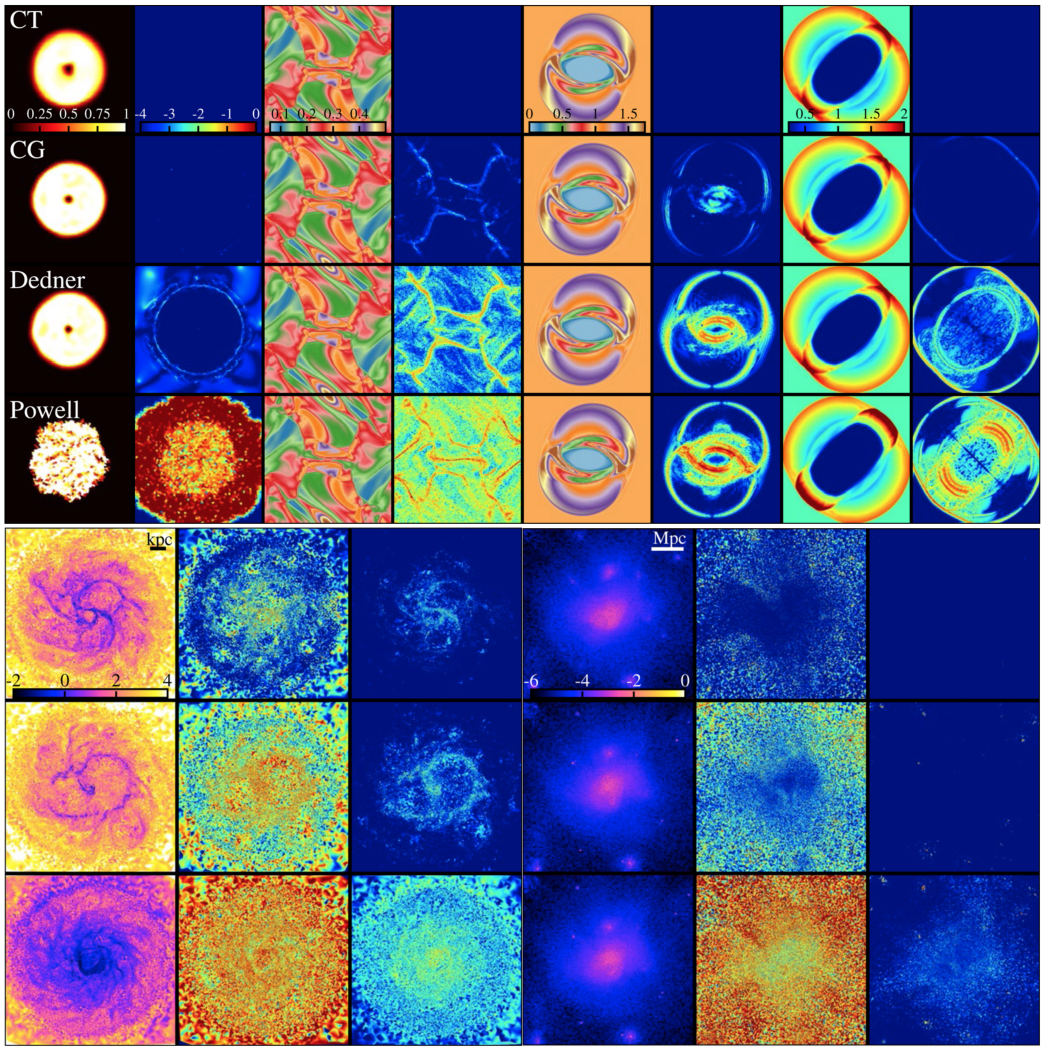

Figure 2.1: Reprint of Figures 4 (top half of this Figure), and 8 (bottom half of this Figure) from Hopkins (2016). Different magnetic solvers implemented in Gizmo are compared in idealised and realistic problems. Top half: pairs of columns display various 2D MHD tests. In each pair, the left column is a fluid quantity while the right column is the relative magnetic divergence. From top to bottom, rows are CT, CG, Dedner-cleaning, and Powell-cleaning solvers. Bottom half: comparison for CG (top), Dedner-cleaning (middle), and Powell-cleaning (bottom) in more realistic astrophysical setups. Three leftmost columns correspond to an isolated, full-physics galaxy simulation. From left to right: ratio of magnetic to thermal pressure, relative magnetic divergence, and relative magnetic divergence to equivalent pressures field. Three rightmost columns are an MHD simulation of the Santa Barbara cluster, now displaying density, relative magnetic divergence, and relative magnetic divergence to equivalent pressures field. For all cases, divergence cleaning methods display non-negligible divergences in simulations.

non-solenoidal waves might not be short enough for them not to impact the magnetic field growth or its configuration. Indeed, Balsara & Kim (2004) report that different MHD schemes can lead to different results, with no guarantee of convergence between methods with increasing resolution. As a result, for this field of study it is essential to understand the numerical results by comparing different numerical methods and focus on numerically divergence-less schemes such as Constrained Transport. Note that CT is not without its own disadvantages. On top of a complicated numerical implementation, this method has a larger memory cost, it requires restrictively small time steps, and produces numerical resistivities η which are relatively high. This latter issue is analogous to the dynamical viscosity introduced by grid discretisation, and there is clear convergence of this method towards lower resistivities as the spatial resolution is increased (Rembiasz et al. 2016). I will thus present for the simulations in this thesis, measurements of the degree of divergence generated numerically, to illustrate the robustness of the RAMSES CT scheme.

2.2 The RAMSES code

The simulations presented in this thesis are generated with the MHD code RAMSES (Teyssier 2002; Teyssier et al. 2006; Fromang et al. 2006), employing mostly the publicly available stable version released on October 2015[1]. For my simulations, I have done significant modifications to this version of RAMSES.

My RAMSES simulations follow the evolution of three massive components: gas, stars, and dark matter. The latter two behave as collisionless fluids, discretised into particles. Their dynamical evolution is governed exclusively by gravity. As a result, each particle moves ballistically, and the only change to their velocity comes from the acceleration dictated by the gravitational potential $\vec{a} = \vec{\nabla}\phi$. To compute the gravitational field, the particles are projected onto the grid using cloud-in-cell

[1]https://bitbucket.org/rteyssie/ramses

interpolation. This builds the density field used to compute gravitational forces. The Poisson equation is solved on the grid through a multi-grid scheme (Guillet & Teyssier 2011).

When treating the gaseous component RAMSES accounts for the full set of MHD equations. It employs SCM coordinates to adapt the equations to cosmological simulations, and we determine their normalisation factors selecting the size of the computational domain $r_* = 1$. The evolution of the magnetohydrodynamical quantities are obtained with numerical solvers. I employ for all my simulations the HLLD 2D Riemann solver (Toro et al. 1994) to calculate the time-centred intercell fluxes and a MinMod slope limiter to reconstruct the cell-centred properties, unless indicated otherwise. In RAMSES, this computation employs an Eulerian approach through a Godunov scheme, discretising the numerical domain in a grid of cubic elements containing the gas, which is allowed to flow through the grid. The code solves the MHD equations treating each discontinuity between cells as a discontinuous boundary Riemann problem, and computing fluxes between cells. I use the Hartex-Lax-van Leer Discontinuities (HLLD) 2D Riemann solver (Miyoshi & Kusano 2005), which is an extension of the HLL Contact (HLLC) Riemann solver (Toro et al. 1994) for magnetohydrodynamics. The Godunov scheme is extended to second order accuracy by applying the predictor-corrector step from the Monotone Upstream-centred Schemes for Conservation Law Limiter (MUSCL; Teyssier et al. 2006). The time integrator then selects a timestep Δt based on a series of criteria for stability: that no particle nor magneto-sonic wave can cross longer than a cell during Δt, that for all cells $\Delta t < t_{\rm ff,gas}$ (defined in eq. 2.26), and that the growth of the scale factor is no larger than 0.1 of its value. To optimise the use of computational resources, RAMSES employs the Adaptive Mesh Refinement (AMR) technique, which focuses the precision of the grid in the regions of interest.

2.2.1 Adaptive Mesh Refinement

A general characteristic of cosmological simulations is that the computational domain contains vast regions of extremely low densities, which are often not of particular interest for our studies. Exceptions are numerical simulations targeted at cosmic voids or the circum-galactic medium (CGM). Unless this is the case, employing an homogeneous grid that resolves with the same spatial accuracy low and high density regions is not the most efficient use of computational resources.

A smarter alternative is to use an algorithm which adaptively modifies the resolution of the simulations in regions of interest. Adaptive Mesh Refinement is one of these techniques. Departing from a pre-defined grid (not necessarily uniform), it sub-divides on-the-fly resolution elements into smaller units, which can in turn be subsequently divided further. This allows the scheme to significantly increase the spatial resolution of the simulation based on a set of user implemented criteria. Whenever these are not satisfied, the scheme de-refines down to a lower level of resolution. While the accuracy of the scheme is still limited by memory and computational costs, the method now makes a better investment of these two resources. AMR allows to use different timesteps in different refinement levels (through sub-cycling, with coarser levels using a twice as long step), but it also introduces some additional computational penalties by reducing the time step when elements are refined. This is to fulfil the CFL condition, required for the convergence and stability of the algorithm. The CFL (Courant-Friedrichs-Lewy) condition requires that the MHD waves (Alfven, slow and fast waves) in our simulations travel in each time step a distance smaller than the separation between the center of two grid elements. A description of the stability of numerical methods is outside of the scope of this thesis, but further information is provided by e.g. Anderson (1995). The AMR structure in Ramses is a fully threaded oct-tree, where every refined cell is divided into 8 finer cells of equivalent size, linked to this parent cell. In this manner, one can reconstruct the entire tree from the orig-

inal cell at level $l = 0$ by following the links between cells. Other AMR structures employ patches of refinement instead, where a volume is covered by groups of many cells simultaneously, typically variable in size.

2.2.2 Cooling and heating in RAMSES

Aside from the MHD equations presented in Section 2.1, many other physical processes are relevant for modelling galaxy formation. Crucial are the radiative ones, responsible for a significant loss of internal energy in the gas component, allowing its collapse to form gaseous structures, such as disks.

Capturing all the physics relevant for the cooling of baryonic matter is a complicated task. Instead, the method commonly employed in simulations is to encapsulate these in a set of temperature and metallicity dependent tables used to compute approximate radiative cooling rates $\Lambda(T, Z)$ with a local thermodynamic equilibrium approximation. This is a good approximation when both dependences on gas temperature T and metallicity Z are taken into account. Our simulations use metal dependent gas cooling as an energy sink, both above temperatures of $T \sim 10^4$ K (Sutherland & Dopita 1993) and below 10^4 K (Rosen & Bregman 1995). As previously indicated, we will always assume gas in our simulations to be monatomic ($\gamma = 5/3$), following the ideal gas equation of state

$$P = \epsilon(\gamma - 1). \tag{2.16}$$

In addition to cooling, realistic simulations also model the impact that photoionisation has on the IGM during reionisation. To reproduce it, we introduce at redshift $z = 10$ a uniform, redshift dependent UV background (Haardt & Madau 1996) in our cosmological simulations as a source term in the energy equation.

2.2.3 A new supercomoving magnetic variable

My implementation of a SCM magnetic field in RAMSES is based on one of the transformations proposed by Martel & Shapiro (1998, equation (A26) in their manuscript)

$$\hat{\vec{B}} = \frac{a^{5/2}\vec{B}}{B_*}. \tag{2.17}$$

This choice implies that the SCM variable, $\hat{\vec{B}}$, does not follow the same transformation as the comoving magnetic field $\vec{B}_{\rm co} = \vec{B}a^2$. There are however two good reasons backing this choice of coordinate. Firstly, the supercomoving magnetic energy density $\hat{\epsilon}_{\rm mag}$ naturally scales as the SCM internal $\hat{\epsilon}_{\rm int}$ and kinetic $\hat{\epsilon}_{\rm kin}$ energy densities,

$$\begin{aligned}
\hat{\epsilon}_{\rm mag} &= \frac{1}{2}\hat{B}^2 = \frac{1}{2}\frac{B^2a^5}{B_*^2} = \frac{a^5\epsilon_{\rm mag}}{B_*^2}, \\
\hat{\epsilon}_{\rm int} &= \hat{\varepsilon}\hat{\rho} = \frac{\varepsilon\rho a^5}{\varepsilon_*\rho_*} = \frac{a^5\epsilon_{\rm int}}{\varepsilon_*\rho_*}, \\
\hat{\epsilon}_{\rm kin} &= \frac{1}{2}\hat{\rho}\hat{v}^2 = \frac{1}{2}\frac{\rho v^2 a^5}{\rho_* v_*^2} = \frac{a^5\epsilon_{\rm kin}}{\rho_* v_*^2}.
\end{aligned} \tag{2.18}$$

Secondly, the momentum conservation equation is equivalent to its physical version replacing the physical quantities by their SCM counterpart. The first allows us to treat all energy densities in the code in the same manner, while the second implies that no modification has to be made to the treatment of the momentum conservation equations in the code. As mentioned before, in selecting this supercomoving coordinate, the induction equation (eq. 2.4) has to be modified to ensure that $\vec{B}_{\rm co} \propto a^2$ remains true. Eq. (2.4) now reads

$$\frac{\partial\hat{\vec{B}}}{\partial\hat{t}} - \hat{\vec{\nabla}} \times \left(\hat{\vec{u}} \times \hat{\vec{B}}\right) + \eta\hat{\nabla}^2\hat{\vec{B}} = \frac{\mathcal{H}}{2}\hat{\vec{B}}, \tag{2.19}$$

where an anti-drag term has appeared on the right-hand side, responsible for giving the a^{-1} scaling of the physical magnetic energy in an expanding volume V, i.e. $E_{\rm mag} =$

$\frac{1}{2}B^2V \propto a^{-4}a^3 = a^{-1}$, where I used that $B \propto a^{-2}$. I account for this modification in the induction equation in the code by simply modifying the uncorrected magnetic field $\hat{B}_{\text{pre-drag}}$

$$\hat{B}_{\text{corrected}} = \hat{B}_{\text{pre-drag}} \left(1 + \frac{\mathcal{H}}{2}\Delta\hat{t}\right), \tag{2.20}$$

simultaneously for each face-centred magnetic field in each cell at the current AMR level, where $\Delta\hat{t}$ is the (SCM, i.e. code units) timestep taken for the evolution of that level. Immediately after, I accordingly update the magnetic field on the coarser grids. The contribution of the magnetic energy to the total energy budget in each cell is corrected by replacing the previous magnetic energy by its new value. No significant difference for our numerical results was found when performing this correction separately for each AMR level, as opposed to when all levels were synchronised in time. I consequently opt for the second method, as it is less computationally expensive by avoiding multiple synchronisation requests of all computing processors and hence reduces the amount of communication. When the difference between $\hat{B}_{\text{corrected}}$ and $\hat{B}_{\text{pre-drag}}$ is small this correction can be written

$$\frac{\hat{B}_{\text{corrected}} - \hat{B}_{\text{pre-drag}}}{\Delta\hat{t}} \sim \frac{\partial\hat{B}}{\partial\hat{t}} = \frac{\mathcal{H}}{2}\hat{B} = \frac{1}{2a}\frac{\partial a}{\partial\hat{t}}\hat{B} \Rightarrow \frac{\partial B}{B} = \frac{\partial a}{2a} \Rightarrow \hat{B} \propto \sqrt{a}. \tag{2.21}$$

Therefore, when this correction dominates the evolution of the SCM magnetic field, it leads to $\hat{E}_{\text{mag}} \propto \hat{B}^2\hat{V} \propto a$. To verify that the implementation of the algorithm is correct, I present two important checks. The first tests whether the expected scaling for the total magnetic energy in the volume V of the simulated box $E_{\text{mag}} \propto a^{-1}$ is recovered. For this, I compute the total supercomoving magnetic energy in a simulation as

$$\hat{E}_{\text{mag}} = \int_{V_{\text{sim}}} \frac{1}{2}\hat{B}^2 d\hat{V} = \sum_{\text{i}}^{\text{All cells}} \frac{1}{2}\hat{B}_i^2\hat{V}_i \tag{2.22}$$

and convert it to physical magnetic energy as follows

$$\hat{E}_{\rm mag} = \frac{1}{2}\hat{B}^2\hat{V} = \frac{1}{2B_*^2}B^2a^5Va^{-3} = \frac{1}{B_*^2}E_{\rm mag}a^2. \tag{2.23}$$

Using $\hat{E}_{\rm mag} \propto a$, it follows that $E_{\rm mag} \propto \hat{E}_{\rm mag}a^{-2} \propto a^{-1}$. The top graph in Figure 2.2 displays for two simulations the growth of $E_{\rm mag}$ normalised to its value at the beginning of the run. The first is a cosmological box filled with a comoving adiabatic uniform density gas of $\rho \sim 6\rho_*$ and no dark matter (blue solid line), which simply expands along with the background Universe. The total magnetic energy in this run follows the expected inverse scaling with a (dashed yellow line), validating my SCM magnetic variable implementation. The second simulation is a cosmological zoom-in simulation of the formation of a galaxy (orange solid line, simulation details in Section 2.4), where the simulated evolution of the universe is first dominated by expansion until structure formation starts at $z \sim 20$. This simulation follows the scaling $E_{\rm mag} \propto a^{-1}$ until $z \sim 20$ and then stops decreasing as structure decouples.

A second important test is to confirm that our SCM variable $\hat{\vec{B}}$ remains divergence-free. In the bottom graph of Figure 2.2, I show a phase space diagram of relative magnetic divergence versus gas density for all cells in the previous galaxy formation simulation at $z = 3$. It demonstrates that our SCM coordinates in RAMSES preserve their crucial capacity to maintain the magnetic field divergence-less down to numerical precision. As this SCM magnetic field will be employed in all cosmological simulations presented in this thesis, Figures 4.1 and 6.2 serve as further proof of the divergence-less properties of my RAMSES version. The inclusion of this term is necessary to guarantee the correct evolution of the magnetic field in the entire simulation, as all resolution elements increase their size with expansion, even in those structures decoupled from expansion.

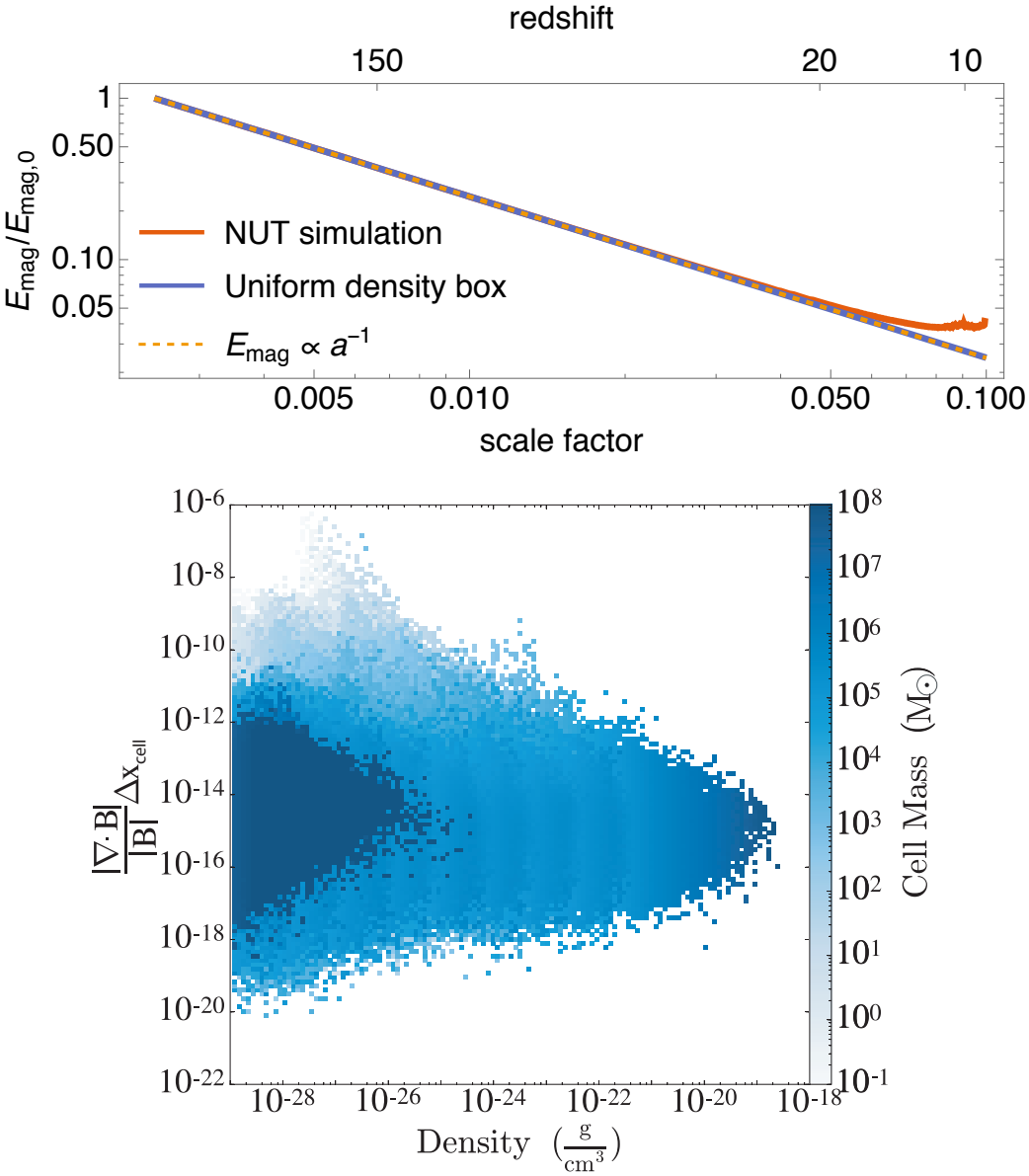

Figure 2.2: Top: physical energy scaling produced by the SCM formalism in my simulations. Solid lines represent the relative growth of the magnetic energy with respect to its initial value as the scale factor increases. An adiabiatic uniform gas box (blue) and the initial stages of a galaxy formation cosmological simulation (orange) both reproduce the expected scaling $E_{\rm mag} \propto a^{-1}$ (dashed). Bottom: relative magnetic divergence distribution as a function of density for the galaxy formation cosmological simulation, at $z = 3$.

2.3 Sub-grid physics: stellar feedback and star formation

Any simulation trying to reproduce the LSS or individual galaxies has to model the stellar component. To characterise galaxies, simulations have to produce an accurate mass and configuration for stars. The transformation of gas into stars forms a collisionless component which, on top of reducing the gas mass, provides the leftover gas with enhanced gravitational stability against fragmentation (Wang & Silk 1994; Westfall et al. 2014). The nuclear processes taking place in stars are also critical in the formation of galaxies: they craft metal elements that facilitate the cooling of baryonic gas when supplied to the ISM through winds and supernova explosions. These latter also impart significant amounts of energy and momentum. SN events modify the multi-phase structure of the ISM (e.g. Agertz et al. 2009b) and provide kinetic forcing that contributes to the turbulence of the medium (e.g. Korpi et al. 1999). Stellar feedback tends to decrease the amount of star formation occurring in galaxies, in a self-regulated process (e.g. Rosdahl et al. 2017).

In my simulations, because I lack the resolution and physics to fully capture the stellar component, I include models for its most important effects: star formation and SN feedback. I neglect radiative transfer and winds from stars. As part of my thesis work, I have extended these sub-grid models to account for the effects of magnetic fields. I present the models and their extensions in the following Sections.

2.3.1 Magneto-thermo-turbulent star formation

The formation of stars takes place as the final stage of a collapse process where gas in galaxies accumulates, atoms eventually become neutral and form GMCs. When these clouds further fragment and collapse, star formation occurs. Unsurprisingly, a tight correlation between the total (atomic and molecular) gas density of a galaxy and the

amount of stars it forms is found. This is known as the empirical Kennicutt-Schmidt law (Schmidt 1959; Kennicutt, Jr. 1998)

$$\Sigma_{\rm SFR} = A_{\rm KS}\Sigma_{\rm gas}^{n}, \tag{2.24}$$

which relates the star formation rate surface density $\Sigma_{\rm SFR}$ with the total gas surface density $\Sigma_{\rm gas}$, although it is also possible to study the correlation of galaxy-averaged star formation rates with atomic or molecular gas separately (Kennicutt & Evans 2012). The measured power-law index of correlation for total gas surface density is $n = 1.4 \pm 0.5$ (Kennicutt, Jr. 1998). This relation can be generalised to a three-dimensional version which dictates how many stars form in a given volume:

$$\dot{\rho}_{*} = \epsilon_{\rm eff}\frac{\rho_{\rm gas}}{t_{\rm ff}}, \tag{2.25}$$

where $\epsilon_{\rm eff}$ is the efficiency of the star formation and $t_{\rm ff}$ is the gas free-fall time

$$t_{\rm ff} = \sqrt{\frac{3\pi}{32G\rho_{\rm gas}}}, \tag{2.26}$$

characterising the collapse. Eq. (2.25) is frequently used as the foundation that underpins star formation models in numerical simulations. In such models, $\epsilon_{\rm eff}$ is fixed to the value which recovers the observed normalisation. Furthermore, to limit star formation to the densest regions of the simulations, these models also introduce a minimum gas density threshold above which star formation is allowed to occur. This density threshold is a numerical artifact with no evident physical significance, and has to be changed to match the properties and resolution of each simulation. Models of this sort have been successful in reproducing galaxy stellar masses in a wide variety of simulations (e.g. Henden et al. 2018). However, as numerical studies probe new regimes with unprecedented spatial resolution, allowing to resolve part of the ISM,

better modelling becomes possible for star formation. Observations of GMCs show that the correlation between molecular gas surface density and star formation rate breaks down at the scale of individual clouds (e.g Pineda et al. 2010), as not all regions of a molecular cloud are forming stars with an efficiency proportional to their density, but rather, star formation concentrates in some parts of these systems. This prompts one to decide which regions form stars based on the local properties of the gas.

In my simulations, I employ a state-of-the-art thermo-turbulent star formation model developed by Devriendt et al. (in prep) based on smaller scale simulations of individual molecular clouds by Padoan & Nordlund (2011) and Federrath & Klessen (2012). I have extended our model to account for the presence of magnetic fields. This model has already been extensively employed in its thermo-turbulent form (e.g. Kimm et al. 2017; Mitchell et al. 2018; Rosdahl et al. 2018). This magneto-thermo-turbulent (MTT) star formation uses the properties of grid cells and their neighbours to determine two aspects:

- Whether the self-gravitational force from the gas within a cell dominates the thermal, turbulent, and magnetic pressure support.
- Given the local values of the support against gravity and gas properties, what is the expected efficiency of gas-to-stars conversion.

This cell forms stars

Part of the task of the MHD solver is to follow compression and collapse of gas as long as numerically possible. Therefore, we would like to restrict the formation of stars to those regions where the gravitational collapse of gas cannot be further captured. This MTT star formation provides a rather elegant, physically-motivated solution. For all cells at the finest level of resolution in the simulation (Rasera & Teyssier 2006), we compute whether the Jeans length from combined thermal, turbulent, and

magnetic support is larger than the size of the cell. If this is not the case and the MTT Jeans length is $\lambda_{\rm J,MTT} < \Delta {\rm x}_{\rm cell}$, the gas in the cell is physically expected to continue collapsing. Consequently, we allow this element to do so through sub-grid star formation. In other words, the process of star formation only takes place once the AMR scheme in RAMSES cannot follow the collapse any further. Note that the need for any artificial density threshold is eliminated in this approach.

Following Federrath & Klessen (2012), the MTT Jeans length is defined

$$\lambda_{\rm J,MTT} = \frac{\pi\sigma_V^2 + \sqrt{36\pi c_{\rm s,eff}^2 G {\Delta {\rm x}_{\rm cell}}^2 \rho_{\rm gas} + \pi\sigma_V^4}}{6\, G\rho_{\rm gas}\Delta {\rm x}_{\rm cell}}, \tag{2.27}$$

where σ_V is the local gas turbulent velocity in the cell and G the gravitational constant. In the presence of magnetic fields, the effective sound speed $c_{\rm s,eff}$ is

$$c_{\rm s,eff} = c_{\rm s}\sqrt{1+\beta^{-1}}, \tag{2.28}$$

which accounts for the isotropic support provided by a small-scale turbulent magnetic field. Throughout the thesis, I define the plasma beta parameter as the ratio of thermal to magnetic pressure

$$\beta = P_{\rm thermal}/P_{\rm mag}(B). \tag{2.29}$$

In code units, the magnetic pressure is simply $P_{\rm mag} = 0.5B^2$, with $B = |\vec{B}|$ the magnetic field in a cell.

This cell has a local star formation efficiency

Various theoretical studies show that molecular clouds have varying star formation efficiencies depending on their properties (Padoan & Nordlund 2011; Hennebelle & Chabrier 2011; Federrath & Klessen 2012; Grisdale et al. 2019). On the other hand,

observations suggest that magnetic fields alone could be providing enough support to prevent star formation in some molecular clouds (Kauffmann et al. 2013). Magnetic fields are also suspected to intervene in star formation through a variety of ways, such as reducing the number of clumps in the ISM or lessening by a factor of a few the star formation rate of individual clouds (Hennebelle & Inutsuka 2019). Therefore, instead of using a unique value of $\epsilon_{\rm eff}$ to match galaxy stellar masses, independent of space and time, we account for the temporal and spatial variability of star formation efficiency in each gas cloud. Writing for each gas cell

$$\epsilon_{\rm ff} = \frac{\epsilon_{\rm cts}}{2\phi_t} \exp\left(\frac{3}{8}\sigma_s^2\right) \left[1 + \mathrm{erf}\left(\frac{\sigma_s^2 - s_{\rm crit}}{\sqrt{2\sigma_s^2}}\right)\right]. \tag{2.30}$$

In this multi-scale model adopted from Padoan & Nordlund (2011), $s = \ln\left(\rho/\left\langle\rho\right\rangle\right)$ is the logarithm of the ratio of density to mean density of the gas, and σ_s its dispersion. The parameter ϕ_t introduced by Krumholz & McKee (2005) accounts for possible uncertainties in the free-fall time, and we fix it to $\phi_t = 0.57$ from simulations of individual GMCs by Federrath & Klessen (2012). We define the critical density

$$s_{\rm crit} = \ln\left(0.067\,\theta^{-2}\alpha_{\rm vir}\mathcal{M}^2 f\left(\beta\right)\right), \tag{2.31}$$

above which gas proceeds to collapse into stars (Hennebelle & Chabrier 2011) and choose $\theta = 0.33$. The θ numerical parameter is introduced to approximate the fraction of the cloud size forming the most significant shock waves. The function

$$f\left(\beta\right) = \frac{\left(1 + 0.925\beta^{-3/2}\right)^{2/3}}{\left(1 + \beta^{-1}\right)^2}, \tag{2.32}$$

extends this critical density to include the presence of magnetic fields, following Padoan & Nordlund (2011). In the previous expressions we also introduced the Mach

number $\mathcal{M} \approx \sigma_V / c_\mathrm{s}$, and the virial parameter

$$\alpha_\mathrm{vir} = \frac{5\,(\sigma_V^2 + c_\mathrm{s}^2)}{\pi\ \rho\ G\ (\Delta \mathrm{x}_\mathrm{cell})^2}. \tag{2.33}$$

σ_V is calculated as the trace of $\vec{\nabla} \cdot \vec{v}$. Note that so far there are no free parameters in this model, and all quantities are measured in the simulations. The only free parameter in our model is ϵ_cts, the value for the maximal amount of gas expected to collapse into stars in the presence of proto-stellar feedback. This (not modelled) feedback is argued to reduce the amount of gas by about a half, i.e. $\epsilon_\mathrm{cts} = 0.5$.

When a cell forms a stellar particle, its mass is drawn from a Poisson distribution (Rasera & Teyssier 2006) of integer multiples of a minimum mass set by the resolution limit of the simulation. In my simulations, the typical mass of a stellar particle will always be $M_* \gtrsim 10^3 M_\odot$. At these masses, each particle is more representative of an entire single stellar population (SSP) than of an individual star. Therefore, my treatment of stellar particles assumes them to be SSPs. An example is the implementation of supernova feedback.

2.3.2 Stellar feedback

Stellar feedback is an essential component to generate a multi-phase galactic ISM (Agertz et al. 2009b). I include it in some simulations, in the form of one of the two models presented below.

Stellar particles produce SN explosions in line with the expected number of events from a SSP estimated using a set initial mass function (IMF) for its star population. In this work, I employ a Kroupa IMF (Kroupa 2001). During these SN events, stellar particles inject mass, energy and momentum back to the ISM. Part of the mass will be comprised by newly formed metals, which will then be advected with the fluid as a simple passive scalar. Unless otherwise indicated, I assume the gas fraction returned

to the ISM to be $\eta_{\rm SN} = 0.213$, of which $\eta_{\rm metals} = 0.075$ correspond to metal elements, assumed to follow solar metallicity ratios. Once the amount of SN is calculated, we assume a typical SN in our simulations to have a mass of $19.135 M_{\odot}$, and produce an energy of $\sim 2 \cdot 10^{51}$ erg, exploding 3 Myr after the birth of a stellar particle.

2.3.2.1 Thermal and radiative feedback

Our first feedback prescription, dubbed *RdTh*, aims to capture the general effects of SN feedback and stellar radiation through a very simple implementation. The most common prescriptions for SN feedback model these explosions as an injection of mass and thermal energy in a few (or simply one) resolution elements. Relying on the premise that accounting for the correct energy and mass injection produces a Sedov-Taylor blast wave, one injects the corresponding quantities into the cell hosting the stellar particle.

The exclusive injection of thermal energy from SN is prone to lead to an overestimation of the radiative losses (Katz 1992) depending on gas density and resolution. With this numerical caveat not withstanding, this model appears too weak to generate galactic outflows as powerful as those observed (Hopkins et al. 2012). Some possibilities to supplement its power are e.g. cosmic rays, or stellar radiation. Through radiation, stars could heat up the ISM gas and contribute to its escape from the galaxy (Murray et al. 2010).

We employ a basic model that aims to capture this local heating that stellar radiation causes on the ISM. Our stars emit energetic ultraviolet (UV) radiation, which is absorbed by dust grains, increasing their temperature and producing thermal infrared (IR) emission. This radiation will in turn transfer momentum and energy to the gas, heating it and boosting outflows (Murray et al. 2010; Roškar et al. 2014). We use the model by Roškar et al. (2014), where the emission of each stellar particle is $\varepsilon_{\rm rad} = 10^{52} {\rm erg}/M_{\odot}$. Our model also requires a UV dust opacity, taken as

$\kappa_{\rm UV} = 1000$ cm$^2/g$ (Draine & Li 2006) at a wavelength of 0.1 μm. The final energy contributed by this component to SN explosion can be computed assuming that each particle provides an infrared energy

$$\varepsilon_{\rm UV} = \varepsilon_{\rm rad} \left[1 - \exp\left(-\kappa_{\rm UV}\ \rho_{\rm dust}\ \Delta {\rm x}_{\rm cell}\right)\right], \tag{2.34}$$

$$\varepsilon_{\rm IR} = \varepsilon_{\rm UV} \left[1 - \exp\left(-\kappa_{\rm IR}\ \rho_{\rm dust}\ \Delta {\rm x}_{\rm cell}\right)\right], \tag{2.35}$$

to its host cell. We complete these equations by selecting an infrared opacity for the ISM $\kappa_{\rm IR} = 20$ cm^2 g^{-1}, corresponding to an opaque medium (Semenov et al. 2003).

2.3.2.2 Mechanical feedback

The previously described thermal feedback prescription does not account for the fact that the limited resolution of simulations may lead to spurious radiative loss of energy (Marri & White 2003).

To circumvent this issue an alternative is to employ mechanical feedback, which adapts the model in those situations where the local resolution of the grid around a SN event is not sufficient to capture its Sedov-Taylor phase. Our prescription was introduced in Kimm & Cen (2014); Kimm et al. (2015), but is briefly presented here. To ensure the adequate amount of momentum and energy is introduced in the ISM, this mechanical feedback, dubbed *Mech*, injects the values corresponding to the snowplow phase if necessary. These are calculated based on local properties such as the number of SN and the density and metallicity of the gas in the neighbouring cells, and anisotropically deposited in the host cell and its neighbours.

This prescription has been compared with other more standard feedback implementations in Rosdahl et al. (2017).

2.3.3 Magnetising stellar feedback

The magnetic energy of SN ejecta is a product of stellar physics and the blast wave. Therefore, in the same manner that SN feedback can modify properties such as thermal energy, it can also alter the local magnetic field. Implementing this extension of the SN feedback will allow us to explore questions such as the potential magnetisation of galaxies by stellar sources.

However, injecting magnetic fields in CT codes such as RAMSES is non-trivial for a variety of reasons. First and foremost, one needs to preserve the solenoidality of the field, to ensure no significant monopolar component is introduced by the injection at any point or level of the grid. While the importance of this aspect might not be so crucial for divergence cleaning schemes, methods like CT are incapable of removing divergence once it appears. This leads to the second major complication: making a local modification only and synchronising it on the domain. As the magnetic field is modified for leaf cells (undivided AMR cells), any modification has to be uploaded to parent cells at coarser levels and communicated to the relevant processors. Finally, the last issue when performing an injection of magnetic field relates to the amount of energy introduced. What is the amount of magnetic energy to be injected? How do we ensure that each event exactly produces this amount of energy?

I have implemented routines in RAMSES that allow to increase or reduce the magnetic energy in a finite volume. The code remains divergence-less even in the scenario where strong magnetic fields are injected with SN events in a zoom-in simulation of a galaxy, with no ab-initio magnetic field - for which relative magnetic divergences could be particularly high. The simulation setup is introduced in detail in Section 2.4.3. Figure 2.3 displays the relative magnetic divergence in this simulation in the case where each SN injects $\epsilon_{\rm mag,inj} \sim 0.01 E_{\rm SN}/V_{\rm cell}$. Even in a simulation with cosmological expansion, complex physics, turbulence, etc. this injection procedure remains divergence-free to less than $< 10\%$.

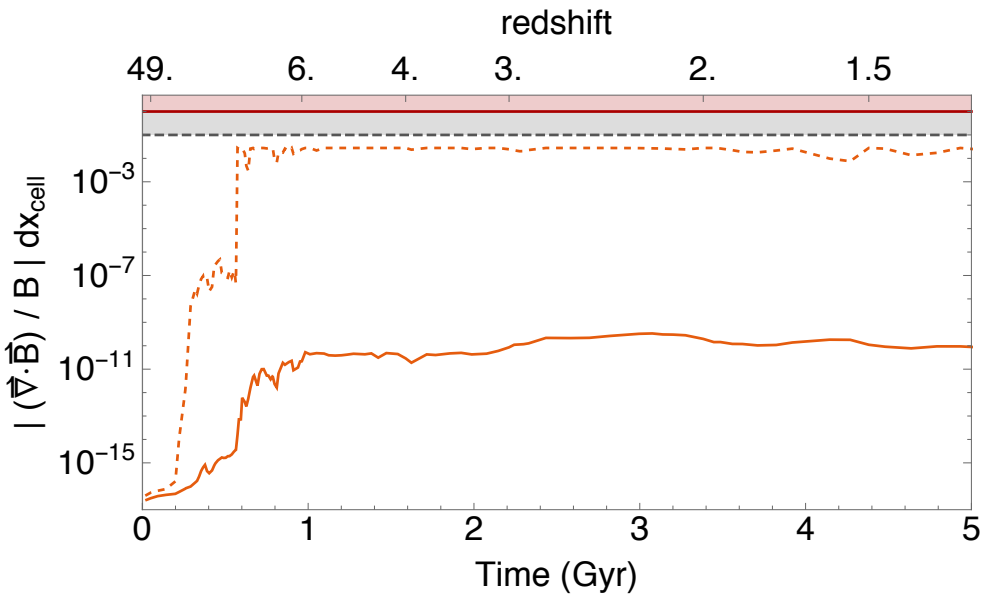

Figure 2.3: Median (solid line) and maximal (dashed line) relative magnetic divergence for a full-physics galaxy formation cosmological simulation (NUT, see Section 2.4.3), where magnetic fields are seeded exclusively through SN explosions ($\epsilon_{\rm mag,inj} \sim 0.01 E_{\rm SN}/V_{\rm cell}$). The maximal relative magnetic divergence found remains below the 10% threshold (horizontal dashed line) delimiting the shaded region, and the median divergence is well-controlled and comparable to these other simulations.

As previously mentioned, a crucial aspect of magnetic injection is to ensure that the modification of the field remains local, i.e. that we do not need to introduce a change in the entire computational domain every time a supernova event takes place. To achieve this goal, the two injection methods I implemented feature compact stencils. One uses a set of six loops centred around a point, and the other is a local quasi-dipole, modified to not have any injected magnetic field lines crossing the boundary of the stencil. The first method is the one employed for the simulations in this thesis. I introduce it here mathematically and it is graphically displayed in Figure 2.4.

The 6-loop injection procedure is the most compact 3D mechanism, and is centred around a grid vertex $(i+1/2, j+1/2, k+1/2)$. In this thesis, magnetic injection is associated with SN explosions. For each SN event, the centre of the injection is the grid vertex closest to the particle hosting the SN. Connected to this vertex there are

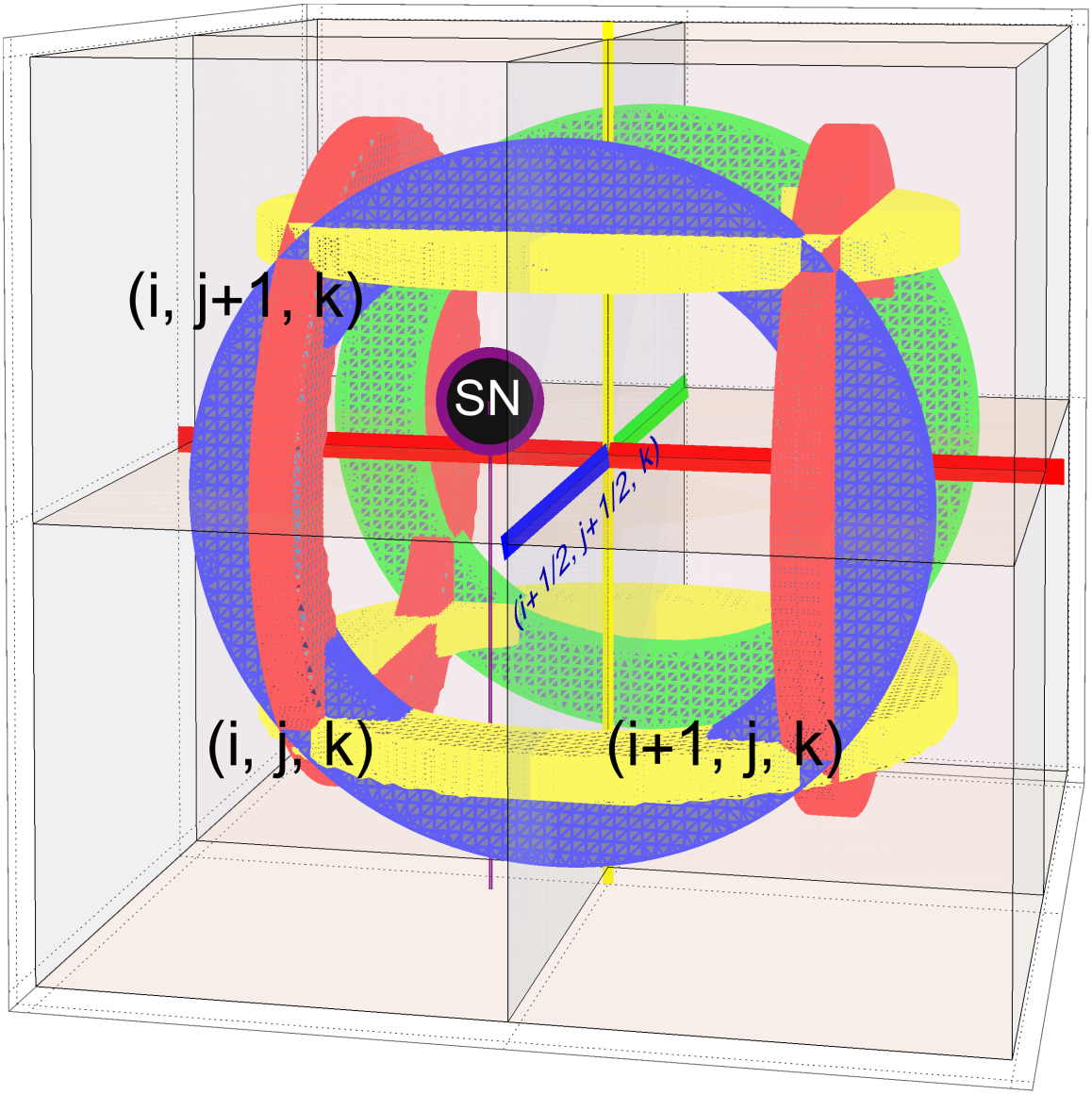

Figure 2.4: This graphic presents the basic morphology and components of the loop method for the injection of magnetic fields, in the case of a SN explosion. The injection scheme operates on a stencil of $2 \times 2 \times 2$ cells. For a SN event, it is centred around the grid vertex closest to the stellar particle. The vertex is surrounded by 6 closed loops, each injecting a magnetic field $B_{\rm inj}$ to the faces it traverses. Each loop has an assigned orientation (not shown, see text) which dictates whether the inserted $B_{\rm inj}$ contribution to the face is positive or negative. Each loop is centred on one of the 6 cell edges connected to the central vertex, identified by thick lines of the same colour as the loop ring.

6 cell edges, and to each of these edges I associate an independent loop of injection. Each of them injects a fixed magnetic field $B_{\rm inj}$ to each of the 4 faces it traverses. Each loop has an associated direction - either clockwise or counter-clockwise when observed from the vertex. The direction is decided by assessing which of the two possibilities maximises the field when the loop is injected. Once a direction is fixed, all face injections by this loop align with it. More explicitly, if we select the edge $(i+1/2, j+1/2, k)$ in Figure 2.4 (in blue), its associated loop will inject

$$\begin{aligned} B_x^{i+1/2,j+1,k} &= B_x^{i+1/2,j+1,k} \pm B_{\rm inj}\,, \quad B_x^{i+1/2,j,k} = B_x^{i+1/2,j,k} \mp B_{\rm inj}\,, \\ B_y^{i+1,j+1/2,k} &= B_y^{i+1,j+1/2,k} \mp B_{\rm inj}\,, \quad B_y^{i,j+1/2,k} = B_y^{i,j+1/2,k} \pm B_{\rm inj}\,. \end{aligned} \tag{2.36}$$

in the four shared faces of cells (i,j,k), $(i+1,j,k)$, $(i,j+1,k)$, $(i+1,j+1,k)$. This makes the injected field divergence-free by construction. The next step is to select a value for $B_{\rm inj}$. Ideally, one would like to calibrate $B_{\rm inj}$ on some observational property of magnetic fields associated with feedback events. Work to calibrate our feedback prescription to reproduce observations of strength and morphologies of magnetic fields in SNR (Reynolds et al. 2012; West et al. 2017) is ongoing. In this thesis, I will explicitly indicate how the value of $B_{\rm inj}$ is selected in each simulation. These are empirical choices generate magnetisations in the simulated galaxies comparable to that observed in galaxies around us, and will serve as a first step to explore this topic.

The last aspect of the injection scheme to be discussed is the amount of energy introduced by each event. In the absence of a pre-existent magnetic field $B_{\rm pre}$, the

injection yields in every of the 8 cells an energy density

$$\begin{aligned}\epsilon_{\rm inj} &= \frac{1}{2}\left[\sqrt{\left(\frac{\Delta B_x^l + \Delta B_x^r}{2}\right)^2 + \left(\frac{\Delta B_y^l + \Delta B_y^r}{2}\right)^2 + \left(\frac{\Delta B_z^l + \Delta B_z^r}{2}\right)^2}\right]^2 \\ &= \frac{1}{2}\left[\sqrt{\left(\frac{2B_{\rm inj}+0}{2}\right)^2 + \left(\frac{2B_{\rm inj}+0}{2}\right)^2 + 0^2}\right]^2 = B_{\rm inj}^2,\end{aligned} \tag{2.37}$$

where the ΔB_i^m is the injected field for the coordinate i in (x, y, z) for the face m left (l) or right (r). This amount of energy results from the fact that each subsequent loop is injected after another, with the order of injection randomly selected. Therefore, each of the loops increases the magnetic field by $B_{\rm inj}$ in two faces, and cancelling in a third face. However, in the presence of a pre-existent magnetic field the increase in magnetic energy produced by the injection depends on the configuration of the pre-existent field $B_{\rm pre}$. An estimate for a randomly oriented $B_{\rm pre}$ is that the increase in magnetic energy density

$$\epsilon_{\rm inj} = \epsilon_{\rm post} - \epsilon_{\rm pre} \sim \vec{B}_{\rm inj} \cdot \vec{B}_{\rm pre} + \frac{1}{2} B_{\rm inj}^2, \tag{2.38}$$

typically with $3/4\ B_{\rm inj}^2 \lesssim \epsilon_{\rm inj} \lesssim 3/2\ B_{\rm inj}^2$, assuming $B_{\rm pre} \sim B_{\rm inj}$ over the entire injected volume. There could be cases where the injection completely fails to introduce a non-negligible increase of the magnetic energy density. In this case, assuming $B_{\rm pre} \lesssim B_{\rm inj}$, performing an injection will re-organise the local field inside the stencil. If a second injection is now performed, the new morphology will allow a successful injection. I introduce the parameter $\epsilon_{\rm sn10} = 10^{-10}$erg / cm^3, which is the magnetic energy density injection expected from $B_{\rm inj} = 10^{-5}$ G (an order of magnitude estimate for the typical magnetic field in SNRs) in a non-magnetised region of volume of (10 pc)^3. When a SN injection does not provide energy above the conservative lower limit $\epsilon_{\rm inj} > 10^{-6}\epsilon_{\rm sn10}$, I perform a second 6-loop injection with the same $B_{\rm inj}$.

On Figure 2.5 I present the distribution of magnetic energy densities injected $\epsilon_{\rm inj}$, normalised to $\epsilon_{\rm sn10}$ in a re-simulation of the NUT galaxy with no primordial magnetic field B_0, where each SN injects 6 loops of magnetic field $B_{\rm inj} \sim \sqrt{0.01 E_{\rm SN}/V_{\rm cell}}$. The vertical red dashed line represents the thermal energy density of a SN in a 10 parsec cell. The purple and green lines correspond to the $\epsilon_{\rm inj}$ expected for this event if $B_{\rm pre} = 0$ in a 10 pc or 20 pc per side cell, respectively. The center of the distribution of injected magnetic energy densities suggests that the majority of injections take place in cells of either 10 or 20 pc per side. However, it also presents broad tails, caused by a variety of factors: (i) the physical cell size varies in the simulations with the scale factor a, (ii) SN events can take place at even coarser levels of refinement, and specially (iii) in the presence of $B_{\rm pre}$, the injected magnetic energy density can wildly vary its efficiency. The amount of events contributing small magnetic energy densities are negligible, these amount $\sim 3\%$ below $\epsilon_{\rm inj}/\epsilon_{\rm sn10} = 10^{-3}$ and $\sim 10\%$ below $\epsilon_{\rm inj}/\epsilon_{\rm sn10} = 10^{-2}$, and could be occurring in extremely low density environments with large cell sizes. On the large energy densities end, SN taking place in the smallest cells and in the presence of a large $B_{\rm pre}$ can lead to a significant injection of energy from term $\vec{B}_{\rm inj} \cdot \vec{B}_{\rm pre}$ in eq. (2.38), and drive substantially higher injected magnetic energy densities. This study has to be performed on-the-fly in my simulations, and will greatly benefit of a future review in terms of absolute magnetic energies. Finally, the sub-panel on the same Figure displays the same distribution, now normalised and split into various redshift bins. While some temporal evolution exists, with the injections progressively becoming more efficient as redshift decreases and $B_{\rm pre}$ in the galaxy increases, the general behaviour of the injection mechanism does not change significantly over time.

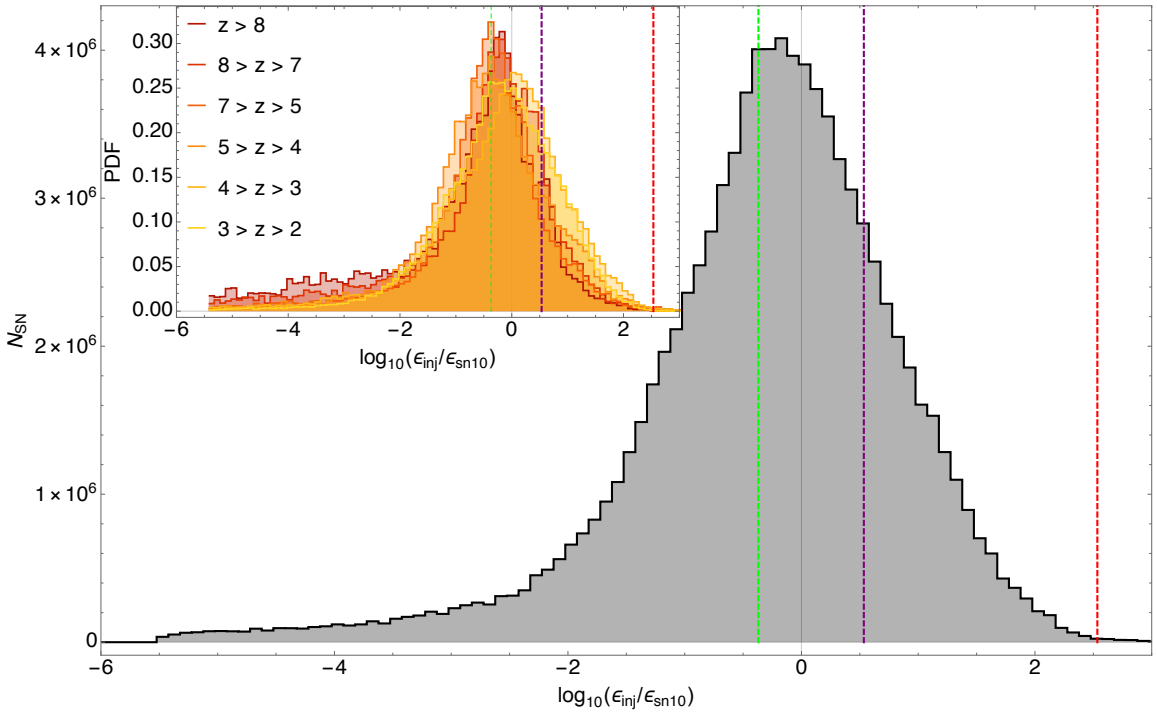

Figure 2.5: Distribution of SN injected magnetic energy densities, normalised to the magnetic energy density estimate $\epsilon_{\rm sn10}$ (see text). Vertical lines display: energy densities for a SN explosion in a 10 pc on a side cell (red), magnetic energy density corresponding to $B_{\rm inj} = \sqrt{0.01 E_{\rm SN}/V_{\rm cell}}$ in a cell of 10 pc on a side (purple) and 20 pc on a side (green). The sub-panel displays the same distribution, split in redshift bins and normalised to unity. Injections are centred around the expected magnetic energy densities (purple and green lines) suggesting that most SN inject reasonable amounts of magnetic energy density in cells of 10 or 20 pc per side. The broadening of the distribution is caused primarily by cell-sizes, and the pre-configurations of the magnetic field before injection.

2.4 Numerical simulations of galaxies

There are various approaches one can take to study the formation, evolution, and properties of galaxies with numerical simulations. Depending on the choice, simulations will be better tailored to understand different aspects of galaxy formation.

2.4.1 Cosmological or isolated

The very first decision to be made is whether the simulation will be idealised (isolated) or cosmological. An idealised simulation contains exclusively the galaxy (or galaxies) studied, and departs from somewhat arbitrary initial conditions. Such simulations lack many important factors beyond the absence of an environmental gravitational field. These galaxies do not form hierarchically, as in a ΛCDM Universe. They do not accrue gas progressively or undergo mergers. On the other hand, they offer a controlled laboratory to understand certain aspects of secular processes and require a lower amount of computational resources, allowing to reach higher resolutions.

At the other end of the spectrum, cosmological simulations capture the environment and hierarchical evolution of galaxies. However, they require following the growth of galaxies over the entire age of the Universe to produce present day analogues. These simulations thus have a large running cost which is mitigated by degrading their resolution. As a result, the analysis of cosmological simulations is intrinsically more complicated.

An alternative to reduce the computational cost of cosmological simulations, is to perform zoom-in simulations. These select regions of interest, and re-simulate them with significantly higher resolution. This reduces the cost of modelling the cosmic environment, and allows better resolution in the galaxy present in the zoom region. The price to pay is a drastic reduction of the galaxy sample size.

In this thesis, I will present simulations mostly of this latter sort. As the hyperbolic

equations of MHD are an initial conditions (ICs) problem, we have to generate ICs tailored to our studies. The advantage of cosmological simulations, is that ICs are specified according to the properties of the Universe. Packages such as MUSIC (Hahn & Abel 2011) provide the user with density and velocity fields for dark matter and gas components. However, no software has been developed yet for the magnetic component. I describe my ongoing efforts with Prof. Oliver Hahn and Dr. Yohan Dubois to prepare a code that allows this in Section 2.4.2.

2.4.2 Magnetic initial conditions

Upon review of eq. (2.4), one rapidly realises that in the absence of any ab-initio magnetic field in the studied domain, the solution to this equation will always be $B = 0$. This is because I did not include any battery terms in the induction equation (such as eq. (1.10)) which are capable of generating magnetic fields. Alternatively, one could produce the magnetic component by employing magnetic sources such as the magnetised feedback implementation described in Section 2.3.3.

Otherwise, these simulations require the addition of an initial magnetic seed to the set of initial conditions. The usual approach in the majority of studies is to simply start from an homogeneous, uniform, magnetic field in the entire domain.

A uniform magnetic seed

Selecting a uniform magnetic field to permeate the entire simulated domain entails a number of caveats, perhaps the most critical being the violation of the cosmological principle by breaking isotropy.

However, employing this type of magnetic seed is a common standard, justified by a number of reasons. First of all, it has been shown that as long as the seed remains weak, its orientation appears to have no significant impact on the field structure and its mean properties in virialised regions (Marinacci et al. 2015). In such virialised

objects, all information about the choice of initial seed configuration is wiped out once amplification and dynamic reorganisation of the magnetic field has taken place (Dubois & Teyssier 2008). In the majority of the simulations of this thesis, I follow this approach, selecting an ab-initio uniform field aligned with one of the three axes of the computational simulation domain. It has been suggested that the configuration of the local field during galaxy collapse might affect the evolution of the magnetic field shortly after (Zeldovich 1983; Rieder & Teyssier 2016). Similarly, I will show how as stronger regimes of the primordial field are probed, some effects commence to appear in the processes of structure formation and the properties of galaxies.

Also note that as we are mostly interested in studying individual galaxies, the initial field can be understood as the main component of a large scale field with coherence on comoving Mpc scales. Strong primordial fields with such coherent length scales could be generated during inflationary processes (Ratra 1992; Barrow & Tsagas 2011; Sharma et al. 2018). Our seed selection does not include however any sort of fluctuation on small scales, which could still influence the formation and evolution galaxies (Brandenburg & Subramanian 2005; Kandus et al. 2011).

A primordial magnetic spectrum

Two main obstacles complicate exploring numerical simulations where the initial configuration of the magnetic field is not uniform but instead possesses a spectral distribution. The first one emerges from the lack of observational constraints and the wide variety of possible theoretical models: which spectrum should be chosen for the magnetic field, if any at all? The second reason more practical: the difficulty of implementing a primordial, divergenceless magnetic field coupled to the other multi-scale ICs. Indeed codes such as MUSIC (Hahn & Abel 2011) produce multi-scale initial conditions for various levels of refinement simultaneously, with smooth transitions of all hydrodynamical quantities across the refinement boundaries. The next step

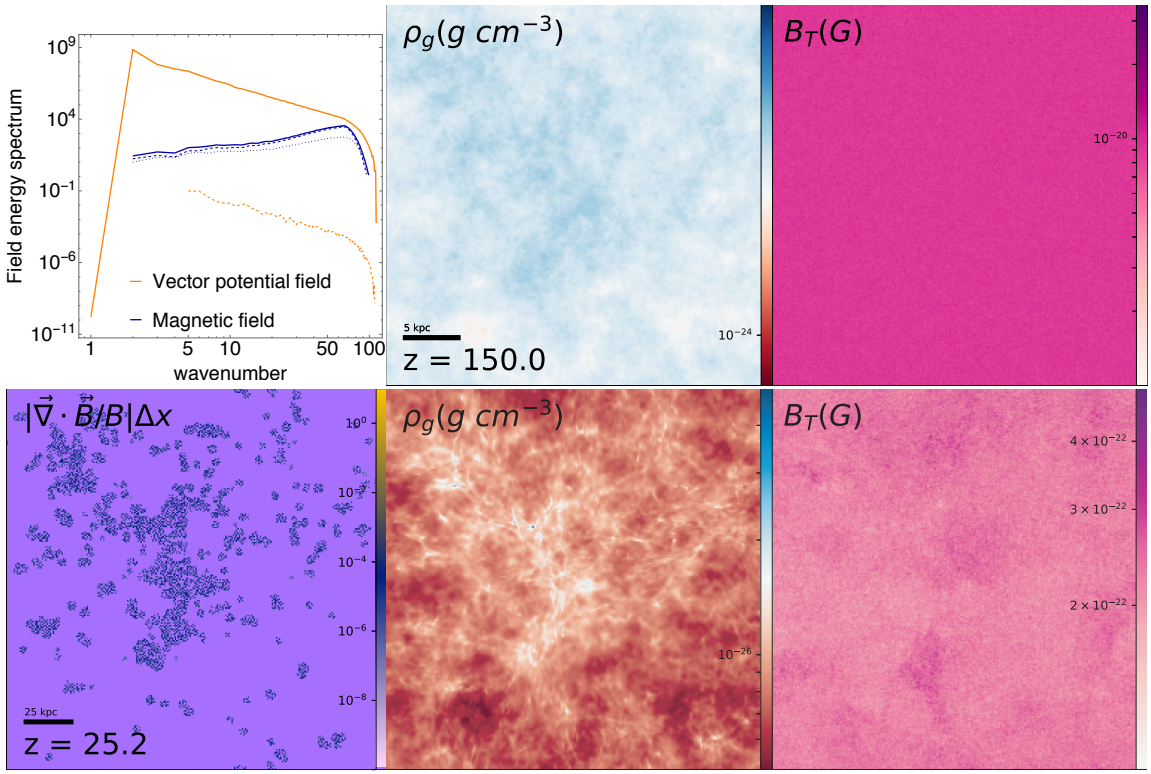

Figure 2.6: Top row: Foremost left panel displays the scaling of the primordial magnetic energy spectrum and the vector potential from which it is generated. Density and magnetic initial conditions for the new magnetic SPHINX simulation (Rosdahl et al. 2018). Bottom row: density, magnetic field, and relative magnetic divergence for the same simulation after a short evolution. These new magnetic initial conditions induce perturbations of the magnetic field on small scales, and remain divergence-less.

towards any progress on modelling primordial magnetism in simulations is thus to develop an extension for these codes that performs this task for the magnetic field.

Future work, in collaboration with Prof. Oliver Hahn, will involve the finalising of my code to generate magnetic initial conditions according to a user-selected spectrum. A working prototype already exists which serves as a proof of concept (see Figure 2.6).

2.4.3 Zoom-in simulations and NUT

The simulations that comprise the majority of this thesis employ the NUT galaxy ICs. These are zoom-in simulations prepared to study the formation of a Milky Way-like galaxy. As described, zoom-in simulations are computational boxes where the

entire domain is refined with a fixed, coarse spatial resolution, and only the region of interest, corresponding to the Lagrangian volume containing all particles which end up in the galaxy at $z = 0$, is refined to a higher level. In my case, this is a sphere centred on the forming galaxy, where I further allow AMR refinement. When running a cosmic zoom-in simulation, there are numerical aspects arising from the duality of resolutions that have to be taken into account to avoid numerical artifacts. One is the mass resolution of the dark matter particles. Once a zoom-in region has been selected, the ICs of the simulation have to be re-generated in accordance with the target high resolution. In other words, lower mass - and therefore more DM particles have to populate the region of interest to avoid under-sampling the dark matter fluid component and provoking artificially strong gravitational collisions.

The ICs for NUT have been prepared accordingly (Powell et al. 2011). This simulation consists of a cubic box with a comoving side of 9 h^{-1} Mpc. In this box resides a dark matter halo of $M_{\rm vir}(z = 0) \sim 5 \cdot 10^{11} M_{\odot}$ that hosts a Milky Way-like galaxy. The zoom-in region, a sphere of comoving diameter 3 h^{-1} Mpc, is placed around this halo. In this region, I use AMR to reach 10 physical parsecs maximal resolution at all times, unless indicated otherwise. The dark matter and stellar particle minimal masses are fixed to be $M_{\rm DM} \sim 5 \cdot 10^4 M_{\odot}$ and $M_* \sim 5 \cdot 10^3 M_{\odot}$ respectively in the zoom region. The time integration of this box starts at $z = 499$. Finally, when generating the NUT ICs, the cosmological parameter values chosen are those of the concordance WMAP5 (Dunkley et al. 2009). These are density parameters $\Omega_{\Lambda,0} = 0.743$, $\Omega_{m,0} = 0.258$, $\Omega_{b,0} = 0.045$, and $\Omega_{k,0} = 0.0$, $\sigma_8 = 0.796$, and reduced Hubble constant

$$h = \frac{H_0}{100} \frac{\text{s Mpc}}{\text{km}} = 0.719. \tag{2.39}$$

NUT is a suite of the same simulation which has been used to methodically include more and more physics i.e. cooling, star formation, stellar feedback, and now, mag-

netic fields, one step at a time to systematically study their impact.

2.4.4 Finding haloes: HaloMaker

As previously indicated, the analysis of cosmological simulations is complicated. One of the difficulties is the identification of galaxies during their evolution. Many of the measurements performed throughout this thesis will rely on a correct computation of galaxy centres, and I therefore require an accurate method for this purpose. I use the HaloMaker code, presented by Tweed et al. (2009) for this purpose.

This program employs a thresholding method to set apart bound structures in a density field, with the capacity of also detecting their substructure (Aubert et al. 2004). The centre of a galaxy is usually identified as the position of its most bound particle. This however can occasionally yield inaccurate results at high resolutions where dense star clusters are formed. To improve the precision my centre finding, I implement into HaloMaker the shrinking spheres centering method (Power et al. 2003). Once a halo is found, I recursively compute the barycentre of the mass in the halo in a sphere of initial radius equal to the virial radius of the halo $r_{\rm vir}$. In each iteration, I reduce this radius by 2.5 % until a criterion for the number of particles in the sphere is met.

In order to identify galaxies, I apply this algorithm to the dark matter component first. I then identify the halo hosting the galaxy, and re-apply the algorithm within this halo but on the stellar and gaseous components combined to obtain the centre of the galaxy.

2.5 Comparing simulations and observations

The comparison of numerical studies with observations has improved significantly as computational models have evolved in complexity and completeness. In this Section,

I describe the procedures I use to take advantage of the sophistication of state-of-the-art simulations in order to generate images analogous to observational data.

2.5.1 Mock optical images

The SUNSET software allows to generate synthetic observations of cubes of the simulation containing stellar particles. SUNSET is a simplified version of the STARDUST algorithm (Devriendt et al. 1999), and allows its user to compute the emission corresponding to each stellar particle according to stellar emission templates. I treat every stellar particle as a SSP and attribute to it the EM spectrum from the stellar population model of Bruzual & Charlot (2003) that better fits its characteristics. I also include dust attenuation by integrating this emission along a line of sight to the observer, absorbing the emission from each star particle according to the amount of dust present. To model dust in my simulation, I follow Kaviraj et al. (2016) and assume a metal to dust mass ratio of 0.4.

Chapter 3

Tracing magnetic fields

3.1 Motivation

The ubiquity of magnetic fields in the Universe (Widrow 2002), present at many astrophysical scales is frequently accompanied by a lack of uncertainty as to their origin. This is typically a result of their complex evolution. Arguably, the best approach to model this evolution is through numerical simulations which solve the MHD equations described in Chapter 2. Indeed, such simulations have already contributed to the study of the numerous channels that could be responsible for magnetising our Universe, be it in the ISM of galaxies (Butsky et al. 2017), galaxy clusters (Vazza et al. 2014), or the LSS (Vazza et al. 2017). However, one could argue that, while they have addressed which mechanisms could produce magnetic fields in these systems, they have not found an answer to what *is* the origin of these magnetic fields.

For instance, as described in the Introduction of this thesis (Chapter 1), the magnetic fields in galaxies could result from one of three processes, each capable of reproducing observations. The fields could be built up through dynamo amplification (Kulsrud & Zweibel 2008; Pakmor et al. 2014; Rieder & Teyssier 2016), or the ISM could be magnetised by feedback from stars or black holes (Beck & Wielebinski 2013;

Butsky et al. 2017; Vazza et al. 2017). Alternatively, they might have a pre-galactic origin, with strong fields being remnants from early Universe or post-recombination processes such as reionisation (Durrive et al. 2017). The fact that the question was already being discussed 30 years ago (Rees 1987) illustrates the longevity of the issue. All these channels are potentially sufficient to produce realistic magnetisation in galaxies on their own. But in the likely case that they operate simultaneously, it will be all the more difficult to disentangle their respective contributions.

This issue is not confined to galaxies: a similar debate exists for galaxy clusters, with the origin of magnetic fields ranging from primordial or plasma dynamo processes to magnetisation by AGN feedback. Extensive numerical work addressing possible mechanisms exists (Ryu et al. 2008; Vazza et al. 2018), and of particular importance are the observational predictions which differentiate each scenario and might provide an answer to the generating mechanism (Donnert et al. 2009; Vazza et al. 2017).

This struggle to separate individual contributions has become one of the major obstacles for progress in the domain. Ideally one would like to be able to differentiate the contribution from each source to the magnetic field and total magnetic pressure/energy at every moment and place in the Universe. Previous studies on this topic have generally taken the approach of turning on and off the different processes to understand how magnetisation evolves differently under changing scenarios (e.g Vazza et al. 2017). However, as the different sources of magnetic fields are not necessarily mutually exclusive and each may be dynamically important on its own, they could affect the generation or evolution of others. Thus, I present in this Chapter an original method I have designed to handle the case where the magnetic field in a simulation can be affected by a variety of sources. Using this novel approach allows to track the contribution from each source separately and their joint effects thus providing a window on the interplay between different scenarios of magnetogenesis.

I also present an implementation of it into the Ramses code that I have co-

developed with Dr. Harley Katz. I describe the algorithm in Section 3.2, and present its theoretical foundation and implementation in the RAMSES code. In Section 3.3 I describe the simulations employed to benchmark it and demonstrate its potential. Sections 3.4 and 3.5 respectively discuss the accuracy and caveats of the method. A summary of the implementation is presented in Section 3.6. The analysis of the physical results of the simulations are deferred to Chapter 5, where I apply the method to cosmological and cosmic zoom-in simulations.

3.2 Magnetic Field Tracers

I take advantage of the linearity of the induction equation and the solenoidal constraint for the evolution of the magnetic field to develop a method that separately follows the individual contributions to the total magnetic field from a variety of sources. The implementation described here is specifically designed for grid-based codes.

In order to isolate the contribution of different sources to the magnetic field we allow the total magnetic field ($\vec{B}$) to be written as

$$\vec{B} = \sum_{m}^{\mathrm{N_{source}}} \vec{B}_{t_m}, \tag{3.1}$$

where $\mathrm{N_{source}}$ is the total number magnetic sources or decompositions. $\vec{B}_{t_m}$ can be thought of as a magnetic field of a specific nature, which evolves without knowledge of the other $\vec{B}_{t_m}$ except for the response that these might trigger from the fluid due to the presence of the total magnetic component. In other words, the dynamics of the fluid in the simulation only respond to the total magnetic field, $\vec{B}$, which then has a dynamical effect on the evolution of each decomposed magnetic field (tracer) $\vec{B}_{t_m}$; however, each tracer $\vec{B}_{t_m}$ is not aware of the presence of any other tracer $\vec{B}_{t_l}$ with $l \neq m$ when the induction equation is solved or the electromotive forces (EMFs) are calculated for this tracer. The algorithm allows to trace the amplification (or reduction) of each

tracer magnetic field separately throughout the simulation, according to the dynamics taking place. This is only possible because the induction equation (eq. (2.4)) and the solenoidal constraint (eq. (2.5)) are linear in $\vec{B}$.

The induction equation (eq. (2.4)) can be expanded in three dimensions

$$\begin{bmatrix} \frac{\partial B_x}{\partial t} \\ \frac{\partial B_y}{\partial t} \\ \frac{\partial B_z}{\partial t} \end{bmatrix} = \begin{bmatrix} \frac{\partial}{\partial y}(v_x B_y - v_y B_x) - \frac{\partial}{\partial z}(v_z B_x - v_x B_z) \\ \frac{\partial}{\partial z}(v_y B_z - v_z B_y) - \frac{\partial}{\partial x}(v_x B_y - v_y B_x) \\ \frac{\partial}{\partial x}(v_z B_x - v_x B_z) - \frac{\partial}{\partial y}(v_y B_z - v_z B_y) \end{bmatrix}. \tag{3.2}$$

By placing a subscript of t_m on each of the components of B in the previous equation, the induction equation for an individual magnetic tracer field, as defined by eq. (3.1), is obtained. To better illustrate this method the change in the B_x component is considered exclusively:

$$\begin{aligned} &\frac{\partial B_x}{\partial t} = \frac{\partial \sum_m^{\mathrm{N_{source}}} B_{x,t_m}}{\partial t} = \\ &\frac{\partial}{\partial y}\left(v_x \sum_m^{\mathrm{N_{source}}} B_{y,t_m} - v_y \sum_m^{\mathrm{N_{source}}} B_{x,t_m} \right) - \frac{\partial}{\partial z}\left(v_z \sum_m^{\mathrm{N_{source}}} B_{x,t_m} - v_x \sum_m^{\mathrm{N_{source}}} B_{z,t_m} \right). \end{aligned} \tag{3.3}$$

Considering the simple case of only two tracer groups, it can be shown that the induction equation satisfies the condition required for the total field to be separated into independent, individual magnetic tracers.

$$\begin{aligned} \frac{\partial B_x}{\partial t} = \frac{\partial (B_{x,t_1} + B_{x,t_2})}{\partial t} &= \frac{\partial}{\partial y}\left(v_x (B_{y,t_1} + B_{y,t_2}) - v_y (B_{x,t_1} + B_{x,t_2}) \right) \\ &- \frac{\partial}{\partial z}\left(v_z (B_{x,t_1} + B_{x,t_2}) - v_x (B_{z,t_1} + B_{z,t_2}) \right) \\ &= \left[\frac{\partial}{\partial y}\left(v_x B_{y,t_1} - v_y B_{x,t_1} \right) - \frac{\partial}{\partial z}\left(v_z B_{x,t_1} - v_x B_{z,t_1} \right) \right] \\ &+ \left[\frac{\partial}{\partial y}\left(v_x B_{y,t_2} - v_y B_{x,t_2} \right) - \frac{\partial}{\partial z}\left(v_z B_{x,t_2} - v_x B_{z,t_2} \right) \right] \\ &= \frac{\partial B_{x,t_1}}{\partial t} + \frac{\partial B_{x,t_2}}{\partial t}. \end{aligned} \tag{3.4}$$

I extend to multiple $\vec{B}$ components the implementation by Fromang et al. (2006), where the evolution of the magnetic field is separated into a multiple step solver, first computing the induction due to the generation of EMFs, then advecting the cell-centred magnetic field, and finally adding the contribution of the EMFs to the magnetic field. The corresponding magnetic induction by the EMFs follows

$$\frac{B^{n+1}_{x,i-1/2,j,k} - B^{n}_{x,i-1/2,j,k}}{\Delta t} = \\ \frac{E^{n+1/2}_{z,i-1/2,j+1/2,k} - E^{n+1/2}_{z,i-1/2,j-1/2,k}}{\Delta y} - \frac{E^{n+1/2}_{y,i-1/2,j,k+1/2} - E^{n+1/2}_{y,i-1/2,j,k-1/2}}{\Delta z}, \tag{3.5}$$

where n is the time step, E is the temporally and edge-averaged EMF, and i, j, k represent the coordinates of the edge or face with director vector aligned with the listed coordinate direction. For instance, $B^{n}_{x,i-1/2,j,k}$ corresponds to the magnetic field of the left face in the $x-$ direction at time step n while $E^{n}_{z,i-1/2,j+1/2,k}$ is the EMF at the top edge of the left face in the $z-$direction of the same cell at the same time.

The first term in eq. (3.5) is linear in B, and therefore

$$\frac{B^{n+1}_{x,i-1/2,j,k} - B^{n}_{x,i-1/2,j,k}}{\Delta t} = \sum_{m}^{\mathrm{N_{source}}} \frac{B^{n+1}_{t_m,x,i-1/2,j,k} - B^{n}_{t_m,x,i-1/2,j,k}}{\Delta t}, \tag{3.6}$$

where $B^{n+1}_{t_m,x,i-1/2,j,k}$ is now the value of the magnetic field at time $n+1$ of the left face in the $x-$direction for the source t_m. The other two terms have the exact same form as the first. So as long as the time and edge-averaged EMFs are linear in B, the induction equation can be separated. For the EMFs at one specific edge

$$E^{n+1/2}_{z,i-1/2,j-1/2,k} = \frac{1}{\Delta t \Delta z} \int_{t_n}^{t_{n+1}} \int_{z_{k-1/2}}^{z_{k+1/2}} E_z(x_{i-1/2}, y_{j-1/2}, z', t') dz' dt', \tag{3.7}$$

and thus

$$
\begin{aligned}
E^{n+1/2}_{z,i-1/2,j-1/2,k} &= \frac{1}{\Delta t \Delta z} \int_{t_n}^{t_{n+1}} \int_{z_{k-1/2}}^{z_{k+1/2}} \sum_{m}^{\mathrm{N_{source}}} E_{t_m,z}(x_{i-1/2}, y_{j-1/2}, z', t') dz' dt' \\
&= \frac{1}{\Delta t \Delta z} \sum_{m}^{\mathrm{N_{source}}} \int_{t_n}^{t_{n+1}} \int_{z_{k-1/2}}^{z_{k+1/2}} E_{t_m,z}(x_{i-1/2}, y_{j-1/2}, z', t') dz' dt',
\end{aligned}
\tag{3.8}
$$

if

$$
E_z(x_{i-1/2}, y_{j-1/2}, z, t) = \sum_{m}^{\mathrm{N_{source}}} E_{t_m,z}(x_{i-1/2}, y_{j-1/2}, z, t). \tag{3.9}
$$

Since,

$$
\begin{aligned}
E^n_{z,i-1/2,j-1/2,k} &= \bar{v}_x \bar{B}_y - \bar{v}_y \bar{B}_x \,, \\
\bar{v}_x &= \frac{1}{4}(v^n_{x,i,j,k} + v^n_{x,i-1,j,k} + v^n_{x,i,j-1,k} + v^n_{x,i-1,j-1,k}) \,, \\
\bar{v}_y &= \frac{1}{4}(v^n_{y,i,j,k} + v^n_{y,i-1,j,k} + v^n_{y,i,j-1,k} + v^n_{y,i-1,j-1,k}) \,, \\
\bar{B}_x &= \frac{1}{2}(B^n_{x,i-1/2,j,k} + B^n_{x,i-1/2,j-1,k}) \,, \\
\bar{B}_y &= \frac{1}{2}(B^n_{y,i,j-1/2,k} + B^n_{y,i-1,j-1/2,k}) \,,
\end{aligned}
\tag{3.10}
$$

neither $\bar{v}_x$ nor $\bar{v}_y$ depend on B and both $\bar{B}_x$ and $\bar{B}_y$ are linear in B. Therefore eq. (3.9) holds, which ensures that eq. (3.8) is also true. Hence the induction (eq. 2.19) is entirely linear in B and therefore separable into the different components, B_{t_m}. As the induction for each of the tracers follows the same algorithm, guaranteed to work for the total magnetic field, the inducted contribution to each of the magnetic tracers is solenoidal by construction (see Fromang et al. 2006). Advection of magnetic fields in RAMSES is done through cell-centred fluxes. Each cell-centred flux is extracted from the corresponding two faces of the advecting cell, and added to the two corresponding faces of the cell advected onto. Therefore, this contribution is equally divergenceless.

In the test presented for the implementation I track the total field in the normal manner as well as each individual tracer field. I do this to demonstrate that follow-

ing the tracer fields individually exactly conserves all of the properties of the total magnetic field (see Section 3.4.1). The caveat of following all fields (as is done in this Chapter to explicitly demonstrate the convergence properties) is that when reconstructing states on cell faces and edges, or refining a cell, slope limiters are generally used to ensure that the reconstruction is second-order total variation diminishing. However, once a generic slope limiter (e.g. MinMod) is applied, it may no longer be the case that all magnetic field properties are perfectly conserved because the slopes may be limited by different amounts, violating the required linearity condition. Thus in the simulations described in this Chapter, I remove all slope-limiters for all the magnetic field quantities (note that hydrodynamic quantities are still slope-limited). However, since one of the tracer fields can be reconstructed by knowing the total field as well as the other tracer fields, in future simulations one would only need to follow $\mathrm{N_{source}} - 1$ tracer fields. By doing this, the slope-limiters can be re-applied to the total field if desired and hence the same exact results as a simulation that does not include the tracers can be recovered. By definition, the reconstruction of the tracer field that is not explicitly followed will also be divergenceless (since the solenoidal constraint is linear in B), and the sum of all of the tracer fields will add up to the total. Furthermore, this method is less computationally expensive as the user can remove one of the fields. The reconstruction done in this way is only slightly less accurate than following every field independently.

3.3 Numerical Simulations

This MHD tracer algorithm has been implemented into the Ramses CT solver, and used to perform the simulations studied in this Chapter. The initial conditions for these simulations correspond to a $(1.25\ \mathrm{Mpc})^3$ comoving box, discretised into a set of 128^3 gas cells and dark matter particles, generated using MUSIC (Hahn & Abel

2011). The simulation is initialised at $z = 150$, using the following cosmological parameters: $\Omega_m = 0.3175$, $\Omega_\Lambda = 0.6825$, $\Omega_b = 0.049$, $\sigma_8 = 0.83$, and Hubble constant $H_0 = 67.11\text{km s}^{-1}\text{Mpc}^{-1}$, consistent with results of the Planck Collaboration (2015). All of our simulations include subgrid physics described in Chapter 2, and heating and cooling processes for the gas component (Section 2.2.2). A UV background (Haardt & Madau 1996) to model reionization is switched on instantaneously at redshift $z = 8.5$. These simulations set an initial metallicity floor of $10^{-3.5} Z_\odot$ to mimic early enrichment by Population III stars (Wise et al. 2012). The quasi-lagrangian AMR refinement has a maximum refinement of 10 physical parsecs at $z = 6$. The MinMod limiter is only applied to non magnetic hydrodynamical quantities.

I include MTT star formation as described in Section 2.3.1, and allow the formed star particles to generate stellar feedback (Section 2.3.2) using the mechanical stellar feedback implementation described in Section 2.3.2.2. Furthermore, we allow each SN event to inject a magnetic field as described in Section 2.3.3 with fixed $B_{\text{inj}} = 10^{-5}$ G. This field is injected both into the total magnetic field and a tracer field associated with SN magnetic energy, initialised to $B_{\text{SN}} = 0$ everywhere.

In total, four simulations were run with my algorithm, varying solely the strength of the primordial magnetic field B_0. In all simulations, this primordial magnetic field was set to a simple uniform value with direction along the z-axis (Section 2.4.2. This primordial magnetic field value is initially set for the total magnetic field and the primordial magnetic field tracer. The four simulations have corresponding comoving primordial magnetic fields $B_0 = 10^{-14}$G (B14), $B_0 = 10^{-13}$G (B13), $B_0 = 10^{-12}$G (B12), and $B_0 = 10^{-11}$G (B11). These strengths are well within aforementioned observational constraints of the present-day cosmic magnetic field, and lead to magnetic fields on the order of a few μG in the simulated galaxies shortly after their collapse.

3.4 Results

Here I introduce first results of the magnetic field tracer algorithm, reviewing its numerical accuracy and its potential to uncover the contribution and interplay of magnetic fields with different origins. In these example runs, the tracers separate two magnetic contributions: the primordial magnetic field, and the magnetic field injected back into the gas when stars explode. Each of these fields dominates in different locations. All four simulations with different primordial magnetic seed strengths are evolved until $z = 6$. In this Chapter, I review these simulations with the exclusive aim of demonstrating the soundness of the numerical implementation and the potential uses of the method. The physical results are presented in Chapter 5.

3.4.1 Energy and magnetic field conservation

In this Section, I illustrate the robustness of the algorithm by directly measuring the conservation of total magnetic energy, the magnetic field on the faces of individual cells, and the solenoidal constraint.

In the top left panel of Figure 3.1, I show the fractional difference between the sum of the total energy contained within each of the tracer fields and the total magnetic field in each of the four simulations (B11-B14). The total energy contained in the tracers ($E_{\rm trace}$) within a given cell is:

$$E_{\rm trace} = \frac{1}{2} V_{\rm cell} \left[\overset{(1)}{\vec{B}^2_{\rm SN}} + \overset{(2)}{\vec{B}^2_{\rm Primordial}} + 2 \left(\overset{(3)}{\vec{B}_{\rm SN}} \cdot \vec{B}_{\rm Primordial} \right) \right], \tag{3.11}$$

where $V_{\rm cell}$ is the volume of the cell, $B_{\rm SN}$ is the magnetic field in the SN-injected component, and $B_{\rm Primordial}$ is the magnetic field contained in the primordial component. The total energy within the simulation volume is conserved nearly to machine accuracy with a fractional difference that does not exceed 10^{-14} throughout the course

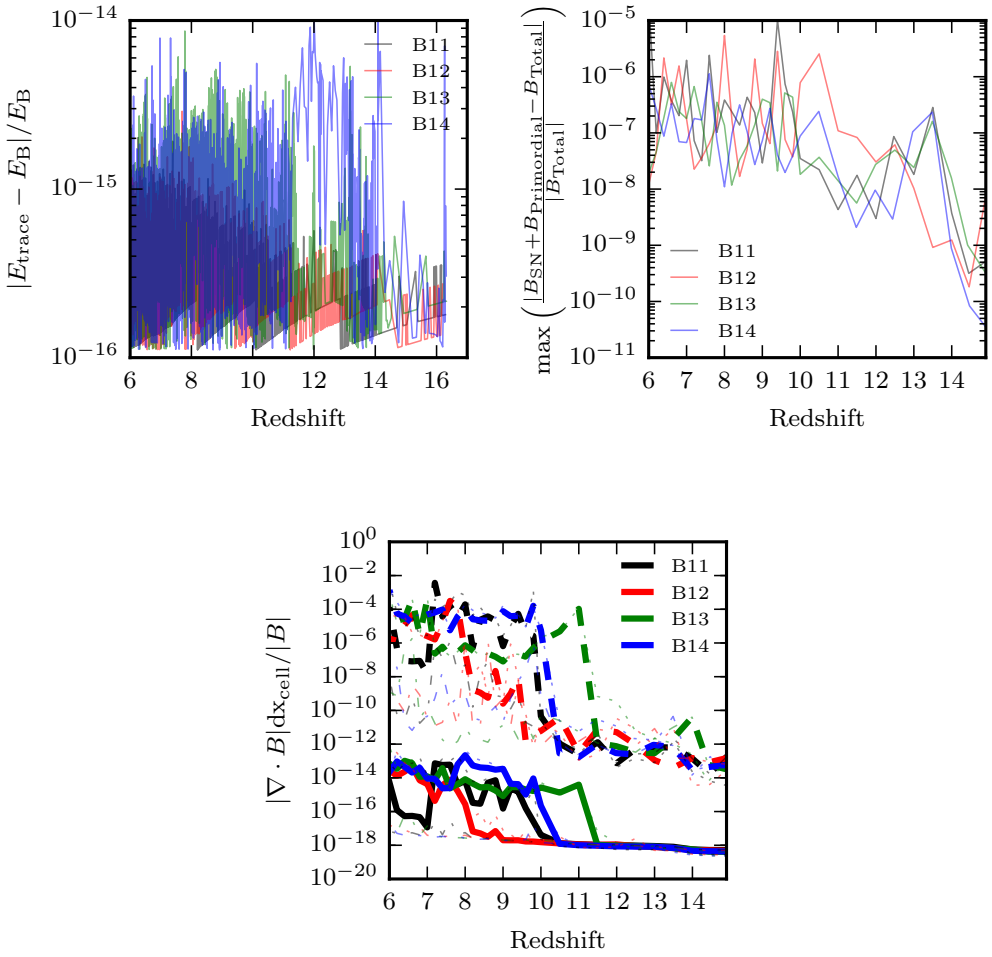

Figure 3.1: (Top left) Fractional energy difference ($|E_{\rm trace} - E_{\rm B}|/E_{\rm B}$) between the sum of the energies stored in the tracer components and the total magnetic energy in the box as a function of redshift. The total magnetic energy is conserved to nearly machine precision regardless of the strength of the primordial magnetic field. (Top right) Maximum difference between the total magnetic field and the sum of the tracer fields ($\max\left(\frac{|B_{\rm SN}+B_{\rm primordial}-B_{\rm total}|}{|B_{\rm total}|}\right)$) in all cell faces and all directions in the simulation as a function of redshift. The maximum difference between the magnetic field stored in the tracer components never deviates more than 0.001% for any cell face over the course of the simulation. (Bottom) Average (solid lines) and maximum (dashed lines) relative magnetic divergence (eq. (2.13)) for the total magnetic field. The thin dashed and dot-dashed lines show the same quantities for the SN and primordial magnetic field respectively. Neither the total, nor the individual tracer fields exhibit divergences that represent more than 1% of the total magnetic field at any point in the simulation. On average the relative magnetic divergences remain below 10^{-13}.

of the simulation. This value fluctuates when magnetic energy is injected with SN explosions; however, it is clear that the total magnetic energy is well-estimated even if it is split into multiple components.

In the top right panel of Figure 3.1, I show the maximum difference between the magnetic field in the tracers and the total magnetic field on all cell faces within the simulation for all four simulations. This difference is divided by the average local magnetic field strength across all six cell faces to avoid local X- and O-points. Over the simulation, the deviation of the magnetic field contained in the tracers from the total magnetic field in any of the faces never reaches more than 10^{-5} of the local magnetic field strength. The maximum error does increase sightly with time before tapering off as more SN injections occur; however, these errors are always negligible compared to the local field strength. Hence the algorithm conserves the local magnetic field strength in addition to the total magnetic energy to a high level of precision.

As discussed in Section 3.2, each tracer field musts satisfy the solenoidal constraint. Due to the implementation of the tracers through a CT method, both for the total and tracer fields, the divergence is constrained to near machine precision. In the bottom panel of Figure 3.1, I show the average and maximum divergence in the total magnetic field as well as in each individual tracer field as a function of redshift. The average divergence in the simulation never increases to more than 10^{-12} of the local total magnetic field and is thus well controlled by the constrained transport algorithm. The same is true for each of the tracer fields. With this precision, the divergence is neither dynamically important nor affecting the induction equation. Also shown in the same panel are the maximal relative magnetic divergences as a function of redshift for each simulation. This value rarely surpasses 10^{-4}, indicating that even in the least controlled environments, the divergence is both negligible for the dynamics and the induction equation. Based on the three tests described, the magnetic fields tracer algorithm conserves all quantities necessary for numerically modelling ideal MHD.

3.4.2 Tracing cosmic magnetic fields with magnetic tracers

I show in the top panel of Figure 3.2, the redshift evolution of the large scale magnetic field from $z = 8$ to $z = 6$. While I will later resort to displaying more physically interesting quantities such as the magnetic energy, here I illustrate how the algorithm performs by showing the primordial magnetic field strength in red, which traces the large scale filamentary structure of the matter distribution. Blue represents instead the SN-injected magnetic field, emanating from the most massive galaxies and penetrating into the IGM perpendicularly to the filaments. The primordial magnetic field is initialised uniformly in the z-direction. As the Universe expands, the energy density of the primordial field decreases in the IGM while it increases as gas condenses into filaments and galaxies. This process will continue as filaments accrue gas and become denser and more massive. However, towards $z = 6$, the strength of the UV background drastically increases (Bolton & Haehnelt 2007; Calverley et al. 2011; Wyithe & Bolton 2011). This is modelled as a uniform heating term in these simulations and has the effect of evaporating the filaments that are not self-shielded (Pawlik et al. 2009). Comparing the snapshot at $z = 7$ with $z = 6$, the most diffuse filaments that appear red at $z = 7$ are missing at $z = 6$ as the UV background has efficiently reduced their density, thus reducing the magnetic field strength. By $z = 6$, the vast ensemble of filaments have not been significantly impacted by the SN-injected magnetic fields, retaining memory of the primordial configuration of the magnetic field.

While the large-scale filamentary structure of the universe is beginning to shape, the first generation of stars forms in the earliest collapsed objects and the total magnetic energy in the SN-injected component increases with decreasing redshift, as more SNe occur. Repeated star bursts allow the magnetic energy to build up around galaxies from the inside-out. SN winds push magnetised gas out of the halo and to expand into the IGM, leading to adiabatic decrease of the magnetic field.

The bottom panel of Figure 3.2 shows the magnetic field around the three most

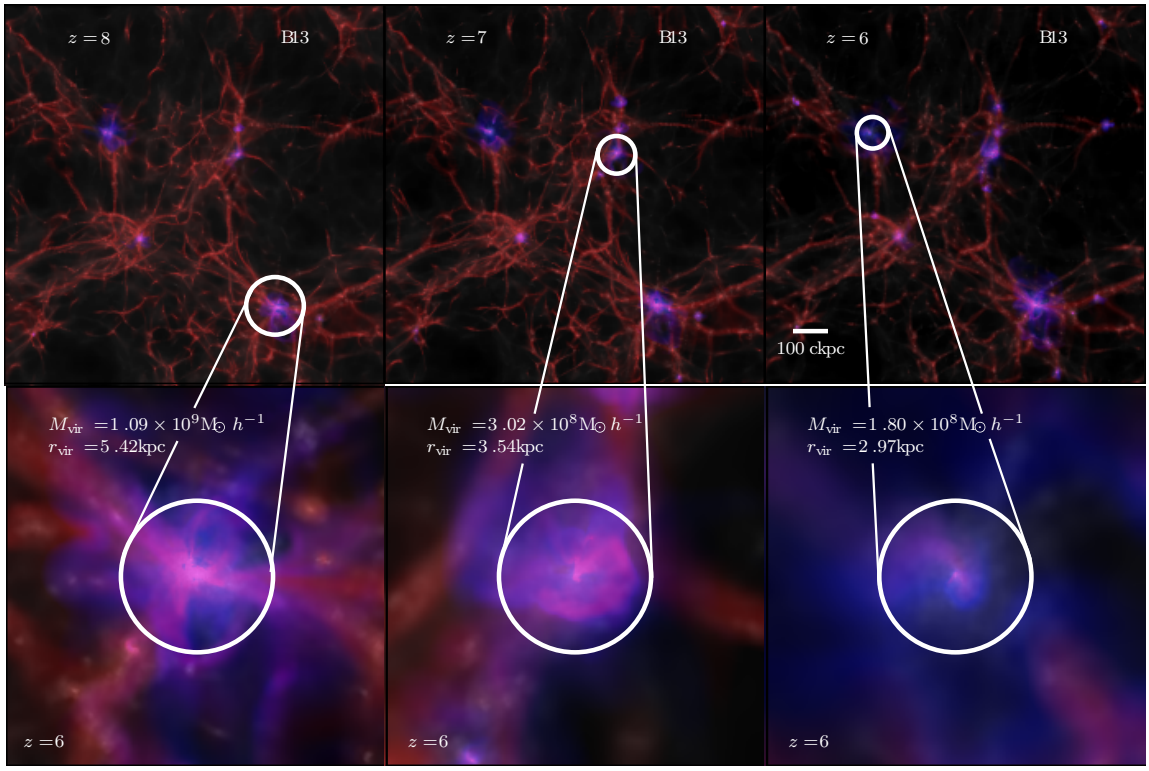

Figure 3.2: (Top) Maps of the magnetic field strength across the full simulation volume for three different redshifts from the B13 simulation. The red regions represent the magnitude of the primordial magnetic field while the blue regions indicate the magnitude of the magnetic field injected during SNe explosions. The dark matter column density is also plotted in grey-scale and the images show a projection along the z-direction of the simulated box. (Bottom) Maps of the magnetic field around the three most massive haloes at $z = 6$. The virial radii of the haloes are indicated with the white circles and scaled to be the same size in all plots.

massive galaxies at $z = 6$. In the left column, three dense filaments are feeding a halo with $M_{\rm vir} = 10^9 {\rm M}_\odot h^{-1}$. These filaments appear bright red in the image and the intensity increases towards the galaxy as magnetic fields are frozen in the gas in ideal MHD and this gas becomes denser. The magnetic field injected from SNe is clearly visible in this image, emanating from the galaxy and propagating into the low density regions between the filaments. At the centre of the halo, the red and blue colours appear blended as there is a contribution from both the primordial field, and the SN-injected field in the same spatial location. When these fields have similar orientation, the total field is amplified; however, in certain regions, the SN-injected field opposes the primordial field which reduces the overall magnetisation in the region. This effect was discussed in Section 2.3.3 and is further explored in Chapter 5.

The second most massive halo appears very similar to the first, as dense, red filaments are feeding the galaxy, while blue magnetised gas emanates from the central regions of the system. In contrast, the third most massive system has a magnetic environment that is completely dominated by the SN-injected component as the filaments feeding the galaxy have likely been disrupted by a combination of an increasing UV background, and SN feedback. The environment around this galaxy is almost entirely blue. As this region is less dense compared to the other two, the magnetic winds driven by SN more easily penetrate into the low density regions of the IGM.

3.5 Caveats

This magnetic fields tracer algorithm is an effective tool to better understand the evolution and associated effects of magnetic fields with different origins. All the limitations associated with numerical MHD are transferred to the traced magnetic fields. Astrophysical MHD simulations have numerical viscosities and resistivities significantly higher than their physical counterparts in nature, which limits our capability

to accurately model various processes of critical importance (e.g. small-scale dynamo, diffusion, turbulent cascade). In this thesis, I will employ this algorithm to compare primordial magnetic field and SN injected magnetic fields. Dynamo mechanisms could amplify differently the tracer fields, naturally increasing the importance of primordial magnetic fields in the simulated haloes as, e.g. a turbulent dynamo could operate from very early times on this ab-initio field. Similarly, the results emerging from the comparison of tracing different fields will significantly depend on spatial resolution, the selected separation of fields, or sub-grid physics. For the specific purpose of this thesis the strength of the magnetic field injected, how often it is injected (based on SN rates), and the properties of the injected fields suffer from considerable uncertainties.

3.6 Summary of the method and applications

In this Chapter I presented a magnetic fields tracer algorithm and its implementation in Ramses. I discussed its robustness using four different high-resolution cosmological MHD simulations, tracing two magnetic fields of different origins: an ab-initio primordial field, and an additional magnetic component injected when SN explode. The main conclusions of this Chapter are:

- The equations for ideal MHD can be linearly decomposed so that individual contributions to the total magnetic field from different sources can be tracked.
- A method conserving magnetic energy, magnetic field on each cell face, and maintaining the solenoidal constraint so that it is neither dynamically important nor affects the induction equation has been implemented in Ramses.

My motivation for designing and implementing this algorithm extends beyond the applications presented in this thesis. I therefore conclude this Chapter with a list of ongoing, future, or envisioned applications of the magnetic field tracers:

- Study the origin of galactic magnetic fields, by tracing in combination primordial magnetic fields, injection from sources such as AGN and SN, and a subgrid algorithm for a fast turbulent dynamo.

- Constrain the relevance of galactic magnetic field at cosmic scales. Employing large cosmological simulations, trace magnetic fields that have been generated by galaxies (e.g. from source injection or subgrid dynamos) to understand the volume fraction occupied by these fields. This could be particularly important for the future generation of telescopes as SKA which might be capable of observing IGM magnetic fields.

- Studying the relevance of primordial magnetic fields of different scales. When generating magnetic initial conditions following a given spectral shape, various wavelength ranges can be separated in different tracers, and used to understand how different structures and their final magnetic fields are affected by multiple scales of primordial magnetic fields.

- Generation of magnetic fields during the epoch of reionisation. A natural extension of the presented method is tracing source terms in the induction equation, which can be directly injected into a magnetic tracer to understand the importance of mechanisms such as the Biermann battery or photon induced currents.

- Non-ideal MHD applications (with the subsequent adaptations to non-linear terms), characterising magnetic amplification, and many others.

Chapter 4

Turbulent amplification in galaxies

4.1 Motivation

As discussed in the Introduction (Chapter 1), magnetic fields are observed to be important in galaxies, at typical strengths corresponding to equipartition with the other forms of energy in the ISM (Wolfe et al. 1992; Bernet et al. 2008; Beck & Wielebinski 2013; Mulcahy et al. 2014). One of the most fascinating open questions of cosmic magnetism is that of its origin, and how magnetic fields evolved from their primordial state to the values we observe in local galaxies or clusters. There are large uncertainties surrounding the formation time and mechanism of magnetic fields in our Universe (Widrow 2002). Theoretical models favour very weak fields to form in the very early Universe, perhaps during inflation (Hogan 1983; Kolb & Turner 1990; Ratra 1992). Most post-recombination mechanisms for magnetism generate fields that are weak (Biermann 1950; Schlickeiser 2012), many orders of magnitude below the micro-Gauss values observed in galaxies around us (Beck & Wielebinski 2013; Mulcahy et al. 2014). Such weak magnetic fields are permitted by constraints on the cosmic magnetic field (Broderick et al. 2012; Neronov & Vovk 2010; Planck Collaboration 2015). Assuming the weakness of primordial fields, a tantalising question emerges:

how is the gap between such fields and the ones observed in galaxies bridged?

Magnetic fields in galaxies represent the largest gap between weak primordial and observed magnetic fields. Indeed, to attain measured strengths on the order of 10^{-5}-10^{-6} G (Beck 2015; Mulcahy et al. 2017), we require dynamo mechanisms of remarkable efficiency. Observational evidence points to the amplification already having occurred at high redshift (Wolfe et al. 1992; Bernet et al. 2008, $z \simeq 2.0$).

Several possibilities for rapid dynamos exist. Examples in decreasing order of popularity are the turbulent dynamo (Vazza et al. 2014; Pakmor et al. 2014, 2017; Rieder & Teyssier 2017a; Vazza et al. 2018), the $\alpha - \Omega$ dynamo (Wang & Abel 2009; Dubois & Teyssier 2010), or once the magnetic field reaches a lower strength threshold and can excite the magneto-rotational instability (MRI, Kitchatinov & Rüdiger 2004), an MRI-driven dynamo (Machida et al. 2013; Gressel et al. 2013).

Numerical studies testing these different dynamos have been performed on various scales. These range from plasma simulations (e.g. Haugen et al. 2004a; Schekochihin et al. 2004; Haugen et al. 2004b; Teyssier et al. 2006; Schober et al. 2015) to isolated galaxies (Dubois & Teyssier 2010; Pakmor & Springel 2013; Rieder & Teyssier 2016). In particular, plasma simulations have shown that a small-scale dynamo converting turbulent energy into magnetic energy is capable of rapidly reaching energy equipartition (Schekochihin et al. 2002; Federrath et al. 2011a, 2014; Schober et al. 2017). These studies are however limited to scales significantly smaller than those of a galaxy and still suffer from resolution limitations as they are not capable of resolving both the inertial and sub-viscous ranges (see Kinney et al. 2002; Schekochihin et al. 2002). At the same time, given the stringent resolution requirements to adequately capture the inertial magnetic range and produce realistic galactic turbulence, studies of chunks of the ISM or isolated galaxies display growth rates which are even lower. Nevertheless, combining all these simulation results point towards the turbulent dynamo being capable of producing the fields we observe in galaxies. Therefore, to develop a more

complete picture, the behaviour of a turbulent dynamo in an explicit cosmological context needs to be studied. This constitutes an extraordinary numerical challenge: at high redshift, galaxies are born small, and progressively grow with time as they accrete gas from their environment and merge with other objects. Continuously capturing the inertial magnetic range and turbulence as galaxies become larger over the span of their lifetimes is thus a daunting task.

In this Chapter, I present my efforts to study the growth of magnetic energy in a Milky Way-like galaxy, simulated at high spatial resolution (up to 10 pc) by means of a cosmological zoom-in simulation. As far as I am aware, this is the first occurrence of a numerical experiment that combines both such a high spatial resolution and a constrained transport scheme for the magnetic field. This work extends the study of magnetic field amplification in isolated spiral galaxies Rieder & Teyssier (2016), by modelling a more realistic evolution of the galaxy through cold gas inflows and galaxy mergers. My results show that a turbulent dynamo is indeed capable of amplifying the magnetic energy of the galaxy in such a context, and that the growth of this energy is affected by environmental properties. This leads to differentiated phases of amplification of the magnetic energy. I also review how various physical models and numerical factors influence my results. Arguably the most interesting variation concerns the amplification of the field in the absence or presence of different stellar feedback models. I find that the amplification is only dominated by feedback during the later stages of galaxy evolution, once the cold gas accretion has considerably dwindled and mergers of galaxies are less frequent.

The structure of this Chapter is as follows: the simulations set-up is first presented in Section 4.2, and the main results in Section 4.3, where I identify amplification occurring during three main stages: the initial collapse of the galaxy (Section 4.3.1), an accretion-driven phase (Section 4.3.2) and a feedback-driven phase (Section 4.3.3). In Section 4.4 I explore the robustness of the proposed division into three phases of

amplification, and discuss the dependency of the results on numerical implementation. The final part of the Chapter is devoted to numerical resolution, reviewing how different AMR resolutions and refinement strategies affect the growth of the magnetic energy. A useful complement to this Chapter can be found in Appendix A, Section A.1, where I describe in more detail how I calculate the Fourier power spectra of various quantities for a disk galaxy in a cosmological simulation. Conclusions of this work are provided in Section 4.6.

Finally, this Chapter explores the possibility of achieving magnetic field strengths comparable to those observed in galaxies by means of kinematic dynamos on galactic or ISM scales, neglecting other mechanisms. Alternative options exist, and their interaction with dynamo amplification is a complex question that we can now start to study with methods like that presented in Chapter 3. I discuss this in Chapter 5.

4.2 Simulations

The initial conditions for all the simulations employed in this Chapter are those of the NUT galaxy, described in Section 2.4.3. For the main simulations, the AMR strategy is quasi-Lagrangian (so that all cells contain approximately the same total mass), up to a maximual resolution of 10 physical parsecs. All the simulations employ the magneto-thermo-turbulent star formation model of Section 2.3, forming stars with large efficiencies ($\epsilon \geq 0.1$) in regions where the gravitational force overcomes turbulent, magnetic and thermal support.

The main runs differ in their stellar feedback implementation, reflected by their labels *B-Mech*, *B-RdTh*, and *B-NoFb*. These stand for the stellar feedback presented in Section 2.3.2.2, Section 2.3.2.1, and no stellar feedback, respectively. Due to its intrinsic capability of capturing the anisotropic expansion through ISM inhomogeneities of SN blast waves, the *Mech* solution is expected to present a better description of post-

shock turbulence. This should lead to a more efficient generation of the corresponding baroclinic vorticity which drives local solenoidal modes of turbulence. Having this solenoidal forcing fosters the post-shock amplification of magnetic energy (Ji et al. 2016) which should be expected in SNR. In any figure where they are inter-compared, the B-Mech, B-NoFb and B-RdTh simulations are colour-coded blue, red and green respectively. These simulations have been evolved down to $z = 2$.

To study the influence of numerical resolution on my results, I perform four supplementary runs with *Mech* feedback, successively decreasing the spatial resolution: B-MR20, B-MR40, B-MR80, and B-MR160. The sub-labels MR20, MR40, MR80, and MR160 indicate a maximal resolution of the AMR scheme of 20, 40, 80, and 160 physical parsecs respectively. In a a second set of runs I implement instead a different refinement strategy (labelled Eur), which combines the AMR refinement with a more Eulerian approach. BMEuRX simulations use a physical gas density threshold, fixed to $\rho_{\rm threshold} = 10^{-24}{\rm g/cm^3}$, above which a given cell below the maximum level of resolution is refined. Through this method the ISM of the galaxy is effectively refined with a uniform grid. The supplementary runs where we vary the resolution and refinement strategy are discussed in Section 4.5.

The main simulations in this Chapter are summarised in Table 4.1.

The majority of the analysis in this Chapter will make use of the region defined as the *galactic region*, which corresponds to a sphere centred on the galaxy, extending out to $0.2\,r_{\rm halo}$, with $r_{\rm halo}$ being the virial radius of the dark matter halo. The centering of this region and its size are obtained using HaloMaker, as described in Section 2.4.4. This accurate centering of my galaxies will be crucial when studying quantities such as rotational velocities or galactic profiles of physical quantities. At the earliest times in our simulations, between time $t \sim 0$ and the formation of the virialised dark matter halo, we are unable to detect the centre of the galaxy. At this point, we fix $r_{\rm halo}(z > z_{\rm coll}) = r_{\rm halo}(z_{\rm coll})$ and the centre of the region to the position of the

Table 4.1: Properties of the simulations used in this Chapter. Table indicates the initial comoving homogeneous magnetic field strength B_0, maximum spatial resolution $\Delta x_{\rm m}$, refinement scheme *Ref*, and stellar feedback model employed.

Simulation	B_0 (G)	$\Delta x_{\rm m}$ (pc)	*Ref*	Feedback
B-Mech	$3 \cdot 10^{-20}$	10	AMR	Mech (sect 2.3.2.2)
B-NoFb	$3 \cdot 10^{-20}$	10	AMR	✗
B-RdTh	$3 \cdot 10^{-20}$	10	AMR	RdTh (sect 2.3.2.1)
B-MR20	$3 \cdot 10^{-20}$	20	AMR	Mech
B-MR40	$3 \cdot 10^{-20}$	40	AMR	Mech
B-MR80	$3 \cdot 10^{-20}$	80	AMR	Mech
B-MR160	$3 \cdot 10^{-20}$	160	AMR	Mech
B-MEuR10	$3 \cdot 10^{-20}$	10	Eul	Mech
B-MEuR20	$3 \cdot 10^{-20}$	20	Eul	Mech
B-MEuR40	$3 \cdot 10^{-20}$	40	Eul	Mech
B-MEuR80	$3 \cdot 10^{-20}$	80	Eul	Mech
B-MEuR160	$3 \cdot 10^{-20}$	160	Eul	Mech
B-MEuR320	$3 \cdot 10^{-20}$	320	Eul	Mech

collapsed proto-galaxy at the time of collapse $t_{\rm coll}$ ($z_{\rm coll}$), defined in Section 4.3.1.

4.2.1 Divergence checks

To demonstrate the accuracy of the CT scheme for my cosmological AMR simulations, I display in Figure 4.1 various properties of the distribution of the relative magnetic divergence for the main runs discussed in this Chapter. The median values for the relative magnetic divergence is practically null at a few 10^{-15}. The interquartile ranges are quite narrow, within ± 1 dex above and below the median values. I also present with dashed lines the 3σ width for the distribution of all leaf (non-refined) cells in the simulations. These relative magnetic divergences are always found to have values smaller than 10^{-10}. Lastly, I also include in the graph the maximal values reached by an individual cell during the course of a specific simulation. These are represented by squares (*Mech*), circles (*NoFb*), and triangles (*RdTh*). Within each shape, I label the level of refinement where the cell containing the corresponding relative magnetic divergence was found, with 1 representing the highest refinement active in a given

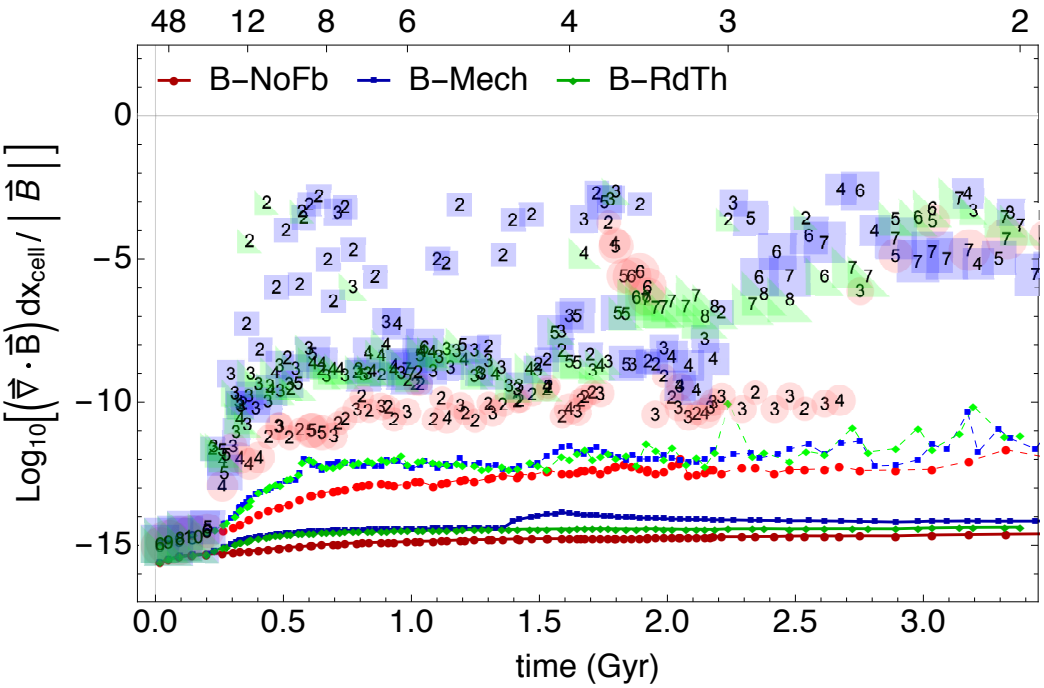

Figure 4.1: Relative magnetic divergences for the entire distribution of leaf cells at all redshifts ($z \geq 2$) in the three main runs studied in this Chapter. Medians and 3σ (99.7 %) of the distribution are represented by solid and dashed lines. Maximal values of the distribution for each output of the simulations are also shown. These are shown by squares (*Mech*), circles (*NoFb*), and triangles (*RdTh*). These shapes are labelled with the cell refinement level. The label 1 corresponding to the highest refinement available, and increasing numbers to subsequently lower refinement levels. No cell in the simulations is found to have a divergence larger than 1% of the local magnetic field strength.

output and subsequently higher values corresponding to coarser levels. For all these simulations, the maximal divergence always remains well below the percent level.

4.2.2 Resolution requirements

In order to capture a significant turbulent dynamo action, it is required to resolve the inertial range of MHD gas turbulence. Federrath et al. (2011b) argue that for a MHD simulation with self-gravitating gas, a minimum of 30 resolution elements per Jeans length is necesary to trigger a dynamo. In the ISM, each gas phase will have a different impact on the evolution of the magnetic energy (Evirgen et al. 2017), and

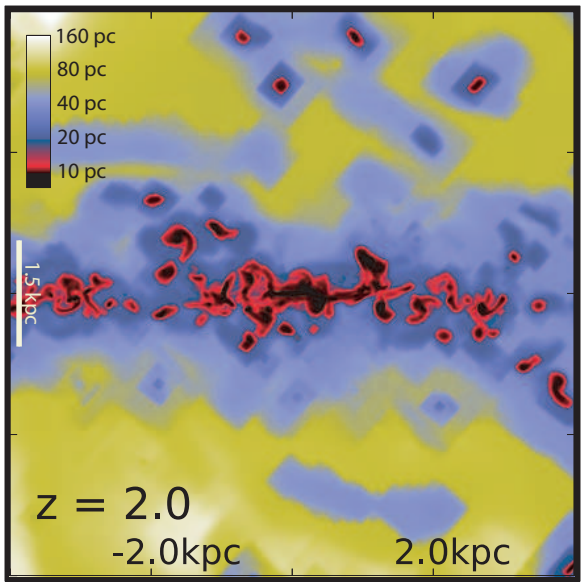

Figure 4.2: Projected view of the density-weighted grid spatial resolution (colour scale). The shown region corresponds to a cube of $(8\ \mathrm{kpc})^3$ centred on the B-Mech galaxy. Galactic disks are mostly resolved with ~ 70 cells of 20 physical parsecs of size, above the threshold proposed by Federrath et al. (2011b) to capture effects of a turbulent dynamo.

thus, this type of study should aim to fulfil this resolution criterion in as much of the volume of the galaxy as possible regardless of the gas phase present. For the case of spiral galaxies, this is a particularly complicated challenge to overcome due to the relatively small thickness of the gas disk. For one of our main simulations, we show in Figure 4.2 how our resolution elements distribute across the thickness of the disk. The typical half-thickness h_s of the gas disk for a galaxy using an exponential profile fit to the gas density $\rho(z) \propto e^{-|z|/h_s}$ is $h_s > 300$ pc. Examples of how these measurements are obtained are provided in Appendix A, Section A.2. At the second highest level of refinement present in our simulations, we find the number of resolution elements is above the number suggested by Federrath et al. (2011b). I dedicate Section 4.5 to discuss in more depth numerical details such as how my simulations also meet the magnetic Reynolds number requirement to trigger turbulent dynamos. As far as I am aware, this work presents, at the time of writing, the highest spatial resolution MHD cosmological simulations of disk galaxies with a CT method.

4.2.3 A weak initial magnetic field

The objective of these simulations is to understand whether purely kinematic processes can generate magnetic fields that are compatible with local galaxy observations. As these dynamos are incapable of producing a magnetic field by themselves, the most challenging but feasible scenario of dynamo amplification is having an extremely weak primordial magnetic field at the beginning of the simulations which serves as a seed for the dynamo. Thus, in these simulations, I provide an initial, homogeneous magnetic field as described in Section 2.4.2. The selected strength corresponds to an extremely weak field with no dynamical effects on the collapsing proto-galaxies. This should yield maximal amplification for our given numerics and spatial resolution without risk to run into saturation. Indeed, due to the limitations of our simulations, we do not expect this amplification to be capable of reaching μG magnetic fields in several Gyr. Therefore, the magnetic component will not back-react on the fluid dynamics. Considering this, all the simulations in this Chapter feature an identical weak initial magnetic field compatible with a Biermann battery (Biermann 1950), but with a different spatial configuration as the initial field is aligned with the z-direction in this work. The comoving strength is $B_{\rm co} = 3 \cdot 10^{-20}$ G, which corresponds to a physical magnetic field $B_{\rm ph} \sim 10^{-17}$-10^{-18} G at $z \sim 40$ (Pudritz & Silk 2002; Widrow 2002).

In line with the discussion in Section 2.4.2, altering the initial spatial configuration of the magnetic seed will potentially alter the evolution of magnetic fields, especially during the collapse phase. I will review this in future work.

4.3 Results

This Section is dedicated to the growth of the magnetic energy in the simulated galaxies, focusing on the effects of cosmological environment and comparing different feedback prescriptions. By the end of the simulated period at $z = 2$, the expectation

for galactic magnetic fields from observations is that they already are in equipartition with the thermal or turbulent energies (Bernet et al. 2008). As a result, the majority of the amplification should have taken place prior to this moment.

As my simulations are cosmological in nature, the studied galaxy will form hierarchically, progressively increasing its mass through both mergers with other galaxies and the accretion of gas from cold filaments and a hot diffuse gas. The morphology of the galaxy for all three main runs by $z = 2$ is shown in Figure 4.3 (B-Mech, B-NoFb, and B-RdTh in each row), where I present in each column respective projections of the gas density and temperature, the magnetic energy density and mock optical images (generated as described in Section 2.5.1). I identify during my simulations down to $z = 2$, three distinct phases for the evolution of the magnetic component, each corresponding to a period when a different set of physical processes dominates the evolution of the galaxy. The three phases are (i) the collapse of the initial density perturbations into a proto-galaxy, (ii) a cold filamentary accretion dominated phase, and (iii) a final period where stellar feedback becomes the main actor as accretion fades.

I review in order each of these phases, studying how cosmological factors alter the growth of the magnetic energy in the galaxy, and how different stellar feedback prescriptions play a role in this process[1].

4.3.1 Formation of the galaxy: the collapse phase

Galaxy formation and evolution in ΛCDM cosmological simulations follows a hierarchical collapse scenario (White & Frenk 1991). The initial density perturbations expand with the background Universe until they reach a turn-around point, dictated by their amplitude. At this point, their magnetic energy hits a minimum due to adiabatic expansion ($\epsilon_{\rm mag} \propto B^2 \propto \rho^{4/3}$). After turn-around, perturbations decouple from

[1]All quantities in this Chapter are expressed in physical units unless otherwise stated.

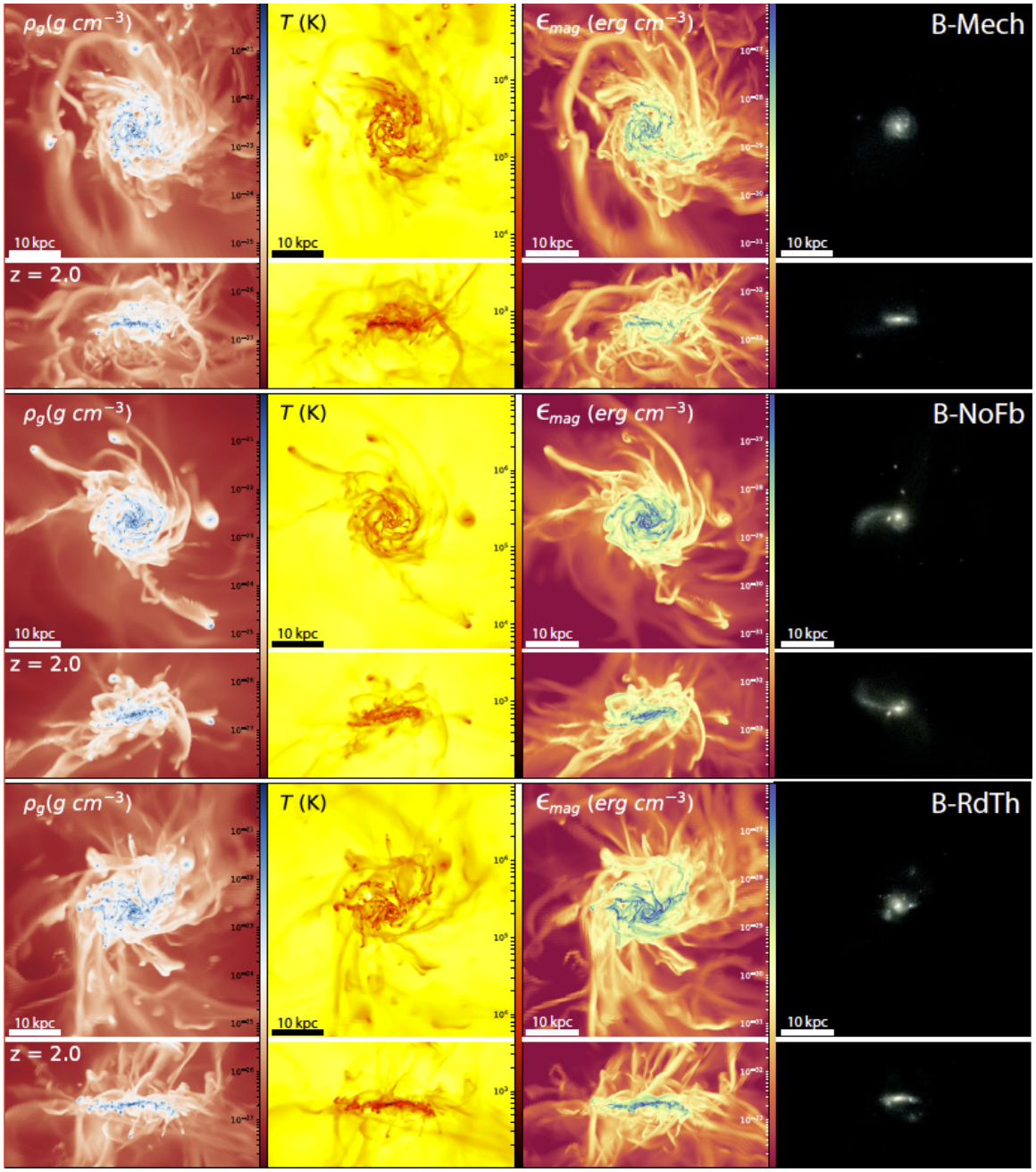

Figure 4.3: Projected physical quantities for the main simulations studied in this Chapter at the end of the studied period ($z = 2$). Each pair of two rows corresponds to face-on and edge-on views of the B-Mech (top), B-NoFb (middle), and B-RdTh (bottom) runs. Each projection is integrated along a 50 kpc on a side box. From leftmost to rightmost, each column represents gas density ρ_g (g cm^{-3}), gas temperature T (K), magnetic energy density $\epsilon_{\rm mag}$ (erg cm^{-3}), and a mock optical image obtained with SUNSET as described in Section 2.5.1 respectively. The filters employed to obtain the colour composite correspond to SDSS [u',g',r'], and no dust absorption has been taken into account. All displayed intensive quantities are mass weighted.

cosmic expansion and commence their collapse. The gravitational potential increases and dissipative processes of the baryonic gas allow it to fall to the centre of this potential. This gas will follow the procedure described for star formation and generate stellar particles. Star formation will take place in the cold phase of our galaxy, and I use its onset to mark the end of the collapse phase. More specifically, I select $t_{\rm coll}$ as the time in the simulation when at least 100 stellar particles have been created, which should correspond to the establishment of a multi-phase ISM.

In Figure 4.4, I show the mass evolution of the galaxy for each of my runs, separated into DM, stellar, and gaseous component for the *galactic region* (i.e. a sphere of radius 0.2 $r_{\rm halo}(z)$ centred on the main galaxy). As $r_{\rm halo}(z)$ is the physical virial radius of the dark matter halo, the galactic region increases as redshift decreases, always containing the entirety of the galaxy and its immediate environment. The selection of the fraction of the radius to be 0.2 follows from the estimated maximal size of the galactic disk when the specific angular momentum of the disk is assumed to be approximately equal to that of the entire dark matter component inside the virial radius of the host halo. This radius is $\sim 4\ \lambda\ r_{\rm halo}$ (Mo et al. 1998, see eq. (14)). The spin parameter of the halo under study is $\lambda \sim 0.05$ at all times (Kimm et al. 2011), as measured following the definition of Bullock et al. (2000). Hence the value of 0.2 used for the *galactic region*. I have also checked that alterations to the size of the region do not significantly modify my results, as long as they contain the whole galaxy.

If I aim to compare the absolute content of magnetic energy in the galaxy throughout time, I need to somehow remove its connection to the mass of the galaxy, which will depend on gas accretion, mergers, or galactic outflows. In other words, the same amount of absolute magnetic energy implies different magnetisations for galaxies of different masses. A similar problem arises when comparing energy densities, as these are dependent on the shape and volume of the galaxy. The problem is aggravated for

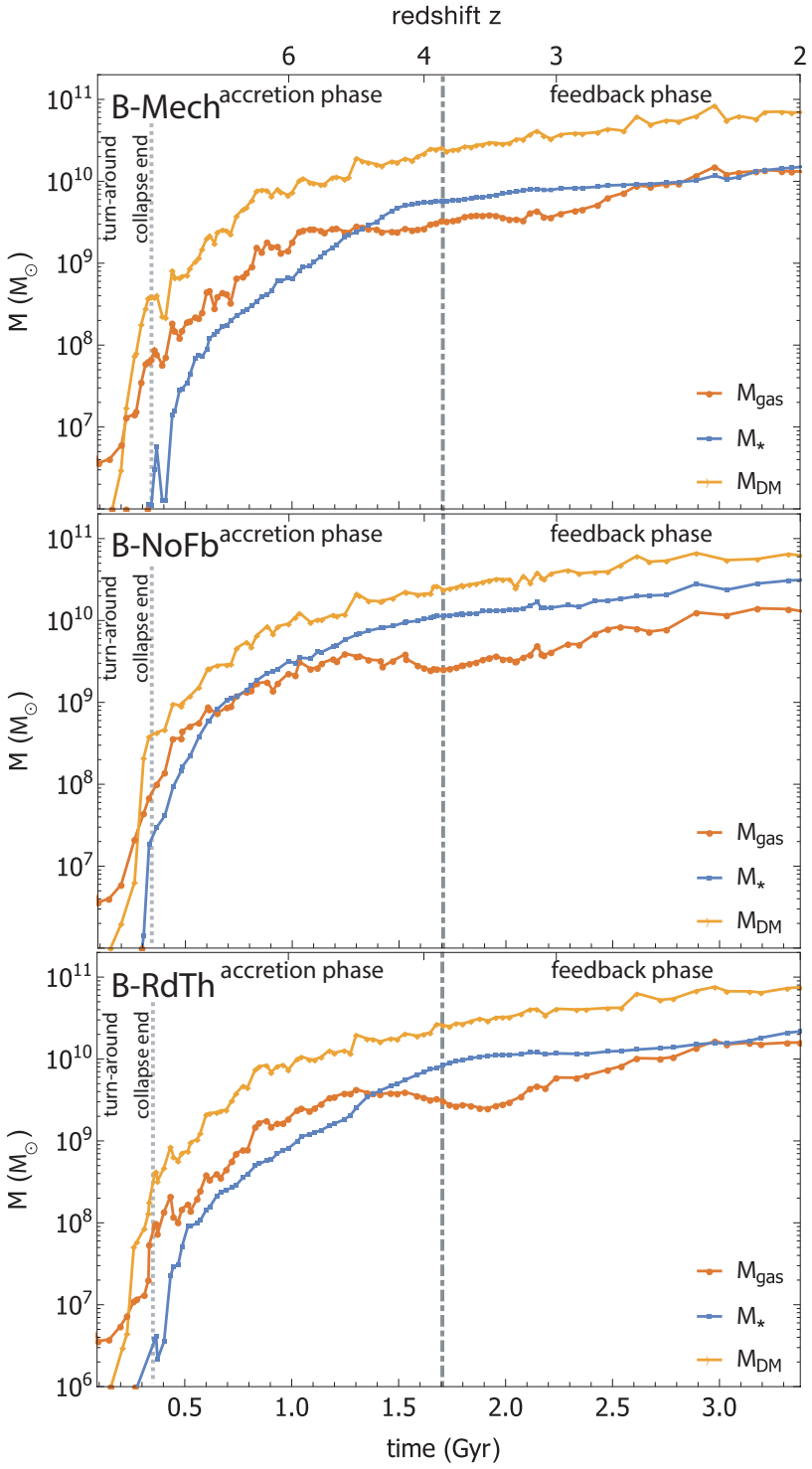

Figure 4.4: Mass content in the galactic regions of the main three simulations decomposed in gas (red), dark matter (yellow), and stars (blue). From top to bottom, simulations are B-Mech, B-NoFb, and B-RdTh. I discriminate between different phases using vertical gray lines for the end of the collapse phase (dotted) and the end of the accretion phase (dot-dashed).

the case of disk galaxies. I get around this problem by employing specific energies in the entirety of the galactic region

$$\varepsilon_x = \frac{E_{\rm x}}{M_{\rm gas}}, \tag{4.1}$$

simply resulting from the ratio of an absolute energy E_x and the gas content $M_{\rm gas}$ in the region. By doing so, I study how much magnetic energy is found per unit mass in the galaxy. Pristine gas accreted into the galaxy will supply material with a lower $\varepsilon_{\rm mag}$, as it will have lost magnetic energy through cosmic expansion. In turn, the growth of this quantity will correspond to some mechanism that genuinely amplifies magnetic energy rather than accumulates it.

Under the assumption that during the initial phase of galaxy formation the collapse of the halo follows an idealised isolated halo, the isotropic collapse of the gas will lead the magnetic energy density to increase with the gas density ρ_g as $\epsilon_{\rm mag} \propto \rho_g^{4/3}$ (Wang & Abel 2009; Dubois & Teyssier 2010; Rieder & Teyssier 2016).

But in a truly cosmological formation scenario, a galaxy is expected to develop higher turbulence levels than in an isolated, idealised case (Klessen & Hennebelle 2010; Elmegreen & Burkert 2010), and accretion-driven turbulence should become even more important as the gravitational potential deepens (Elmegreen & Burkert 2010). I show in Figure 4.5 the evolution of the specific magnetic energy $\varepsilon_{\rm mag}$ inside the galactic region during the first stages of the formation of the galaxy, including the entirety of the collapse phase and the first stages of the accretion stage. I normalise each of these magnetic energies to their measured values at turn-around, $\varepsilon_{\rm mag,ta}$. These are similar to percent level for the three main runs. Furthermore, the magnetic amplification during collapse and particularly the times of the collapse for the halo are robust with respect to the employed feedback model.

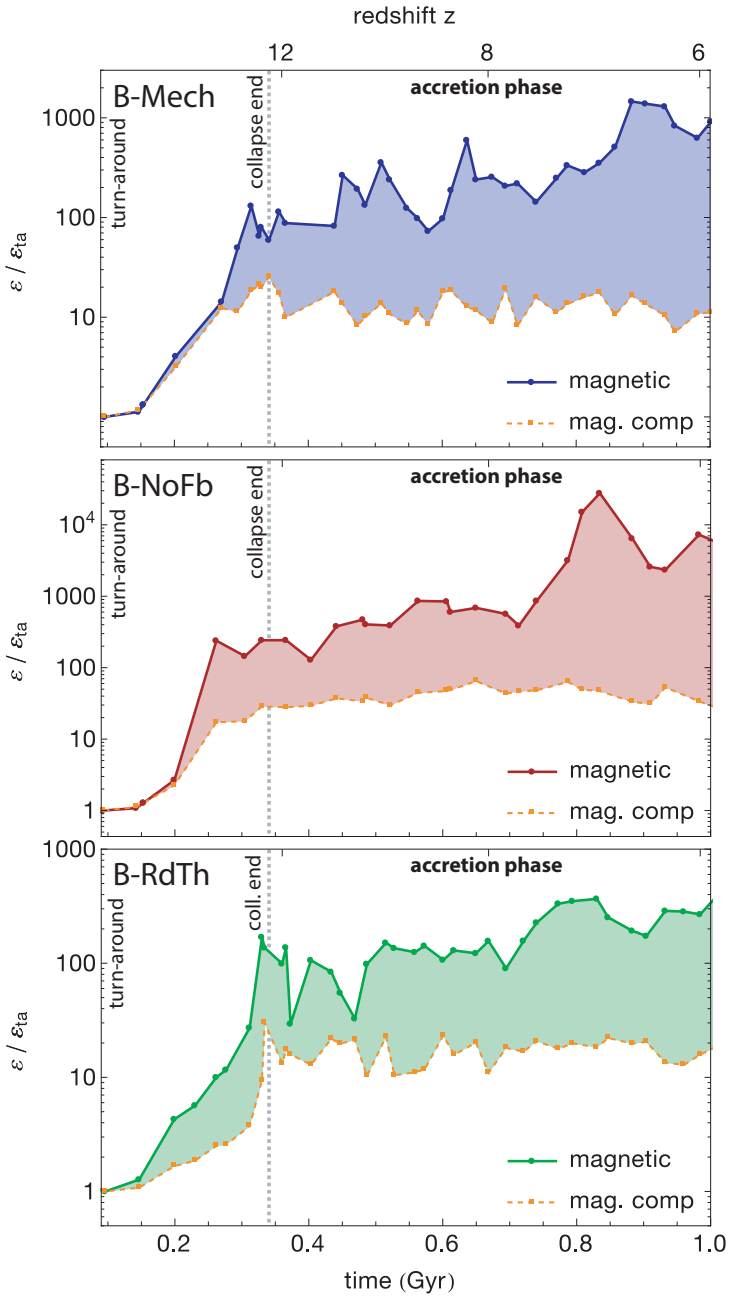

Figure 4.5: Growth of the specific magnetic energy in the three main runs during the early stages of formation of the galaxy, comprising the entirety of the collapse phase and the beginning of the accretion phase. Measurements are for the galactic region, and panels display from top to bottom B-Mech (blue), B-NoFb (red), and B-RdTh (green) runs. The dashed orange lines illustrate the expected evolution of the specific magnetic energy if the exclusive source of magnetic energy growth was adiabatic isotropic collapse and expansion (i.e. no anisotropy, stretching, or numerical dissipation; see equation 4.3). Each run has its energy normalised to the value at turn around (more details in text). Finally, the vertical dotted line indicates the end of the collapse phase.

A quantitative estimate of the collapse time for a top hat density perturbation is

$$t_{\rm coll} = \frac{2}{3H_0} \frac{1}{(1+z_{\rm coll})^{3/2}}. \tag{4.2}$$

where $z_{\rm coll}$ is selected as the redshift at which this perturbation reaches the linearly extrapolated critical over-density for an Einstein-de Sitter universe (e.g. Peebles 1994). This time also corresponds to the onset of star formation in my simulations, and we have $t_{\rm coll} \sim 0.34$ Gyr ($z_{\rm coll} \sim 13$), with turn-around time (and redshift) $t_{\rm ta} \simeq 0.5\, t_{\rm coll}$ ($z_{\rm ta} \sim 22$). These former are indicated by the vertical dotted line and in reasonable agreement formation times of the galaxy, which can be estimated by the position of the first peak of the dashed curves in Figure 4.5. The measurement of the specific magnetic energy in the galactic region at the time of collapse $\varepsilon_{{\rm mag},C}$ can be taken as an estimate of the amount of amplification generated by the collapse of the galaxy. I will use these values as a reference for the amount of amplification corresponding to the collapse phase. These are in reality upper limits, as the expansion of the Universe will decrease the magnetisation of the gas accreted onto the galaxy, and numerical dissipation will also significantly reduce the magnetic energy in the galaxy. These values are indicated by horizontal dashed lines in Figure 4.6, and are a fairly good match to the compressionally generated magnetic energy in the galaxy (orange dashed lines in Figure 4.5). The values found for $\varepsilon_{{\rm mag},C}$ vary by a factor of 4 between runs, indicating that stellar feedback already reduces the magnetic amplification in the later stages of the collapse of the proto-galaxy, by expelling magnetic energy and gas from the system. If the value for these energies were taken immediately after the collapse of the galaxy (position of the first peak), their spread would be somewhat reduced but still present.

From Figure 4.5, specific magnetic energies $\varepsilon_{\rm mag}$ in simulations are observed to grow by a factor $\sim 100 - 200$ between the time of turn around (beginning of the

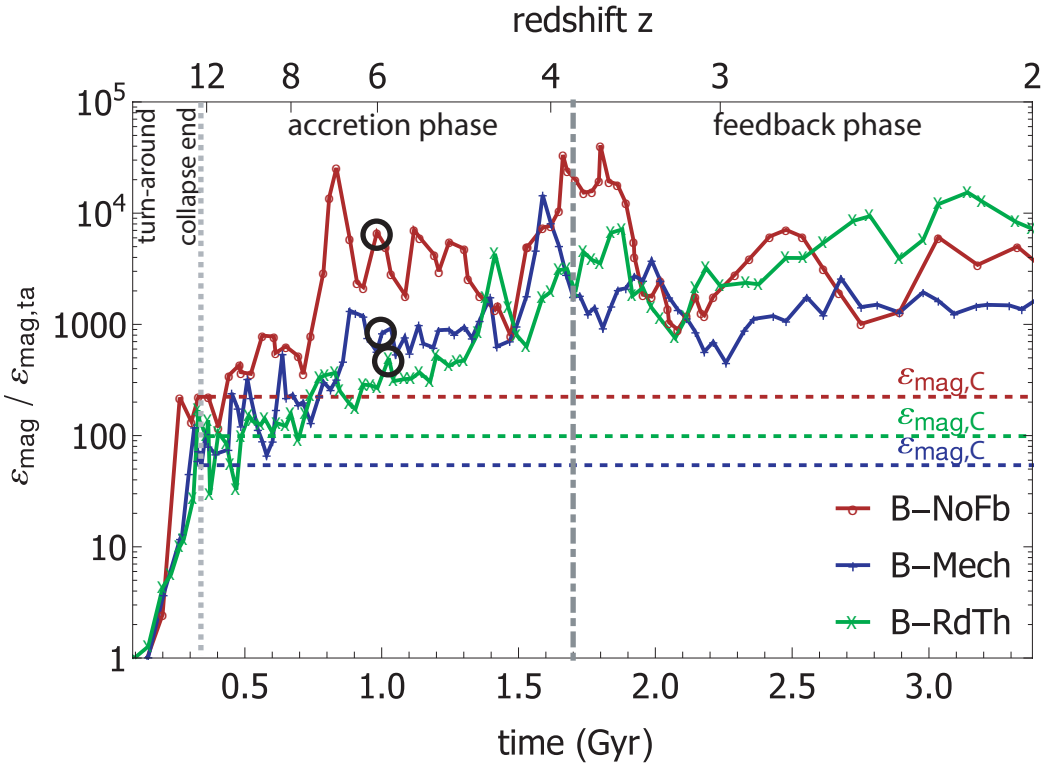

Figure 4.6: Growth of the specific magnetic energy (solid lines) in the galactic region of the three main runs: B-Mech (blue), B-NoFb (red), and B-RdTh (green). Dashed lines indicate the upper limit for the specific magnetic energies attributed to collapse $\varepsilon_{\mathrm{mag},C}$ for each run (see text). Vertical lines are used to mark the division between each of the identified phases: end of the collapse (dotted) and accretion-dominated phase (dot-dashed). The specific energy of each simulation is normalised to its turn around value. Circles indicate the time corresponding to the mergers displayed in Figure 4.12

time axis) and the end of the collapse period (vertical dotted lines). These values are about an order of magnitude above the ones derived analytically by Lesch & Chiba (1995). In their work, these authors use the spherical top hat model and estimate the magnetic field strength is amplified by $f_c \sim [r_{\rm ta}/(0.2r_{\rm halo})]^2 \sim 100$ from turn-around until disk formation. This in turn corresponds to a specific magnetic energy increase of $f_c^2\,[(0.2r_{\rm halo})/r_{\rm ta}]^3 \sim 10$ in the galactic region, when assuming the gas mass within a sphere of radius $r_{\rm ta}$ is conserved exactly. This matches my estimates for the isotropic adiabatic collapse evolution of the specific magnetic energy (orange dashed curve in Figure 4.5). This latter estimate is obtained assuming that each individual cell in the galactic region has undergone an isotropic and adiabatic collapse from the time of turn-around. Therefore, its magnetic energy is given by

$$E_{\rm mag}^{\rm cell}(t) = \frac{{\rm dx}_{\rm cell}^3}{\frac{4}{3}\pi r_{\rm gal}^3(t_{\rm ta})} \times \langle E_{\rm mag}(t_{\rm ta})\rangle \left(\frac{\rho_g^{\rm cell}(t)}{\langle\rho_g(t_{\rm ta})\rangle}\right)^{4/3}, \tag{4.3}$$

where for quantity X, $\langle X\rangle$ stands for its average value over the entirety of the galactic region at a given time. The adiabatic isotropic estimate for the specific magnetic energy of the galactic region at time t follows from adding the contributions of all cells enclosed within the region at that time, and dividing it by the total amount of gas present in the region.

I emphasize that this estimate does not only assume that the collapse is adiabatic and isotropic, but it also considers that no decrease of the field occurs due to cosmological expansion numerical resistivity. Realistically, the strength of the magnetic field achieved merely by collapse should decrease with time because (a) the expanding Universe reduces the magnetisation of material accreted at later times ($B \propto a^{-2}$) and, (b) even though the initial collapse might be close to isotropic, material will subsequently be fed to the galaxy through filamentary accretion and mergers. Filamentary accretion is expected to bring in material with lower magnetisation due to the lower

amount of compression undergone by the infalling gas. These cold streams of gas are also expected to possess a low level of turbulence at the mass range of the NUT halo (Mandelker et al. 2017). The impact of mergers on the evolution of the magnetic component is more complex and I defer their treatment to section 4.3.2. Shortly before the initial collapse phase ends ($t \gtrsim 0.25$ Gyr), the estimate of isotropic and adiabatic amplification systematically underestimates the measured specific magnetic energies by an amount which progressively increases with time (solid curves in Figure 4.5). This amount oscillates between $\varepsilon_{\rm mag} \sim$ 10-20 $\varepsilon_{\rm mag,ta}$ during the simulations (i.e. until $z = 2$). It is representative of an scenario where the galaxy accretes material with constant specific magnetic energy during its evolution, without any amplification or decay of the magnetic field beyond that of the initial compression.

In summary, my simulations show that at the end of the collapse phase, the level of turbulence induced in the forming galaxy has amplified the specific magnetic energy within the galactic region by approximately one order of magnitude beyond the isotropic adiabatic collapse scenario. This considerable deviation has also been found for larger virialised objects such as clusters of galaxies (see Dolag et al. 2005a; Dubois & Teyssier 2008; Marinacci et al. 2015). For smaller structures, however, results in the literature resemble more closely to the scaling of the energy density $\epsilon_{\rm mag} \propto \rho_g^{4/3}$. This is the case even for the recent work of Pakmor et al. (2017). This scaling arises from their lower spatial and mass resolution (see my resolution study in Section 4.5). When carefully reviewing Figure 4.5, there is some evidence that the amplification towards the end and immediately after the collapse phase ($0.25 \lesssim t \lesssim 0.5$ Gyr), could be mainly driven by turbulent accretion. I display in Figure 4.6 the three main runs together. This Figure presents evidence that as the power of the stellar feedback prescription increases (the B-RdTh run being the most powerful), the difference with the isotropic collapse estimate decreases.

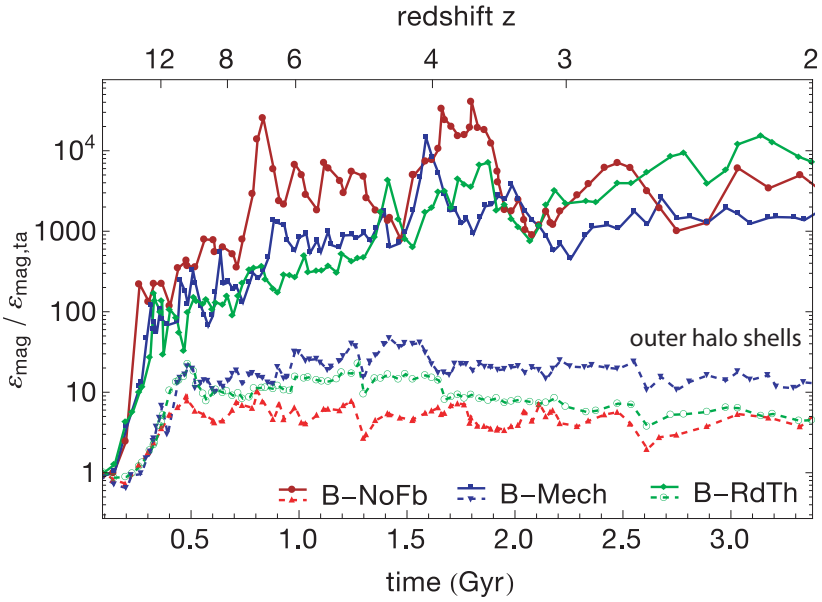

Figure 4.7: Specific magnetic energy evolution in a thin shell around the halo of the galaxy ($1 < r/r_{\rm halo} < 1.05$, dashed lines) compared to the same quantity in the galactic region (solid lines). Specific magnetic energies within the outer halo shell decrease over time as gas is accreted. Stellar feedback appears to contribute to the magnetic energy budget in the shell through magnetised outflows.

4.3.2 Turbulent amplification: the accretion phase

As mentioned before, the accretion of pristine gas contributes to reducing specific magnetic energies as time goes on. This is due to a lower magnetisation of the accreted material as cosmic expansion dilutes it. As shown in Figure 4.7, the specific magnetic energy measured inside a thin spherical shell bounded by radii $r_{\rm halo} < r < 1.05\, r_{\rm halo}$ is significantly lower than the specific magnetic energy inside the galactic region, and it also exhibits a tendency to slowly decrease with time. The presence of stellar feedback mitigates this decay to some degree by transferring gas with higher magnetisation from the galactic region out into the halo. This justifies the presence of higher specific magnetic energies in the outer halo shell of the B-Mech and B-RdTh runs when compared with the B-NoFb run. The specific magnetic energy of the virialised intra-halo region (i.e. $r < r_{\rm halo}$) would therefore decrease if the halo was only assumed to

incorporate this pristine, weakly-magnetised fresh gas.

In the accretion-dominated phase, which extends from $z_{\rm coll} \sim 13$ until $z_{\rm acc} \sim 4$, the galaxy continuously grows in mass and size, principally through accretion from cold filamentary flows (Tillson et al. 2015). Once the collapse phase has ended and the average gas density of the galaxy is approximately fixed, growth of specific magnetic energy beyond $\varepsilon_{\rm mag,C}$ requires stretching the magnetic field through dynamo processes. In particular, a turbulent ISM can generate exponential amplification of the magnetic energy through a turbulent dynamo (Rieder & Teyssier 2016). The level of ISM turbulence during this period depends mostly on gas accretion, either directly (Klessen & Hennebelle 2010; Elmegreen et al. 2009b) or through accretion-fuelled processes such as gravitational instabilities (Elmegreen & Burkert 2010; Krumholz & Burkhart 2016). Even when turbulence is instead assumed to be generated through stellar feedback processes, accretion is still attributed an increasingly relevant role with higher redshifts (Hopkins et al. 2013). Klessen & Hennebelle (2010) find that the total mass of the galaxy is an important factor to determine the importance of accretion-fuelled turbulence. The halo mass also sets whether cold accretion operates (Birnboim & Dekel 2003; Dekel & Birnboim 2006; Ocvirk et al. 2008). As galaxies and haloes accumulate more mass, cold accretion progressively shuts down and the resulting turbulence rapidly decays.

In the absence of feedback, virialised gas in the hot halo can cool and fall down to the galaxy. At the redshifts and halo masses relevant for these simulations, feedback is necessary to maintain the existence of a non-negligible hot phase of gas (Agertz et al. 2009b), and accretion onto the galaxy proceeds mainly through cold filaments (Tillson et al. 2015). Note that feedback could also be reducing the budget of both absolute and specific energies available to drive turbulence through accretion by launching massive and disruptive galactic winds.

Bearing in mind this complex picture, I analyse the evolution of turbulence in the

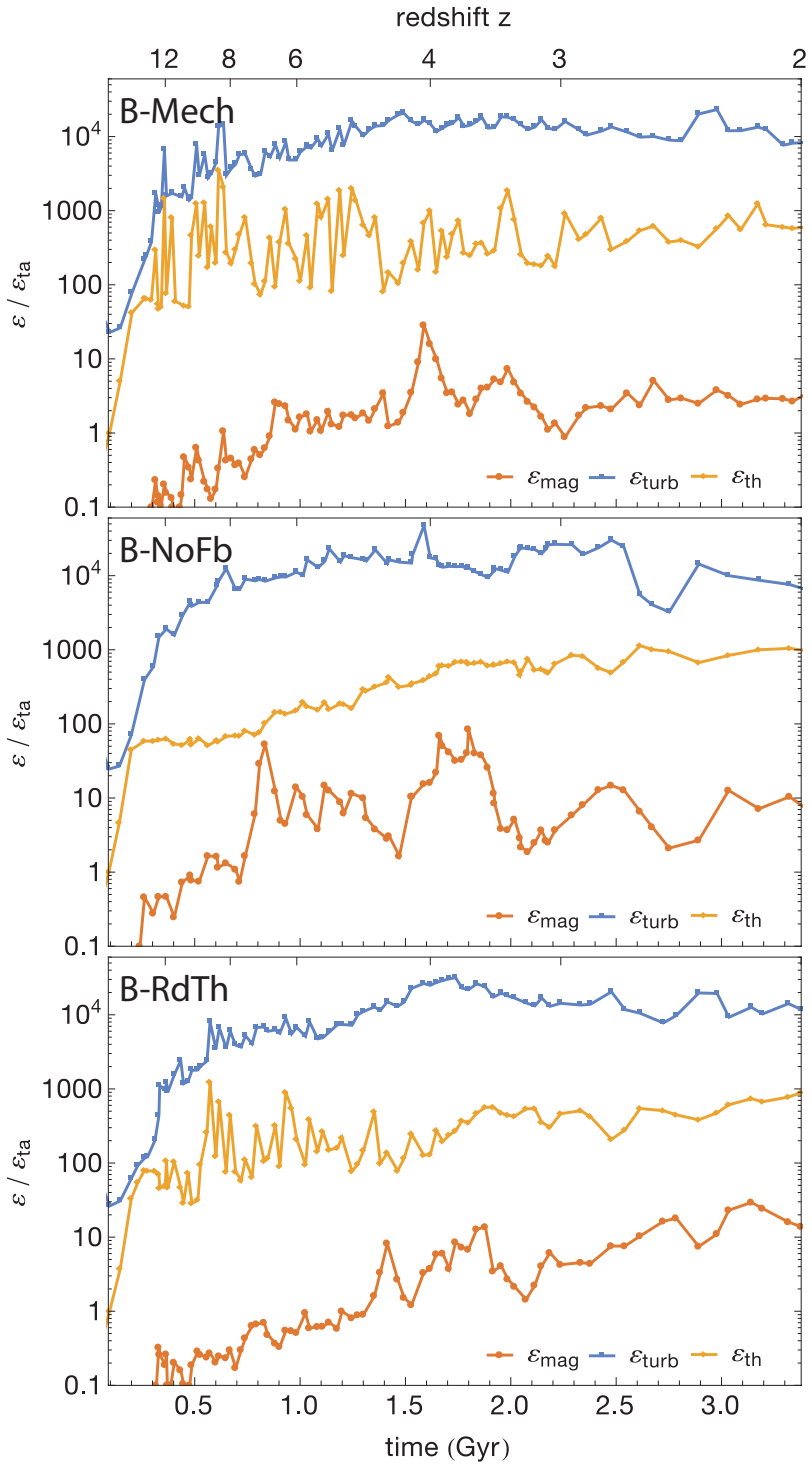

Figure 4.8: Comparison of the specific magnetic (red), thermal (yellow) and turbulent (blue) energies within the galactic region for the B-Mech (top), B-NoFb (middle), B-RdTh (bottom) runs. All energies have been normalized to a unique $\varepsilon_{\rm ta}$ value (see text). To facilitate the comparison, $\varepsilon_{\rm mag}$ curves have been boosted by 15 orders of magnitude.

galactic region by measuring specific turbulent energies (Figure 4.8), radial velocity profiles (Figure 4.9) and turbulent kinetic energy spectra (Figure 4.13).

Once again, I normalise all specific energies displayed in Figure 4.8 to the turn-around value $\varepsilon_{\rm ta} = 10^{10}{\rm cm}^2{\rm s}^{-2}$, which represents the specific thermal energy of the galactic region at this moment in time ($t \sim 0.1$ Gyr). To calculate the absolute turbulent energy $E_{\rm turb}$ I sum up the contribution of each cell whithin the galactic region:

$$E_{\rm turb} = \sum_{i=1}^{N_{\rm cells}} \frac{1}{2} m_i v_{{\rm turb},i}^2, \tag{4.4}$$

where m_i is the gas mass, and the turbulent velocity of the gas cell is defined as $v_{\rm turb,i} = \sqrt{v_{r,i}^2 + (v_{t,i} - v_c(r))^2}$, with $v_{r,i}$ and $v_{t,i}$ the radial and tangential components of the gas velocity respectively, and from which the bulk motion of the galactic region has been subtracted. For this, I define the circular velocity $v_c(r) = \sqrt{GM(r)/r}$, where $M(r)$ is the total mass within the sphere of radius r. I employ two different procedures to remove the circular velocity depending on whether a disk with substantial rotational support exists. If the measured spin parameter of the galactic region, $\lambda = L/(\sqrt{2}\, M(r_{\rm gal})\, v_c(r_{\rm gal})\, r_{\rm gal}) < 0.5$ (with L the angular momentum, and the definition of Bullock et al. (2000)), $v_c(r)$ is subtracted from the tangential velocity (i.e. the vector formed by the two non-radial components of the velocity field) in each cell. After the formation of the disk, when $\lambda > 0.5$, I substract v_c only from the toroidal velocity, in a cylindrical coordinate system where the z-axis is aligned with the gas angular momentum of the disk and goes through the centre of the galactic region. I present in Figure 4.9 turbulent velocity dispersion profiles $\sigma_{\rm turb}(r)$, being the dispersion of $v_{\rm turb,i}(r)$ at each radial bin. The formation of a stable gas disk occurs around $z \sim$ 4.5-4.0 in all the main simulations, as confirmed by visual inspection. This transition correlates with the end of the accretion phase and occurs shortly after the gravitational potential of the galactic region becomes dominated by the stellar component. For simplicity of the analysis, the transition is taken to occur at the same

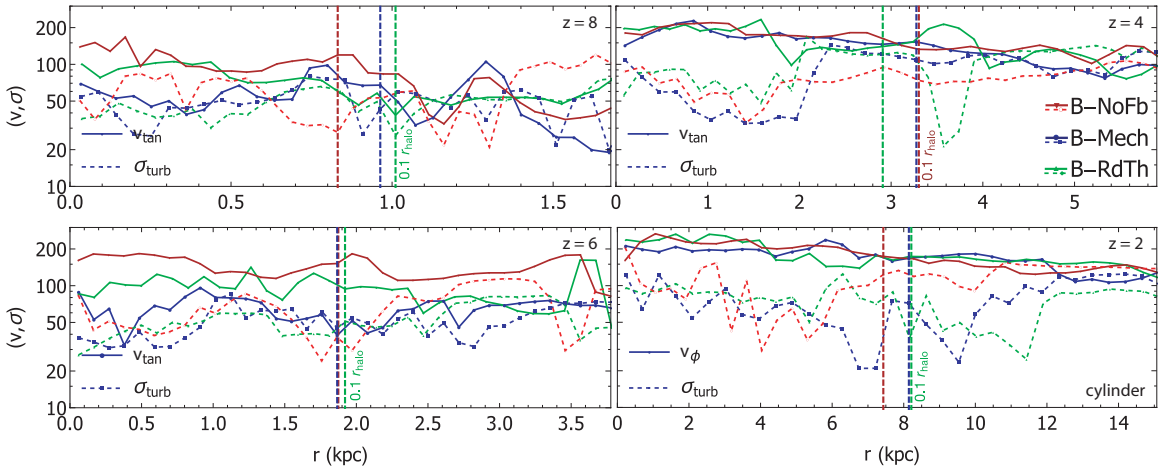

Figure 4.9: Galactic region radially averaged velocity profiles for B-Mech (blue), B-NoFb (red), and B-RdTh (green). I employ cylindrical coordinates for $z = 2$, with their poloidal component aligned with the galactic region angular momentum vector. Solid lines display the tangential, $v_{\rm tan}$, (or toroidal, v_ϕ,) component, dashed lines the turbulent velocity dispersions $\sigma_{\rm turb}$. Vertical dashed lines represent $0.1\,r_{\rm halo}$. As redshift decreases, galaxies become less dominated by turbulence and a clear rotation curve is established.

time $t_{\rm acc/fb}$ ($z_{\rm acc/fb} = 4$) in all runs.

When reviewing the evolution of the specific magnetic energy during the accretion-dominated phase in Figure 4.6 two features are identified: the first are sharp peaks present throughout the entire phase, and the second an underlying continuum upon which these peaks rest, which steadily grows with time. I attribute the presence of peaks to individual merger events, while the growth of the smooth underlying component corresponds to *in situ* turbulent amplification. I consequently address them separately.

Monotonic turbulent amplification of the specific magnetic energy results in an exponential growth $\varepsilon_{\rm mag} \propto e^{\Gamma_\varepsilon t}$, with characteristic time scale Γ_ε. Such an exponential growth typically indicates a turbulent dynamo process (Federrath 2016). Exact values of characteristic time scales obtained by fitting exponential curves to $\varepsilon_{\rm mag}$ (see Figure 4.6) are given in Table 4.2 for both the accretion and feedback-dominated epochs of amplification. During the accretion dominated epoch, these growth factors are

approximately on the order of $\Gamma_{\varepsilon,\mathrm{acc}} \sim 2$ Gyr^{-1}, in fair agreement with the analytic estimate $\Gamma_\varepsilon \sim \sigma_{\mathrm{turb}}/l \sim 1.5 - 3$ Gyr^{-1}, provided one picks a dissipation scale, $l \sim$ 10 - 20 pc, characteristic of the resultion achieved in my simulated galaxies. From the numbers listed in Table 4.2, it can be seen that during the accretion phase, Γ_ε is larger in the absence of feedback. The amplification is also reduced as the strength of the sub-grid feedback implementation increases (the B-RdTh run yields a lower value than the B-Mech run). Stellar feedback thus has a detrimental effect on magnetic energy amplification during the accretion phase. Potential explanations of this behaviour are an increase in turbulent diffusion caused by stellar feedback (Gressel et al. 2008), a suppression of gravitational instabilities, feedback diluting magnetic fields into the hot phase, or a reduction of small scale solenoidal turbulence relative importance (Grisdale et al. 2017). More specifically, stellar feedback could be hampering clump formation triggered by larger scale gravitational instabilities in the galaxy. As solenoidal modes are expected to produce higher growth rates (Federrath et al. 2011a) and stellar feedback can efficiently drive solenoidal turbulence (Korpi et al. 1999) one would expect that in the presence of stellar feedback, the fraction of specific turbulent energy in solenoidal modes within the galactic region should increase. However, I find the opposite during the accretion phase: stellar feedback reduces the fraction of solenoidal specific turbulent energy in my runs on scales $L < 1$kpc by $\sim 10\%$. A detailed study of this complex interaction between feedback, turbulence modes, and magnetic fields amplification is beyond the scope of this work. However, I note that, despite the anisotropic nature of the stellar feedback implementation in the B-Mech run, with the potential to yield a higher amplification of the magnetic energy than the B-NoFb run because of an intrinsically more efficient capability to drive solenoidal turbulence than its isotropic B-RdTh counterpart, this does not happen at least in these specific simulations. This interpretation is underpinned by the measurement of the specific turbulent energies presented in Figure 4.8. It is clear from that Figure that, at least

for $z > 4$, the level of turbulent energy (blue curves) measured in the B-NoFb run is at least comparable to, if not higher than the values measured in both feedback runs. These findings corroborate both the observational standpoint that stellar feedback does not rank as the favoured mechanism to drive turbulence in high-redshift clumpy galaxies (Elmegreen et al. 2009a) and cosmological simulations of magnetised Milky Way-like galaxies performed with a different (moving mesh + divergence cleaning) technique (Pakmor et al. 2014).

As feedback heats the ISM gas, another significant difference between the B-NoFb run and its feedback counterparts, is that this former displays a larger difference between thermal and turbulent specific energies (yellow and blue curves in Figure 4.8 respectively). This supports the claim made by Evirgen et al. (2017) suggesting that the contribution from the hot phase of the ISM to the amplification of magnetic energy is negligible. A possible explanation may be that the flow resides in this phase for a short time compared to the dynamo time scale. By contrast, these two timescales become comparable for the warm and cold phases, indicating that these latter are responsible for most of the amplification. For these reasons, we expect the cold phase to be the most efficient at amplifying the field in my simulations. In an effort to quantify this, Figure 4.10 displays density-temperature ($\rho_{\rm gas}$-$T_{\rm gas}$) phase diagrams, colour coded by specific magnetic energy, for the galactic region at $z = 6$. In the three runs, I divide the ISM following Gent (2014) and Evirgen et al. (2017). Accordingly, I distinguish three different ISM phases: cold and dense, warm, and hot and diffuse. Hereafter, I will simply refer to them as cold (blue), warm (orange), and hot (purple). These phases are separated by constant specific entropy lines in Figure 4.10. The fraction of gas mass contained in each phase is shown in Figure 4.11. I find the fraction of gas in the hot phase negligible (less than 10%) in all three runs and at all times (see bottom panel of Figure 4.11). During the very early stages of evolution ($z \geq 7$), the amount of hot gas in the B-NoFb run is significantly lower than

that of both feedback runs (Agertz et al. 2009a), but it progressively grows as the the cooling time scale overtakes the compression time scale and the stable standing shock is pushed outside of the galactic region (Dekel & Birnboim 2006). In fact, at later times ($z \leq 4.5$), the B-NoFb run even has comparatively more hot gas than both feedback runs due to its less efficient, quasi metal-free cooling[2]. In any case, as is clear from Figure 4.10 and Figure 4.11, most of the specific magnetic energy concentrates in the mass dominant cold phase as well as, to a lesser extent, the coldest part of the warm phase. This trend is especially marked for the no B-NoFb run (middle panel of Fig 4.10) where $\varepsilon_{\rm mag}$ is strongly concentrated in the density and temperature ranges $10^{-23}{\rm g\,cm^{-3}} < \rho_{\rm gas} < 10^{-20}{\rm g\,cm^{-3}}$ and $10^3\,{\rm K} < T < 10^4\,{\rm K}$ respectively. In the feedback runs, the specific magnetic energy occupies a wider locus in the phase diagram, and is more homogeneously distributed across the cold and warm phases. As previously mentioned, this reinforces the idea that SN feedback is detrimental to magnetic energy amplification during the accretion phase: because feedback heats up the gas, during most of the accretion-dominated phase ($12 > z > 4.5$), the B-NoFb run contains on average $10-20\%$ more gas in the cold phase than both feedback runs (Figure 4.11).

Another striking feature of the phase diagrams presented in Figure 4.10 is the absence of correlation between specific magnetic energy and gas density in all three runs, which would have indicated, had it been present, an adiabatic-like amplification of the magnetic field. Instead, Figure 4.9 shows that the B-NoFb run has the largest absolute velocity dispersion $\sigma_{\rm turb}$ of all three simulations throughout a large fraction of the galactic region ($r \lesssim 0.1\ r_{\rm halo}$) at the higher redshifts ($z \geq 4.5$) of the accretion phase. This is not a very large effect, as these values are generally comprised between 40 - 80 km s^{-1} in the B-NoFb run, compared to 30 - 60 km s^{-1} for the B-Mech and B-RdTh runs, but remains nonetheless systematic. In all three runs, turbulent velocity

[2]Note however that, at least for $z > 2.5$, this hot halo gas is unable to sever the filaments of cold gas directly supplying the galactic region Tillson et al. (2015).

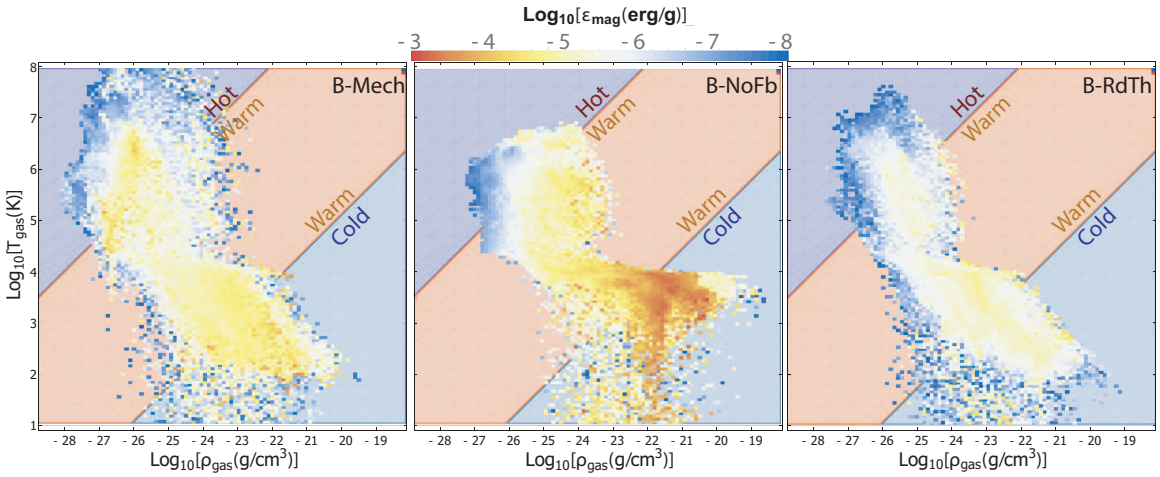

Figure 4.10: Phase diagrams for gas density ($\rho_{\rm gas}$) vs temperature ($T_{\rm gas}$) colour coded by specific magnetic energy ($\varepsilon_{\rm mag}$). Sampled gas corresponds to all cells within the galactic region at $z = 6$. From left to right, panels are for simulations B-Mech, B-NoFb, and B-RdTh. I identify three ISM phases following Gent (2014). They correspond to the shaded parts of the diagrams: hot (purple, top left), warm (red, central), and cold (blue, bottom right). These phases are separated by lines of constant specific entropy $s \propto [\log T - (\gamma - 1) \log \rho_{\rm gas}]$.

profiles subtly increase with r, so that in the external galactic region ($r \gtrsim 0.1\ r_{\rm halo}$), they all reach typical values on the order of $\sigma_{\rm turb} \sim$ 50-100 km s^{-1}, dominated mostly by radial velocity dispersion. The presence of higher degrees of turbulence in the external part of galaxies is not a surprising finding, especially when non-negligible cold inflows are present (Klessen & Hennebelle 2010). As redshift decreases, the velocity dispersion in the B-RdTh and B-Mech runs increases monotonically, to reach a similar (or even slightly higher) level that in the B-NoFb run by $z = 4$. It is interesting to note it is at this redshift when the disk forms, even though there are hints of an earlier appearance in the B-NoFb run.

Throughout the accretion period and particularly at the end ($z \sim 4$), all three runs display sharp peaks in their specific magnetic energies (see Figure 4.6). Peaks are correlated with mergers, which stretch the magnetic field out of galaxies in tidal streams during close encounters, as reported by studies such as Roettiger et al. (2002); Kotarba et al. (2011). These increases are followed by subsequent decreases in the

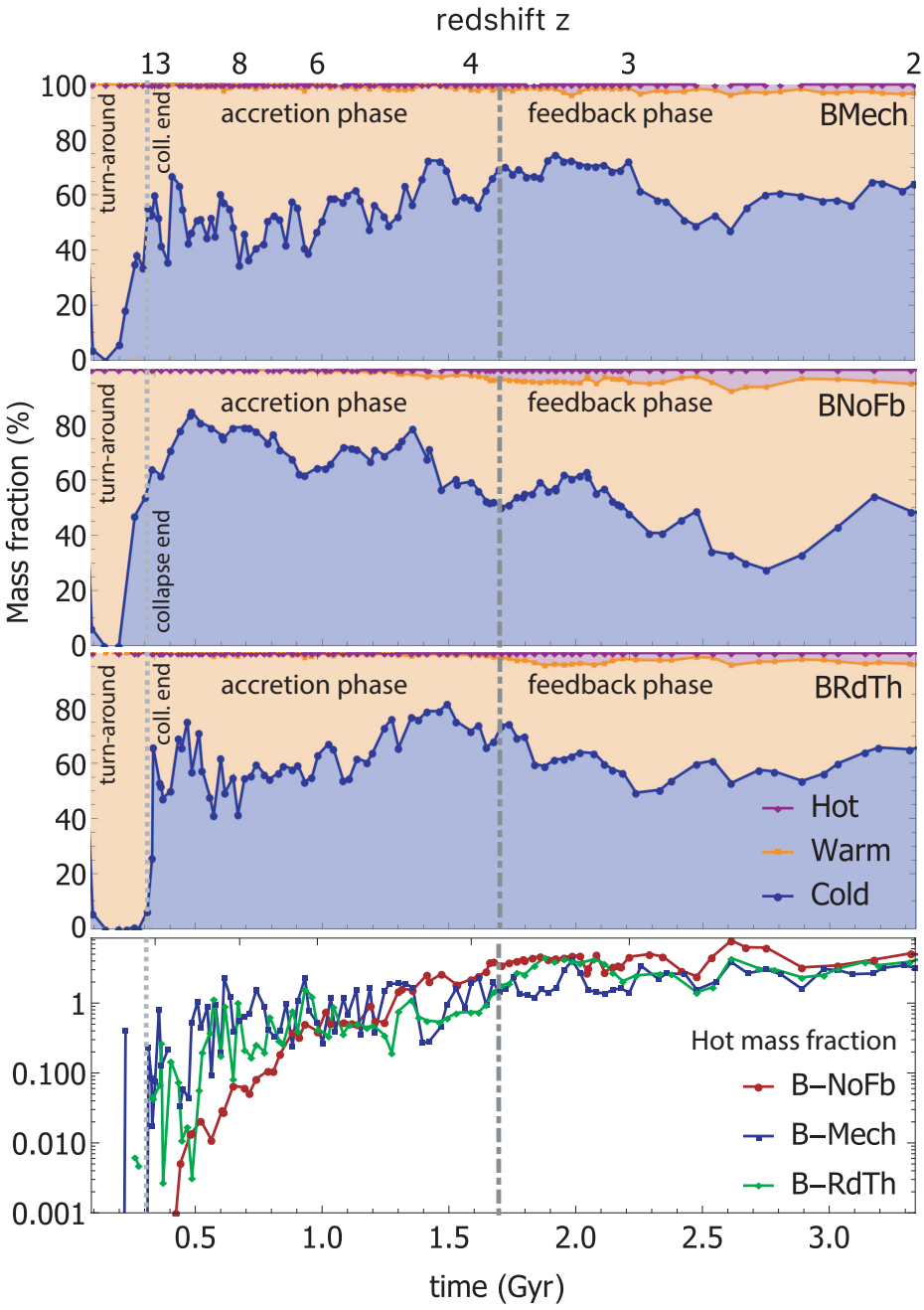

Figure 4.11: Gas mass fraction within the different ISM phases of the galactic region (hot - purple; warm - orange; cold - blue). From top to bottom, runs displayed are B-Mech, B-NoFb, and B-RdTh. For the sake of increased clarity, I present in the bottom panel a zoom view focused on the hot phase mass fraction of all three runs.

Table 4.2: Specific magnetic energy growth timescales Γ_ε, derived from exponential fits to the specific magnetic energies profiles during the accretion phase, $\Gamma_{\varepsilon,\mathrm{acc}}$, and the feedback phase, $\Gamma_{\varepsilon,\mathrm{fb}}$. All Γ_ε are measured in Gyr^{-1}. See Section 4.4 for details of the procedure employed for the fit.

Run	$\Gamma_{\varepsilon,\mathrm{acc}}$	$\Gamma_{\varepsilon,\mathrm{fb}}$
B-NoFb	2.7 ± 0.2	-2.0 ± 0.5
B-Mech	2.3 ± 0.1	0.3 ± 0.2
B-RdTh	2.0 ± 0.1	1.7 ± 0.2

magnetic energy, generally attributed to numerical dissipation (Kotarba et al. 2011; Geng et al. 2012; Pakmor et al. 2014). Note that the main difference between my work and the simulations of these authors (besides a significantly higher spatial and mass resolution, potentially making the merger peaks more prominent in my work) is that in their work saturation of the magnetic field values is already reached even before the merger happens. This does not happen in the simulations with the magnetic seed employed here. Energy equipartition is only reached for higher initial values of the magnetic field, as will be seen in Chapter 6. Such saturation of the magnetic field is typically interpreted in the aforementioned publications as evidence of numerical convergence. However, the high level of residual magnetic divergence inherent to some of the divergence cleaning methods used casts doubts on the role played by numerics in the evolution of the magnetic energy. This is especially worrisome given the results reported in the comparative study presented by Mocz et al. (2016), where the magnetic pressure in two idealised isolated disk simulations that differ only by their induction equation solver (CT vs divergence cleaning) leads to final values which differ by more than an order of magnitude (see Figure 6 of Mocz et al. 2016).

To better illustrate the general scenario of mergers events, I display in Figure 4.12 projections of the gas density, temperature and pressure, along with the specific magnetic energy in a volume centred on the galactic region, for an ongoing merger occurring around $z \sim 6$ in all three runs. The peaks in the specific magnetic energy coincident with this merger event are also marked as black circles in Figure

4.6. From the combination of Figures 4.6 and 4.12 it is clear that mergers boost magnetic energy within the galactic region (solid circles on the gas density panels of Figure 4.12) by stretching field lines, and perhaps inducing compression in the galaxy. Moreover, $\varepsilon_{\rm mag}$ peaks in the B-NoFb run achieve considerably higher values than their feedback run counterparts, as field lines smoothly follow merger stream flows in the absence of feedback. In the presence of feedback these very same field lines are strongly disrupted, and even though the level of turbulence may rise within the galactic region and amplify the field, a fraction of the resulting magnetic energy is expelled by outflows into the halo (see also Dubois & Teyssier 2010), generating the radial filamentary magnetic structures seen in the magnetic energy density maps of Figure 4.12. More quantitatively, a higher specific magnetic energy is measured in the outer regions of halos in the feedback runs (see Figure 4.7). As a consequence, even though a significant amount of magnetic energy is generated by bulk stretching during mergers, a large fraction of this energy is lost through outflows in the presence of feedback. Once the merger concludes and the galaxy settles, significant numerical magnetic reconnection occurs as the gas (and field) falls onto the galaxy and more magnetic energy gained during the merger is lost (see Figures 4.17 and 4.18 where the amplitude of the merger peaks is greatly reduced in lower spatial resolution, but otherwise identical runs). Since these losses are strongly correlated with resolution, better resolving the circumgalactic medium appears to be required to properly capture the amplification of magnetic energy by mergers. At a fixed resolution, the use of fixed nested grids as implemented in Vazza et al. (2014) for LSS simulations, sets a unique turbulent and magnetic energy dissipation scale, which appears to alleviate the problem. Bearing in mind these resolution caveats, we find, in agreement with Rieder & Teyssier 2017b for cosmological simulations of dwarf galaxies, that mergers have a negligible contribution to the evolution of the magnetic energy within the galactic halo.

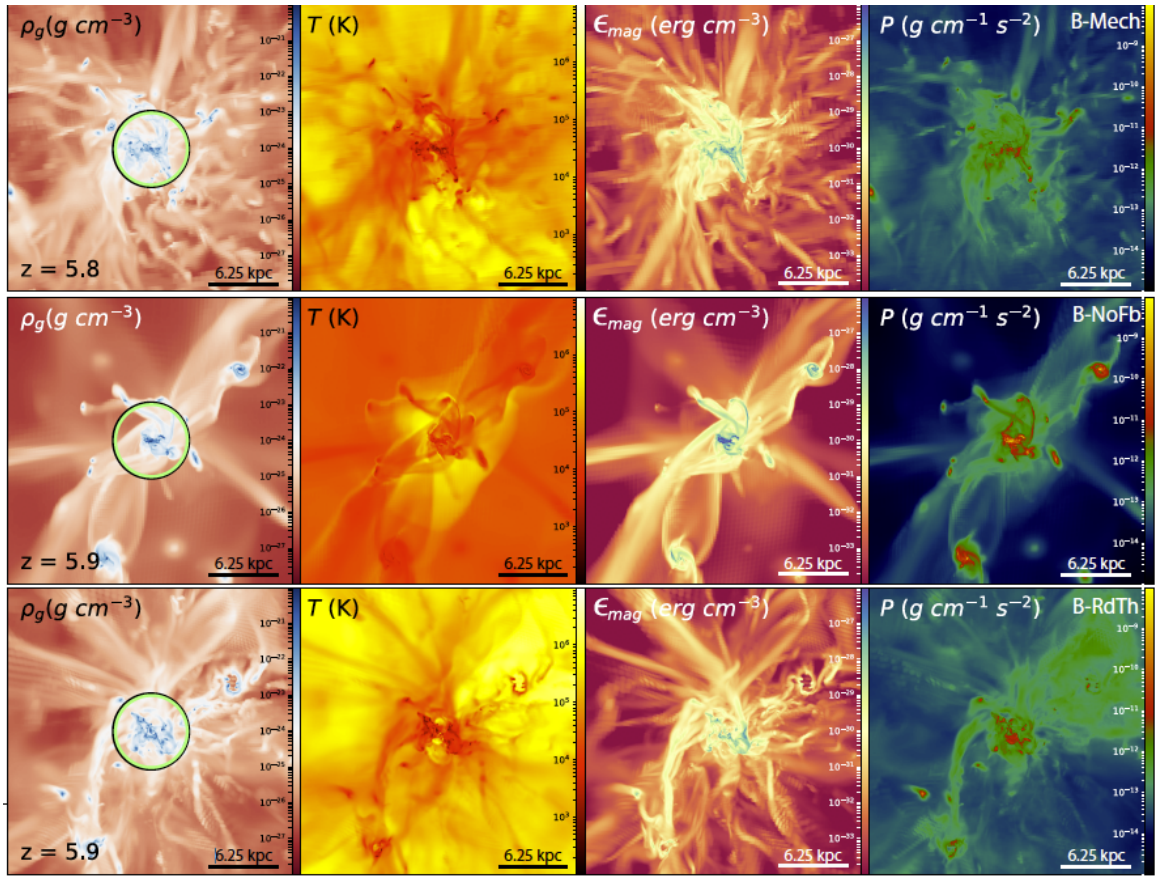

Figure 4.12: Projections of a (25 kpc)^3 cubic volume centred on each galactic region for the three runs during a merger event ($z \sim 6$). Density, temperature, magnetic energy density and thermal pressure are displayed respectively from left to right. From top to bottom, runs are B-Mech, B-NoFB, and B-RdTh. In both feedback runs magnetic field lines around the central galaxy are disrupted by the strong gas outflows. These outflows reduce the efficiency of magnetic stretching during the merger, perhaps generating the observed shallower peaks in the specific magnetic energy compared to the no feedback run. Galactic regions are indicated as circles on the gas density images (left column). Intensive variables are mass weighted. The exact times and redshifts for each image correspond to the points encircled in black on Figure 4.6.

To further assess the presence of a turbulent dynamo, I measure turbulent kinetic and magnetic energy spectra for each simulation, which I show in Figure 4.13. These are calculated by performing a Fast Fourier Transform (FFT) of cubic boxes with 1024^3 cells, centred on the galactic region in each run, and with a physical box length of $l = 0.4\, r_{\rm halo}$, so as to encompass the whole galactic region. For the sake of numerical performance, my FFT calculation assumes periodic boundary conditions, which, although clearly unrealistic at these scales, still provides a good approximation due to the high gas density and magnetic field contrast between the galaxy and its surroundings. In other words, the tenuous circumgalactic medium acts as a zero-padding region that isolates the galaxy, ensuring that the power in Fourier modes at any scale but the largest is dominated by that of the galaxy ISM. The impact of periodicity and shape of the galaxy disk on the measured spectra are discussed in more detail in Appendix A, Section A.1, so I only mention at this stage that the disk shape results in a power law decay of the density spectra as a function of the spatial angular wavenumber $\propto k^{-7/4}$ for $k_s \geq \frac{\pi}{h_s}$. As previously discussed, kinetic energies were calculated from velocities with bulk motion and circular velocity $v_c(r)$ removed. All spectra are displayed in comoving units: dark matter halo physical radii grow $\propto (1+z)^{-1}$, so their comoving size remains roughly constant with time, which facilitates the analysis and comparison of the different spectra across the entire redshift range.

The turbulent kinetic energy spectra for B-NoFb from $z \sim 8$ to $z \sim 4$ exhibit a cascade with power law scaling between Kolmogorov $\mathcal{E}_{\rm turb} \propto k^{-5/3}$ (Kolmogorov 1941, indicated by black dashed lines in the left column panels of Figure 4.13) and Burgers $\mathcal{E}_{\rm turb} \propto k^{-2}$ (indicated by gray dashed lines on the same panels) at intermediate scales $0.3\ {\rm kpc}^{-1} < k_{\rm co} < 3\ {\rm kpc}^{-1}$, i.e. in the inertial range, where $k_{\rm co}$ represents the co-moving spatial angular wavenumber. These cascade spectra for the turbulent kinetic energy indicate a transfer of energy from large scales towards smaller

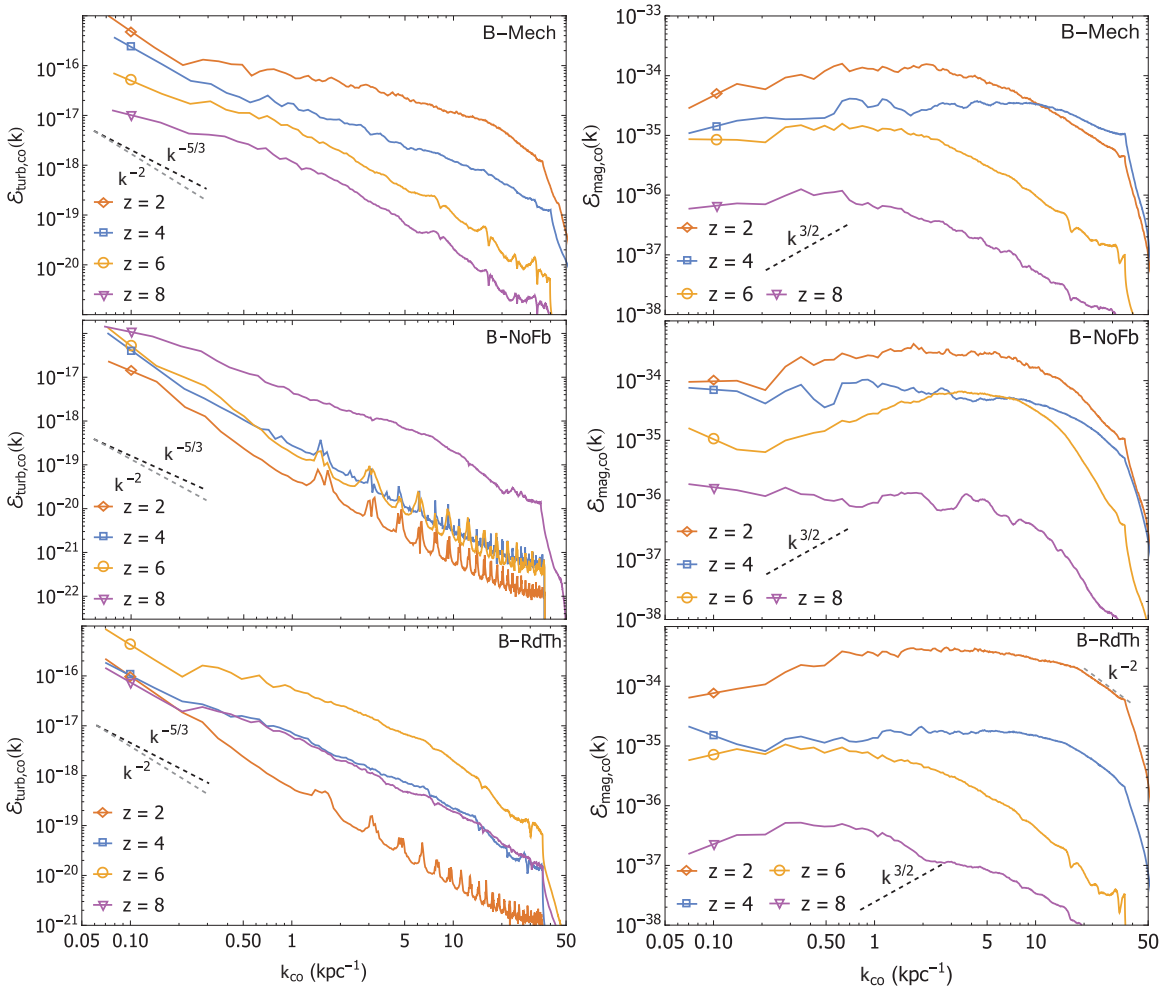

Figure 4.13: Comoving turbulent kinetic (left) and magnetic (right) energy power spectra for simulations B-Mech, B-NoFb, and B-RdTh, correspondingly from top to bottom. Dashed lines indicate Kolmogorov (black), and Burgers (gray) turbulent scalings for the kinetic energy in the left column, and Kazantsev scaling for the magnetic energy in the right column. Spikes in the turbulent kinetic energy spectra are associated to resonances with AMR grid levels.

eddies, consistent with fully developed turbulence resulting from continuous accretion. On the other hand, the feedback runs, and especially B-Mech, inject energy and/or momentum on small scales (see e.g. Kimm et al. 2015, for detail), as expected from SNe explosions. This generates extra power on scales ranging typically from $3\ \mathrm{kpc}^{-1} < k_{\mathrm{co}} < 30\ \mathrm{kpc}^{-1}$, flattening the power law index of the spectra as the scale height of the disk increases (see Section A.1). Note that the energy injection scale into the galaxy can be identified by the break present in all spectra around comoving wavenumber $k_{\mathrm{co}} \sim 0.2\ \mathrm{kpc}^{-1}$ (corresponding to physical wavelengths of $\sim$3 and $\sim$10 kpc at redshifts 8 and 2 respectively; see left column of Figure 4.13).

Because small scale turbulence more rapidly amplifies the magnetic field due to its short e-folding times, the magnetic energy generated by the dynamo is fed back towards large scales, as evidenced by an inverse cascade in the magnetic energy spectra (right column panels of Figure 4.13). In agreement with simulations by Bhat & Subramanian (2013) and Federrath (2016) these inverse cascade spectra typically have a shallower slope than the Kazantsev spectrum ($\mathcal{E}_{\mathrm{mag}} \propto k^{3/2}$ Kazantsev 1968) on large scales ($k_{\mathrm{co}} \leq 1\ \mathrm{kpc}^{-1}$), characteristic of compressible flows with magnetic Prandtl numbers $\mathrm{Pm} > 1$ in the kinematic stage (the magnetic energy is much smaller than the kinetic energy see Figure 4.8). I estimate the numerical $2 < \mathrm{Pm} < 10$ for the employed ideal MHD scheme, see Rembiasz et al. (2016) for detail. I argue that part of this shallowness arises from the disk-like shape of my galaxies and the complexity of the system (bursty injection of energy and momentum by SN in a multiphase ISM subject to accretion and mergers). Indeed, when going from the largest (box size) to the smallest scales (single grid cell), the power in magnetic energy spectra of isothermal turbulent boxes first increases as steeply as Kazantsev, then flattens as it reaches a maximum on scales corresponding to multiple elements of resolution, before decaying (e.g. Figure 5 of Haugen et al. 2004a). My simulations display the same global qualitative behaviour but the inverse cascade spans a range of wave numbers

which comprises both the scale length and scale height of the galaxy, so the galaxy shape naturally influences the energy spectra slopes. A perhaps clearer imprint of this effect can be found on the smallest scales (large k) where my spectra exhibit a steep 'disk-like' decay following $\mathcal{E}_{\rm mag} \propto k^{-7/4}$ (see Figure A.2 and discussion in Section A.1) instead of the somewhat shallower decay observed in simulations of turbulent boxes (Haugen et al. 2004a; Schekochihin et al. 2004; Bhat & Subramanian 2013; Federrath 2016, both for compressible and incompressible fluids). Isolated galaxy simulations are expected to have less power on large scales (greater than the galaxy length scale) by construction. However, similar magnetic spectra to the ones presented are also observed in such simulations (Rieder & Teyssier 2016; Butsky et al. 2017), and in a cosmological simulation of a dwarf (Rieder & Teyssier 2017b). A difference worth noting is that Butsky et al. (2017) (see their Figure 5) obtain magnetic energy spectra in the kinematic regime steeper than Kazantsev on intermediate to large scales, which might be the result of their SN seeding of magnetic field.

For a more detailed look at the time evolution of the magnetic energy spectra when a merger occurs, Figure 4.14 displays the evolution of $\mathcal{E}_{\rm mag}$ for B-Mech, around a merger event at $z = 4$. As redshift decreases, the stretching resulting from material and magnetic field being pulled out of the galaxy amplifies the field. Furthermore, as the magnetic field is stretched, the window defined by the disk of the galaxy is temporarily blurred, eliminating the the $k^{-7/4}$ decay, and the spectrum displays an inverse cascade all the way up to $k_{\rm co} \sim 10$ kpc^{-1} ($k_{\rm ph} \sim 50$ kpc^{-1}). However, once the merger completes, tidal gas streams fall back onto the galaxy and magnetic energy is lost due to numerical reconnection. Present day simulations seem to the lack resolution to properly capture the amplification of turbulence and magnetic energy associated with the merger process. As a result, mergers only act as temporary enhancers of the field, both in the galaxy and the circumgalactic medium (see also Rieder & Teyssier 2017b).

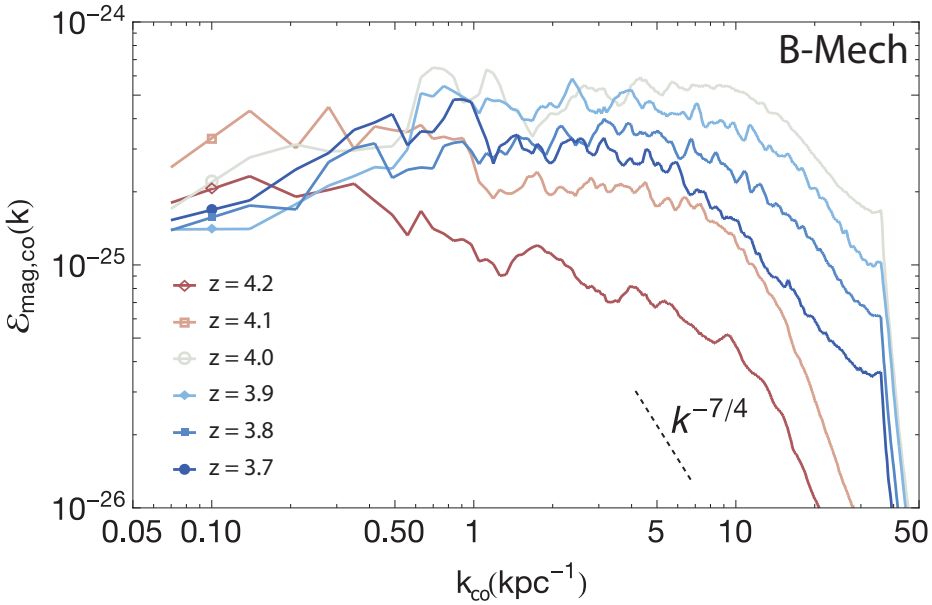

Figure 4.14: B-Mech comoving magnetic energy spectrum evolution throughout the merger occurring around $z = 4$. Redshift evolves from high (red) to low values (blue). As the merger proceeds, power is gained on small scales due to the window function set by the disk being blurred. Once the merger has finished, the field is confined in the galaxy disk again and the decay due to the shape of the disk progressively propagates to larger scales.

The presence of a turbulent cascade in the kinetic turbulent spectra and an inverse cascade in the magnetic energy spectra between $z = 8$ and $z = 4$, regardless of whether SN feedback is implemented or not, proves that during the accretion phase, a turbulent galactic dynamo is triggered, amplifying the magnetic energy on small scales and feeding it back to larger galactic scales.

4.3.3 Feedback driven amplification

The final period of amplification is dominated by local galactic effects instead of accretion. Galaxies have grown to a size where gas accretion represents the source of a small fraction of their baryonic mass content, as indicated by Figure 4.15. The progressive shut down of cold accretion flows, and the increased stability of the gas disk as the stellar component grows also reduce the impact of accretion (Dekel & Birnboim 2006; Klessen & Hennebelle 2010; Cacciato et al. 2012). Thus, inflow-induced turbu-

lence declines, especially in the inner regions of the disks. Outer regions still seem to display accretion-driven turbulence (see Figure 4.9 and Klessen & Hennebelle 2010; Hopkins et al. 2013) that could maintain or even amplify the field locally (Pakmor et al. 2017). Transfer of magnetic energy from the outer parts of galaxies towards the centre has been reported in other studies (Machida et al. 2013), significant enough to strengthen the inner field once a dynamo powerful enough is activated in the external region. However, this does not happen in the simulations presented in this Chapter. Instead, as there are no sub-grid processes forcing turbulence nor injecting energy or momentum in the B-NoFb run, and accretion loses importance, both specific and absolute turbulent energies, required to maintain the growth of the field, decay (Table 4.2). Numerical resistivity also contributes to the decay of the magnetic energy, but the decline of turbulence eventually leads to the onset of the final field topology as argued in Rieder & Teyssier 2017a. Note however that, contrary to what I measure for the B-NoFb run, even without an explicit feedback model (that of Springel & Hernquist 2002), Pakmor et al. (2014) report that after the formation of a Milky Way-like galaxy they still find linear growth of the magnetic field, which they attribute to differential rotation.

On the other hand, even after accretion has significantly diminished, runs with stellar feedback still exhibit considerable amounts of turbulent energy throughout the galaxy (at least an order of magnitude more that B-NoFb, see Figure 4.13 and e.g. Federrath 2016, for a discussion of stellar feedback-induced turbulence). The belief that compressive forcing due to SNe can drive solenoidal turbulence is now well established (Korpi et al. 1999; Mee & Brandenburg 2006; Federrath et al. 2010), and subsequently, considerable amplification is expected trailing SN blasts (Ji et al. 2016). Regardless, because of considerable numerical turbulent and magnetic dissipation at the limited resolution of my simulations, and the neglect of magnetic field injection by SN explosions, which might constitute a considerable source of magnetic energy

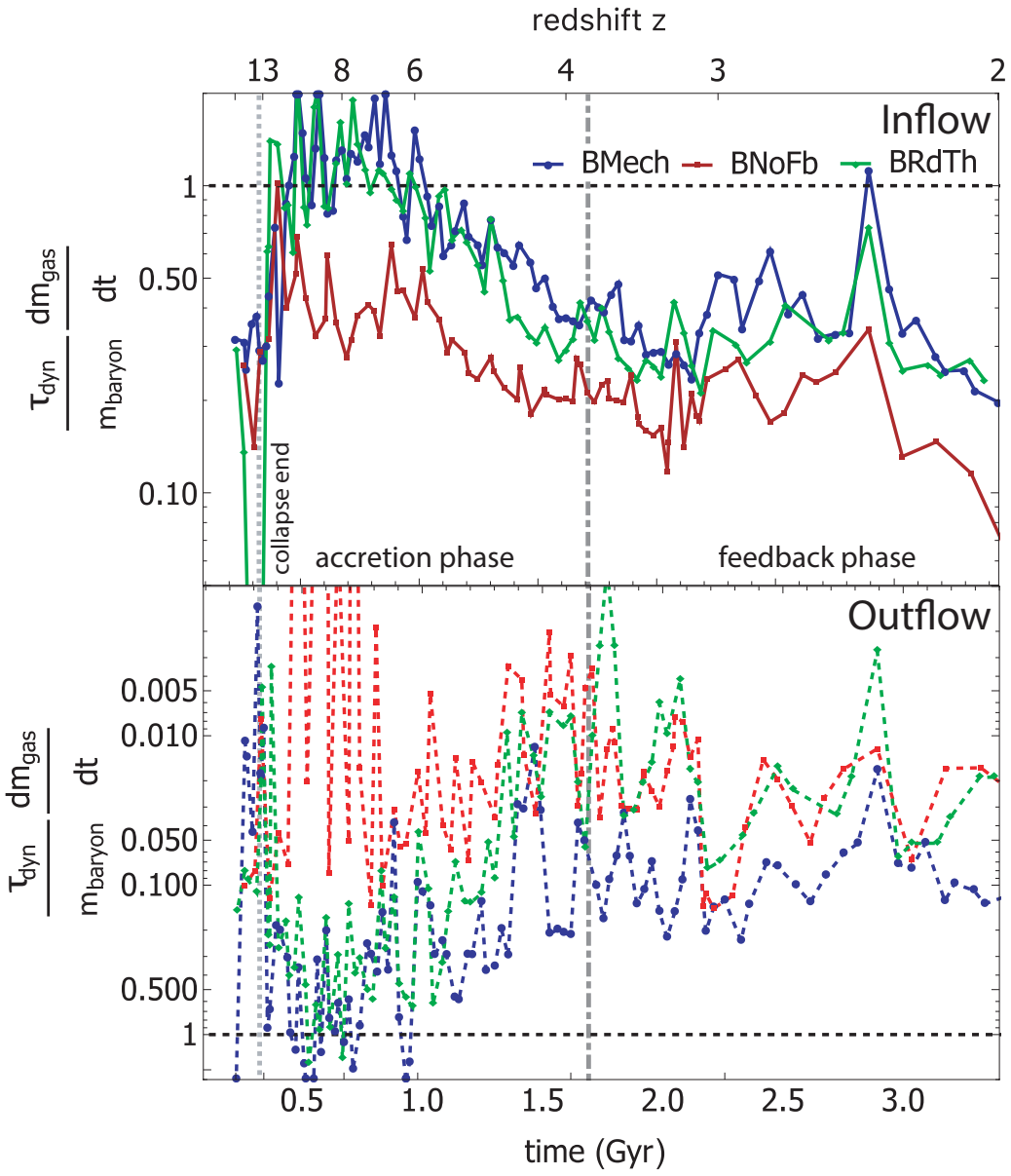

Figure 4.15: Top and bottom panels display the corresponding ratios of inflowing and outflowing gas across the galactic region boundary to the total baryonic mass contained within the region, computed during an entire dynamical time for the three main studied runs. For each simulation, the galactic region dynamical timescales is computed as $\tau_{\rm dyn}(z) = 2\pi\ 0.2\ r_{\rm gal}(z)\ v_c^{-1}\,(r_{\rm gal}(z))$.

(see e.g. Butsky et al. 2017, and Chapter 5), the results I present in this Chapter only provide a lower limit on the importance of SN during a dynamo amplification feedback dominated phase.

Bearing in mind these caveats, SN driven turbulence remains capable of driving exponential amplification of the magnetic energy in runs B-Mech and B-RdTh through a turbulent dynamo (as indicated by the turbulent kinetic and magnetic energy spectra corresponding to this phase on Figure 4.13). Table 4.2 shows that B-RdTh displays a larger growth rate, $\Gamma_{\varepsilon_{\rm mag}}$, than B-Mech. However, both runs have lower $\Gamma_{\varepsilon_{\rm mag}}$ than during their accretion-driven phase. A reasonable suspicion is that this is related to the fact that accretion and gravitational instabilities in a differentially rotating disk driver a larger fraction of solenoidal turbulence, more efficient at amplifying the magnetic field. Admittedly, this latter property will depend both on the specific subgrid implementation for stellar feedback and on the numerical resolution, as vorticity generated behind shock waves is difficult to capture, but the conversion of compressible turbulence into solenoidal modes within the small volume covered by a quasi 2D-like galaxy is limited. As B-RdTh is more efficient at perturbing the gaseous disk of the galaxy and driving a fountain, it is therefore not surprising that this run reaches higher $\Gamma_{\varepsilon_{\rm mag}}$ than its B-Mech counterpart. B-Mech is in turn more efficient driving outflows out of the region (see Figure 4.15), which are responsible for injecting magnetic energy in the rest of the halo, causing the higher specific magnetic energies that can be read off Figure 4.7.

In summary, while in the accretion driven phase, feedback appears only detrimental to amplification of the magnetic field ($\Gamma_{\varepsilon_{\rm mag}}$ values in Table 4.2 are slightly lower for B-Mech and B-RdTh than for B-NoFb), in the feedback-driven phase it is the main driver of the observed amplification the field, resulting in the values of $\Gamma_{\varepsilon_{\rm mag}}$ being both largely dependent on the model selected during this phase, and of opposite sign to B-NoFb (see Table 4.2), where decay and pristine gas accretion dominate the

evolution.

Finally, in comparison with isolated simulations of MW galaxies (Rieder & Teyssier 2016), where there is no modelling of any accretion phase, or any hierarchichal formation at all, my cosmological simulations display a lower growth-rate $\Gamma_{\varepsilon_{\rm mag}}$. This is especially interesting in the case of B-RdTh, as this run features a very similar subgrid feedback model as one in the isolated galaxy runs by Rieder & Teyssier (2016). Small disparities could arise from a combination of a slightly diminished feedback specific energy injection and the subdominant cosmic accretion of poorly magnetised gas, which will act to somewhat reduce our $\Gamma_{\varepsilon_{\rm mag}}$. However, the most likely cause of significant discrepancy is that the fixed gravitational potential in their study, where no fresh gas is accreted after the initial collapse phase, facilitates the escape of outflows from the galaxy far into the halo, thus promoting the establishment of a galactic fountain, which will stretch (and therefore amplify) the field more efficiently than in our cosmological set-up.

4.4 Discussion

One of the important findings of this Chapter is the identification of the amplification of the magnetic energy by three distinct phases during the lifetime of a galaxy. In this Section, I discuss the robustness of this result. While given the typical evolution of spiral galaxies, it is reasonable to suggest that such an amplification behaviour in three stages might be universal, numerics affect the duration and amplification occurring during these phases in various manners.

Firstly, a collapse driven phase of amplification is separated from the later phases of galaxy evolution. It is constrained to occur between the turn-around time of the collapsing perturbation and the moment when the forming galaxy has generated its first stars. I measure these two moments as $z_{\rm ta} \sim 22$ and $z_{\rm coll} \sim 13$. The latter redshift

strongly correlates with a change of behaviour in the magnetic energy amplification. During the collapse phase, it is mostly the result of frozen magnetic field lines in the ideal MHD approximation being dragged by the collapsing gas. The trajectories are dominated by gravity, and magnetisation levels are comparable across all three simulations, with the stellar feedback subgrid implementation having a noticeable, but subdominant effect. While the existence of such a phase is difficult to dispute, this does not mean that the amplification is unaffected by numerical considerations. In fact, two aspects have considerable impact on the amplification found during the collapse phase. One is numerical resolution, which I discuss in more detail in Section 4.5. It mainly affects the amount of turbulent amplification measured above the expected level for isotropic collapse. The second one is the orientation and structure (i.e. spatial variation) of the initial seed. This aspect is not explored here, and will be further discussed analysed in Chapter 6. I note that simple variations of the initial seed field presented here could alter the amplification factor of the specific magnetic energy by about a dex.

After this initial collapse, galaxies rapidly develop a multiphase ISM and are mostly fed by cold filamentary gas flows (see Tillson et al. 2015). This second phase is identified as the accretion phase of amplification. Turbulent motions in the multiple phase ISM are deemed responsible for the growth of the magnetic field. This implies the presence of turbulent dynamo amplification, for which $E_{\rm mag}$ follows an exponential growth. During this epoch, I only measure a weak rotational support of the gas and any differential rotation amplification should therefore be negligible. On the other hand, a turbulent dynamo fed by resolved vortical motions exponentially amplifies the magnetic energy. Filamentary accretion flows naturally drive solenoidal turbulence, but whether they can transfer a significant amount of turbulent kinetic energy to the entire ISM is still a matter of debate. However, I find that, while stellar feedback does not prevent amplification of magnetic energy to occur when implemented, it

appears to be slightly detrimental to it. As a consequence, the turbulent amplification found during this phase is primarily attributed to accretion flow driven gravitational instabilities. As amplification is linked to turbulence, a higher numerical resolution will yield considerably higher growth rates by pushing down the numerical dissipation scale and resolving a larger span of the turbulent cascade. The typical growth rates of specific magnetic energy that I measure during this phase are on the order of $\Gamma_{\varepsilon_{\rm mag}} \sim 2\ {\rm Gyr}^{-1}$ (see Table 4.2), and are relatively independent of the feedback prescription employed.

The beginning of the accretion phase coincides with the end of the collapse phase $z_{\rm coll} \sim 13$, itself determined by cosmological (and star formation) arguments, but turbulent amplification inside the proto-galaxy is likely to have already started before this redshift. As time progresses, the mass growth of the galaxy and the decrease in gas accretion rate by the galaxy steadily reduces the relevance of cold accretion flows, eventually leading to the termination of accretion-driven magnetic energy amplification. In the absence of other turbulence driving mechanisms (B-NoFb run), any amplification is likely confined to the outer regions of the galaxy and an overall decay of the specific magnetic energy is observed. This decay is, by-and-large, the result of numerical resistivity. However, galaxies host energetic phenomena, such as stellar feedback, stirring up the ISM. The diminishing importance of accretion-driven turbulence thus leads to a smooth transition to a feedback-dominated regime. In my simulations, this latter is observed to take place after the galaxy mass becomes star dominated and shortly after the formation of a thin gas disk. In fact, one could even argue for the presence of an intermediate transition phase once the galaxies become star dominated (especially in the absence of feedback), when the stability of the gas disk is enhanced by the presence of a dominant stellar component, and the growth rate is slightly reduced. This should be interpreted with caution though, due to the complication of having to disentangle merger/interaction effects with external objects.

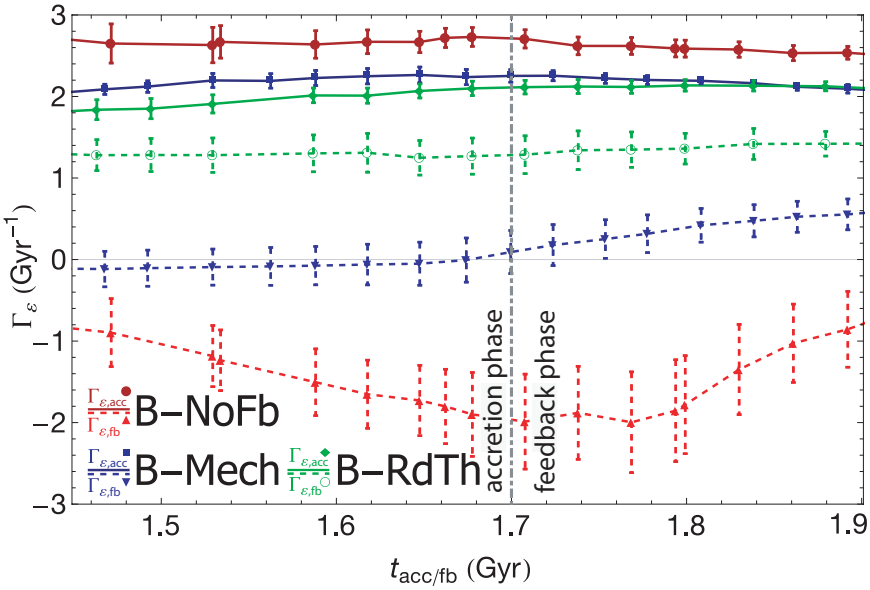

Figure 4.16: Measured exponential growth parameter $\Gamma_{\varepsilon_{\rm mag}}$ versus time of phase transition $t_{\rm acc/fb}$ for the three runs B-NoFb (red), B-Mech (blue) and B-RdTh (green). Solid coloured lines indicate accretion phase values $\Gamma_{\varepsilon_{\rm mag},\rm acc}$, while dashed lines represent feedback phase values $\Gamma_{\varepsilon_{\rm mag},\rm fb}$. Note that the distinction between phases is robust regardless of data binning or specific choice for the time at which the phase transition takes place.

The transition from accretion to feedback driven amplification is estimated to occur at $t_{\rm acc/fb} \sim 1.7$ Gyr (or equivalently, $z_{\rm acc/fb} \sim 4$).

The final phase of amplification, which I consequently name the feedback phase of amplification, is characterised by lower amplification rates. Tables are now turned and stellar feedback becomes the main mechanism responsible for the amplification. As a result, the B-NoFb run, which displayed the highest growth rate now exhibits a magnetic energy decay while the B-RdTh run shifts from the lowest growth rate to the highest. As for the accretion dominated phase, the turbulent nature of the amplification implies that higher numerical resolution will better capture the flow turbulence and lead to higher growth rates. A large spread of growth rates are found for this phase, which depend sensitively on feedback implementation -2.5 Gyr^{-1} $< \Gamma_{\varepsilon_{\rm mag}} < 1.5$ Gyr^{-1}.

The distinction provided between accretion and feedback dominated phase is

somehow motivated by the values measured for $\Gamma_{\varepsilon_{\rm mag}}$, and therefore underpinned by the robustness of these measurements. In Table 4.2 I show best fits of this parameter to magnetic growth time scales. These are calculated employing 7 bins to fit data spanning either the entire duration of the accretion phase or that of the feedback phase, with an exponential function $A \exp\left[\Gamma_{\varepsilon_{\rm mag}} t\right]$. For each phase, data is smoothed using a 0.2 Gyr window function to minimise the contribution of sharp features and better recover the smooth background behaviour of the curve. As the end of the collapse phase is considered to be clearly defined, A is fixed to its value $\varepsilon_{\rm mag,C}$ for the accretion phase. It is left as a free parameter for the feedback phase. To probe the robustness of the transition between the two phases, in Figure 4.16 I display the different values of $\Gamma_{\varepsilon_{\rm mag}}$ I obtain when varying $t_{\rm acc/fb}$. Modifying the binning of the data or the size of the window function has a negligible impact on the fitted values of $\Gamma_{\varepsilon_{\rm mag}}$, but they are more sensitive to the choice of the epoch at which the phase transition takes place, $t_{\rm acc/fb}$. This is not very surprising, as varying $t_{\rm acc/fb}$ results in the inclusion of a larger fraction of the opposite phase in the estimate of the value of $\Gamma_{\varepsilon_{\rm mag}}$. However, as shown by Figure 4.16, the amount of uncertainty is quite limited: values of $\Gamma_{\varepsilon_{\rm mag}}$ remain fairly constant over a reasonable range of $t_{\rm acc/fb}$ for all phases and all runs. Even for the phase where the estimate $\Gamma_{\varepsilon_{\rm mag}}$ varies the most (feedback phase of the B-NoFb run, dashed red line of Figure 4.16), the measurements display a clear decay of the magnetic energy, in stark contrast with a clear amplification in the matching accretion phase (solid red line on the same plot).

The amplification of the specific magnetic energy reached in the simulated galaxies by $z = 2$ becomes all the more remarkable when considering that these latter mainly grow via low-magnetised gaseous inflows, and lose magnetic energy via outflows. Contrary to isolated simulations of galaxies (e.g. Dubois & Teyssier 2008; Rieder & Teyssier 2016), stellar feedback need not necessarily be the dominant component which drives magnetic amplification in cosmological simulations. However, once

accretion becomes unimportant, these idealised simulations resemble more closely the cosmic scenario, and stellar feedback probably plays an important role in preventing the decay of the magnetic energy or generating further amplification. In any case, whatever the driving process, numerical resolution is the decisive factor to obtain the correct rate of amplification (Rieder & Teyssier 2017b). Extrapolating my numerical results to physical ISM magnetic resistivities (and assuming non-ideal MHD effects on small scales such as ambipolar diffusion do not play a major role), would lead to saturation of the magnetic energy in timescales shorter than a Gyr, i.e. well within the accretion phase.

4.5 Refinement tests

As previously discussed, the main factor that is expected to have a significant impact on the amplification of magnetic energy throughout the entire simulation is numerical resolution. The higher the spatial resolution, the smaller the scales that can be captured, and the larger the span of the turbulence cascade that can be captured. Smaller scale turbulence has shorter e-folding times and therefore yields faster amplification. At the same time, the numerical viscosity, which also scales with resolution, is reduced and turbulence is thus dissipated at larger wavenumbers, increasing the inertial range span. And finally, the numerical magnetic resistivity decreases as well, and the decay of the magnetic field is thus less pronounced.

As a simple way to quantify the importance of this resolution effect, I run and compare five B-Mech-like runs (Table 4.1) that differ exclusively in their maximum spatial resolution (B-Mech, B-MR20, B-MR40, B-BMR80, and BMR160 with $\Delta x_{\rm m} =$ 10, 20, 40, 80, and 160 pc respectively). These are shown in Figure 4.17, which is an analogue of Figure 4.5, now comparing different spatial resolutions instead of feedback prescriptions. The adiabatic isotropic amplification estimate of the specific magnetic

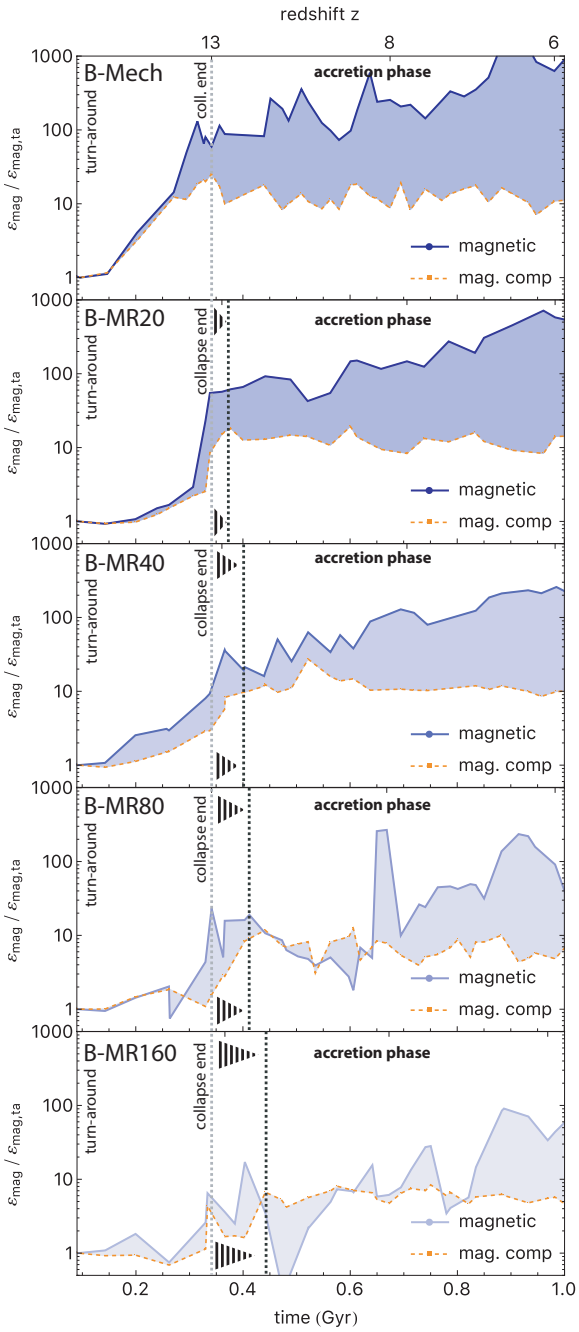

Figure 4.17: Growth of the specific magnetic energy during the collapse phase and the early stages of the accretion phase (analogue to Figure 4.5). Panels now display identical B-Mech simulations but with decreasing spatial resolution from top to bottom $\Delta x_{\rm m} = 10$, 20, 40, 80 and 160 physical parsecs. As further AMR levels are removed, the time of collapse is delayed in the simulations. Similarly, amplification rates $\Gamma_{\varepsilon_{\rm mag}}$ are reduced as the capture of the turbulent cascade worsens (see values in Table 4.3).

energy for the four runs with the highest resolution reaches a similar value ($\sim 10\varepsilon_{\rm ta}$), but appears slightly inferior for the lowest resolution ($\sim 7\varepsilon_{\rm ta}$). The collapse phase is completed around ~ 0.35 Gyr for the B-Mech run and seems to be delayed by no more than 0.05 Gyr at the four highest resolutions, while it is delayed by ~ 0.1 Gyr for the lowest resolution (the gravitational force softening scales with spatial resolution). As expected, both the initial collapse amplification and the later turbulent growth are augmented as resolution increases, although there seems to be a reasonable level of convergence between B-Mech and B-MR20. I expect this to be the result of only a fraction of the galaxy being resolved at 10 pc in B-Mech, as shown by Figure 4.2. The growth parameters measured for this early accretion phase, $\Gamma_{\varepsilon_{\rm mag},\rm early}$ are shown in Table 4.3. As expected, increasing spatial resolution leads to more rapid amplification rates (Rieder & Teyssier 2016; Pakmor et al. 2017).

To illustrate the robustness of the accretion and feedback phases with resolution, Figure 4.18 presents the evolution of $\varepsilon_{\rm mag}$ at different spatial resolutions for the whole duration of the B-Mech simulation. The existence of the accretion and feedback phases appears to be quite insensitive to the numerical resolution. Once again, growth rates $\Gamma_{\varepsilon_{\rm mag}}$ measured for the different phases are shown in Table 4.3. These values are calculated in the same way as those reported in Table 4.2. Note that during the feedback phase only B-Mech and B-MR20 possess enough resolution to capture turbulent dynamo growth. In B-MR40 and B-MR160 the magnetic field decays. Similarly, the growth factor for B-MR80 is small and compatible with null.

Turbulent amplification also depends on the value of magnetic Reynolds numbers. Haugen et al. (2004a); Brandenburg & Subramanian (2005) indicate that a magnetic Reynolds number Rm above a critical value $Rm_{\rm crit} \sim 30 - 35$ is required in order to trigger a turbulent dynamo given $Pm = 1$. The critical Reynolds number is thus slightly lower for the range of Pm values expected in my simulations (see eq. (10) and Figure 2 in Haugen et al. 2004a, $Rm_{\rm crit}(Pm) \sim 35 Pm^{-1/2}$).

Table 4.3: Expontential fits for the growth of the specific magnetic energy $\Gamma_{\varepsilon_{\rm mag}}$ in the five resolution runs. Values are for the period displayed in Figure 4.17 (early), and the accretion (acc) and feedback (fb) phases. All $\Gamma_{\varepsilon_{\rm mag}}$ timescales are measured in Gyr^{-1}. Calculations of the growth rates are as for Table 4.2. Last column displays a rough estimate of the magnetic Reynolds number Rm in the galaxy (see text). The estimated Rm is above or similar to the critical magnetic Reynolds number required for turbulent amplification $Rm_{\rm crit} \simeq 30$ in all runs but B-MR160.

Run	$\Gamma_{\varepsilon_{\rm mag},\rm early}$	$\Gamma_{\varepsilon_{\rm mag},\rm acc}$	$\Gamma_{\varepsilon_{\rm mag},\rm fb}$	Rm
B-Mech	2.3 ± 0.2	2.3 ± 0.1	0.3 ± 0.1	160
B-MR20	2.4 ± 0.1	1.9 ± 0.1	0.6 ± 0.3	120
B-MR40	2.0 ± 0.1	1.9 ± 0.1	-0.2 ± 0.1	60
B-MR80	1.0 ± 0.2	1.2 ± 0.1	0.1 ± 0.2	30
B-MR160	0.7 ± 0.1	0.9 ± 0.1	-0.3 ± 0.1	15

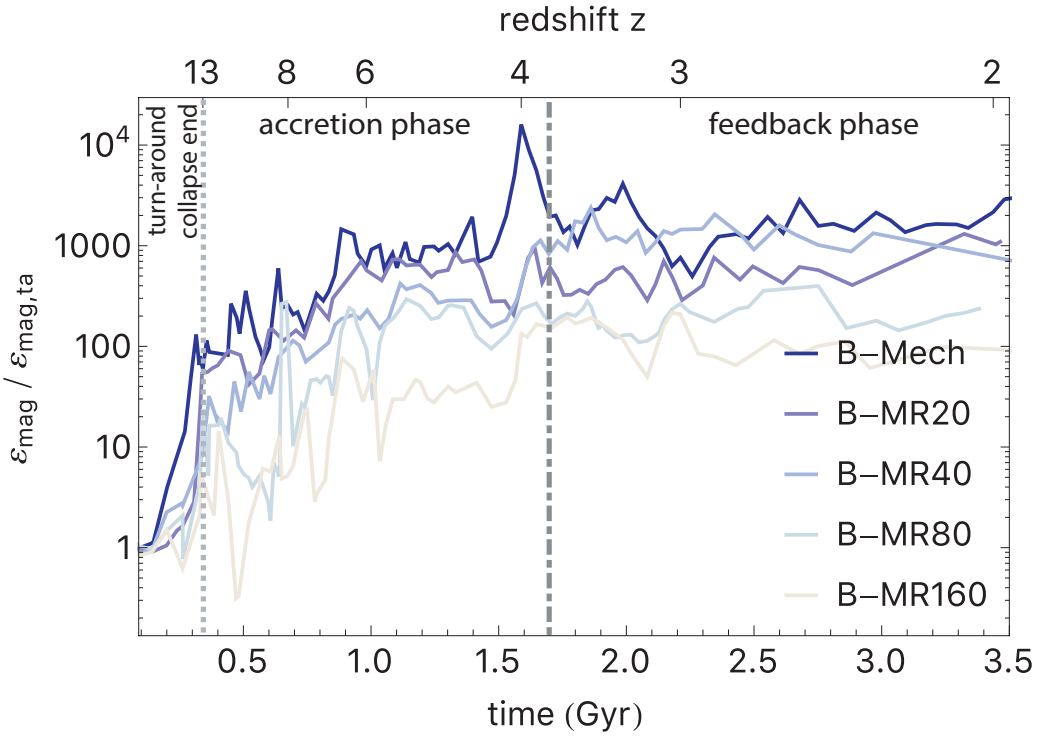

Figure 4.18: Time growth of the specific magnetic energy in the galactic region. Lines represent runs with decreasing resolution from dark blue (B-Mech) to cream (B-MR160). Regardless of the resolution, the three-phase evolution is recovered. B-MR160 appears to be a limiting case, displaying almost no growth. The phases and separations between them are the same as shown in Figure 4.6.

If I define a local magnetic Reynolds number as a function of the local diffusivity η, and typical length $L_{\rm sys}$, and velocity $V_{\rm sys}$ of the studied system

$$Rm = \frac{L_{\rm sys} V_{\rm sys}}{\eta}, \tag{4.5}$$

it can be used to compute a bulk estimate of the magnetic Reynolds number in the ISM of the galaxy. In order to do that, I fix the scale length of the system to be equal to the entire thickness of the disk $L_{\rm sys} = 2h_s \sim 1.2$kpc. Note that h_s is in the range $0.6\,\mathrm{kpc} - 0.4\,\mathrm{kpc}$ between redshifts $z = 8$ and $z = 2$, and that this scale is expected to somewhat increase with decreasing resolution.

Teyssier et al. (2006) argue that the amount of local numerical diffusivity introduced by the Godunov solver in RAMSES is on the order of $\eta \sim 0.5|u|\Delta x$, with $|u|$ the (1D) flow velocity, and Δx the size of a resolution element. Assuming that $|u| \sim V_{\rm sys}$, I can compute an approximate magnetic Reynolds number $Rm \sim Rm(\Delta x) = 2L_{\rm sys}/\Delta x$. Under these assumptions our magnetic Reynolds numbers (presented in Table 4.3) fulfil $Rm \gtrsim Rm_{\rm crit}$ for all runs but B-MR160. Accordingly, some degree of turbulent amplification is expected for all the different resolution runs but B-MR160, and possibly B-MR80. This seems in good agreement with the growth parameters presented in Table 4.3.

Growth rates likewise depend on turbulence properties such as Mach number $\mathcal{M}$, or Helmholtz mode fraction. For significantly higher magnetic Reynolds numbers, Federrath et al. (2011a) find that purely solenoidal turbulence forcing produces higher growth rates than compressional forcing. Nonetheless, they find amplification for both types of forcing, especially in the case of supersonic turbulence. I thus expect for a similar behaviour for my simulations, with $\langle \mathcal{M} \rangle \sim 10^{1.5}$ and a typical fraction of solenoidal turbulence $\sim 50 - 70\%$ in the galactic region. Their scaling of supersonic growth rates $\propto \mathcal{M}^{1/3}$ is also expected to broadly apply to these simulations.

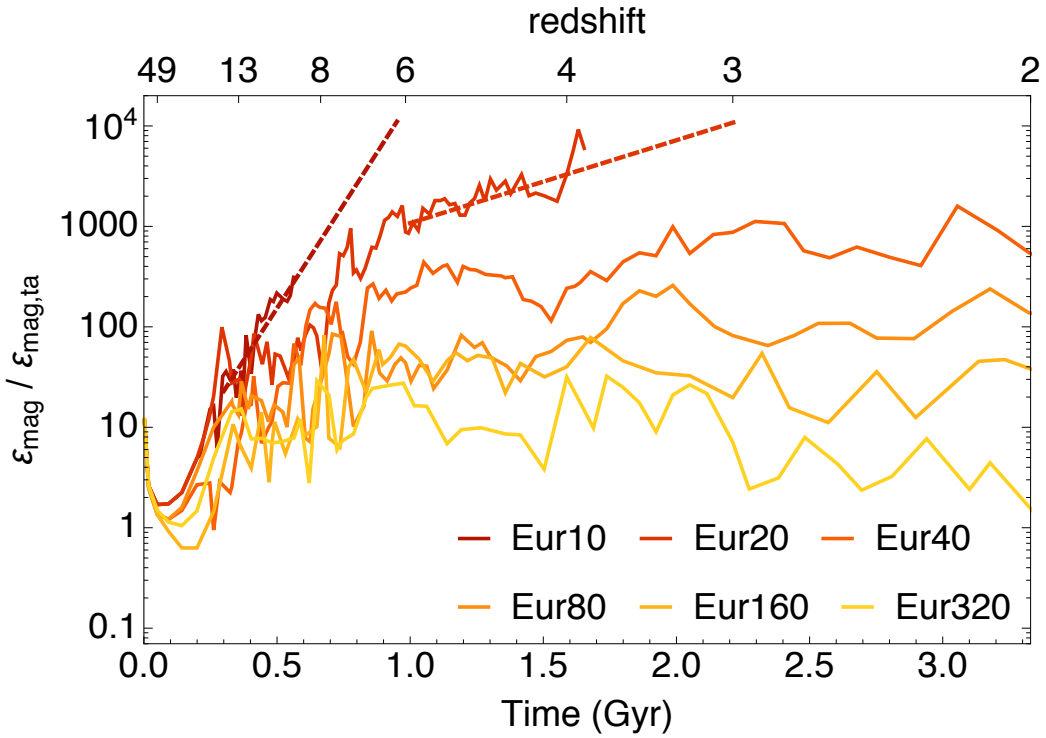

Figure 4.19: Growth of the galactic region specific magnetic energy for the simulations with density-threshold refinement ($\rho_{\rm th} = 10^{-24}$g/cm^3). Lines are runs with decreasing resolution from dark red (10 pc) to yellow (320 pc). This refinement criterion conserves the three-phase evolution and provides faster and roughly constant increase of the growth factor with spatial resolution. Dashed lines are exponential fits to the current values for 10 pc and 20 pc.

Finally, I briefly review the preliminary results of the BMEuRX runs that resolve the galaxy with a uniform grid in Figure 4.19. When comparing what is the impact of increasing the resolution in the two schemes on the growth of the specific magnetic energy in the galaxy, the quasi-Eulerian approach leads to a faster convergence towards faster amplification rates. As a result, at a given spatial resolution, the BMEuR run possesses a faster growth factor than its corresponding BMR simulation. As more levels of refinement are permitted in the AMR scheme, the increase in the growth factors is dwindled. However, when using the density-threshold refinement, the value of the growth factors during the accretion phase is approximately increased by $\sqrt{2}$. This can be quickly observed from Figures 4.18 and 4.19. The three-phase evolution of the specific magnetic energy is also observed with this new refinement strategy.

This resolution study confirms the three-phase character of the turbulent dynamo amplification during its purely kinematic regime. Further increase of resolution is expected to lead to a higher level and more rapid amplification.

4.6 Conclusion

In this Chapter, I performed high resolution cosmological zoom-in simulations of a Milky-Way like galaxy (extending the NUT suite to MHD, see Powell et al. 2011, for detail about the original simulations) with the RAMSES-MHD code (Teyssier 2002; Fromang et al. 2006; Teyssier et al. 2006), which uses a constrained transport scheme to solve the magnetic field induction equation and therefore guarantees a divergence of the field as low as numerically possible.

I study the evolution of the magnetic energy within this galaxy starting from an extremely weak primordial seed field and using three simulations named as B-NoFb, B-Mech and B-RdTh where the only difference between simulations is the stellar feedback sub-grid model implemented. My main findings are that:

- the evolution of the magnetic energy can be decomposed as a smooth exponential amplification/decay component on top of which sharp spikes, corresponding to merger events, superimpose (Figure 4.6).

- the amplification of the magnetic energy occurs in three main phases: an initial collapse phase, an accretion-driven phase, and a stellar feedback-driven phase (Figure 4.6). During the two latter phases amplification occurs due to the presence of a turbulent dynamo.

- during the collapse phase, magnetic energy amplification closely follows an isotropic adiabatic approximation, but is already accompanied by turbulent motions which drive a larger growth of the magnetic field (Figure 4.5).

- the accretion-driven phase accounts for a significant fraction of the amplification, and does not require the presence of stellar feedback to sustain the turbulent dynamo. As a matter of fact, during this phase, feedback is found to be *detrimental* to amplification, as the B-NoFb run reaches the highest amplification level (Figure 4.16).

- the contribution of mergers to the overall amplification is negligible. Mergers trigger temporary enhancement of the field, primarily by stretching magnetic field lines. In the absence of stellar feedback, these lines are not disrupted and generate sharp spikes of amplification, but once merging events conclude, the field lines fall back onto the galaxy and most of the corresponding magnetic energy is lost through numerical reconnection (Figure 4.14).

- as the galaxies grow in size and cosmic accretion dwindles, their disks stabilise and, in the absence of stellar feedback, the level of turbulence decreases and the specific magnetic energy decays. This typically occurs around $z \sim 4$ (Figure 4.16).

- in the runs where stellar feedback is present, it is able to drive a significant turbulent dynamo *after* the accretion phase, which further amplifies the field. The most efficient feedback implementation (B-RdTh run), which was the most detrimental during the accretion phase, sustains the highest growth of $\varepsilon_{\rm mag}$ (Figure 4.16).

- employing a density-threshold criterion to fully resolve the galaxy with a uniform spatial resolution leads to faster amplification rates and a roughly consistent increase of growth factors with maximal spatial resolution (Figure 4.19).

Although this Chapter presents quantitative measurements of the specific magnetic energy growth rates, $\Gamma_{\varepsilon,\rm acc}$, the numerical values reported here should only be

considered as lower limits. This is because the numerical resolution, which determines the magnetic resistivity (as well as the shear and bulk viscosities) of the gas flow is necessarily limited. The expectation is instead that, as the resolution is increased, the value of this latter will drop and the growth rate of magnetic energy will rise accordingly. I provide in this Chapter my first attempt to quantify this resolution effect in Section 4.5, which appears somewhat encouraging. However, further work is needed to properly establish the level of convergence reached so far, given the complex interplay between the numerics, multiphase ISM and implemented subgrid physics.

This difficulty notwithstanding, these results can be compared to other similar numerical approaches. By the end of the collapse phase, the specific magnetic energy of my galaxies is found to lie a factor $\sim$ 5-10 above the level predicted by isolated galaxy simulations or analytical estimates. The magnetic energy growth during the feedback phase in my simulation only is slightly weaker than in isolated spirals simulations by Rieder & Teyssier (2016).

Finally, given the level of resolution we can currently achieve, a much higher amplitude of the initial cosmic seed field is needed to reach saturation of specific magnetic energy through turbulent galactic dynamo amplification. I plan to address the potential impact of the back-reaction induced by such a saturated field on the three-phase amplification of cosmic magnetic fields in future work.

Chapter 5

Magnetic fields in galaxies: primordial versus stellar origin

5.1 Motivation

Each main mechanism of magnetisation has a different timescale to magnetise a galaxy when operating individually. Given the amplification rates observed in CT MHD simulations of galaxies, a turbulent dynamo operating on a weak seed magnetic field will attain present day field strengths over a period of several hundreds of Myr (e.g. Chapter 4 in this thesis, Rieder & Teyssier 2016, 2017b). Alternatively, if galactic magnetic fields are produced by stars and injected to the ISM through winds or SNe, galaxies will reach their present field strengths on the order of a few Myr after the formation of their first stars. A strong primordial magnetic field will help galaxies reach μG magnetic fields even more rapidly, already by collapse onto a proto-galaxy.

An interesting question to ask is how strong a primordial magnetic field must be to directly compete with stellar-generated magnetic fields in galaxies. These two types of magnetic fields emerge at intrinsically different spatial scales and through very different processes. Therefore, another relevant question to ask is whether a strong

enough primordial magnetic field would be distinguishable from one generated by SN explosions. Is there a correlation or anti-correlation between primordial magnetism and SN-generated fields? Does it change during the evolution of the galaxy?

In this Chapter, I apply my Magnetic Tracers algorithm (introduced in Chapter 3) to address these questions and others related to the competition of primordial magnetic fields with those generated by stars. Due to numerical limitations hampering dynamo activity, the simulations presented here will not feature significant turbulent dynamo amplification. The presence of a strong total magnetic field will generate a back-reaction that further suppresses any turbulent amplification. This lack of capturing dynamo activity requires further caution when interpreting my results. Using the Magnetic Tracers I will directly distinguish whether a magnetic field has a primordial or stellar origin and I will study the evolution of the two kinds of fields in temperature and gas density phase space. In Section 5.2, I describe the two simulations analysed with the tracers. One, a simulation of a cosmological volume containing a sample of galaxies, and the other a cosmological zoom-in simulation of a galaxy from the Nut suite. In Section 5.3, I analyse the results of these simulations, first addressing more global magnetisation properties with the cosmological volume simulations in Section 5.3.1, and then studying magnetism in the ISM of the Nut galaxy in Section 5.3.2. The main conclusions of the Chapter are summarised in Section 5.4.

5.2 Simulations

The two sets of studied simulations are summarised in Table 5.1. The first set (*B14*, *B13*, *B12*, *B11*) comprised of cosmological volume simulations will be used to explore magnetic fields in the environment around galaxies. These simulations differ exclusively in the strength of the primordial field B_0. The details of the cosmological

Table 5.1: Properties of the simulations used in this Chapter. Table indicates the initial comoving homogeneous magnetic field strength B_0, and stellar feedback injection $B_{\rm inj}$ (see text), physical spatial resolution Δx, and feedback prescription.

Simulation	Run name	B_0 (G)	$B_{\rm inj}$	Δx	Mech	Tracers
Cosmological volumes	*B14*	10^{-14}	10^{-5} G	10 pc	Mech	✓
	B13	10^{-13}	10^{-5} G	10 pc	Mech	✓
	B12	10^{-12}	10^{-5} G	10 pc	Mech	✓
	B11	10^{-11}	10^{-5} G	10 pc	Mech	✓
NUT	MB20+Inj	$3 \cdot 10^{-20}$	$2\sqrt{0.01 E_{\rm SN}/V_{\rm cell}}$	10 pc	Mech	✗
	MB12	$3 \cdot 10^{-12}$	✗	10 pc	Mech	✗
	TrMB12+Inj	$3 \cdot 10^{-12}$	$2\sqrt{0.01 E_{\rm SN}/V_{\rm cell}}$	10 pc	Mech	✓

simulations are given in Chapter 3, Section 3.3. Haloes in the cosmological volume simulations were identified with the spherical top-hat collapse model of the AMIGA Halo Finder (Gill et al. 2004; Knollmann & Knebe 2009).

The second set are new cosmological re-simulations of the NUT galaxy (ICs described in Section 2.4.3). They will be used to investigate in more detail the magnetic field in an individual galaxy. The three new NUT simulations include the same physics and cosmological parameters as the simulations described in Chapter 4 (Section 4.2). All three runs: MB12, MB20+Inj, and TrMB12+Inj feature *Mech* feedback (Section 2.3.2.2), and employ the same quasi-Lagrangian AMR refinement with a maximal physical resolution of $\Delta x_{\rm m} = 10$ parsecs. The runs differ only by the mechanism used to magnetise the simulations. Run MB12, features a strong primordial magnetic field $B_0 = 3 \cdot 10^{-12}$ G. Run MB20+Inj, employs instead the same extremely weak field used in Chapter 4 ($B_0 = 3 \cdot 10^{-20}$ G), but also injects magnetic fields with supernova explosions, where $B_{\rm inj} = 2\sqrt{0.01 E_{\rm SN}/V_{\rm cell}}$, and $E_{\rm SN}$ is the energy of a SN (see Figure 2.5). This choice of injected magnetic field has already been used before by e.g. Vazza et al. (2017). Finally, TrMB12+Inj is the Magnetic Tracers run. It combines a strong primordial magnetic field $B_0 = 3 \cdot 10^{-12}$ G (its energy will be shown in green in Figures 5.8, 5.9, 5.10, 5.11, 5.12), while also injecting magnetic fields through SNe in the same manner as MB20+Inj (shown in Figures 5.8, 5.9, 5.10, 5.11, 5.12 in red). The

SN injected magnetic fields and the strong primordial fields are traced independently. Their interaction energy (see term (3) $2\vec{B}_{\rm SN} \cdot \vec{B}_{\rm Primordial}$ in eq. (3.11), which will be shown in Figures 5.8, 5.9, 5.10, 5.11 in blue).

5.3 Results

The main results of this Chapter are separated in two parts. In Section 5.3.1, I aim to understand global magnetisation properties and how different primordial magnetic fields strengths all still within the current observational constraints affect the energy budget in a small simulated portion of the cosmos containing low mass galaxies. In Section 5.3.2, I proceed to study with more detail these two sources of field using the Magnetic Tracers to shed some light on their interrelation during the evolution of a Milky Way-like galaxy.

5.3.1 Primordial versus SN: stellar origin of magnetic fields in cosmological volumes

I discussed how a primordial and a SN-generated magnetic field compete to occupy the space in and around galaxies in Chapter 3, Section 3.4.2. Figure 3.2 illustrated how the two fields dominate different regions of the cosmos: the primordial magnetic field is more prevalent in the LSS, whereas the SN-generated magnetic field dominates hot bubbles of gas around galaxies.

In this Section I use Magnetic Tracers to study the energy contained in each tracer throughout the evolution of the (*B14*, *B13*, *B12*, *B11*) cosmological simulations. The energy of the tracers ($E_{\rm trace}$) within a cell is given by eq. (3.11). The key aspect of this equation that was not yet discussed in this thesis is that by splitting the total magnetic field into multiple components, cross terms $2\vec{B}_{\rm SN} \cdot \vec{B}_{\rm Primordial}$ appear in the energy calculation. Note that these terms are not always positive. In the case where

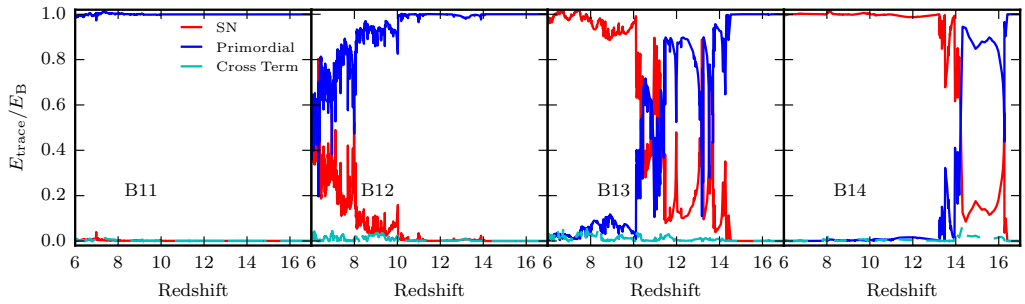

Figure 5.1: Fraction of the total magnetic energy in the box contained in the primordial field in the simulations, the SN generated field, or the cross term between the two components as a function of redshift for each simulation. The solid regions of the cyan line indicate redshifts at which the cross term is positive while the few dashed regions indicate that the cross term is negative. The simulations were designed to sample the parameter space where the primordial component dominates the energy at $z = 6$ (*B11*) to where the SN component dominates at $z = 6$ (*B14*). The *B12* simulation exhibits approximately equipartition of the total magnetic energy at $z = 6$.

magnetic tracer fields are oriented in opposite directions, they will lead to a negative energy contribution to the total magnetic energy.

5.3.1.1 Global properties

In Figure 5.1, I show the fraction of the total energy contained in the primordial field, the SN-injected field, and the cross term as a function of redshift for each of the four cosmological volume simulations. In the *B14* simulation (rightmost panel), which contains the weakest primordial magnetic field, as soon as the first generation of stars explode at $z \sim 16$, the total energy contained within the SN-injected field is nearly equal to the total magnetic energy in the primordial field. However, when the SN bubbles from this first generation of stars expand, the energy in the SN-injected magnetic field quickly dissipates until around $z = 14$ when a sustained period of star formation ensues in the simulation causing the energy in the SN-injected magnetic field to rapidly dominate that of the primordial field in the redshift range $13 \geq z \geq 6$.

By increasing the strength of the primordial magnetic field, the redshift at which the SN-injected field dominates the total magnetic energy budget occurs at later

times. For the *B13* and *B12* simulations, the equipartition between the primordial and SN energy occurs at $z \sim 10$ and $z \sim 6$, respectively, while for the *B11* simulation, the energy in the primordial field completely dominates the total magnetic energy in the cosmological volume at all redshifts simulated.

The cyan lines in each of the panels of Figure 5.1 represent the magnetic energy contained in the cross term. Interestingly the energy in this component rarely reaches more than a few percent of the total in the volume simulations ran. As already mentioned, the cross term component can be either positive or negative depending on the exact orientation of the tracer fields near galaxies; however, in neither case does it ever represent a significant fraction of the total in my simulations. This is to be expected, as the relevance of this term strongly depends on the correlation between the magnetic fields being traced and becomes most important when the two magnetic fields are comparable in strength. In the cosmological volumes studied here, one tracer typically dominates over the other. However, primordial and SN-generated magnetic fields can develop a non-negligible cross term energy component at later stages in the evolution of galaxies, once other mechanisms like their large-scale rotation become important. This is studied in more detail in Section 5.3.2.

Even though the energy contained in the SN-injected magnetic field dominates the total magnetic energy by $z = 6$ in both the *B13* and *B14* simulations, this does not necessarily mean that this component affects the majority of the volume of these simulations. The images in the top row of Figure 3.2 show that the regions magnetised by SN rarely extend more than $\sim$ 100 kpc from their host galaxies and that most of the volume of the simulations is only aware of the presence of the primordial magnetic fields. I quantify this in Figure 5.2 by plotting the volume filling factor of the energy contained in the SN-injected magnetic field as a function of redshift for each of the four simulations. I define volume filling factor as the fraction of the simulation volume where at least 1% of the local magnetic energy is comprised of the SN-injected

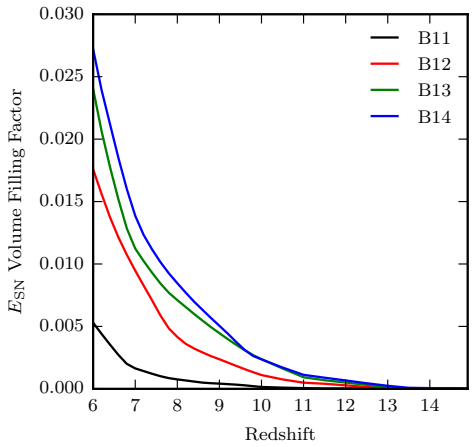

Figure 5.2: Volume filling factor of the regions where at least 1% of the total magnetic energy in the cell has come from SN explosions as a function of redshift. Different colour-codings indicate the runs with different initial magnetic field strength. Even though the SN magnetic energy dominates the total magnetic energy in the *B13* and *B14* simulations, less than 3% of the total volume is significantly affected by this component of the magnetic field.

component. By $z = 6$, the volume filling factor of SN-injected magnetic energy is only $\sim 2.7\%$ for the *B14* simulation, decreasing to $\sim 0.5\%$ for the *B11* simulation. Thus in all simulations, the volume of the simulation filled by SN-injected magnetic energy is essentially negligible compared to the total. Primordial magnetic fields are expected to dominate a majority of the cosmic volume, even in the presence of strong astrophysical sources (Vazza et al. 2017).

As redshift decreases, the rate at which SN-injected magnetic energy fills the volume accelerates. Thus if this simulation was run for another ~ 13 Gyr to $z = 0$, it is likely that SN injected fields may be able to fill a more significant portion of the IGM. The exact volume filling fraction however is probably subject to how star formation and SN injections are modelled. The star formation rate density is expected to turn over at $z \sim 2$ (Madau & Dickinson 2014) and therefore the volume filling factor cannot grow indefinitely. Nevertheless, magnetised winds emanating from galaxies

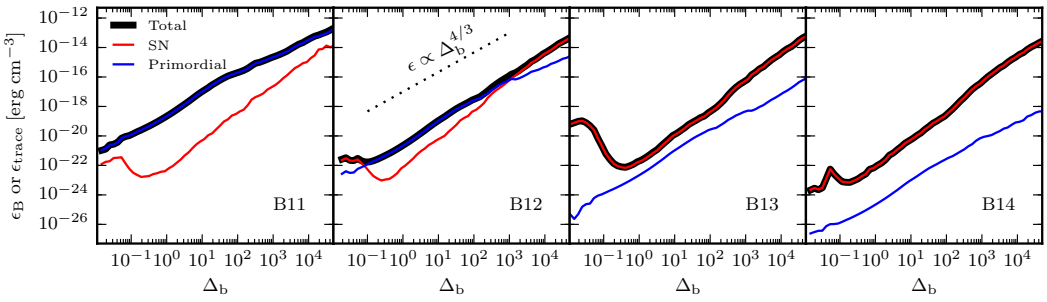

Figure 5.3: Total magnetic energy density over all cells in the simulation and magnetic energy density in each of the tracer components as a function of baryonic over-density at $z = 6$ for each simulation. For low values of the primordial magnetic field, the SN field dominates the total energy over the whole box at all over-densities while the reverse is true of high values of the primordial magnetic field. When the total magnetic energy is in approximate equipartition (*B12*), SN magnetic energy dominates at the highest and lowest over-densities (i.e. inside galaxies and SN heated regions) while the primordial magnetic field dominates at mean density (i.e. the IGM).

may provide a plausible channel for magnetising the IGM by $z = 0$ (e.g. Dubois & Teyssier 2010; Beck & Wielebinski 2013; Vazza et al. 2017).

Although the majority of the simulation volume is not affected by the SN-injected magnetic field, one of the main advantages of the Magnetic Tracers algorithm is that I can separate the effects of each tracer field both in time (as shown) as well as based on environment. Figure 5.3 shows the fraction of total magnetic energy density at a given baryon density, $\Delta_b = \rho_b/\bar{\rho}_b$ where $\bar{\rho}_b$ is the mean baryon density at a given redshift, for the four simulations at $z = 6$. The total magnetic energy density at fixed density is well described by a power-law in all simulations, except at $\Delta_b \lesssim 0.1$ where SN dominate the energy density in the *B12*, *B13*, and *B14* simulations and strong deviations from the mean trend can be seen. This density represents a very small fraction of the total volume of the simulation and can rapidly change with time depending when the most recent SN occurred.

The blue lines in each panel of Figure 5.3 represent the energy density in the primordial magnetic field as a function of density. For adiabatic evolution, the magnetic energy density scales as $\Delta_b^{4/3}$. Blue lines exhibit power-law slopes consistent with

this value. The red lines exhibit steeper slopes than $\Delta_{\rm b}^{4/3}$ because magnetic fields are injected at a higher strength than the local primordial field at a given density and then they cascade to lower densities as SN bubbles expand (see Vazza et al. 2017 who also find a steeper slope for the injected field). The *B13* and *B14* simulations (third and fourth panels) are dominated by SN-injected magnetic energy at all densities and thus the total line has a steeper slope than 4/3. In contrast, the *B11* (first panel) simulation is dominated by the primordial magnetic field at all densities and thus exhibits a slope of 4/3. The *B12* simulation (second panel), which exhibits equipartition in total magnetic energy at $z = 6$ between the two tracer fields, shows the most interesting behaviour in the magnetic energy density as a function of gas density. At $\Delta_{\rm b} \gtrsim 1000$ and $\Delta_{\rm b} \lesssim 0.1$ the SN-injected energy density dominates while at densities between these two regimes, the primordial component dominates. Thus in this simulation, although there is energy equipartition between the traced fields at $z \sim 6$, the SN-injected field only dominates inside of galaxies and in SN remnants.

5.3.1.2 Magnetic fields in haloes

I now focus on each component of the magnetic field inside virialised haloes. The first question addressed is what percentage of the total magnetic energy within the virial radius of haloes is represented by the primordial and SN-injected fields. In Figure 5.4 I show the ratio of total energy in each tracer field to the total energy within a halo as a function of halo mass at $z = 6$. In all simulations most of the haloes with $M_{\rm vir} \lesssim 10^8$ M$_\odot$ have magnetic energy completely dominated by the primordial component. These systems are extremely inefficient at forming stars (e.g. Kimm et al. 2017) and thus the amount of magnetic energy injected by SN is limited in these galaxies. However, for more massive haloes in the *B12*, *B13*, and *B14* simulations, the SN-injected magnetic energy becomes very important and at $M_{\rm vir} \sim 10^9$M$_\odot$, most of the energy contained within the haloes is dominated by the SN-injected

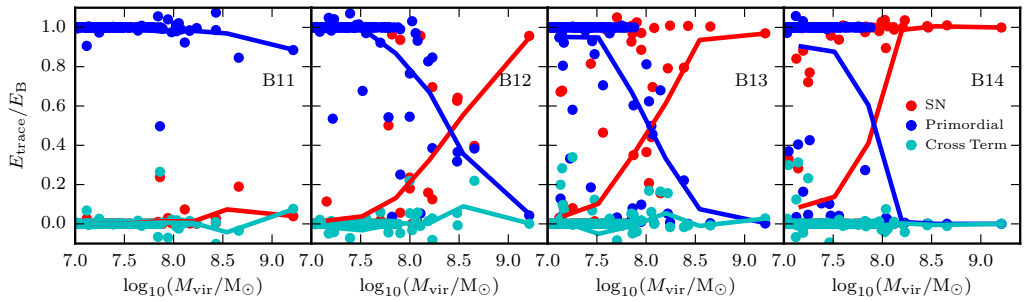

Figure 5.4: Ratio of the fraction of total magnetic energy in each of the tracer magnetic fields compared to the total within the virial radius of a halo as a function of virial mass for each of the four simulations at $z = 6$. Red, blue, and cyan represent the energy in the SN injected field, the primordial field, and the cross term, respectively. The coloured lines show the average ratio in bins of virial mass. The virial mass where equipartition occurs between the SN injected and primordial fields increases with the strength of the primordial magnetic field. Equipartition never occurs in the *B11* simulation for any halo mass probed by my simulation.

component. The mass at which the crossover occurs between SN-injected dominated and primordial-dominated shifts to progressively larger mass for increasing primordial magnetic field strength. For the *B12* and *B13* simulations, there is considerable scatter at intermediate masses between which tracer field dominates the total energy. This is likely caused by the exact star formation history of each individual halo. In no simulation does the cross term contribute on average a significant fraction of the total energy, consistent with the results of Figure 5.1. In certain haloes, the cross term can contribute up to $\sim 40\%$ of the total energy; however, these cases are rare. SKA will have the potential of observing magnetic fields in the surroundings of galaxies and clusters, which could probe primordial magnetic fields (Johnston-Hollitt et al. 2015; Taylor et al. 2015). These results allow to constrain in my simulations a maximal halo mass below which, for a given primordial magnetic field strength, the magnetic energy of a halo is dominated by the primordial component. Upcoming applications of this algorithm have the potential to determine the regions around galaxies where future observations should aim to detect magnetic fields of primordial nature, and which halo masses are dominated by primordial magnetic fields.

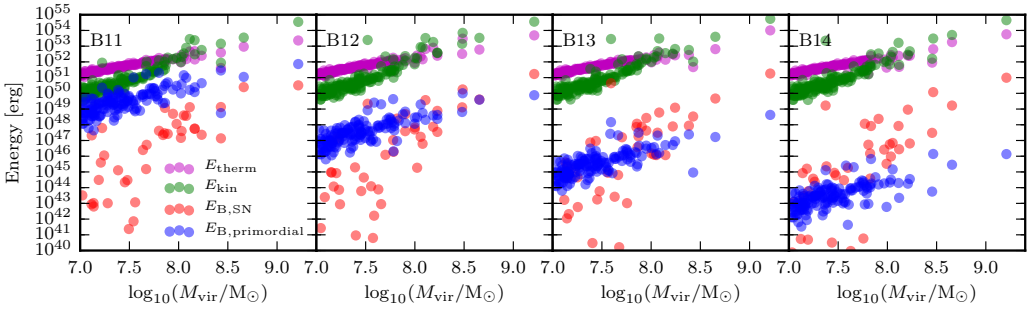

Figure 5.5: Total thermal energy (purple), kinetic energy (green), magnetic energy in the SN injected field (red), and magnetic energy in the primordial field (blue) within the virial radius of individual haloes in each of the four simulations at $z = 6$. The thermal energy dominates for low mass haloes while the kinetic energy is dominant for haloes with $\log_{10}(M_{\rm vir}/{\rm M}_\odot) > 8.0$. The total primordial magnetic energy within haloes decreases with the strength of the primordial magnetic field. In no simulation is the magnetic energy in the entire halo in equipartition with its thermal or kinetic energy.

A natural question is whether the energy contained within the magnetic field in a halo is in equipartition with the thermal and kinetic energy of that halo. In Figure 5.5, I show the total thermal energy, kinetic energy, and magnetic tracer fields energies as a function of halo mass at $z = 6$ for each of the four simulations. In no simulation is the total magnetic energy comparable with either the thermal or kinetic energy. At the grid resolutions obtained in the dark matter haloes in my simulations, turbulent amplification in the haloes is expected to be negligible if at all existent, especially when compared with the magnetic energies expelled from the galaxies. Typical morphologies of observed magnetic fields in haloes are also consistent with being driven by galactic outflows (Dahlem et al. 1997). For the *B11* simulation, with the highest primordial magnetic field, only for the lowest mass galaxies does the total magnetic energy approach values of 10% of the kinetic energy. For most other mass systems, the magnetic energy in the entire halo is far below the other energies.

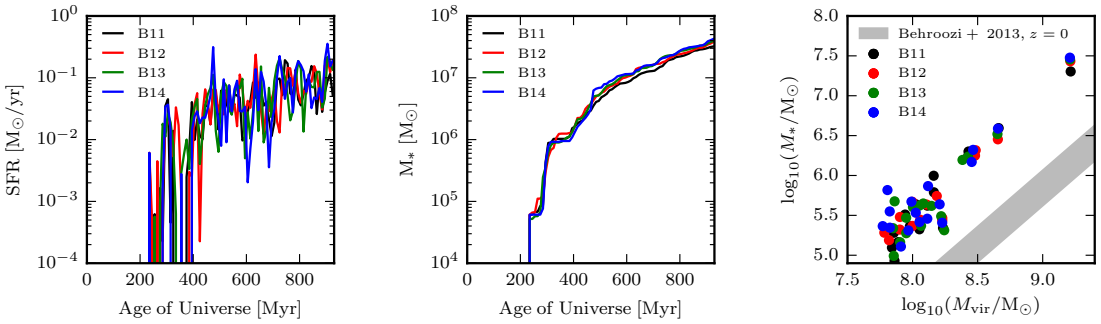

Figure 5.6: (Left) Star formation rate as a function of age of the simulation. (Centre) Total stellar mass as a function of the age of the simulation. (Right) Stellar mass-halo mass relation for central galaxies in each of the four simulations. The grey shaded region shows the local extrapolated stellar mass-halo mass relation from Behroozi et al. (2013).

5.3.1.3 Impact of magnetic fields on star formation on cosmological scales

Because of the variations in total strength of the magnetic fields within haloes of different masses (see Figure 5.5), it is interesting to understand whether the magnetic fields have an impact on star formation in galaxies. In the left and central panels of Figure 5.6, I show the star formation rate (SFR) and total stellar mass formed as a function of the age of the universe for each of the four simulations with varying primordial seed strengths. In all simulations, by $z = 6$, the total mass in stars formed is nearly identical as are the SFRs. Stochasticity in the employed star formation algorithm means that at a fixed time, the SFR is expected to deviate between the simulations by a small fraction; however, it is clear that the general trend is the same between all four simulations.

Since the relationship between stellar mass and halo mass is expected to be reasonably steep such that more massive haloes are expected to form stars much more efficiently (Moster et al. 2013; Behroozi et al. 2013), the total stellar mass formed and the total SFR in the simulation may only be representing the high mass haloes in the simulation. Thus in the right panel of Figure 5.6, I show the stellar mass-halo

mass relation at $z = 6$ for each of the four simulations. I find no systematic offsets in stellar mass for a given halo mass between the simulations, even for the lowest mass haloes, indicating that the magnetic fields in my simulation have a negligible effect on the resulting stellar masses, regardless of the primordial seed strengths that I have chosen to model. This is true even for the *B11* simulation which has a magnetic field strength at the highest gas densities that is larger than the strengths that my SN-injection can obtain (see Figure 5.3). Note that the simulations overpredict the expected stellar mass for a given halo mass compared to predictions by Behroozi et al. (2013). Observational studies find limited evolution for the stellar mass-halo mass ratio (Hatfield et al. 2016) in the redshift range $0.75 < z < 1.7$. As a result, it is possible that the major uncertainty when comparing our data with the presented relation comes from the extrapolation to significantly lower halo masses. No change in the global SFR may be expected, as the employed primordial seed strengths are not high enough to prevent accretion of gas onto haloes. Previous work suggests that for this to happen, one needs a primordial seed strength $\gtrsim 10^{-9}$ G (Marinacci & Vogelsberger 2016).

5.3.2 Primordial versus SN origin: inside galaxies

Building on the results of the previous Section, I present here the preliminary analysis for a set of cosmological re-simulations that study how primordial and SN-generated magnetic fields interact and compete to permeate the ISM of a Milky Way-like galaxy. The simulations with strong magnetic field ($B_0 = 3 \cdot 10^{-12}$ G), aim to address a scenario where primordial and SN-generated fields have comparable strengths in the galaxy. The choice of $B_0 = 3 \cdot 10^{-12}$ G leads to $\sim$ 1 dex more total magnetic energy density than the *B12* simulation and $\sim$ 1 dex less than *B11*. Therefore, in the densest regions ($\rho_{\rm gas} > 10^{-22}$g/cm^3), the mean SN-generated magnetic field eventually dominates, as observed in Figure 5.3.

In Figure 5.7, I compare once again the specific magnetic energy found in the galactic regions of the three simulations: MB12, MB20+Inj, and TrMB12+Inj. Simulation MB12 with strong primordial magnetic field but no injection achieves the lowest magnetic energy of the three runs. It has almost constant $\varepsilon_{\rm mag}$, with dynamo amplification inhibited by the back-reaction of the field (which has strong values in this Chapter when compared with the negligible magnetisations of Chapter 4) so that the dynamo in this simulation maintains the specific magnetic energy against numerical decay but does not amplify the field. The absence of amplification is evident when comparing the relatives evolutions of $\varepsilon_{\rm mag}$ in Figures 4.18 and 5.7. In comparison MB20+Inj with an extremely small primordial field and SN-injected fields achieves the highest specific magnetic energy. Counterintuitively, the simulation with both a strong primordial magnetic field and magnetised stellar feedback (TrMB12+Inj) tends to sit between the other two runs. This is however likely the result of the magnetic field injection being less efficient, as discussed in Section 2.3.3.

5.3.2.1 Tracing the origin of magnetic fields in a Milky Way-like galaxy

The most interesting aspects of these simulations are unveiled once I separate the magnetic field in TrMB12+Inj into the different tracers. The time evolution of the traced magnetic energies in simulation TrMB12+Inj is shown in Figures 5.8 and 5.9. The left panels of these Figures show the gas density in cyan, the gas temperature in dark orange, and the total magnetic energy density in green. The right hand panels display the decomposition of the magnetic energy into each of the tracers. Green corresponds to the primordial magnetic energy, red to the SN-generated magnetic energy, and blue to the interaction magnetic energy. In these projections, whenever the cross-term magnetic energy is negative, it is removed from both the stellar and the primordial magnetic energy in equal parts.

The magnetic energy originating from different sources evolves with decreasing

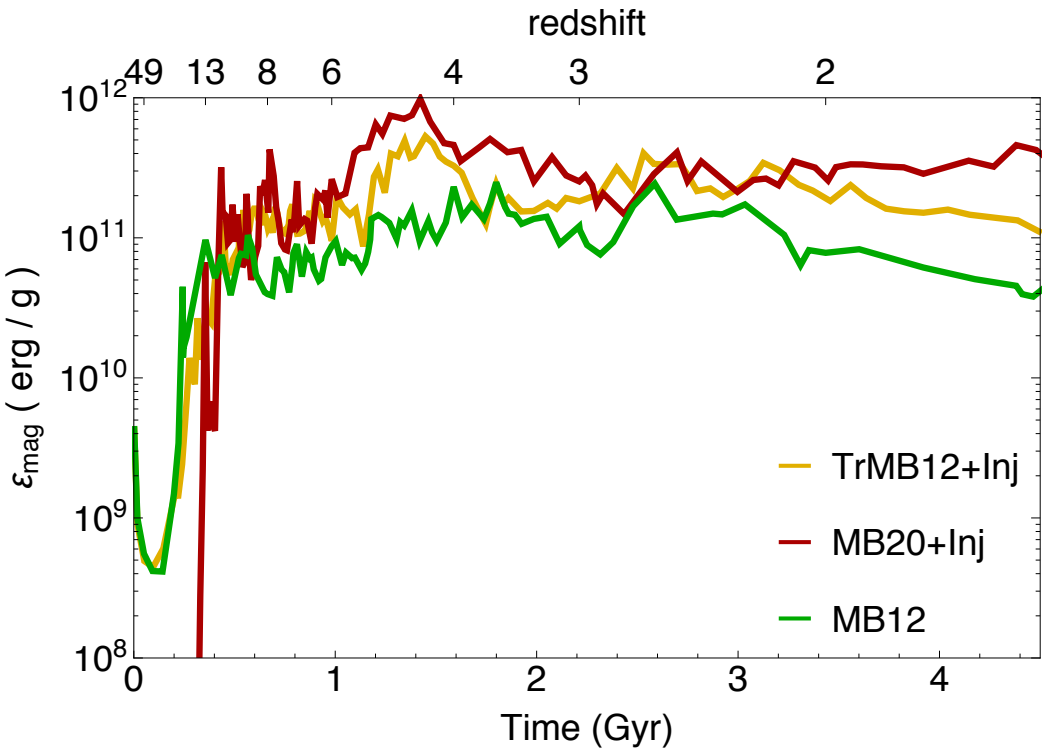

Figure 5.7: Specific magnetic energy evolution in the galactic region of the MB12, MB20+Inj, and TrMB12+Inj simulations. SN-injected magnetic energy continually increases the amount of magnetic energy in the galaxy. In the presence of a strong primordial field, injections becomes less efficient. In the absence of injection, the specific magnetic energy remains approximately constant at the value attained through collapse.

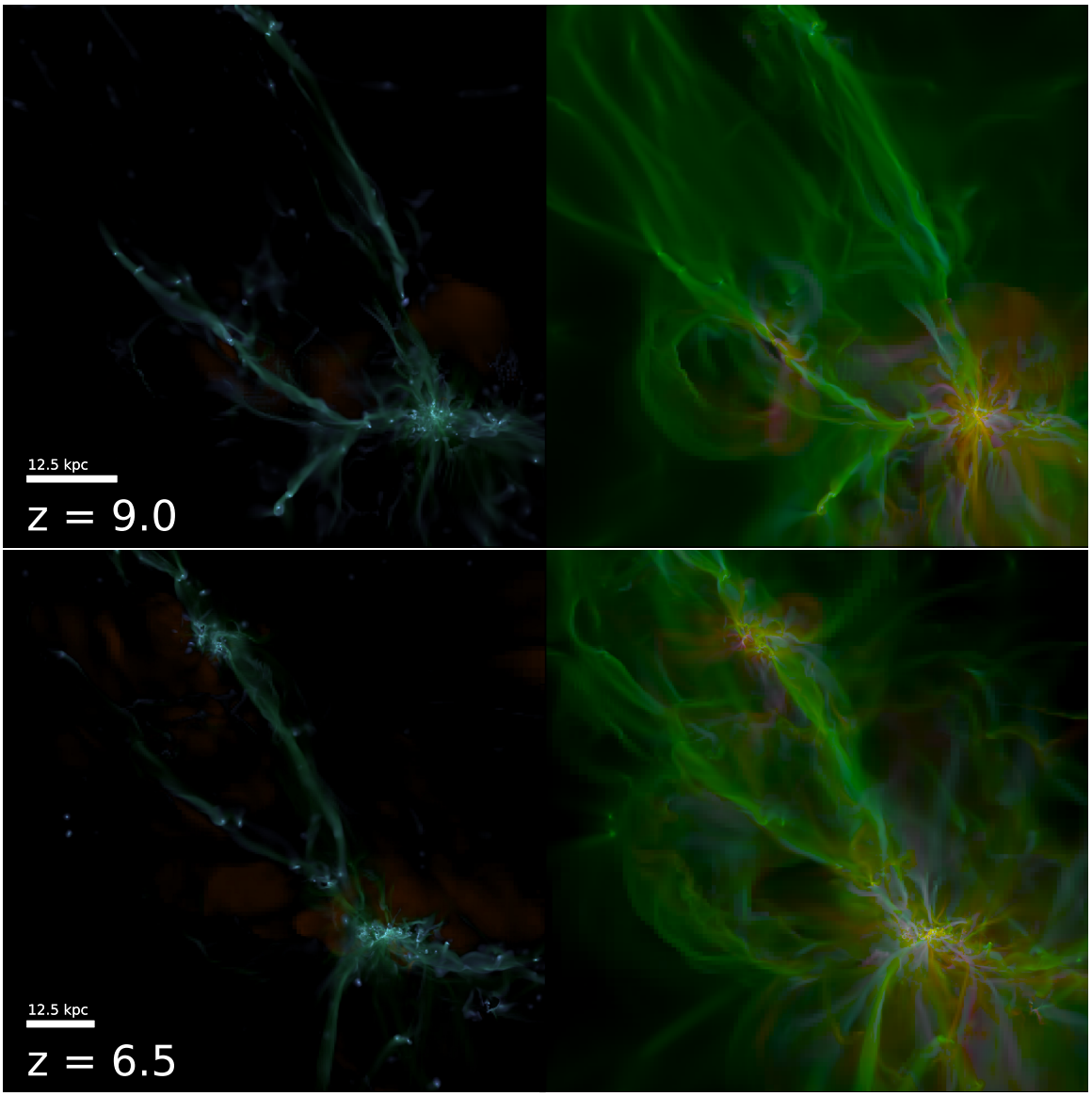

Figure 5.8: Snapshots of the time evolution of the galaxy (left) and the magnetic tracers (right) in the TrMB12+Inj simulation. Projections are obtained from boxes of (750 comoving kpc)^3 of the region where the Nut galaxy forms. Colours in the left column indicate the gas density in cyan, gas temperature in dark orange, and magnetic energy in green. In the right column: SN-generated magnetic energy is in red, primordial magnetic energy is in green, and cross-term interaction energy is in blue. The top row corresponds to redshift $z = 9$, and the bottom row to $z = 6.5$. See text for details on the treatment of the negative cross-term energy in the projections. At high redshift, the magnetic energy in the galaxy is dominated by a combination of primordial and stellar, while the LSS is dominated by primordial energy.

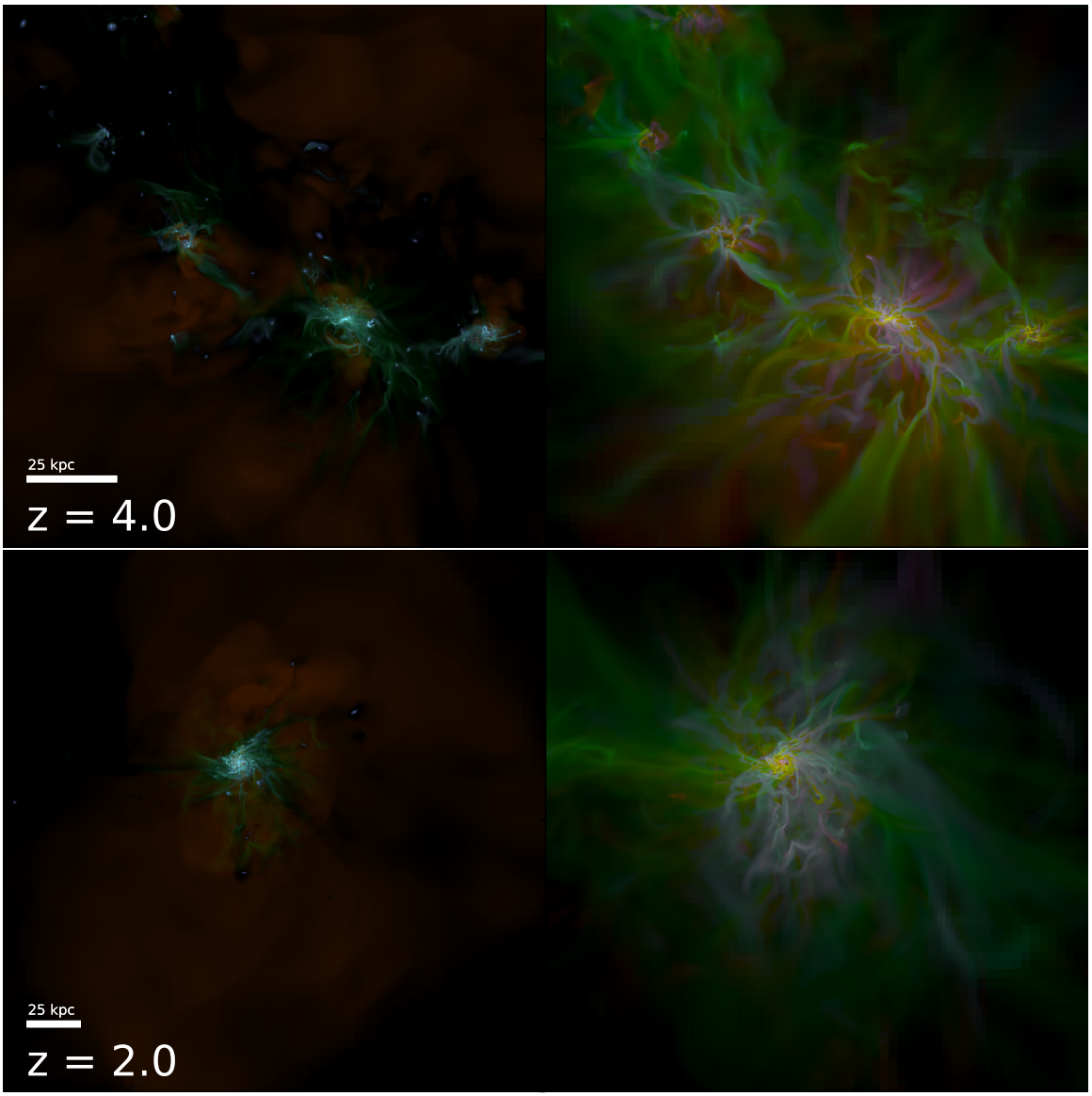

Figure 5.9: Continuation of Figure 5.8, now for redshifts $z = 4$, $z = 2$. As redshift decreases, the amount of cross-term interaction energy inside the galaxy and in the CGM increases. An important contribution from the negative component of this cross term appears (see top panel in Figure 5.11). This increased significance of the interaction between the two fields appears shortly after the galaxy develops a rotationally dominated disk.

redshift as more stellar generated magnetic energy is injected and the simulation transitions away from being dominated by a primordial field characterised by green-coloured filamentary structure in the images. Shortly after the formation of the galaxy at $z \sim 4$, the magnetic energy inside the galaxy is mostly represented by yellow tones, resulting from the combination of stellar and primordial magnetic energy which are similar in value as confirmed more quantitatively in Figure 5.11 (top panel), and discussed below. The hot bubbles inflated by stellar feedback are filled with SN-generated magnetic energy, and at high redshifts (right-hand panels of Fig 5.8) their intersection with the filaments feeding the galaxy display significant cross terms (in blue). As redshift decreases, purple colours permeate the CGM (right-hand panels of Fig 5.9), implying significant energy in both the cross term and the SN-generated magnetic energy. By $z \sim 4$ the SN-generated magnetic energy extends ~ 100 kpc into the galactic halo.

To look in more detail at the distribution of the tracer energies in the galaxy, I present a face-on projected close-up view of it in Figure 5.10. In this Figure, no region of the galaxy displays solely one of the three colours attributed to SN-injected (red), primordial (green), or cross-term interaction magnetic energies (blue). Instead, most of the galaxy is characterised by varying shades of yellow, cyan, or purple, indicating combinations of different magnetic energies. This serves as clear proof that a complex interaction of the primordial and SN-injected magnetic fields occurs.

Top panel in Figure 5.11 displays the evolution of the specific magnetic energy contained in each of the tracers in the galactic region of the TrMB12+Inj simulation. An interesting result is illustrated in this Figure, while both types of energy are comparable at all times, the total magnetic energy is dominated during the accretion phase ($z > 4$) by SN-injection (constituting $\sim 2/3$ of the total energy), whereas in the feedback phase ($z < 4$) primordial magnetic energy prevails (containing $\sim 70\%$ of the total energy). There are various reasons for this. The first is related with the efficiency

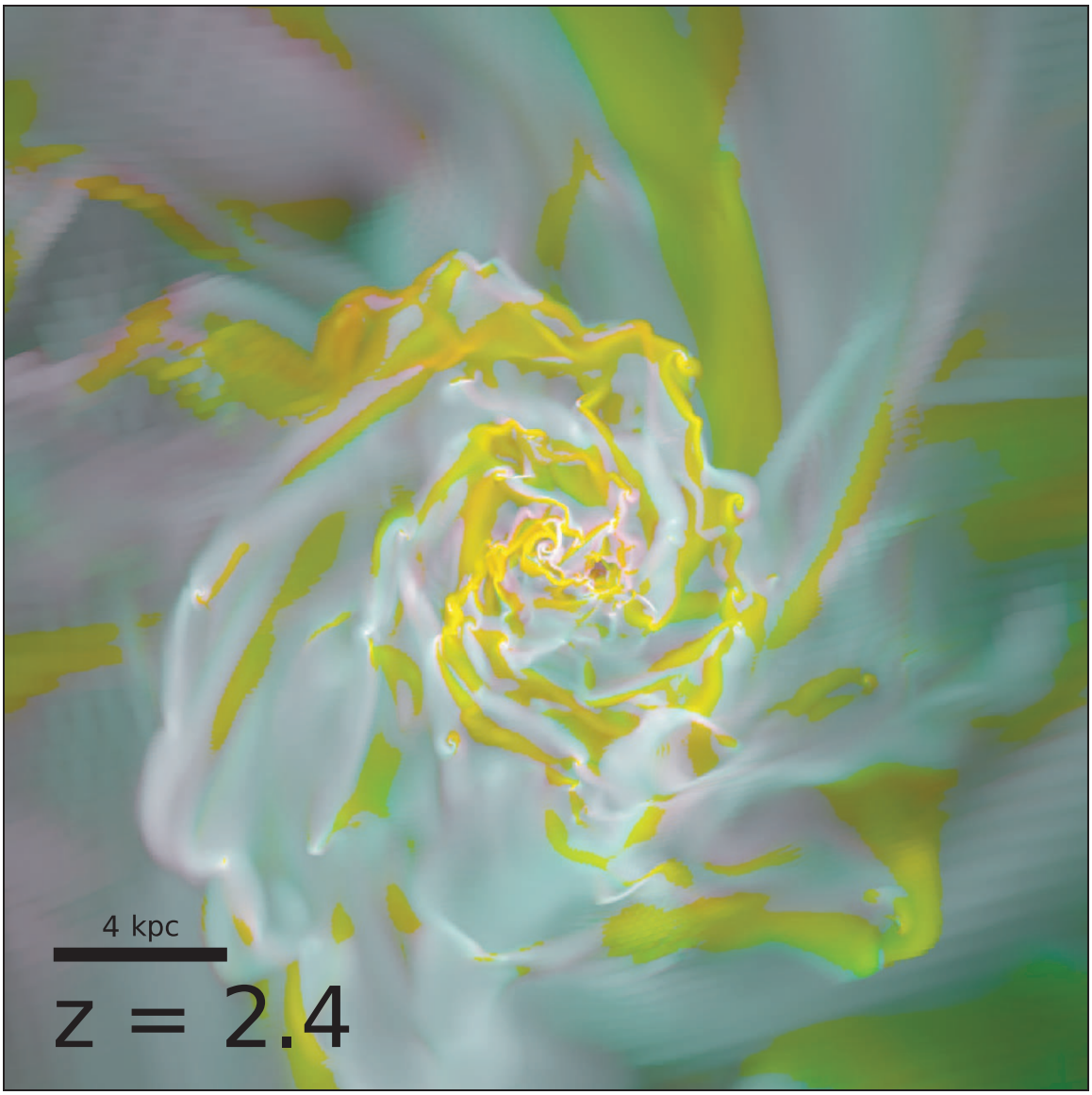

Figure 5.10: Face-on zoom projection of a box of side (25 physical kpc)^3 centred at the TrMB12+Inj galaxy at redshift $z \sim 2.4$. Colours as for Figure 5.8. The image displays no region in the galaxy characterised solely by primordial, stellar, or cross-term interaction energy. Instead, it shows a complex interaction of the different forms of magnetic energy. Yellow represents a combination of SN and primordial magnetic fields. Purple signifies regions where a combination of SN-injected and cross-term magnetic energy dominate, and cyan indicates regions where it is a combination of primordial and cross-term magnetic energy what dominates the total magnetic energy.

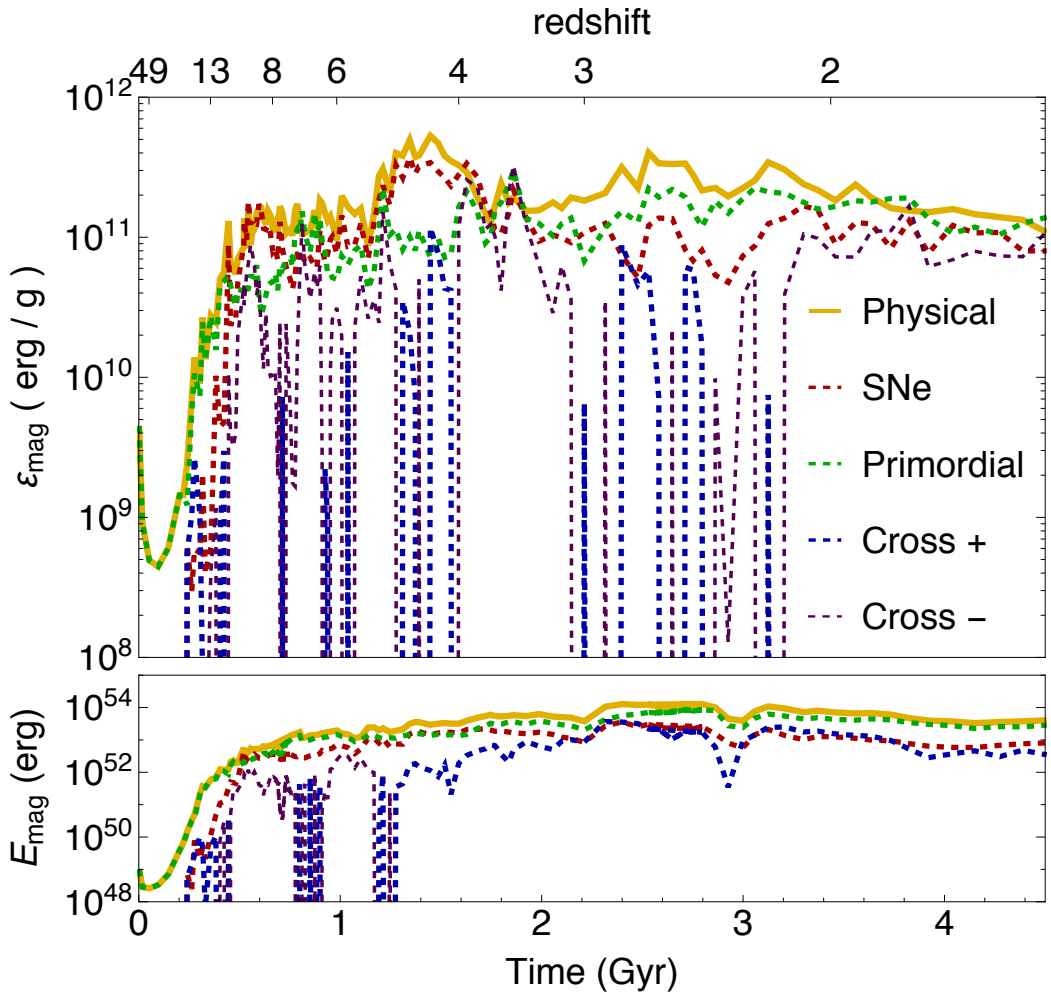

Figure 5.11: (Top) Specific magnetic energy growth in the galactic region of the TrMB12+Inj (yellow) simulation, now decomposed into each of the magnetic tracers, SN injected (red), and primordial (green). The cross-term magnetic energy is represented in blue when positive and purple when negative. The total magnetic energy is first dominated by SN injected magnetic fields and later by primordial fields. At the latter stages of the evolution, during the feedback phase ($z < 4$), the negative cross-term energy becomes relevant. The organisation of the field on large scales and the numerical incapability of the tracers to interact with each other are likely responsible for this (see text and Figure 5.13). (Bottom) Evolution of the magnetic energy in the halo of the galaxy (without the galactic region) over cosmic time. While the halo is dominated by primordial magnetic energy, SN-injected magnetic energy remains relevant $\sim 10\%$. Towards lower redshifts $z < 4$, the cross-term magnetic energy reaches the $\sim 10\%$ levels, indicating that a significant interaction between the two traced magnetic fields is occurring. This suggests that recovery of information from the primordial magnetic field is complicated due to the pollution provided by SN events in the galaxy.

of injecting magnetic fields with SN. During the collapse of the galaxy, the primordial magnetic energy spectrum breaks the uniformity of the field and commences to inject at the scale of the forming galaxy. At high redshift, the primordial magnetic energy is cascading from galactic scales to small scales. Meanwhile, SN events inject magnetic energy at the smallest scales by design due to the employed injection mechanism. This allows a large build-up of SN energy, which will roughly account for 2/3 of the total specific magnetic energy during the accretion phase. During the feedback phase, when the magnetic energy is re-organised by the rotation of the galaxy, there is also a large amount of magnetic energy in the small scales, reducing the efficiency of the injection of magnetic fields. Another reason is that the primordial energy accreted with cold gas contains a large amount of magnetic energy and will remain prevalent in this newly accreted gas, magnetising it to $\sim \mu$G levels. The impact of primordial magnetic fields and the magnetisation of inflowing gas on a forming galaxy will be discussed in more detail in Chapter 6. A final reason is that at high redshift, SN are capable of expelling all the pristine gas out of the environment of the galaxy, dominating the magnetic energy around the galaxy, however, at lower redshifts, they only drive winds that can penetrate into the halo and lose SN-injected magnetic energy to the halo. However, these SN events are no longer capable of removing all the pristine gas present in the surroundings of the galaxy. I find that if the primordial magnetic field of the Universe is strong enough, its contribution to the magnetisation of galaxies during the first ~ 4 Gyr of the Universe does not decrease as more stellar magnetic energy is generated, but remains important. Future work will recover more information on how these tracer energies are stored in the galaxy by reviewing the tracers magnetic energy spectra.

To quantify the gas density and temperature regimes where primordial as opposed to SN-generated magnetic fields dominate, I present in Figure 5.12 temperature versus gas density phase space diagrams coloured according to the value of $\varepsilon_{\rm mag,SN}/\varepsilon_{\rm mag,prim}$.

Regions in red are dominated by stellar injected magnetic energy, whereas in green are dominated by primordial fields. Figure 5.12 shows that at high redshift ($z = 7$) the cold phase ($T < 10^4$ K) of the galaxy is mostly dominated by both tracers. The hot phase ($T > 10^6$ K) is, as one would expect, dominated by the stellar magnetic energy, whereas there is a phase of intermediate temperatures ($10^4\text{K} < T < 10^6\text{K}$) and low densities ($\rho < 10^{-26}\text{g/cm}^3$) which is governed by primordial magnetic energy, likely associated with pristine and recently accrued gas. At redshift $z = 3$, primordial magnetic energy accumulates and dominates in the a band of temperatures $T \sim 10^2 - 10^3$ K of the galaxy, while the stellar magnetic energy dominates part of the hot phase ($T > 10^4$ K, $\rho \sim 10^{-24}\text{g/cm}^3$). This suggests that, if a strong primordial magnetic field was present in our Universe, the magnetic energy currently found in galaxies might be partially a remnant of these magnetic fields which would have impacted their evolution (see Chapter 6). This does not however imply that its signature can be recovered, as evidenced by the complex interaction I described between this primordial field and the SN injected one.

There are a number of further caveats to be considered this far. Note that in the presence of a strong primordial magnetic field that leads to magnetic saturation by collapse, dynamo action will be inhibited by the back-reaction of the saturated magnetic field, and is instead maintaining the level of magnetic energy rather than amplifying it. This maintenance of the field might be occurring in simulations MB12, MB20+Inj, and TrMB12+Inj through galaxy rotation. Another important caveat is that the results presented here are for a particular primordial magnetic field $\vec{B_0}$ strength and configuration. Chapter 6 will show that there exists an upper limit for B_0 above which my simulations find a large impact on galaxy formation. As B_0 is decreased, the relative importance of SN injected fields increases. My findings could depend on the value selected for the injected magnetic field. Therefore, the results discussed here should serve as a first glimpse at how different magnetogenesis

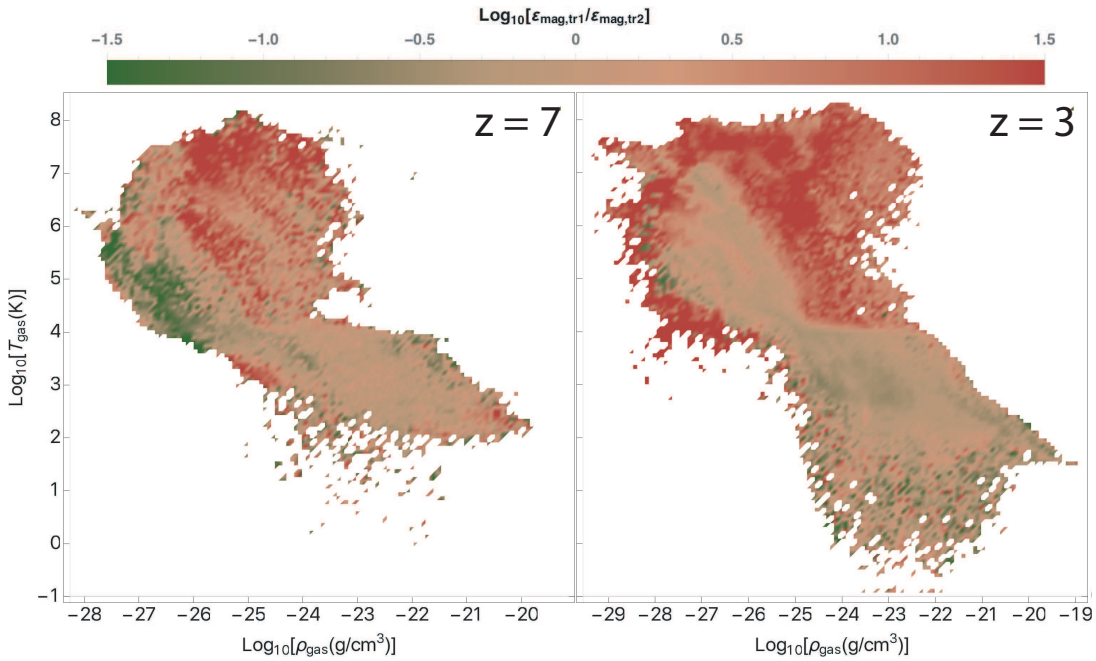

Figure 5.12: Phase diagrams for the ratio of $\varepsilon_{\mathrm{mag,\ SN}}/\varepsilon_{\mathrm{mag,\ prim}}$ over the gas density ρ_{gas} vs gas temperature T_{gas}, studied for the galactic region of the TrMB12+Inj simulation. The left panel shows $z = 7$ and the right panel shows $z = 3$. Overall, primordial energy dominates at the coldest temperatures of the warm phase, whereas the stellar injected is the main source of magnetic energy in the hot gas.

scenarios can affect galaxy formation. Future work will involve a careful calibration of the injected stellar magnetic field and a more in-depth analysis of primordial magnetic fields, together with the inclusion of a sub-grid model for dynamo amplification to review how all three and their different possible combinations interact with each other.

Figures 5.8 and 5.9 showed some stellar magnetic energy being ejected to the halo of the galaxy (red colours), remaining mostly in the CGM of the galaxy at high redshift and expanding inside the halo at latter times. The bottom panel of Figure 5.11 shows the absolute total and traced magnetic energies. The SN-injected energy is important through time, but displays a large cross-term budget of magnetic energy at low redshift. Both the SN-injected and cross-term energies represent each $\sim 10\%$ of the total magnetic energy. Given the large degree of interaction between the two, this suggests that no signature of a primordial magnetic field can be recovered from

the CGM of galaxies and most of the halo. Further study will clarify on this question.

Finally, another particularly interesting aspect to be observed in Figure 5.11 is the evolution of the cross-term magnetic energy. Throughout most of the galaxy's evolution this energy is negligible in comparison to the tracer magnetic energies and fluctuates between positive and negative values. However, as the galaxy stabilises and forms a disk, the cross-term magnetic energy stops oscillating around negligible values and becomes comparable with the tracer magnetic energies, taking negative values. It is reasonable for the interaction energy to increase as the dynamics of the galaxy become dominated by large scale rotation. This is because when the magnetic tracers are arranged by the same large scale process, they occupy the same dynamical space and are forced to interact with each other. At the moment of writing, the reason behind the cross-term negative value remains uncertain, but likely follows from two numerical considerations. The first is that when injecting magnetic energy, the orientation of the employed injection loop is selected to maximise the total magnetic energy injected. As a result, when a loop injects more energy than it removes, the injection proceeds, even when this introduces a significant amount of negative energy. However, this energy should remain significantly below either of the tracers, and certainly below the physical energy. The second numerical consideration is what is probably responsible for the majority of the rise of the negative cross-term, namely magnetic reconnection. The general idea is depicted in Figure 5.13. When a flow causes a portion of the total magnetic field in a region to reconnect two magnetic field lines corresponding to two different tracers, the physical energy is lost. However, the inability of the tracers to perceive the presence of other magnetic fields implies that their magnetic energy cannot be lost. Instead, these tracer fields represent the lost magnetic energy through the generation of a negative cross-term due to the anti-alignment of their magnetic field lines. As a result, the negative cross term measured for TrMB12+Inj at $z < 2$ likely emerges from magnetic reconnection. It would

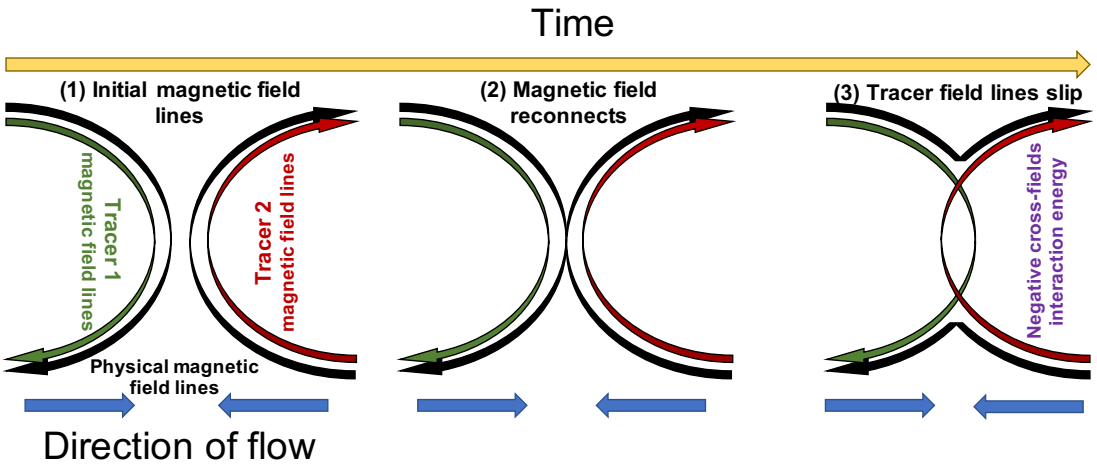

Figure 5.13: Schematic illustrating the generation of negative cross-term interaction energy through magnetic reconnection. When two total magnetic lines (black) generated by two different magnetic tracers (green and red) reconnect, they remove total magnetic energy. The tracer fields however cannot reconnect and the lines simply slip through each other. To account to the loss of magnetic energy, the tracers are anti-aligned in the same spatial region, and generate a negative cross-term contribution to the total tracers energy (i.e. right-most panel of this Figure, the red and green lines in the reconnected region).

be useful to run further simulations of disk galaxies with these two magnetisation mechanisms and Magnetic Tracers to determine whether this is a stochastic result yielded by the ultimate configuration of the large scale galactic magnetic field.

5.4 Conclusions

This Chapter presents a first demonstration of the use of my magnetic tracers algorithm. Through two sets of simulations, one a cosmological volume and the other a cosmological re-simulation of the Nut galaxy, I study the competition and interaction of a primordial magnetic field with a magnetic component injected when SN explode. The set of cosmological volume simulations serves as a pathfinder numerical study for future work on the different magnetic sources which might magnetise the LSS. I use them to assess the importance of primordial magnetic fields versus supernova

injected magnetic fields in small cosmological volumes containing low mass galaxies ($10^7 M_\odot < M_{\rm halo} < 10^9 M_\odot$) at high redshift ($z \sim 6$). The main conclusions from the cosmological volumes described in Section 5.3.1 are:

- The importance of the primordial magnetic field is expected to decrease with time due to cosmic expansion unless it can be significantly amplified in haloes. In contrast, SN-injected fields become more important with cosmic time as more stars are formed (Figure 5.1).

- In the context of large-scale structure, primordial magnetic fields and those injected from SN possess different topologies. Primordial magnetic fields dominate the majority of the volume of the simulations, whereas SN-injected magnetic fields are confined to galaxies and the vicinity of their dark matter haloes by $z = 6$ (Figure 3.2). The volume filling factor of SN-injected magnetic fields to increase as a function of decreasing redshift (Figure 5.2).

- There exists a lower limit to the virial mass ($M_{\rm vir} \sim 10^8 - 10^{8.5} M_\odot$) below which SN-injected magnetic fields lose relevance compared to primordial magnetic fields. This mass limit is found to depend on the strength of the primordial magnetic field, and is also expected to be dependent on numerical resolution and the filtering mass due to reionization (Figure 5.4).

- Consistent with other work (Marinacci & Vogelsberger 2016), I find the global cosmic star formation properties to be unchanged within the range of primordial magnetic fields strengths probed in this work (Figure 5.4).

In Section 5.3.2, I focus instead on a cosmological re-simulation of an individual galaxy, to understand how both a primordial magnetic field and SN injected magnetic fields, co-evolve to produce the total magnetic field of a galaxy. I take advantage of the Magnetic Tracers to find that:

- When accounting for a primordial magnetic field and stellar injection of magnetic fields through SN events, both are capable of generating the magnetic fields we observe in current galaxies (from results in simulations and MB12, and MB20+Inj see also Figure 5.7), I find a complex interaction of the two sources of magnetic fields (Figure 5.10). Both sources provide comparable amounts of energy even at low redshift (Figure 5.11).

- The primordial and SN-generated magnetic fields are distinguishable in phase space (Figure 5.12), where the primordial magnetic tracer tends to dominate in the cold regions ($T \sim 10^2 - 10^3$ K) of the intermediate densities ($\rho > 10^{-25}$g/cm^3) of the galaxy an the SN injected field dominates the magnetic energy budget in the hot gas ($T > 10^4$ K, $\rho \sim 10^{-24}$g/cm^3).

- It is likely complicated to recover information about the primordial magnetic field from the haloes of Milky Way-like galaxies, due to the pollution from SN-generated magnetic fields and the large degree of interaction between the primordial field and the SN-generated (Figure 5.11).

- The interaction of the two traced magnetic fields is non-negligible locally (Figure 5.10) and capable of influencing the dynamics of the galaxy, because the cross-term interaction energy contains a significant fraction of the total magnetic energy (Figure 5.11). This applies especially at lower redshifts, when the large scale rotation of a galaxy rearranges the distribution of the traced magnetic energy among $E_{\rm prim}$, $E_{\rm SN}$, and $E_{\rm cross}$. Therefore, studying separately different sources of magnetism that are comparable in magnetic energy cannot illuminate their behaviour in combination.

These results represent the first demonstration of separating the contribution of primordial magnetic fields and SN-injected fields in two sets of simulations, providing a methodology for future, more detailed studies of magnetogenesis. They are subject

to the specific parameters selected for our simulations and the particular numerical implementations of the sub-grid physics. Nevertheless, the qualitative conclusions serve as an important step towards better understanding the complexity of galactic and cosmic magnetism.

Chapter 6

Primordial magnetic fields and the formation of galaxies

6.1 Motivation

Not much is known about primordial magnetogenesis. Depending on their overall strength, coherence length, or spectral distribution, cosmic magnetic fields could affect structure formation in various ways, acting as a reheating source during recombination (Trivedi et al. 2018), modifying density and vorticity perturbations (Tsagas & Maartens 2000), dark matter haloes (Varalakshmi & Nigam 2017; Cheera & Nigam 2018), or even the density perturbations (Kim et al. 1996) themselves. The configuration of primordial magnetic fields resulting from different magnetogenesis scenarios needs to be taken into account for the propagation of UHECRs (Wittor et al. 2017; Alves Batista et al. 2017), and could affect the magnetisation of the filaments in the cosmic web (Marinacci et al. 2015). For these reasons, the properties and evolution of primordial magnetic fields in a cosmological context have been studied by various authors (Vazza et al. 2014; Marinacci et al. 2015; Gheller et al. 2016).

On smaller scales, very little is known on how magnetic fields can affect the evolu-

tion of individual galaxies. Various interesting possibilities have been studied in the literature. Some of them are the capability of magnetic fields of destabilising spiral arms (Inoue & Yoshida 2019) or reducing the number of star formation sites in the ISM (Hennebelle & Iffrig 2014). They are also expected to affect the global dynamics of galaxies (Moss et al. 2007), and have been proposed as a mechanism to reduce angular momentum in galaxies (Sparke 1982), or drive inward gas flows in galactic bars (Moss et al. 2000; Beck et al. 2005). These latter effects are of particular interest, as they could significantly decrease the size of a galaxy, alter its morphology, and contribute to the formation of galactic bulges.

The theoretical uncertainty surrounding magnetogenesis is reflected in the considerable freedom for selecting the magnetic field initial configurations. Whenever strong enough primordial magnetic fields are employed - but still within the observational constrains described in Chapter 1 (Section 1.2.1), the amount of magnetic energy contained in the pristine gas becomes non-negligible, both inside and around galaxies, thus potentially altering galaxy properties (Dubois & Teyssier 2010; Marinacci & Vogelsberger 2016; Safarzadeh & Loeb 2019).

In this Chapter, I study the impact of primordial magnetic fields on the Milky Way-like galaxy NUT, re-simulated at high-resolution under various simple primordial magnetic configurations. I quantify how these simple primordial magnetic fields affect galaxies at high redshifts, assessing how significant the repercussions are, particularly in comparison with different stellar feedback prescriptions. I also explore how these effects translate into observational signatures, with an emphasis on morphological, dynamical, and stellar emission properties at $z = 2$. I argue that some of these changes are caused by magnetic braking, and discuss whether the encountered changes are still expected to be present in the case where galactic magnetic fields have a non-primordial origin.

In Section 6.2 I present the suite of simulations, and in Section 6.3 I introduce

the procedure used to measure many of the physical quantities. My main results are summarised in Section 6.4, where I first address the impact that primordial magnetic fields exert on the galaxy in Section 6.4.1. I finish this section by describing magnetic braking. Section 6.4.2 is devoted to the observational signature of these effects for galaxies at $z \sim 2$. I conclude the Chapter in Section 6.5.

6.2 Simulations

The simulations studied in this Chapter employ once again the NUT ICs (Section 2.4.3). Unless otherwise stated, they include the same overall physics as the runs described in Chapter 4 (Section 4.2). In the current Chapter, I vary the feedback prescription and the strength and orientation of the primordial seed.

To check that the divergence of the magnetic field remains under control even when the primordial seed has high amplitude, I display in Figure 6.2 the maximal (dashed) and average (solid) relative magnetic divergence for all cells in all simulations. It is clear that the curves representing the maximal divergence never exceed the 10% level.

All simulations use the MTT star formation sub-grid model (Section 2.3.1). While a subset of the runs in this Chapter does not include stellar feedback (*NoFb*; *NB20*, *NB12*, and *NB10*), the rest of them use the stellar feedback implementations described in Section 2.3. Either the mechanical model (Section 2.3.2.2: *Mech*; *MB20*, *MB14*, *MB13*, *MB12*, *MB10*), or the thermal model with radiation boosting (Section 2.3.2.1: *RdTh*; *RB20*, *RB12*, *RB10*).

Following common practice, my simulations include an initial magnetic seed in the form of an ab-initio, uniform, and homogeneous primordial magnetic field. I explore a range of simple configurations by changing the magnetic field strength and orienting it along one of the three axes of the simulated domain $\left(\vec{i}, \vec{j}, \vec{k}\right)$. Note that more complex seed fields are more realistic, however as a first step assessing their potential

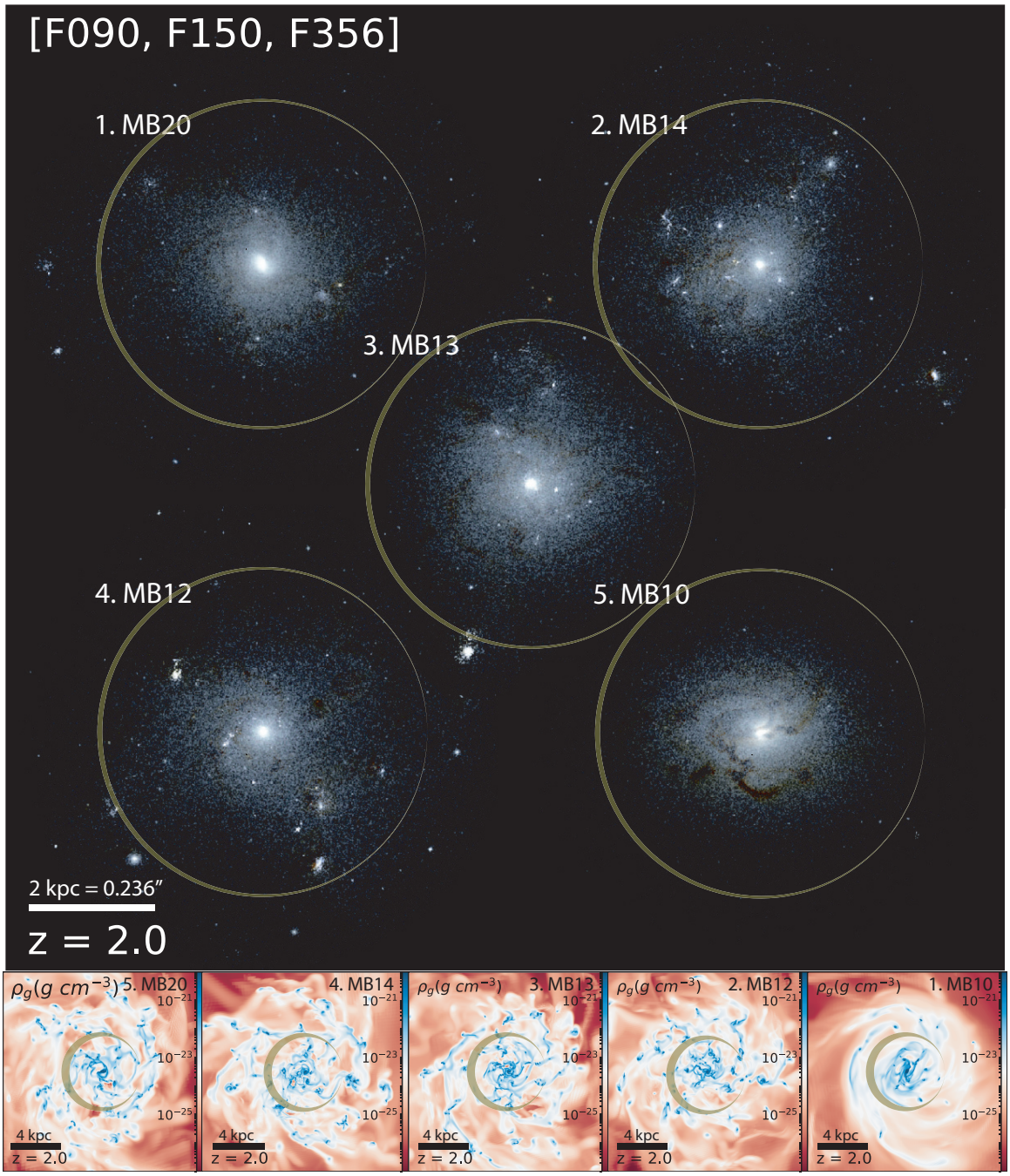

Figure 6.1: (Top) Rest-frame UVJ mock observations of the NUT galaxy at $z = 2$ through the $[F090W, F150W, F356W]$ *JWST*/NIRCam filters. B_0 is increased from *1.MB20* to *5.MB10*. Each panel is centred on the galaxy. I include translucent golden circles of radii 3 kpc, exactly centred on each galaxy to aid the visual comparison of their sizes (see also scale bar in Figure). (Bottom) Gas density projections ρ_g of the same galaxies, now with panels 16 kpc across.

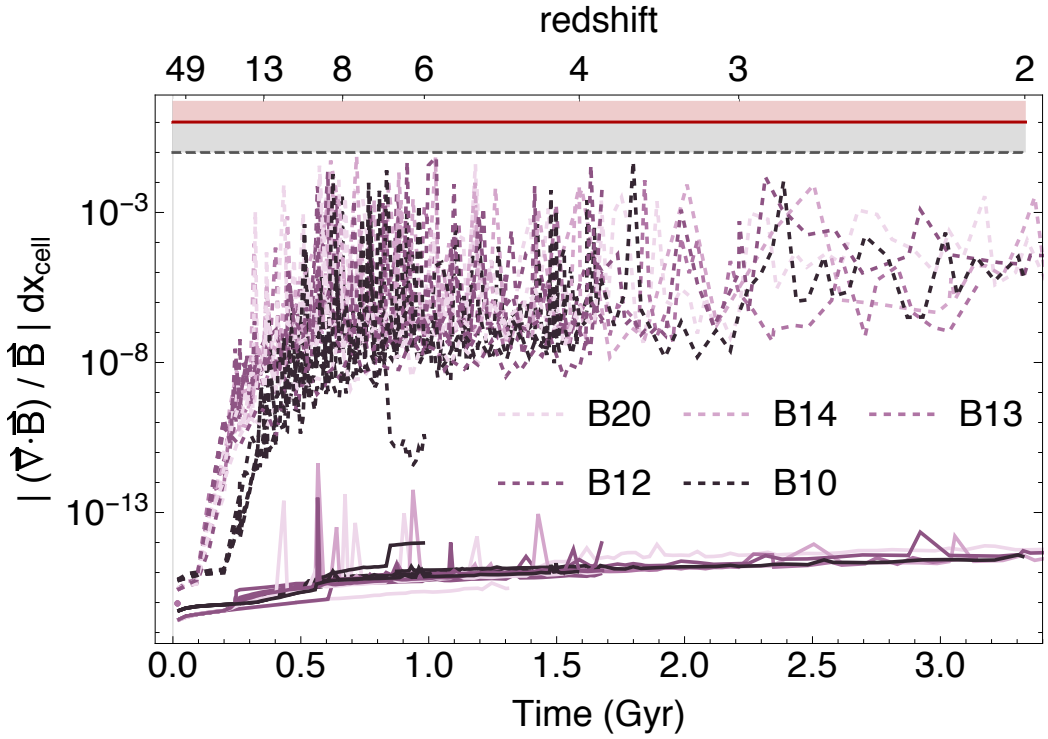

Figure 6.2: Evolution of the relative magnetic divergence in the entire numerical domain for all simulations. Dashed lines correspond to the maximal values, while solid lines represent their average. Red and gray lines display $|\vec{\nabla}\cdot\vec{B}/\vec{B}|\Delta x_{cell}$ =1 and 0.1 ratios. Note that maximal values never exceed 10% displaying the robustness of the CT scheme.

impact on galaxy formation and evolution, I restrict my work to these elementary cases. The entire set is listed in Table 6.1. More specifically, the comoving primordial magnetic field strength B_0 is varied across the range $3 \cdot 10^{-20} \leq B_0 \leq 3 \cdot 10^{-10}$ G. The *B20* simulations ($B_0 \sim 10^{-20}$ G) feature an extremely weak field that does not affect the gas dynamics at any point during the run. From a strength of *B14* ($B_0 \sim 10^{-14}$ G) upwards, magnetic fields in the simulated proto-galaxy reach values on the order of μG after the collapse of the primordial galactic density perturbation. These fields are then amplified further to magnetise the entire galaxy. The *B13* ($B_0 \sim 10^{-13}$) and *B12* ($B_0 \sim 10^{-12}$) runs display magnetisations in the entire galaxy on orders of $\sim 1 - 10\,\mu$G already from their collapse. The *B10* runs are the scenario with the highest field probed here: $B_0 \sim 10^{-10}$ G. This strength is below the current observational upper limit, but very close to it. Indeed, $B_0 = 3 \cdot 10^{-10}$ G is only 1 dex lower a magnetic energy density than the Planck+SPT upper limit. I also explore three different orientations in each of the *MB20*, *MB14*, *MB12*, and *MB10* models. Due to the large computational cost of these simulations, all y-oriented ($\vec{j}$) runs are evolved down to $z = 6$ only, the x-oriented ($\vec{i}$) ones to $z = 4$, and the z-oriented ones ($\vec{k}$) to $z = 2$. Therefore, the accretion phase ($13 > z > 4$) can be studied with at least two runs of different orientation for each value of the primordial magnetic field strength. It is during this phase that the environment is expected to have its largest impact on the evolution of the magnetism in the galaxy. To further examine how primordial magnetic fields and stellar feedback influence one another, I also run several identical simulations, now changing the sub-grid feedback model prescription. All simulations with stellar feedback other than *Mech* have primordial magnetic field aligned with the box z-axis ($\vec{k}$). Alternatively, all simulations with a non-z axis alignment employ the *Mech* feedback. Our fiducial models for stellar feedback, primordial magnetic field strength, and orientation, are respectively labelled *M* (*Mech*), *B12*, and $\vec{k}$, where the first letter indicates the feedback model, the *BX*

Table 6.1: Comoving primordial magnetic field strength and orientation $\vec{B}_0$, stellar feedback model, and gas mass percentage with average thermal to magnetic pressure ratio (β) lower than 10^3 in the galactic region at $z = 6$, for each run discussed in this Chapter.

Simulation	$\vec{B}_0$ (G)	Feedback	$M_{\rm gas}^{z=6}$ ($\beta < 10^3$)
MB20	$3 \cdot 10^{-20}\,\vec{k}$	Mech	0%
MB20y	$3 \cdot 10^{-20}\,\vec{j}$	Mech	0%
MB20x	$3 \cdot 10^{-20}\,\vec{i}$	Mech	0%
NB20	$3 \cdot 10^{-20}\,\vec{k}$	✗	0%
RB20	$3 \cdot 10^{-20}\,\vec{k}$	RdTh	0%
MB14	$3 \cdot 10^{-14}\,\vec{k}$	Mech	4%
MB14y	$3 \cdot 10^{-14}\,\vec{j}$	Mech	2%
MB14x	$3 \cdot 10^{-14}\,\vec{i}$	Mech	6%
MB13	$3 \cdot 10^{-13}\,\vec{k}$	Mech	26%
MB12	$3 \cdot 10^{-12}\,\vec{k}$	Mech	63%
MB12y	$3 \cdot 10^{-12}\,\vec{j}$	Mech	63%
MB12x	$3 \cdot 10^{-12}\,\vec{i}$	Mech	72%
NB12	$3 \cdot 10^{-12}\,\vec{k}$	✗	80%
RB12	$3 \cdot 10^{-12}\,\vec{k}$	RdTh	64%
MB10	$3 \cdot 10^{-10}\,\vec{k}$	Mech	99%
MB10y	$3 \cdot 10^{-10}\,\vec{j}$	Mech	99%
MB10x	$3 \cdot 10^{-10}\,\vec{i}$	Mech	100%
NB10	$3 \cdot 10^{-10}\,\vec{k}$	✗	100%
RB10	$3 \cdot 10^{-10}\,\vec{k}$	RdTh	99%

indicates the initial magnetic field strength, and the last letter provides the orientation of the primordial magnetic field.

6.3 Measuring the properties of the galaxy

In this Chapter, I focus once again on the galactic region, with the centre of galaxies computed as described in Section 2.4.4, and the radius of the region $r_{\rm gal} = 0.2\ r_{\rm vir}$, as was explained in Section 4.3.1.

6.3.1 Global galactic properties

The global galactic properties are measured within the entire galactic region, unless otherwise indicated. I employ time-averaged measurements to smooth out temporary perturbations and concentrate instead on the secular evolution. The process is as follows:

1. for each given redshift ($z = 10$, 8, 6, 4, and 2), I estimate a dynamical timescale $\tau_{\rm dyn}$, corresponding to the time required for a test particle to complete one full circular orbit with
$$v_{\rm circ}(r) = \sqrt{\frac{GM(r)}{r}}, \tag{6.1}$$
at radius $r = 0.2\ r_{\rm vir}$, where $M(r) = M_{\rm g}(r) + M_{\rm DM}(r) + M_*(r)$ represents the total mass contained within a spherical region of radius r. This is the sum of the gas M_g, dark matter $M_{\rm DM}$ and stellar M_* masses. For the duration of $\tau_{\rm dyn}$, the global properties of the galaxy should remain relatively unchanged, unless a disruptive event like a merger takes place.

2. I compute for all time outputs within an interval of duration $\tau_{\rm dyn}$ centred on a given redshift, the value of each quantity (with always a minimum of 3 outputs inside the interval).

3. For each quantity, its final value and error for the interval are chosen as the time-weighted median and interquartile range[1] respectively.

Note that by computing my results in this manner, the quoted error bars do not strictly reflect the uncertainty of the estimate, but also represent a measure of its time variation and non-secular changes during $\tau_{\rm dyn}$. In other words, error bars yield information about the variability of the measurement during this timescale. I have further examined projections of the gas and stellar densities for various data points

[1]If time-weighted averages and standard deviations are used of median and interquartile range, changes to results are negligible.

to check that those possessing large error bars are mostly associated with non-secular events of galaxy evolution, such as mergers.

6.3.2 Mock imaging with Sunset

I assess the observational impact of magnetic fields on the appearance of galaxies by studying synthetic face-on projections of them. These are generated with the SUNSET code following the procedure outlined in Section 2.5.1. In the measurements presented in this Chapter, I use all stellar particles in cubic boxes of size $(8\text{kpc})^3$ centred on the galaxy. I compute their emission in the corresponding *JWST* NIRcam filters[2] [F090W, F150W, F356W]. At $z = 2$, these filters correspond to UVJ rest-frame.

To generate the presented colour and concentration measurements, I compute the Petrosian radii $\mathcal{R}_P$ (Blanton et al. 2001) and Petrosian fluxes within 2 $\mathcal{R}_P$ for each image. Concentration parameters are defined as $C_{50} = r_{50}/r_{90}$ where r_X is the radius at which $X\%$ of the Petrosian flux is contained.

6.4 Results

Once the primordial magnetic field reaches the minimum threshold necessary to seed galactic dynamo processes, the specific value of the primordial strength becomes relatively unimportant. After the dynamo has amplified the field, no information regarding the initial conditions can be recovered. However, this is likely not the case for primordial magnetic fields with a much larger strength ($B_0 \gtrsim 10^{-14}$ G). Throughout the literature, studies consistently point out that such strong fields might have a non-negligible impact on the general population of galaxies and structure formation (Tsagas & Maartens 2000; Marinacci et al. 2015; Varalakshmi & Nigam 2017; Safarzadeh & Loeb 2019).

[2] https://jwst-docs.stsci.edu/display/JTI/NIRCam+Filters

The first process in the formation of our simulated galaxy is the collapse of the original density perturbation. Collapse folding and compressive motions alter the magnetic properties of the galaxy. Depending on the geometry, different arrangements between magnetic field lines and velocity flows will develop (Zeldovich 1983). Later cold gas accretion, the main supply of galaxy gas also is anisotropic. As such, one expects the geometry of cosmological structures to interact with the intrinsically vectorial cosmic magnetic fields. The effect of local relative orientation should also be more significant when the coherence scale of the cosmic magnetic field is comparable to the length scale of density perturbations like filaments and walls. I plan to study the effects of $\vec{B}_0$ orientation on galaxies and their environment in more detail in future work.

To better illustrate the implications of the primordial magnetic field strength, I show in Figure 6.3 the normalized triaxial dimensions of the baryonic ellipsoid of inertia of the galaxy (left panel), and its angular momentum (right panel). These are measured at the end of the collapse phase ($t_{\rm coll}$), as defined in Chapter 4. All galaxies collapse to similar shapes by $t_{\rm coll} \sim 0.34 - 0.36$ Gyr. Only for the most extreme primordial magnetic field (*B10* simulations) is the collapse slightly delayed to $t_{\rm coll} \sim 0.4$ Gyr. The smallest semi-axis of the galaxy is always the y-axis, closely followed by the x-axis. From $B_0 \gtrsim 10^{-12}$ G, evidence of the magnetic field influencing the shape becomes more pronounced.

Angular momenta display a similar behaviour to shapes. At $t_{\rm coll}$, the angular momentum of the galaxy is mainly contained in the x-y plane. Most normalised galaxy angular momenta yield $\vec{L}/{\rm mod}(\vec{L}) \sim (0.97, 0.22, 0.11)$. Temporary modifications of angular momentum induced by magnetic fields do not modify the post-collapse morphology (Sur et al. 2012). After collapse the angular momentum of the galaxy is dominated by cold accretion flows (Kimm et al. 2011; Tillson et al. 2015).

The most evident impact of the primordial magnetic fields is found when increas-

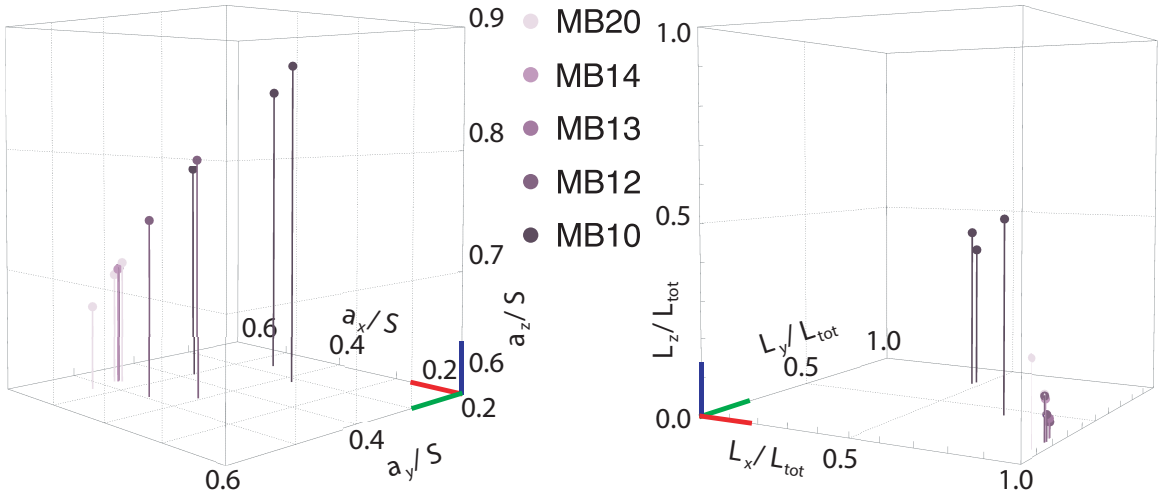

Figure 6.3: Geometric properties of the galaxy at collapse ($t_{\rm coll}$) for different primordial magnetic strengths (represented by the colours indicated in the legend). (Left) Normalized baryonic ellipsoid of inertia axes ($S = @\sqrt{a_x^2 + a_y^2 + a_z^2}$). (Right) Normalized angular momenta. As magnetisation increases, the shape of the galaxy elongates in the z-axis direction. Employed coordinates align the simulated box axes. The RGB coloured trihedra portray the direction of increase along each of the corresponding intermediate, minor, major (left) and xyz (right) axes. For the two strongest B_0 probed (*MB12* and *MB10*), magnetic fields affect the process of collapse.

ing their strength B_0. As the *MB20* simulations have negligible magnetic energy compared with all other components by at least 15 orders of magnitude, I employ them as a reference of the non-magnetised case. Increasing B_0 up to 10^{-14} G (*MB14* runs), the effect of magnetic fields remains marginal with collapse only leading to a saturation in some parts of the galaxy. As a result, only insignificant deviations with respect to the *MB20* runs are measured. However, as the magnetic field amplitude is further increased, β becomes low for a larger fraction of the galaxy, and amplification through simple compression is reduced. *MB13* starts to display a small amount of variation in galaxy angular momentum, and both *MB12* and *MB10* have magnetic fields strong enough to delay the collapse process and alter the galaxy's shape.

Once the galaxy has collapsed, its growth will be mainly governed by cold gas supplied by cosmic filaments. A higher strength of the primordial magnetic fields implies that the magnetic energy supplied by primordial gas accretion could be non-

negligible in comparison with that in the ISM of the galaxy, especially given that dynamically important magnetic fields can back-react on the turbulent dynamo and reduce magnetic growth rates. In this regime, one suspects that not only the strength of the primordial magnetic field will affect the properties of galaxies, but also its local orientation and its spatial coherence length.

In the light of this discussion and the measured mass fraction of the galactic region with significant magnetisation (Table 6.1), I expect my runs to behave as follows: *B20* will display virtually no magnetic effect; *B14* will show only small deviations from *B20*. *B13* will constitute an intermediate case where the effect of magnetic fields start to manifest. Finally, *B12* and *B10* already displayed a clear impact at the end of the collapse phase, so will show the largest departure from *B20*.

Section 6.4.1 is devoted to effects on the global morphological and dynamical properties of galaxies and explores the potential influence of magnetic braking. Section 6.4.2 discusses how the presence of primordial magnetic fields at high redshifts would manifest itself in simple observations of galaxies in UVJ rest-frame.

6.4.1 Impact on global galactic properties

Morphology

The global morphology of a spiral galaxy can be defined through its disk half-thickness h_s and radial scale R_s. In order to understand whether primordial magnetic fields have an impact on the morphology of my simulated galaxies, I thus review how these two parameters change as a function of primordial field configuration. The h_s and R_s scales are computed fitting exponential density profiles, independently for both the gaseous and stellar components. Appendix A, Section A.2, describes this fitting procedure and showcases particular examples. I display the variation of the gas-vs-stellar radial scale (left panels) and half-thickness (right panels) in Figure 6.4, as a function of increasing primordial magnetic field strength. Each row of panels

corresponds to subsequently decreasing redshifts, as indicated in each panel. Different symbols represent runs with different feedback prescriptions, and the strength of the primordial magnetic field in each run is indicated by the colour of the points, becoming darker as the strength of the magnetic field is increased. Data points corresponding to runs with a $\hat{k}$-oriented primordial magnetic field are marked with a thicker countour line and are the only ones available down to $z = 2$. In Figure 6.4 dashed lines correspond to equal scale lengths for the stellar and gaseous components.

While expecting magnetic fields to induce changes in the morphology of the gaseous component is quite natural, given the absence of a direct interaction between the stellar component and magnetic field one would anticipate this latter to be, by-and large unafected. However, it is still possible that the magnetic fields influence the stellar component indirectly by affecting the process of star formation, especially at high redshift, where the stellar population is relatively young.

The two topmost panels of Figure 6.4 correspond to the impact of different primordial magnetic fields on the galaxy morphology shortly after collapse. At this stage, given the stellar particle resolution of the simulations the stellar component is not resolved enough to accurately determine the galaxy's morphology, and thus it is not displayed. Similarly, due to the absence of a well-defined rotationally-supported disk and an irregular shape of the galaxy at this redshift, h_s is a measure of the galaxy scale length along its main rotation axis. From the Figure, one can clearly observe the trend that an increase of strength of the primordial field leads to further support against collapse, thus yielding larger gaseous scale lengths. Both R_s and h_s are nearly doubled when comparing the strongest B_0 run, *MB10*, with *MB20*. In the absence of feedback (square symbols), the effects of B_0 less pronounced. The *RdTh* feedback model (diamonds) features a radial extension of the galaxy, but at the expense of a reduction in its thickness.

During the accretion phase, opposing trends to that obtained immediately after

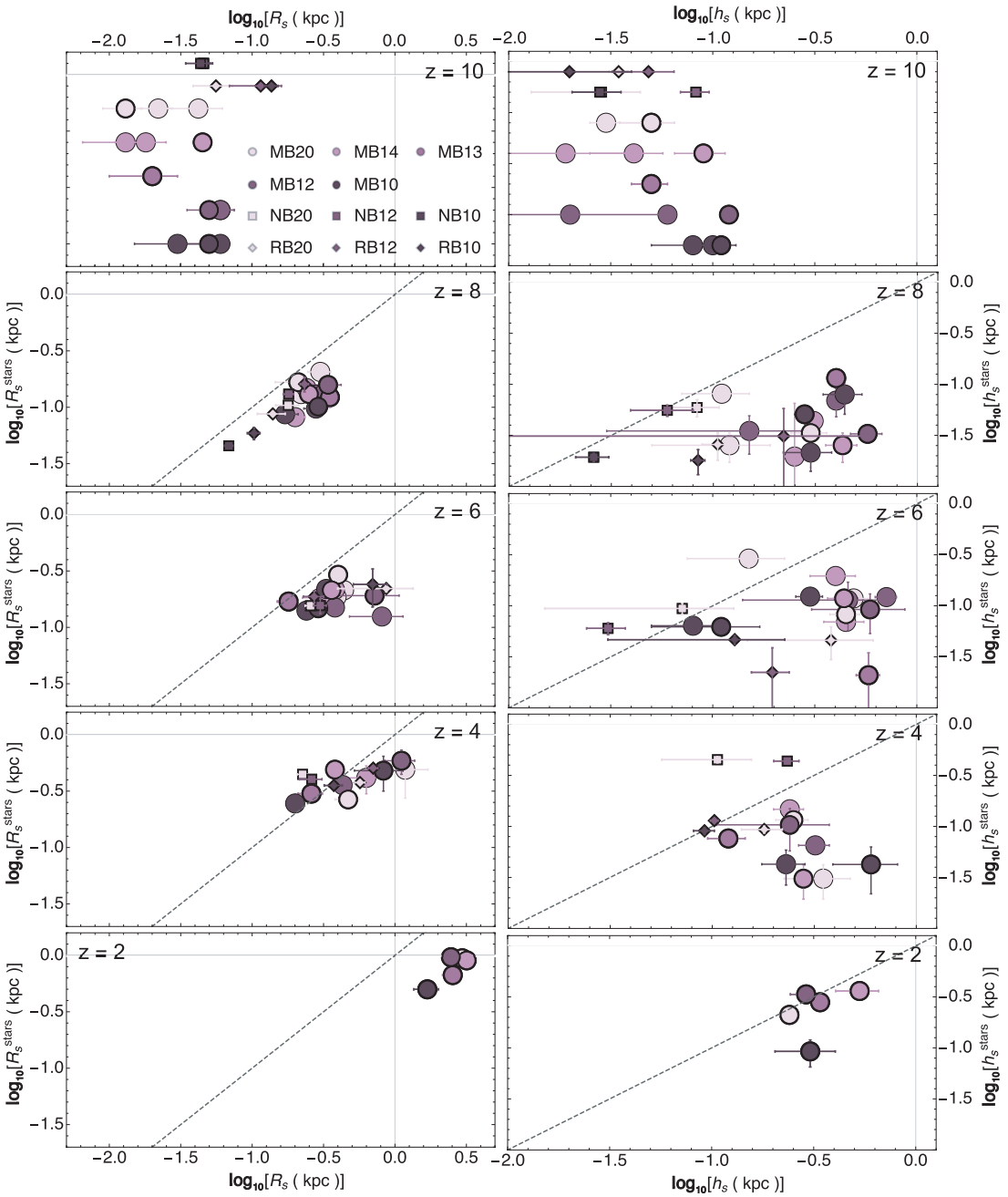

Figure 6.4: Variation of the galaxy stellar radial scale $R_s^{\rm stars}$ vs. gas radial scale R_s (left column) and stellar half-thickness $h_s^{\rm stars}$ vs. gas half-thickness h_s (right column) as a function of primordial magnetic field strength. The field strength is represented by the colouring of data points, with B_0 increasing as the shades of purple darken. Circles (*Mech*), diamonds (*RdTh*), and squares (*NoFb*) correspond to different feedback prescriptions. Data points associated to *Mech* runs with $\vec{B}_0$ oriented along the box $\vec{k}$ direction are highlighted by a thicker countour line. Finally, panels from top to bottom display decreasing redshifts: $z = 10$, 8, 6, 4, and 2. Note that for $z = 10$, neither $R_s^{\rm stars}$ nor $h_s^{\rm stars}$ are shown due to the absence of a significant galactic stellar component.

collapse emerge. R_s shifts from increasing with B_0 to decreasing. A similar behaviour is observed for the stellar component $R_s^{\rm stars}$. This behaviour starts to manifest at $z = 8$ and is strongly asserted by $z = 2$, well after the end of the accretion phase and once the galaxy acquires a fully developed rotationally-supported gas disk. Note that this can be somewhat difficult to spot, as some runs display large deviations from the bulk of the distribution of data points with the same B_0. These display significantly larger logarithmic error bars, both in radial and thickness properties and are mostly associated with merger events temporarily disturbing the morphological appearance of the galaxies. Examples are *RB20*, *RB10*, *MB12*, and *MB12y* at $z = 6$, or *MB12* and *MB20x* at $z = 4$. At $z = 2$, the radial extension of the gas disk is halved from 3 kpc in the absence of significant magnetic fields (run *MB20*), to 1.5 kpc for the highest B_0 (*MB10*). Interestingly, a larger relative reduction of this scale is found for the stellar component, which might be attributed to a more centrally compact distribution of the star formation as B_0 is increased. Once again, in the absence of feedback, B_0 seems to not alter the radial scales significantly between *NB20* and *NB12* at any redshift $z \lesssim 4$.

The effect of B_0 on the half-thickness is hard to establish before $z \sim 10$ due to the limited spatial resolution of my numerical simulations. During the accretion phase, significant turbulence is driven by accretion-related processes (Elmegreen & Burkert 2010; Klessen & Hennebelle 2010). These processes determine the half-thickness of the gas component, establishing it around $h_s \sim 300 - 400$ pc, albeit with a large spread, especially at high redshift ($z > 4$). This leads to a lack of sensitivity of h_s to B_0. If any thing, intermediate primordial magnetic fields (*B14*, *B13*, *B12*) seem to yield thicker h_s. As time progresses, all runs but *MB10* seem to converge towards equality between h_s and $h_s^{\rm stars}$. By $z = 2$, the presence of dynamically important magnetic fields leads to an extra thickening of the rotationally-supported gaseous disk of about 100 pc as compared to *MB20*, except *MB10*. I attribute the reduction of $h_s^{\rm stars}$ in

MB10 to the inclusion of magnetic pressure in my star formation algorithm. Indeed, this requires star forming clumps to reach higher masses before they overcome the additional pressure generated by magnetic energy (Section 2.3.1). This accumulation of gas is more likely to take place closer to the disk mid-plane, where the gas density is higher. Finally, there exists a more significant scatter across the half-thickness panels than across the radial scale ones. A more in-depth analysis of the influence of magnetic fields on the disk thickness might reveal further interesting properties, such as disk flaring, but this is beyond the scope of the current work addressing global instead of spatially resolved galaxy properties.

While the magnetic fields at play in my simulations are of primordial nature, any impact on the half-thickness arises from galactic magnetic pressure, and therefore is expected to also occur when magnetisation is caused by other mechanisms (e.g. turbulent dynamo or from compact sources feedback). Whether this is the case for the radial scale as well is unclear. The impact on this quantity is likely related on how magnetic fields affect the angular momentum of the galaxy, an issue which I address in the next Section.

Dynamics

The presence of magnetic fields in the ISM has been reported to generate various changes on its dynamics: from turbulence modes and scales (Kinney et al. 2002; Schekochihin et al. 2004; Zamora-Avilés et al. 2018), to amount of gas collapsing into molecular clouds and star forming regions (Hennebelle & Chabrier 2011; Hull et al. 2017), and the mass fraction in the multiple ISM phases (Villagran & Gazol 2018). Even on larger scales, magnetic fields could influence dynamical properties such as the gas rotational velocity. Through magnetic braking and angular momentum transport, magnetic fields could reduce galactic rotation and establish inward gas flows (Sparke 1982; Beck 2015). Alternatively, Ruiz-Granados et al. (2010) suggest that magnetic

fields could boost galactic circular velocities at large radii.

I address in this section how magnetic fields influence the global dynamical properties of my simulated galaxy. I review the non-coherent, small-scale dynamical changes focusing on a simple parameter to represent turbulence: the total turbulent velocity dispersion $\sigma_{\rm rms}$. It is computed in a spherical coordinate system (r, θ, ϕ), co-moving with the galaxy, as the root of the sum of the squared mass-weighted average deviations of each velocity component from the mass-weighted average velocity value in shells of radius r.

Similarly, to study changes on the dynamics at galactic scales, I measure the rotation of the galaxy in terms of the spin parameter. This parameter indicates the degree of rotational support of a given component (stars or gas). It was briefly introduced in Section 4.3.2 but I now describe it in more detail. For each component i (either gas or stars), it is defined

$$\lambda^{i}_{\rm rot} = \frac{L_i}{\sqrt{2} r M(r) v_{\rm circ}(r)} \simeq \frac{L_i E_B^{1/2}}{G M(r)^{5/2}}, \tag{6.2}$$

following Bullock et al. (2000). In equation (6.2) r is the radius of the entire galactic region ($0.2 r_{\rm vir}$), L_i the angular momentum of the i component in the region, E_B the binding energy, G the gravitational constant, and $M(r)$ the total mass enclosed in the region.

As previously done for scale lengths, I plot in Figure 6.5 the evolution of these quantities for the gas and star components, starting shortly after collapse through the entirety of the accretion phase down to $z = 2$. I separate the dynamics of each component by representing $\sigma_{\rm rms}$ vs $\lambda_{\rm rot}$ (left column) and $\sigma^{\rm stars}_{\rm rms}$ vs $\lambda^{\rm stars}_{\rm rot}$ (right column) for gas and stars respectively.

For the gaseous component, stronger primordial fields cause a clear and significant reduction of $\lambda_{\rm rot}$ especially for $z < 8$. This can amount up to an absolute decrease of

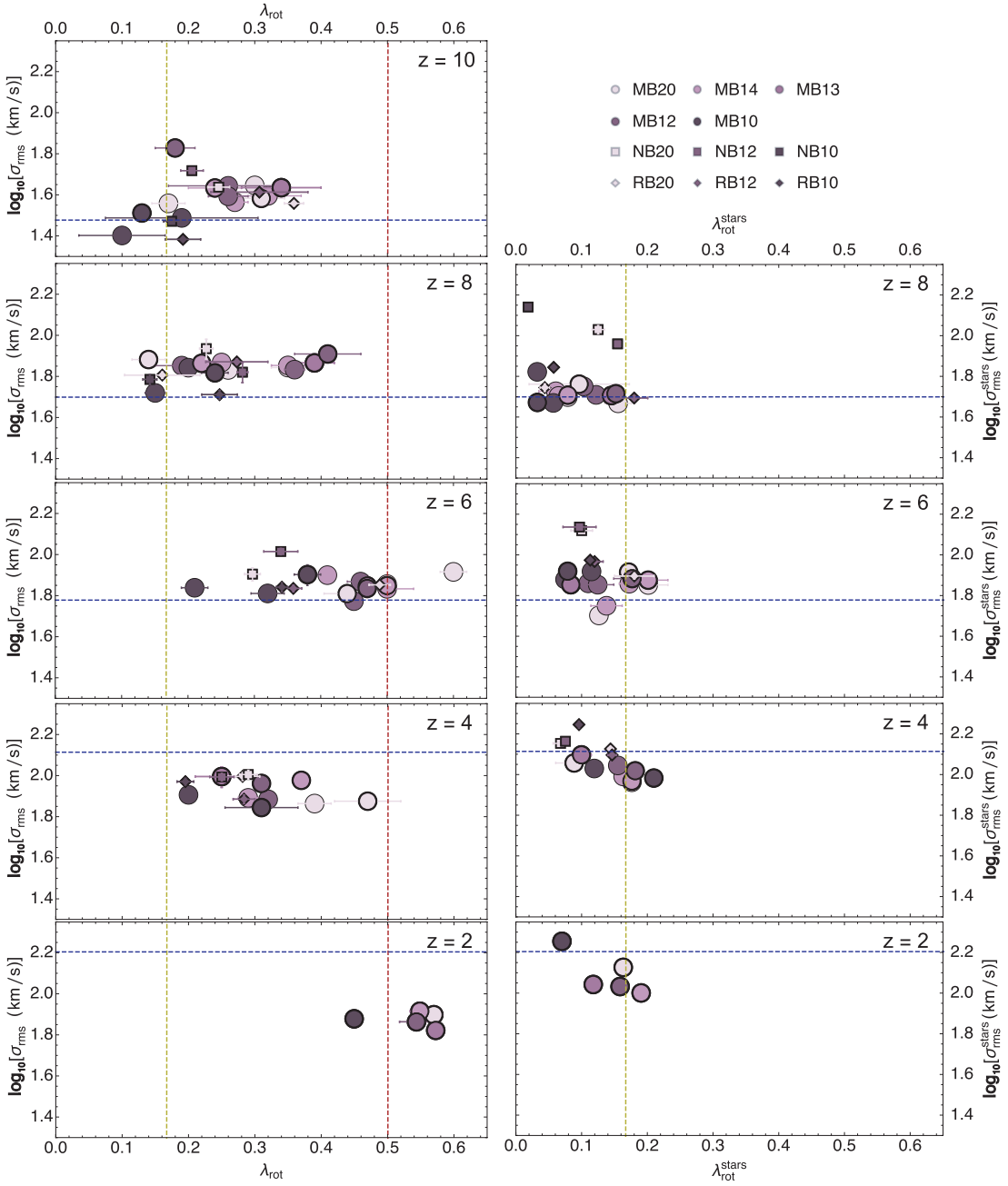

Figure 6.5: Variations of the gas ($\sigma_{\rm rms}$ vs $\lambda_{\rm rot}$; left column) and stellar ($\sigma_{\rm rms}^{\rm stars}$ vs $\lambda_{\rm rot}^{\rm stars}$; right column) dynamical properties of the galaxy when increasing the primordial magnetic field B_0, as represented by increasingly darker shades of purple. Data points legend (shown at the top right of the figure) is as for Figure 6.4. Stellar component quantities are not shown for $z = 10$ due to the lack of enough stellar particles in the galaxy to perform a robust measurement. The horizontal line corresponds to the circular velocity of the galaxy at a given redshift. The vertical lines demarcate rotational support (red) and a third of this value (olive).

0.2. This behaviour appears quite independent of the stellar feedback model, but in its absence (square symbols), the reduction is not evident. At $z = 2$, the spin parameter is stabilised well above the minimal threshold for rotational support ($\lambda_{\rm rot} \gtrsim 0.5$, red dashed vertical line) and is only slightly changed by B_0, except for *MB10*, which exhibits significantly lower support from rotation.

During the accretion phase ($z \gtrsim 4$), there is no evidence to support that changing the stellar feedback prescription, let alone the magnetic field, has a significant impact on $\sigma_{\rm rms}$. This is somewhat expected: turbulence during this phase is dominated by accretion related processes, be it through direct energy injection (Klessen & Hennebelle 2010), gravitational instabilities (Elmegreen & Burkert 2010), or the regulation of stellar feedback by infalling gas (Hopkins et al. 2013). I also find that none of the merger events that made clear alterations in the morphological properties have a significant imprint on the dynamics, neither by separating the values from the distribution nor by stretching the error bars.

As the support of the stellar component is purely dynamic, and once heated this collisionless fluid cannot cool, it leads to a lower level of coherent rotation than the gas, hence the lower spin parameters $\lambda_{\rm rot}^{\rm stars}$. Note that this value would be much higher (and comparable to the gas $\lambda_{\rm rot}$) if one considered exclusively the young ($\lesssim 100$ Myr) stellar population. This $\lambda_{\rm rot}^{\rm stars}$ remains close to the vertical olive dashed line on Figure 6.5, which indicates a value corresponding to a third of the minimal threshold for rotational support. The stellar spin parameter also manifests albeit to a degree some reduction as B_0 increases. This follows from the reduction of the spin parameter of the gas component, to which it couples through the star formation process. Stellar spin parameters are affected to some degree by the feedback prescription selected, but changes appear stochastic.

Interestingly, unlike $\sigma_{\rm rms}$, $\sigma_{\rm rms}^{\rm stars}$ displays a clear trend as magnetisation increases. This is because $\sigma_{\rm rms}^{\rm stars}$ is more directly linked to $\lambda_{\rm rot}^{\rm stars}$ as the collosionless fluid can-

not cool: if the coherent rotation of the stellar component is reduced, its turbulent component has to increase correspondingly in order to maintain dynamical support against gravity. This anti-correlation can best be observed in Figure 6.5 at $z \lesssim 4$. $\sigma_{\rm rms}^{\rm stars}$ also receives a substantial contribution from the stellar feedback prescription (or its absence). Both *RdTh* and *NoFb* runs display higher $\sigma_{\rm rms}^{\rm stars}$ than *Mech* runs, no matter the increase caused by B_0.

The effects of magnetic fields on gas turbulence after the accretion phase are likely to remain present even in the case when these are not of primordial origin. On the other hand, changes in the spin parameter will depend on whether the mechanism causing this loss of angular momentum can be fostered by magnetic fields injected on much smaller scales. I now proceed to review this process in more detail.

The observed reduction in the spin parameter of the gaseous component as B_0 increases implies a transfer of the angular momentum present in the gas. In the absence of this support, the galaxy radially compresses, hence the measured decrease of R_s. To better quantify this, in Figure 6.6 I plot the rotation curves of the gas in the galaxy at $z = 4$ (top panel) and $z = 2$ (bottom panel). At $z = 4$ rotational support of the disk is not completely established yet (see Figure 6.5, left column, third panel from top). $\sigma_{\rm rms}(r)$ seems to follow the circular velocity of the gas $v_{\rm circ,gas}$ (not shown) on Figure 6.6 and shifts to the circular velocity of the dark matter $v_{\rm circ,DM}$ (not shown) at approximately $3 - 4\,R_s$. This is in approximate agreement with the radial distance at which the observed total mass distribution profile is found to be truncated (Barteldrees & Dettmar 1994). As B_0 increases, the transition happens at progressively smaller radii. Visual inspection of the galaxies does not highlight any particular features at $3 - 4\,R_s$, which points towards a continuum process.

I plot on the bottom panel Figure 6.6 the same rotation curves at $z = 2$, after the observed compression of the galaxy in MB10 has taken place. These rotation curves are in general agreement with observations of massive disk galaxies at $z = 2$.

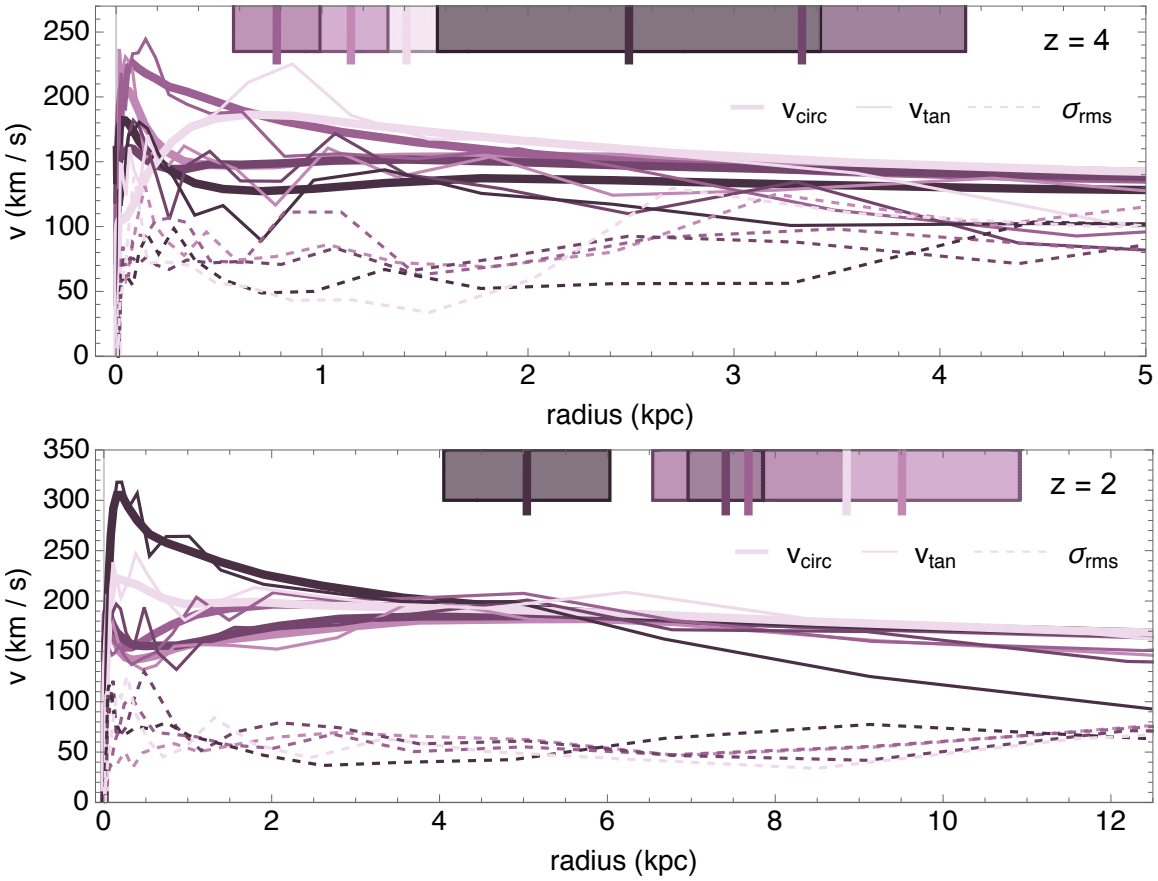

Figure 6.6: Rotation curves for the gaseous component of the galaxy at $z = 4$ and $z = 2$. Solid thick lines correspond to circular velocities $v_{\rm circ}(r)$ (eq. 6.1), solid thin lines correspond to the tangential velocity $v_{\rm tan}(r)$, and dashed lines to the total turbulent velocity dispersion $\sigma_{\rm rms}(r)$. Different colours display runs with increasing B_0: MB20, MB14, MB13, MB12, and **MB10** from the lightest to darkest purple. Vertical marks at the top of the plot panels correspond to $3R_s$, with shaded bands indicating associated errors (see text for detail).

My simulations match typical rotation velocities $v_{\rm tan} \sim 150 - 200$ km/s (Sofue & Rubin 2001) and turbulent support $\sigma/v_{\rm tan} \sim 0.1 - 0.3$, with $\sigma \sim 30 - 80$ km/s (Erb et al. 2004; Cresci et al. 2009). *MB10* displays a much higher central peak velocity than the other runs, dominated by a more concentrated stellar component. At these redshifts, increasing B_0 enlarges the deviation of $v_{\rm tan}$ from $v_{\rm circ}$ at distances $r \gtrsim 3\ R_s$. Rotation curves appear flat at the largest distances displayed in the plot, but progressively become more inclined as B_0 is increased. *MB10* resembles a decreasing rotation curve, enhanced by the significant central peak of $v_{\rm tan}$. Recent observations by Genzel et al. (2017) found decreasing rotation curves at $z = 2$, which could also be interpreted as evidence for a lack of dark matter. According to my findings, decreasing rotation curves could be the result of magnetic braking in the outskirts of galaxies, which naturally arises in MHD simulations of ΛCDM galaxies with high values of B_0. The steepness of my rotation curves in the inner region also increases with the light concentration of the galaxies (see Figure 6.12), in accordance with observations (Swaters et al. 2009). This supports the argument that magnetic fields do not abruptly alter the evolution of spiral galaxies, but rather lead to higher central concentrations by some process gradually driving gas mass inward.

Magnetic braking in spiral galaxies can potentially operate through complementary channels. One possibility is the direct outward transport of angular momentum by toroidal Lorentz stresses. In this case, the radial and zenithal field lines are stretched azimuthally, and unbend at larger radii where the pressure is lower. Another possibility is radial and/or vertical deflection of the orbital gas trajectories. Finally, radial deceleration of inflows could reduce the angular momentum supply, and inward magnetic acceleration of gas in the galaxy by zenithal magnetic lines would lead to turbulent dissipation of angular momentum.

In order to check for magnetic Lorentz forces, I review the forces on gas orbits. I restrict myself to an analysis of the most direct forms of this force. First, I look

at the toroidal component of the Lorentz force, and a second is looking at the radial acceleration of gas by this same force. I compute the radial and toroidal components of the Lorentz force F_L on a disk of gas in cylindrical coordinate frame (r, ϕ, z), where the z dimension is aligned with the total angular momentum of the galaxy

$$F_{L,r} = \vec{F_L} \cdot \hat{r} = \left[\left(\vec{B} \cdot \vec{\nabla} \right) \vec{B} - \frac{1}{2} \vec{\nabla B}^2 \right] \cdot \hat{r} = \left(B_r \overset{(1)}{\partial_r B_r} + \frac{B_\phi}{r} \overset{(2)}{\partial_\phi B_r} + B_z \overset{(3)}{\partial_z B_r} - \frac{1}{r} \overset{(4)}{B_\phi B_\phi} \right) - \frac{1}{2r} \overset{(5)}{\partial_r B^2}, \tag{6.3}$$

$$F_{L,\phi} = \vec{F_L} \cdot \hat{\phi} = \left[\left(\vec{B} \cdot \vec{\nabla} \right) \vec{B} - \frac{1}{2} \vec{\nabla B}^2 \right] \cdot \hat{\phi} = \left(B_r \overset{(1)}{\partial_r B_\phi} + \frac{B_\phi}{r} \overset{(2)}{\partial_\phi B_\phi} + B_z \overset{(3)}{\partial_z B_\phi} + \frac{1}{r} \overset{(4)}{B_r B_\phi} \right) - \frac{1}{2r} \overset{(5)}{\partial_\phi B^2}, \tag{6.4}$$

both expressed in rational units. I compute these quantities term by term for a region centred on the galaxy, aligning the toroidal plane of coordinates with the rotating gas disk. All velocities are taken relative to the frame of the galaxy (i.e. removing its bulk motion). Gradients are computed through central differences of neighbouring cells, employing the complete structure of the AMR grid. In Figure 6.7, I show close views of the galaxy at $z = 2$ which are density-weighted maps of $a_{\mathrm{mag},\phi} = F_{L,\phi}/\rho_g$, $a_{\mathrm{mag,r}} = F_{L,r}/\rho_g$ obtained by filtering forces in the galactic disk ($z < |500\mathrm{pc}|$) for my two highest magnetisation models *MB12* and *MB10*. A positive contribution of $a_{\mathrm{mag},\phi}$ leads to magnetic orbital acceleration (shown in blue), while a negative contribution leads to magnetic braking (shown in red). When considering the overall spatial distribution of this toroidal acceleration, both magnetic orbital braking and acceleration primarily occur for gas density structures mainly located in the outskirts of the galaxy (see sub-panels of Figure 6.7). Dipolar acceleration and deceleration structures surround galaxy-scale magnetic field lines and magnetic pressure gradients. These regions coincide with gas spiral arms, which I find also double as magnetic arms. This strong correlation is a behaviour often found in ideal MHD simulations

(Pakmor et al. 2014; Mocz et al. 2016; Butsky et al. 2017), which struggle to explain the observed displacement between magnetic and density spiral arms (Chamandy et al. 2014; Mulcahy et al. 2017). Interestingly, braking and inward forces marginally dominate magnetic stresses in the dense gas in the inner parts of the galaxy ($r < 2$ kpc), particularly for *MB10*. Inflows onto the galaxy also present magnetic stresses, dominated by an outward force (with contributions from all terms in equation (6.3)). I plot the radial magnetic forces for the inflowing material (filtered as $v_{\rm gas,r} < 0$) for the same two models (*MB12* and *MB10*) at various redshifts in Figure 6.8. The dominance of the outward magnetic force (in green) over its inward counterpart leads to overall less angular momentum supply to the outskirts of the galaxy, facilitating accretion and inward gas transport. For lower B_0 values I find the coherence length of magnetic acceleration structures to be reduced. Magnetic pressure (term 5 in eq. (6.3) and (6.4)) tends to dominate over magnetic acceleration in the entirety of the galactic region, with a density-weighted average magnetic acceleration on orders of $0.01 - 1$ km s^{-1}Myr^{-1}. However, more significant coherent acceleration (or braking) can appear locally, reaching values of up to several 10 km s^{-1}Myr^{-1} in *MB12* and *MB10*. I also find that the global magnetic acceleration roughly scales as $a_{\rm Brake} \propto B_0$, becoming only significant for primordial magnetic fields $B_0 \gtrsim 10^{-13}$ G. The turbulence and stresses induced by opposing acceleration and braking components allow angular momentum to be transported outward. In the case of the radial component of the magnetic force, the inward component (shown in purple) within the disk predominates through contributions from terms (1), (3), (4). On the other hand, the outward component (shown in green) dominates in the outskirts, mostly by the contribution from magnetic pressure.

To investigate more explicitly the dominance of braking forces (red coloured regions) in the galaxy and the galactic region, and study their dynamic importance, I perform a rough order of magnitude estimate of the magnetic spin-down of the

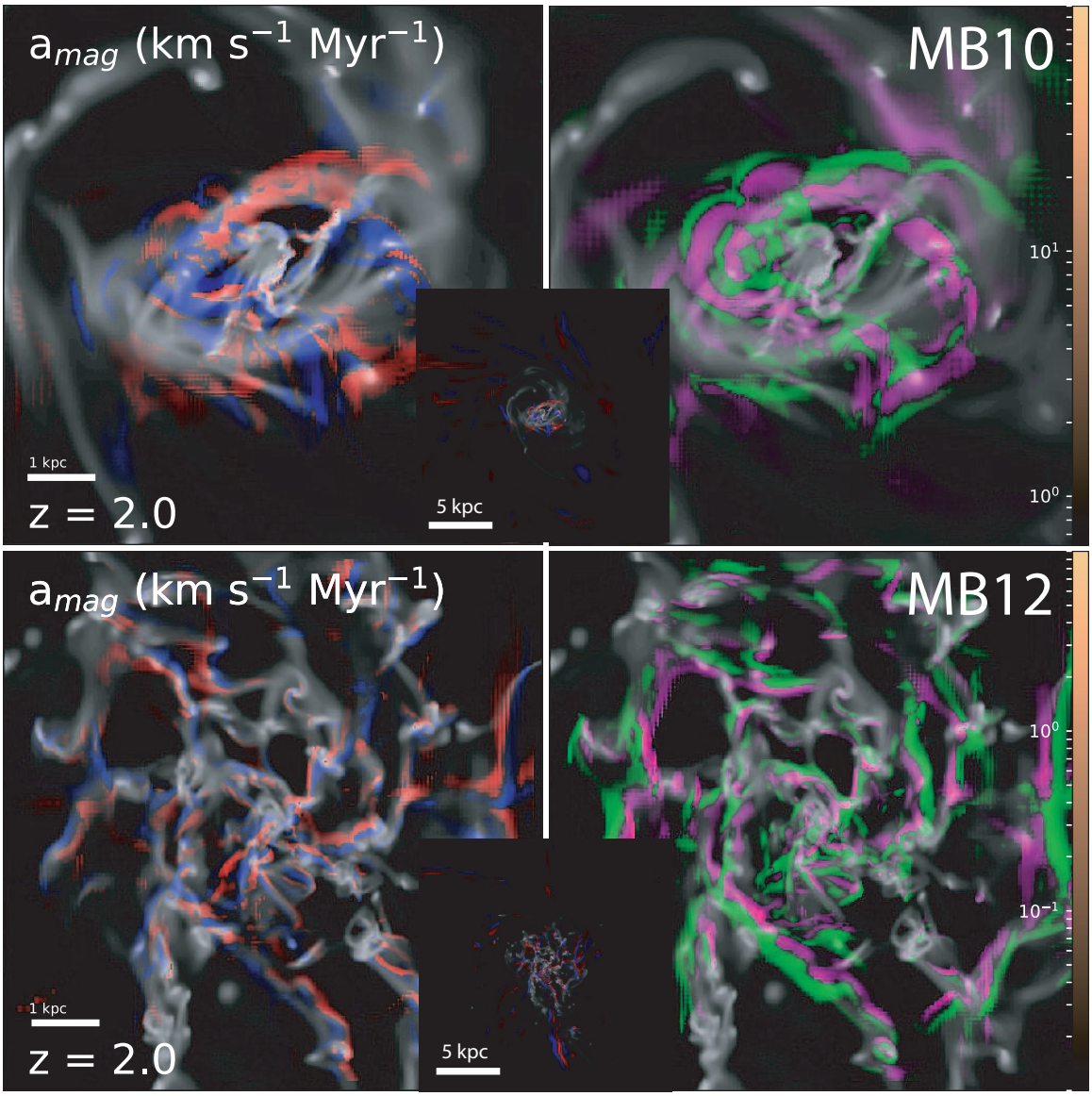

Figure 6.7: Magnetic acceleration due to toroidal (left column) and radial forces (right column) for the *MB10* (top row) and *MB12* (bottom row) runs. Colour scales represent magnetic orbital braking (red), magnetic orbital acceleration (blue), inward magnetic acceleration (magenta), and outward acceleration (green). Gas density is overplotted in gray scales. Coherent magnetic structures are identified on kpc scales.

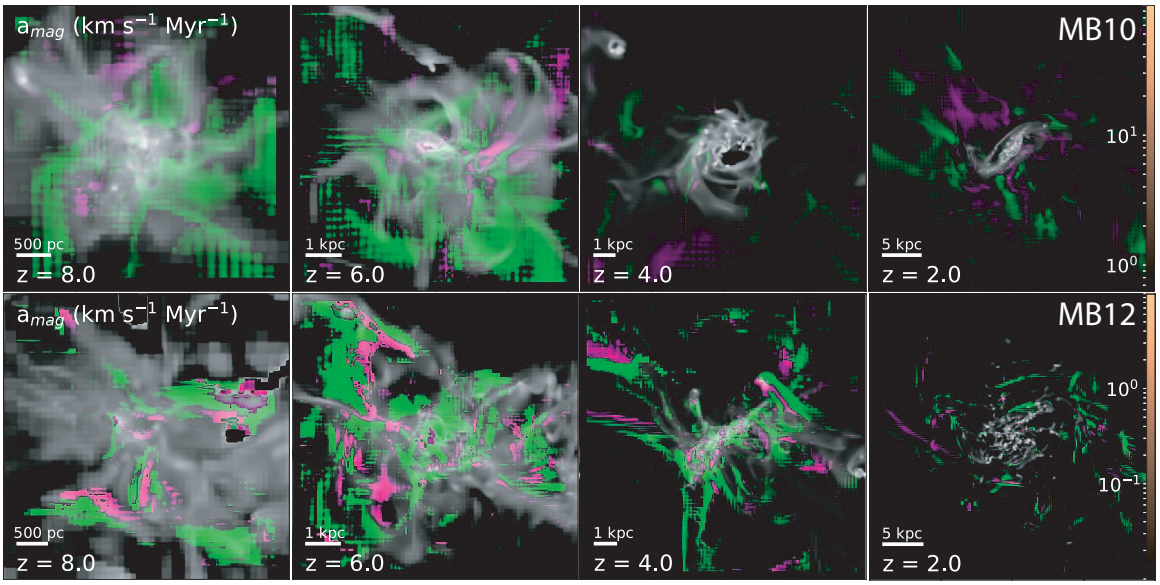

Figure 6.8: (Top row) Radial acceleration for inflowing ($v_r < 0$) gas in the *MB10* run. (Bottom row) Same as top row, but for the *MB12* run. Colour scales represent inward magnetic acceleration (magenta), and outward acceleration (green). Infalling gas inflows appear to be dominated by magnetic forces working against accretion and the toroidal rotation of the galaxy. As in Figure 6.7, the projected gas density is overplotted as a gray scale.

galactic angular momentum L_z in the inner galactic region ($r < 0.1\ r_{\rm vir}$)

$$S_D^{\rm in} = \frac{d_t L_z}{L_z}\tau_{\rm dyn} = \frac{\sum_{i=0r_{\rm vir}}^{0.1r_{\rm vir}} r_i\ \rho_{g,i}\ V_{\rm cell,\ i}\ a_{\phi,i}}{\sum_{i=0r_{\rm vir}}^{0.1r_{\rm vir}} r_i\ \rho_{g,i}\ V_{\rm cell,\ i}\ v_{\phi,i}}\tau_{\rm dyn} \tag{6.5}$$

and in the outer galactic region ($0.1\ r_{\rm vir} < r < 0.2\ r_{\rm vir}$)

$$S_D^{\rm out} = \frac{d_t L_z}{L_z}\tau_{\rm dyn} = \frac{\sum_{i=0.1r_{\rm vir}}^{0.2r_{\rm vir}} r_i\ \rho_{g,i}\ V_{\rm cell,\ i}\ a_{\phi,i}}{\sum_{i=0.1r_{\rm vir}}^{0.2r_{\rm vir}} r_i\ \rho_{g,i}\ V_{\rm cell,\ i}\ v_{\phi,i}}\tau_{\rm dyn} \tag{6.6}$$

where r_i is the distance between a cell i and the centre of the region, $\rho_{g,i}$ is the gas density of the cell, $V_{\rm cell,\ i}$ corresponds to its volume, $v_{\phi,i}$ is the toroidal velocity of the gas in the cell around the galactic rotation axis, and $\tau_{\rm dyn}$ is the dynamical time of the galaxy at a given time computed as indicated in Section 6.3. The measured spin-down parameters correspond exclusively to magnetic stresses and therefore fail to capture the contribution to the galactic angular momentum from outflows, inflows, and other forces of different nature within the galaxy. Bearing these caveats in mind, I show in Figure 6.9 the resulting spin-down parameters (inner and outer galactic region in the left and right panels, respectively).

The figure indicates that for the *MB12* and especially the *MB10* runs, magnetic braking is a non-negligible effect when considering the evolution of the angular momentum of the galaxy. It is also interesting to note that the distribution of magnetic field lines leads to magnetic acceleration during a significant fraction of time in the outskirts of the galaxy for *MB10*, *MB12*, and *MB13*, in agreement with the suggestion of Ruiz-Granados et al. (2010). The importance of direct magnetic braking in *MB10* seems to explain its noticeable deviation from all the other runs, where it appears magnetic effects are important to a milder extent and require the action of stellar feedback to clearly manifest.

To summarise, I find evidence in my simulations for a mechanism braking the rotation of galaxies. Magnetic stresses appear to drive baryonic mass towards their

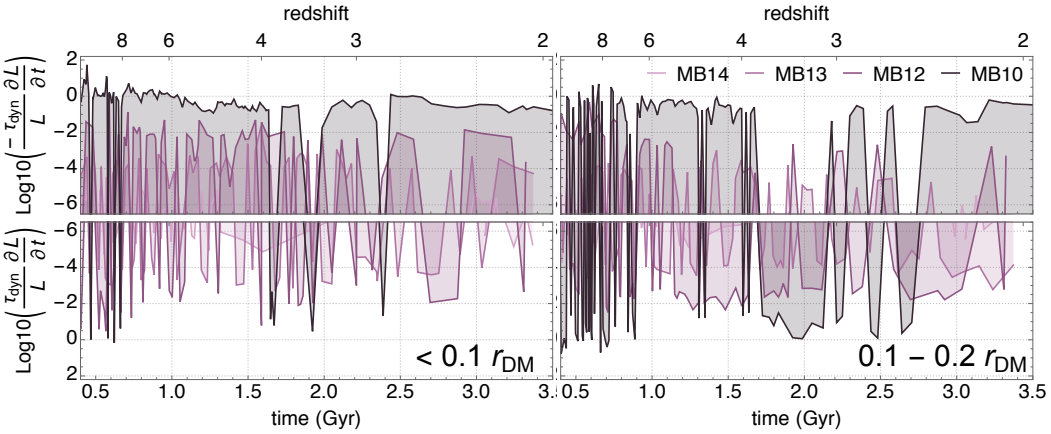

Figure 6.9: Spin-down parameters for the *MB* runs. The left panels represent the inner fraction of the galactic region ($r/r_{\rm vir} < 0.1$), the right panels correspond to its outer part ($0.1 < r/r_{\rm vir} < 0.2$). Top panels show the decrease of relative angular momentum per dynamical time, while bottom panels display its increase. The *MB10* run clearly stands out, with strong magnetic fields affecting the dynamics of the galaxy (see text).

centre, both through outward transport of angular momentum and magnetic acceleration of inflowing gas. These latter reduce the angular momentum accreted by the galaxy by pushing inflows outward (i.e. reducing their linear momentum) by means of a magnetic pressure dominated Lorentz force (term (5) in eq. (6.3)). Note that this magnetic pressure gradient is expected to be present to some degree even when the magnetisation is not of primordial origin. Other possible consequences are put forward by Sethi et al. (2010) and Pandey et al. (2019), where the former authors argue that heating from a primordial magnetic field $B_0 \sim 4 \cdot 10^{-9}$ G could lead to direct collapse of gas onto super massive black holes while the latter authors discuss how strong primordial magnetic fields of $B_0 \sim 10^{-10}$ G can dramatically reduce the angular momentum of infalling gas into massive haloes through tidal torques. According to their calculations, this angular momentum loss facilitates the formation of direct collapse black holes (DCBH).

Magnetic fields increase the size of gas clumps in my simulation (see Figure 6.1, and also Figure 7.1; Iffrig & Hennebelle 2017, also observe that smaller clumps are

inhibited by the presence of magnetic fields in the ISM). These can gravitationally drive angular momentum outward while displacing these clumps towards the galactic centre (Elmegreen et al. 2009b). Given the effect I measure, strong magnetic fields can also contribute to the formation of bulges by magnetic stresses and magnetic braking (see Figure 6.5, bottom right panel). These fields could also influence the evolution of mergers (Wang & Abel 2009), although I don not explore this possibility in this work, both concentration parameters (Figure 6.12) and centrally peaked circular velocity of my *MB10* run support this idea. Magnetic braking might also be at play in the outskirts of galaxies magnetised through other mechanisms than large-scale seeding (e.g. turbulent dynamo, or astrophysical sources). For these other mechanisms, I expect a behaviour comparable to or milder than my *MB12* run. Finally, the magnetisation of the infalling gas is likely to play a role on the effects observed.

6.4.2 Magnetic fields and galactic observables at z = 2

Having demonstrated that magnetic fields have the capacity of modifying global properties of galaxies, in this section, I review whether such an impact could be observed with upcoming facilities such as *JWST*.

The stellar mass M_* is one of the most fundamental properties of a galaxy, and represents the integrated star formation rate over time. These star formation rates are themselves regulated at first order by a combination of gas accretion (e.g Sanchez Almeida 2017) and stellar feedback (e.g. Hayward & Hopkins 2017). Both the stellar mass of a galaxy and its star formation rate (SFR) can be estimated by observations of galaxies using various estimators (Kennicutt & Evans 2012). In Figure 6.10 I present the changes in specific star formation rates (sSFR) vs stellar masses in the galactic region when the strength of the primordial magnetic field B_0 varies. This sSFR is

defined as the amount of stars with ages $t - t_{\rm birth}$ lower than a timescale Δt

$$\mathrm{sSFR}_{\Delta t}(t) = \frac{\mathrm{SFR}_{\Delta t}}{M_*}(t) = \frac{1}{M_*}\frac{M_*\left(0 \leq t - t_{\rm birth} < \Delta t\right)}{\Delta t}, \tag{6.7}$$

where $t_{\rm birth}$ is the time of formation (birth) of a star particle. I study the averaged sSFR (measured as described in Section 6.3) employing different timescales Δt: a longer one consistent with estimators such as FIR ($\Delta t = 100$ Myr; Figure 6.10, left column), and a shorter one, more frequently associated with UV or Hα observations ($\Delta t = 10$ Myr; Figure 6.10, right column).

While magnetic fields are expected to play a major role in the process of star formation on small scales, I find them to have an insignificant impact on the final stellar mass of galaxies, in accordance with previous studies (Su et al. 2017). As expected, the most important factor at play in the evolution of M_* are different implementations of stellar feedback. Varying the prescription introduces variations of $\sim 0.2-0.5$ dex, while removing the feedback altogether can boost stellar masses up to an order of magnitude. As redshift decreases, the two feedback prescriptions employed seem to converge in terms of M_*. From the highest redshift down to $z = 2$, it is hard to detect any systematic effects due to the presence of magnetic fields. The stellar mass of the galaxy appears as insensitive to the orientation of the primordial magnetic field as to its strength, which legitimates the standard usage of uniform (or even lack of) primordial magnetic fields for large-scale simulations that aim to produce stellar mass functions, at least for halos hosting galaxies with masses $M_{\rm gal} \sim 5{\cdot}10^{11} M_\odot$ and larger. I stress that the presence of magnetic fields alters other aspects of galaxy formation, but not their stellar mass. While there is a non-negligible spread in the SFR for both indicators employed, the effect of magnetic fields is once again unclear, regardless of the feedback implementation studied. I find larger deviations and error intervals for the 10 Myr measurement, as expected. As a consequence of magnetic fields driving

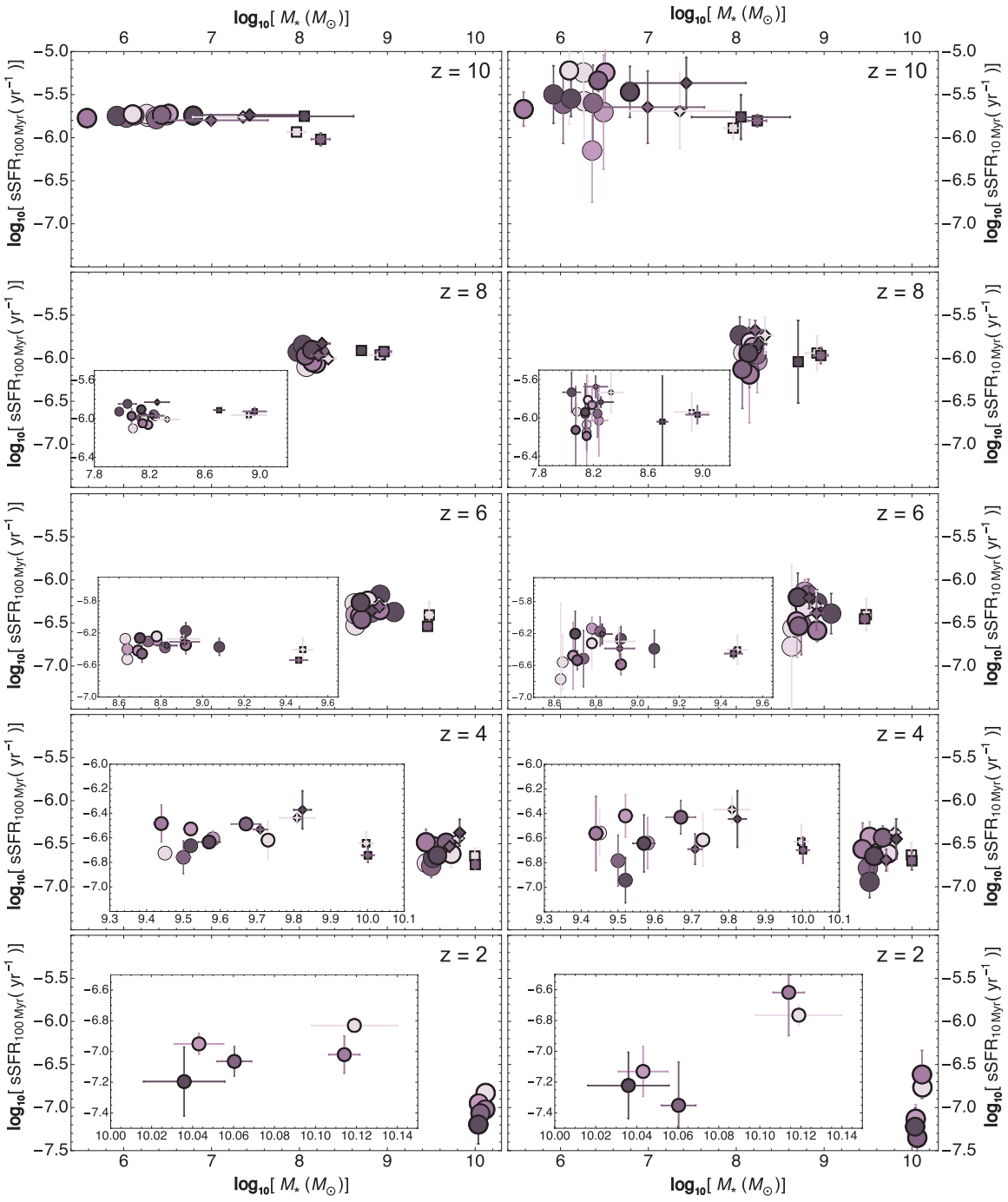

Figure 6.10: Specific star formation rates (sSFR) vs stellar mass (M_*) for different strength of the primordial magnetic field B_0. The larger the strength of the magnetic field the darker the shade of purple for the corresponding data points. The left column corresponds to a sSFR averaged over a 100 Myr period, while right column represents a sSFR averaged over 10 Myr. Data points legends are the same as for Figures 6.4 and 6.5. Subsequent rows correspond to $z = 10$, 8, 6, 4, and 2 respectively from top to bottom. Subpanels are zooms around the bulk of the distribution of data points.

gas inward in the galaxy, the sSFR should decrease with stronger magnetic fields at the later times, once the cold gas supply brought in by filaments has been exhausted. This would be associated with a depletion of gas in the inner regions of the galaxy. While this could be argued from Figure 6.10, the evidence based on these 5 simulations is relatively circumstantial. Primordial magnetic fields do not seem to influence the sSFR, at least to first order. Magnetic fields do nonetheless significantly alter the appearance of the ISM in the simulated galaxies (which I plan to examine in future work) and the time evolution of the stellar mass. In other words, while stellar masses become remarkably similar with time for all simulations (by $z = 2$, their variation is $[\Delta M_*/M_* \sim 1\%]_{\rm Mech}$), the star formation history (SFH) of the galaxy is changed by B_0. I show this in Figure 6.11, where I display the SFH for each of the *MB* runs and their time integral, namely, their cumulative stellar mass.

As the strength of B_0 increases in Figure 6.11, high SFRs are shifted towards later epochs, pushing the initial peak of star formation around $t \sim 1.5$ Gyr ($z \sim 4$) to $t \sim 2.3$ Gyr ($z \sim 3$). The deviations become significant for $B_0 > 10^{-12}$ G (*MB12* and *MB10*). This behaviour is in accordance with the results of previous MHD studies of SFR on molecular cloud scales (Hennebelle & Iffrig 2014). At approximately $t \sim 2.1$ Gyr, all simulations display a secondary peak of star formation, associated with an occurring merger. The strength of this peak is slightly increased as B_0 increases. In *MB10*, this is followed by an extended period of high star formation at $z \lesssim 3$, during which the cumulative stellar mass catches up with the simulations featuring a lower B_0 strength. On top of modifying the SFH, the presence of magnetic fields also affects the spatial distribution of the stellar component, and to some degree $\sigma^{\rm stars}_{\rm rms}$. For high B_0 values, these effects should in principle be reflected in parameters such as the colour or the concentration of galaxies.

Observations have a strong record in the study the evolutionary tracks of massive galaxies. Strong starbursts have been observed to occur in very compact nuclear

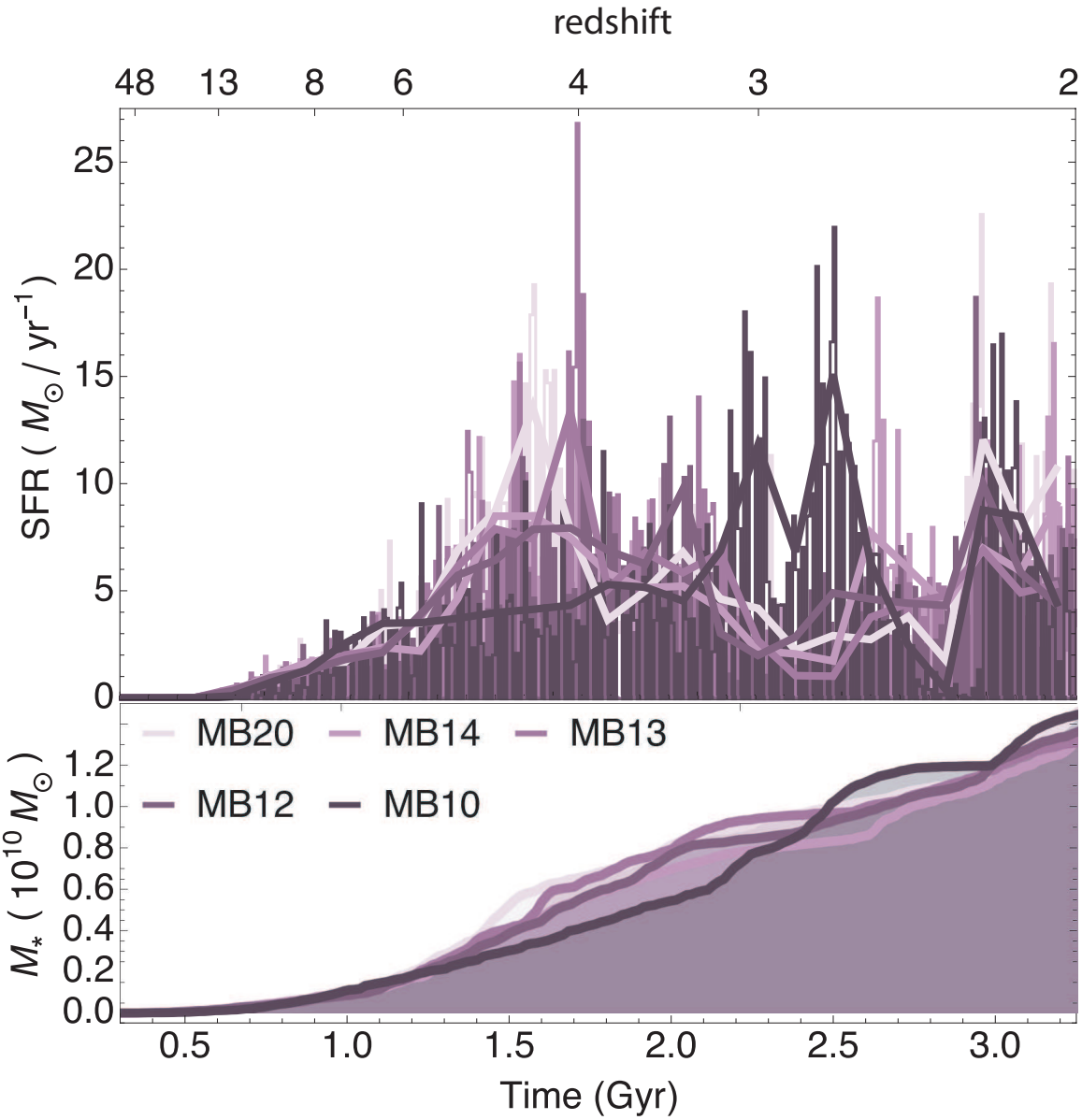

Figure 6.11: (Top) Star formation history for each of the *MB* runs as a function of time, for shorter ($\sim$ 10 Myr; thin bins) and longer ($\sim$ 100 Myr; thick lines) periods of time. (Bottom) Cumulative stellar mass in the galactic region for each of the runs, corresponding to the integral of the star formation rates plotted in the top panel. As for previous figures, darker shades of purple indicate larger B_0. Stronger B_0 delay the growth of the cumulative stellar mass, yet all simulations end with approximately the same stellar mass by $z = 2$.

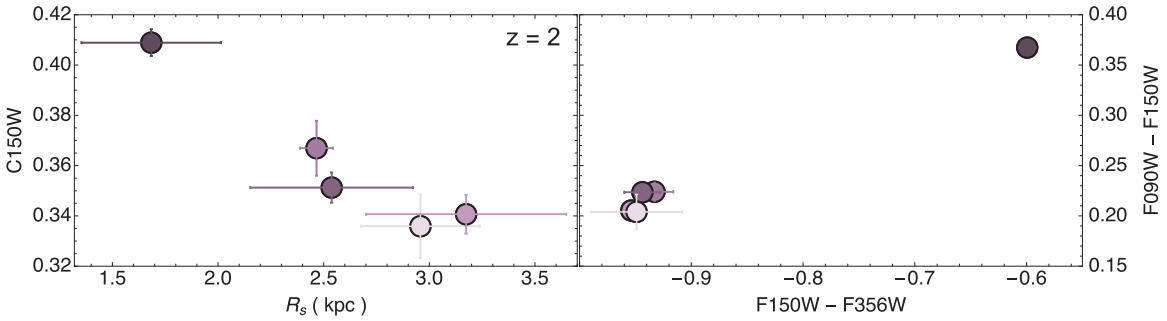

Figure 6.12: Variation of the rest-frame V-band concentration parameter $C150W$ (left) and rest-frame $U-V$ vs $V-J$ colours from $F090W-F150W$ vs. $F150W-F356W$ (right) for various strengths of the primordial magnetic field at $z=2$. See Section 6.3 for details on the way the quantities are calculated.

regions at $z \gtrsim 4$, generating important fractions of stellar mass very rapidly and building up concentrated stellar cores (e.g. Toft et al. 2014; Ikarashi et al. 2015; Oteo et al. 2017; Gómez-Guijarro et al. 2018). As the stellar population resulting from such a burst ages, the compact stellar cores should display redder colours at $z \sim 2$. Therefore, both higher concentration and redder colours could help in distinguishing these characteristic bursty SFH from a smoother secular evolution. Measuring these observational features as a function of the magnetic field strength in my simulations should shed light on the effect of magnetic fields on the SFH of galaxies. The rest-frame UVJ bands are of particular interest as wavebands where the most prominent changes in spectral features occur as the stellar populations evolve (Patel et al. 2012). Indeed, the rest-frame $U-V$ and $V-J$ colours have been widely used to identify and study post-starburst galaxies (e.g. Wild et al. 2014; Wilkinson et al. 2017).

I average colour and concentration measures over $\tau_{\rm dyn}=0.4$ Gyr to generate mock *JWST* observations at $z=2$ (as described in Section 6.3). Figure 6.1 presents face-on rest-frame UVJ snapshots of the studied galaxy from the 5 B_0 runs available at that redshift. These are obtained by convolving the galaxy spectrum with the [$F090W$, $F150W$, $F356W$] *JWST*/NIRCam filters.

More quantitatively, the the rest-frame V-band concentration parameter $C150W$

(top), and rest-frame $U-V$ vs $V-J$ colours from $F090W-F150W$ vs $F150W-F356W$ (right panel), from z-oriented runs are shown in Figure 6.12. An increase in $C150W$ (left panel) as the magnetic field increases is in agreement with the behaviour of R_s and $R_s^{\rm stars}$ previously discussed. The colours (left panel) are fairly independent of B_0, except for the extreme *MB10* run, where the galaxy becomes redder in agreement with observations of the colour evolution of post-starburst galaxies. This observed colour is the result of a lower fraction of stars formed for *MB10* over the past ~ 0.5 Gyr than for the other runs, after undergoing a much stronger star formation burst.

6.5 Conclusions

In this Chapter, I generated high resolution cosmic zoom-in simulations of a Milky Way-like spiral galaxy, and used them to explore the impact of changing the primordial magnetic field strength on its global morphological and dynamical properties.

The suite of simulations employed featured different stellar feedback prescriptions *Mech* (M), *RdTh* (R) and *NoFb* (N), presented in Section 6.2. These simulations were seeded with a uniform primordial magnetic field of varying comoving strength B_0. I sampled each strength with three different orientations for the highest studied redshift and progressively reduced the number of simulations as redshift decreased down to $z=2$, because of computational costs. All the values of $B_0=10^{-X}$ Gauss (BX), were chosen to lie below the current observational upper limit ($B_0 \lesssim 10^{-9}$ G, Planck Collaboration 2015): *B20*, *B14*, *B13*, *B12*, and *B10*. I then studied in detail the way magnetic stresses modify the global properties of galaxies. Finally, I examined how such modifications are reflected in observable quantities. My main findings are:

- Strong magnetic fields can provide an additional support against the initial collapse of the galaxy, slightly delaying its formation and temporarily increasing its size both radially and vertically (Figures 6.3 and 6.4).

- Strong primordial magnetic fields can reduce the radial scale of the gas disk significantly as the galaxies evolve. By redshift $z = 2$, the strongest magnetic field studied brings the disk radial scale down to half its size (Figure 6.4). As a consequence, the stellar disk size is also drastically reduced. Both these reductions are accompanied by a large transfer of angular momentum, reflected in the reduction of the spin parameter $\lambda_{\rm rot}$ (Figure 6.5).

- The presence of magnetic fields in the ISM thickens the gas disk after it has been established. The stellar disk height appears to correlate well with that of the gas disk for moderate values of B_0. However, once B_0 becomes stronger (*MB10*), the stellar disk becomes significantly thinner, as gravity is only able to overcome magnetic pressure close to the disk mid-plane, where gas densities are higher. During the accretion phase and before the disk settles, I observe no clear effects of B_0 on the half-thickness of the disk (Figure 6.4).

- Altering the stellar feedback prescription does not induce significant changes on the effects of B_0 on morphological properties. However, in the absence of feedback, the effects of magnetic fields on these properties are greatly reduced, until extremely high values of the magnetic fields are probed (*NB10*). This is understood in terms of a coupling between the stellar feedback dynamical forcing and magnetic stress.

- Primordial magnetic fields reduce the gas and stellar spin parameters, as B_0 increases (Figure 6.5), and this effect becomes significantly reduced for extremely high primordial magnetic field strengths (*MB10*).

- No clear effects are observed in the gas $\sigma_{\rm rms}$ of my galaxy (Figure 6.5). However, a trend is found for $\sigma_{\rm rms}^{\rm stars}$ to increase with B_0. Once again, in the absence of feedback, no clear differences in the dynamics are found between *NB20* and *NB12*.

- Non-negligible magnetic forces are found in runs with $B_0 > 10^{-13}$ G, which lead to magnetic braking in the galaxies by transporting angular momentum outward (Figures 6.7 and 6.8). Significant direct reduction of the angular momentum accreted by the galaxy is only found for *MB10* (Figure 6.9).

- In agreement with previous studies (Su et al. 2017), magnetic fields do not alter the total M_* of the simulated galaxy (Figure 6.10). However, I find that they influence its SFH and the spatial distribution of star formation regions (Figures 6.11 and 7.1).

- The changes in the radial scales of the galaxy R_s and $R_s^{\rm stars}$ are reflected in the concentration parameter $C150W$ of mock *JWST*/NIRcam observations (Figure 6.12).

- Galaxies with the highest magnetic fields at the same point in their evolution appear redder in rest-frame $U - V$ vs $V - J$, in agreement with observed post-starburst galaxy colours (Figure 6.12).

Overall, I find that magnetic fields have the potential to influence the growth and properties of galaxies as they evolve. While the effects explored in this Chapter arise from primordial magnetism, the question of which of these remain in place when galactic magnetic fields are seeded through other mechanisms as e.g. by stellar winds and SNe is still open. Even though my *fiducial* model *MB12* does display changes in the properties of the galaxy, these are minor, suggesting that only extreme primordial magnetic fields are likely to induce significant changes in galaxies. I plan to follow-up on this issue beyond the initial exploration presented in this Chapter.

Chapter 7

Conclusions

Magnetic fields are observed in most astrophysical objects and environments in our Universe. In fact, they are believed to permeate the entirety of our Cosmos (Widrow 2002). They are not only ubiquitous, but are most likely present from the early stages of our Universe (Kandus et al. 2011). Observational evidence exists for magnetic fields in high redshift ($z \sim 2$) galaxies with magnetic field strengths comparable to those in present day ones (Bernet et al. 2008), implying that they were already relevant in galaxies shortly after their formation. Because magnetic energy is believed to make up a large fraction of the energy budget of the interstellar medium (Beck 2015), magnetic fields are likely to have influenced the formation and evolution of galaxies in ways that are still not well understood. It becomes even harder to understand how magnetic fields might shape galaxies when we realise that we are not certain how galactic magnetic fields are generated in the first place.

In this thesis, I presented my efforts to better understand the origin of galactic magnetic fields and the role these might play in shaping galaxies.

Tackling these questions through observations of galaxies and their magnetic fields is complicated. As explained in Section 1.3.1, directly observing magnetic fields is already challenging in the local Universe, with the task becoming even more arduous

with increasing redshift, up to the point that there is no current prospect of observing magnetic fields during the first few hundred millions of years after the formation of the first galaxies. As a result, we cannot obtain much information about the state of magnetic fields in galaxies shortly after their formation, and hence cannot deduce their influence on the early evolution of galaxies. The best method instead to approach these questions is through numerical simulations, which are capable of following the formation and evolution of galaxies through cosmic time. While it is challenging to self-consistently model magnetic fields in simulations due to the vast range of scales and amount of processes involved, they can be used to improve our understanding of galactic magnetic fields.

In this thesis I described how I extended the Ramses MHD code to better model magnetism in the context of galaxy formation by introducing a super comoving variable for magnetism, and accounting for magnetic fields in the processes of star formation and stellar feedback (Chapter 2). I also described my development of a new algorithm to better understand how magnetic fields produced by different scenarios conspire to produce the total magnetic field (Chapter 3). There are three favoured channels for magnetising galaxies: turbulent dynamos converting interstellar gas kinetic energy into magnetic energy, stellar and active galactic nuclei feedback (not explored in this thesis) providing strongly magnetised gas to the ISM, and/or ubiquitous primordial magnetic fields strong enough to generate the fields observed in current galaxies by the mere collapse of primordial perturbations. Using Ramses to build on previous numerical work with idealised isolated galaxies, I investigated how, now in a cosmological context, a turbulent dynamo contributes to the amplification of the magnetic field in a Milky Way-like galaxy, and studied the role played by the cosmological environment (Chapter 4). Using the new tracer method to separate magnetic fields, I studied how the two other favoured magnetisation channels, namely supernova-generated and primordial magnetic fields, compete to magnetise the same

simulated galaxy (Chapter 5). Finally, exploiting the ability of numerical simulations to follow the evolution of galaxies and to provide vast amounts of information for these systems, I assessed how the evolution of the same galaxy is altered by magnetic fields in controlled cosmological experiments where I modified the initial level of magnetisation, i.e. the strength and orientation of the primordial magnetic field (Chapter 6).

7.1 Summary

Amplification through a turbulent dynamo is a convenient mechanism to provide strong magnetic fields in structures such as galaxy clusters or galaxies, due to the combination of rapid amplification times and the ubiquity of turbulence (Schekochihin et al. 2002). However, numerical simulations of galaxies struggle to test the feasibility of this process, which requires extreme ranges of spatial resolution in order to capture a reasonable fraction of the inertial range. Resolving sub-viscous scales for the magnetic component in these simulations is even more challenging and would require more sophisticated approaches outside the scope of this thesis.

With these caveats in mind, I devoted Chapter 4 to studying the turbulent dynamo, simulating with the MHD code Ramses (Teyssier 2002; Teyssier et al. 2006) a Milky Way-like galaxy, Nut (Powell et al. 2011), submerged in a realistic cosmological environment. The simulations I generated achieve high spatial resolutions (~ 10 pc physical) and include a sophisticated state-of-the-art sub-grid set of physics that captures the main processes taking place in galaxies. I studied how this turbulent dynamo operates in the simulated galaxy under three different stellar feedback prescriptions. I found that the growth of the magnetic energy per unit gas mass occurrs in three main phases: first through compression during the collapse of the galaxy, and then through some degree of turbulent amplification driven by cold gas accretion

from filaments penetrating the halo during an intermediate phase, and finally through a stellar feedback phase. In addition, satellite merger events appear to provoke sharp spikes (i.e. $\sim$ 100 Myr timescales) in the magnetic energy, but they are dissipated shortly after they occur. Given the growth factors of turbulent amplification found in my simulations, I expect future higher resolutions experiments to yield extremely fast amplification rates. As computational power increases, higher resolution simulations will also be able to better reproduce the turbulent amplification expected in nature. However, convergence towards these values appears to be far from current prospects.

In Chapter 5 I employed the tracer algorithm presented in Chapter 3 to perform the first sets of simulations that allow a direct comparison of the consequences of two sources of magnetisation operating simultaneously in the same run. Whether the magnetic field has a primordial or stellar origin, it is observed to reach μG levels in galaxies shortly after their formation. By separately tracing each of these fields in the simulation, I concluded that their relative importance in the magnetisation of the CGM and the LSS depends significantly on the comoving strength of the primordial magnetic field.

In Section 5.3.1 I used simulations of cosmological volumes to show that how magnetic fields generated in galaxies penetrate into the IGM, with a rapidly increasing filling fraction that is likely to be significant by $z = 0$. I found that galaxy haloes above a virial mass of $M_{\rm vir} \sim 10^8 - 10^{8.5} M_\odot$ are dominated by the magnetic energy injected during SN events. These simulations make a case for considering in future work both magnetic field injection by AGN, and more complex configurations for the primordial magnetic field.

In Section 5.3.2 I employed the same tracer algorithm on new simulations of the Nut galaxy. These simulations serve to better understand how the two sources of magnetic fields contribute to the total magnetic energy budget. For a primordial magnetic field that by itself could lead to typical values of magnetisation observed in

present day galaxies, the additional injection of magnetic energy by supernovae only slightly increases the overall magnetisation of the galaxy. In this case, neither the primordial nor the SN-generated magnetic energy, significantly dominates the energy budget. Instead, they distribute their energy differently in the gas temperature-density phase space, with the primordial field preponderant at the coldest temperatures in intermediate density gas, and the SN-generated magnetic energy dominating the hot gas. A significant amount of the energy injected by SN events enters the galaxy halo, polluting it and interacting with the primordial magnetic field. This indicates that it will be difficult to retrieve much information about the primordial magnetic field here. Equally surprising is the fact that despite the injection of SN-generated magnetic energy by $z \sim 1.5$, the amount of primordial magnetic energy in the galaxy remains significant in comparison to that provided by supernovae. Therefore, if a strong primordial field is present in our Universe, it might influence galaxies throughout their evolution. Perhaps the most fascinating finding from tracing two fields with different origins is that they develop a complex interaction which stores a non-negligible fraction of the total magnetic energy budget. This becomes particularly relevant when a large-scale process independent of the traced energy sources governs galactic dynamics and re-organises both traced fields. Interestingly, as redshift decreases, the magnetic energy contained in this interaction term becomes negative. This might be due to my numerical implementation of the magnetic tracers, or driven by the large-scale re-arrangement of the traced fields.

Finally, given the importance of strong primordial magnetic fields, even in the presence of other sources of magnetism, as highlighted in Chapter 5, I was compelled to investigate how primordial magnetic fields could affect the evolution of galaxies. Using idealised isolated simulations of galaxies, several studies have addressed the impact of magnetic fields on the ISM revealing changes in its structure, local star formation, dynamics, etc (Evirgen et al. 2017; Ramos-Martínez et al. 2018; Hennebelle

& Iffrig 2014). However, the impact of primordial magnetic fields on the global properties of galaxies is not yet fully understood, as it requires following the formation of a galaxy in a cosmological context. I embarked in such a study in Chapter 6. I investigated how various initial magnetic fields, all with strengths well within current observational limits, affect the properties of the NUT galaxy simulated with different feedback prescriptions. I found that magnetic fields provide additional support to the gas in a proto-galaxy hence delaying its collapse, but that they have minor effects on the shape and rotation of the galaxy. By $z = 2$, I find that stronger magnetic fields can considerably shrink both the gaseous and stellar radial scale lengths of a galaxy. The size decrease is accompanied by a loss of angular momentum. The scale height of the gas also seems to midly increase ($\sim$ 100 pc) in the presence of magnetic fields. Interestingly, these morphological effects are most obvious in the presence of stellar feedback, suggesting that stellar feedback and magnetism couple to impact the global ISM. The global turbulence of the gas in the galaxy appears unaffected by the presence of magnetic fields. A candidate mechanism responsible for the observed changes in disk size and angular momentum is magnetic braking operating in the galaxy, through outward pressure exerted onto the incoming gas, and for the case of the strongest primordial magnetic field probed, direct forces opposing the large-scale rotation. In agreement with previous studies, magnetic fields do not influence the stellar mass of the simulated galaxy by $z = 2$ (e.g Su et al. 2017), but they do influence the spatial distribution of where star formation occurs, as well as the star formation history of the galaxy. I find that the simulation with the highest magnetisation displays colours in $U-V$ bands consistent with post-starburst galaxies. Furthermore, the change in the morphologies of the galaxies affects the concentration parameter extracted from mock observations in the rest-frame V band. Other effects according to my simulations to which magnetic fields could contribute are decreasing rotation curves and the formation of galactic bulges. However, the effects observed

in my simulations could be the result of a magnetisation too high ($B_0 = 3 \cdot 10^{-10}$ G), even though it is still well below the current Planck Collaboration (2015) constraints.

Overall, magnetic fields are a particularly intriguing component of our Universe. We are well aware of their existence and ubiquity, and they play an important role in many processes occurring in our Universe. However, we remain in the shadows for questions regarding their origin and their effects on cosmological and galactic scales. This thesis puts forth the idea that each of the three pathways here explored (i.e. primordial origin, stellar origin, and turbulent amplification) can magnetise a galaxy to its present-day values. However, for the first time, it shows that their interaction is complex and non-negligible, and needs to be studied in detail.

7.2 Future directions

If something is clear from this thesis, it is that there remains a vast amount of uncertainty surrounding magnetic fields. Building on the studies presented here, I now outline a number of potential - and in many cases, ongoing - projects that will contribute to our understanding of this fascinating and mysterious component of our Universe.

7.2.1 Comparing with radio observations

As discussed in Section 1.3.1, the best way to retrieve information regarding magnetic fields in extragalactic systems is through observations in the radio waveband. The next step for my work is to therefore generate mock radio observations that can be compared with present and future surveys.

Two main methods can be employed for this: one is through maps of Faraday Rotation Measures (RM, Dolag et al. 2005b; Pakmor et al. 2018), while another possibility is to produce direct maps of synchrotron emission (Vazza et al. 2015, 2017;

Marinacci et al. 2017). As I proceed with my studies of magnetism in galaxies, I will develop software to compare my current numerical simulations with observations, starting with the simpler RM maps, and building up progressively to more complex synchrotron maps.

I will then use the set of simulations presented in Chapter 6 to validate these map-making codes and to study how radio observations of my galaxies change under different magnetisations and stellar feedback models. These mock images will be extremely useful to then complement my future studies of magnetism, especially for those discussed in Section 7.2.4.

7.2.2 Magnetic Initial Conditions

Section 2.4.2, presented the case for using magnetic initial conditions (BICs) when studying magnetogenesis scenarios. In that Section I also showed my first efforts, in collaboration with Prof. Oliver Hahn, to generate BICs for cosmological simulations following a user specified magnetic energy spectrum, rather than assuming a spatially uniform magnetic field. The current objective is to complete this algorithm and study various test cases to ensure its correct performance. Then we will assess the importance of BICs for structure formation and magnetic fields in the LSS. Indeed, once this software is finalised, it will be openly distributed to the community, either through a stand-alone implementation or integrated in the current or future versions of MUSIC (Hahn & Abel 2011).

7.2.3 Towards a sub-grid model for dynamo amplification

Chapter 4 illustrated the extreme difficulty faced by cosmological numerical simulations to produce turbulent amplification in galaxies. This problem is aggravated for spiral galaxies due to the small Jeans scale of their disk. Another aspect exposed by the simulations I presented is that, while AMR refinement is needed to approach the

resolutions required to accurately model the formation of galaxies, it also makes it difficult to trigger dynamo amplification and interpret the results of simulations due to the presence of various numerical resistivities emerging from different cell sizes.

An extension of the AMR approach is the following quasi-Eulerian technique. On top of the usual AMR scheme in my simulations, the extra simulations in Chapter 4 (i.e. the *BMEuRX* simulations) utilised a physical density threshold above which the ISM of galaxies and their surroundings were refined to a fixed resolution, effectively a uniform grid. The study presented in that Chapter can be extended to understand in better detail how different regions of the ISM amplify the magnetic field and because the simulations have uniform spatial resolution they can also give an estimate of numerical resistivities and viscosities in the galaxies. An interesting project would be to employ these simulations to better understand the characteristics of the dynamo process in direct comparison to magneto-hydrodynamical turbulence box simulations such as those by e.g. Schekochihin et al. (2002); Federrath (2016). From such comparisons, I could develop a realistic sub-grid model for dynamo amplification in cosmological simulations of galaxies. This model would not only allow me to include this channel of magnetisation in large scale simulations, but would also be useful for the project of Section 7.2.4.

7.2.4 On the origin of galactic and cosmic magnetic fields

One of the most discussed topics of this entire thesis has been the question of the origin of galactic magnetic fields, and in fact, the origin of magnetic fields of the Universe at large. Through the techniques discussed, the advances proposed in Sections 7.2.1, 7.2.2, and 7.2.3, and especially, the Magnetic Tracers algorithm introduced in Chapter 3, I present here a two pronged approach to use numerical simulations to further study the origin of galactic and cosmic magnetic fields.

My thesis showed how cosmological re-simulations of individual galaxies with mag-

netic tracers can follow various channels of magnetisation. New generations of cosmological re-simulations with magnetic tracers will feature sub-grid dynamo amplification and state-of-the-art models for star formation and magnetised feedback, all carefully calibrated. Equally, the development of the BICs software described in 7.2.2 will allow me to test different models of magnetogenesis, which are likely to alter the spectral distribution of the primordial magnetic field. The constraining potential of the magnetic tracers will best manifest itself when combined with the mock radio observations software discussed in Section 7.2.1. I will be able to generate mock radio maps displaying the separate contribution from each magnetic field traced. This will indicate whether a particular magnetogenesis scenario has a concrete observational signature.

Arguably a more exciting prospect is provided by combining all these pieces for cosmological simulations of large volumes. While this will be an ambitious project, it has the potential to significantly advance our understanding of the magnetic field of our Universe. Using the magnetic tracers with BICs, magnetised stellar and AGN feedback, and a sub-grid dynamo in large cosmological simulations, one could study how different magnetogenesis scenarios magnetise the intergalactic medium and the large-scale structure and how galaxies pollute the cosmic magnetic field of the Universe. Finally, through mock observations of these simulations and the separation of the emission in each corresponding tracer, we will be able to make predictions for the detection of the cosmic magnetic field complementary to those proposed by Vazza et al. (2017). Importantly, the cosmological simulations I propose will be capable of untangling the degree of pollution by galaxies in different cosmological environments from the primordial magnetic field contribution to the cosmic magnetic field. This will be fundamental for future facilities when they try to detect this cosmic magnetic field. As a result, the project will deliver predictions for telescopes such as SKA which are poised to obtain revolutionary insights on cosmic magnetism, and to perhaps finally

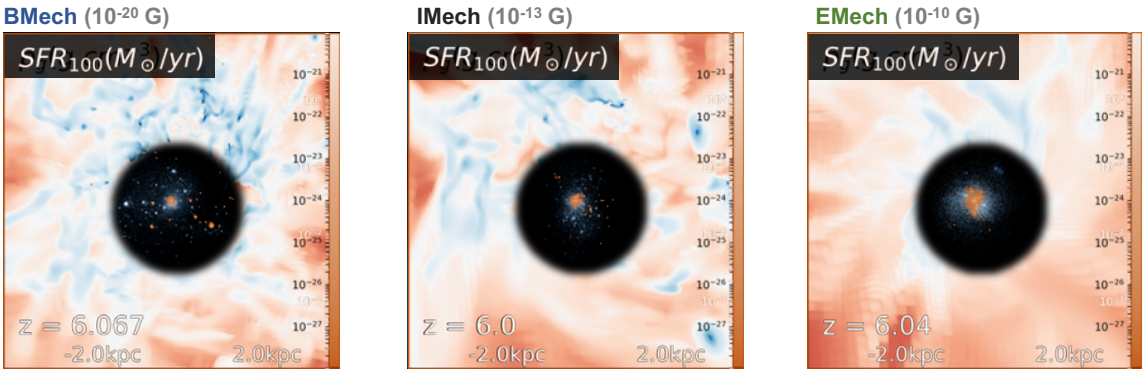

Figure 7.1: Overlay of different projected quantities centred on the Nut galaxy at $z = 6$ high (right, $B_0 = 3 \cdot 10^{-10}$ G), intermediate (center, $B_0 = 3 \cdot 10^{-13}$ G), and essentially no (left, $B_0 = 3 \cdot 10^{-20}$ G) magnetisation. Bottom of each graph displays gas density (red to blue colourscale). The central circle, displays the rest-frame UVJ stellar emission (following Section 2.5.1). Finally, I display on top of the Figure in orange colors the average star formation rate during the last 100 Myr for each simulation. Increasing the magnetic field strength alters the distribution of star formation regions in the galaxy.

determine the primordial magnetic field of our Universe.

7.2.5 Magnetism, radiation, and the epoch of reionization: SPHINX

As a recent member of the SPHINX collaboration (P.I. J. Rosdahl, Rosdahl et al. 2018), I contributed to the now accepted PRACE proposal to run new state-of-the-art simulations of the epoch of reionization (EoR). The relevant part of the 54 million computing hours awarded is a set of simulations which will include magnetic fields. Various authors have pointed out the relevance of magnetic fields in the distribution and timescales of star formation in galaxies (Hennebelle & Iffrig 2014; Iffrig & Hennebelle 2017). My work in Chapter 6 commented on this, and a modification to account for magnetic fields in the star formation prescription in my simulations leads to different distributions of star forming regions (see Figure 7.1). As a consequence, magnetic fields have the potential to considerably influence the process of reionization of our Universe by altering escape fractions from galaxies during this early epoch.

These simulations will serve to study this and also the properties of magnetic fields in galaxies during the EoR, and the impact they have on their galaxies. We are already running the first simulations, with preliminary results suggesting that indeed, magnetic fields alter the reionization of the Universe.

As part of this set of simulations, an interesting extension which I am currently exploring is to couple magnetic fields to radiation through the Biermann battery, photoionisation momentum transfer and radiation pressure terms in the induction equation[1]

$$\frac{\partial \vec{B}}{\partial t} - \vec{\nabla} \times \left(\vec{u} \times \vec{B} \right) - \eta \nabla^2 \vec{B} = -\frac{c}{e n_e^2} \vec{\nabla n_e} \times \vec{\nabla p_e} - \frac{c}{e} \vec{\nabla} \times \vec{f}_{\rm rad}, \tag{7.1}$$

as previous authors tested for smaller systems (Gnedin et al. 2000; Durrive & Langer 2015). These radiation forces $\vec{f}_{\rm rad}$ have contributions from various processes such as Thompson scattering, or momentum transfer from photons to electrons (an example of their calculation is the work by Doi & Susa 2011), which will generate currents that will induce magnetic fields. With these new simulations also featuring Magnetic Tracers, we will be able to check whether the EoR is a contender for being an important source of the magnetogenesis in the Universe.

[1]The full induction equation is presented here in non-comoving coordinates, where the new quantities introduced when compared with eq. (2.4) are respectively the light speed c, the electron number density n_e and electro pressure p_e, and the radiation forces $\vec{f}_{\rm rad}$. The first term of the right hand side corresponds to the Biermann battery, while the radiation forces $\vec{f}_{\rm rad}$ can be decomposed in the two mentioned contributions following Doi & Susa (2011).

Appendix A

Further numerical calculations

A.1 Fast Fourier Transforms of a galaxy

In this appendix the characteristics of the spectrum of a disk galaxy embedded within a cubic box are addressed, as this is used extensively to interpret results in the main body of the text and disentangle physical properties from numerical artefacts in a given spectrum. We caution that our approach does not fully differentiate features caused in the spectral analysis by the gas density structure. A more localised analysis based, e.g. on wavelets, would be required to fully characterise which of the spectral features are exclusively generated by turbulence. The aim of this section is to provide a better understanding of the overall impact of the morphology of the galaxy. More specifically, one assumption commonly made in the calculation of a FFT is that of domain periodicity. While it is not adequate for the case of an individual galaxy, an accurate spectrum can still be calculated if precautions are taken. Similarly, it is important to discriminate the galaxy from its environment in a cosmological simulation and to recognise features associated with its overall shape (disk scale height and length) instead of the dynamics of the gas flow within it.

First, we have to discriminate the studied object from its environment. This

occurs by definition in isolated simulations of galaxies, where all the effects only are the result of the presence of a galaxy. Fortunately, physical quantities (i.e. kinetic and magnetic energies) have values in the galaxy several orders of magnitude above the ones found in its environment. This naturally acts as an effective 0-padding: the Fourier modes outside the galaxy are negligible with respect to the amplitude obtained for the ones within the galaxy, as long as the wavelength remains smaller than the size of the region of interest. In physical terms, the energy $E(k)$ contained in a given scale k smaller than the scale of the galaxy $k > k_{\mathrm{gal}}$ is found to be negligible in the environment compared with the energy corresponding to the same mode within the galaxy. Accordingly, the studied scale k has to be smaller than the largest scale corresponding to the galaxy. As the size of the studied galaxy roughly scales with the size of the box (with a side length $l = 0.2\, r_{\mathrm{halo}}$), and the radial scale of the galaxy is typically $\sim 0.1\, r_{\mathrm{halo}}$, this corresponds to $k_{\mathrm{gal}} \sim 2\, k_{\mathrm{min}}$, where k_{min} stands for the minimum spectrum scale represented. Smaller ks should therefore be discarded from the analysis even though we still display them on the figures.

In addition, wavenumber scales k on the order of the overlapping of the galaxy with its periodic occurrences should be neglected. Correlations can be found between modes that bridge the shortest distance between the studied object and its periodic analogue. For the aforementioned size of the box and galaxy, the maximum scales k that can be affected by periodicity are again $k_p \sim 2\, k_{\mathrm{min}}$.

Due to the small volume of the box covered by the galaxy, the next consideration is the actual shape of the galaxy. It can be simplified to either a sphere during early stages of formation and a thick disk otherwise. For the case of a disk, a uniform density disk of half-thickness $h = \alpha h_{\mathrm{gal}}$ and polar radius $r_{\mathrm{polar}} = \beta r_{\mathrm{gal}}$ is studied, where $h_{\mathrm{gal}} \sim 200$ pc and $r_{\mathrm{gal}} \sim 3$ kpc are the half-thickness and radius resulting from fitting the gas density profile of the B-Mech galaxy with an exponential form. Figure A.1 displays how the variations of the α and β parameters for a disk affect its

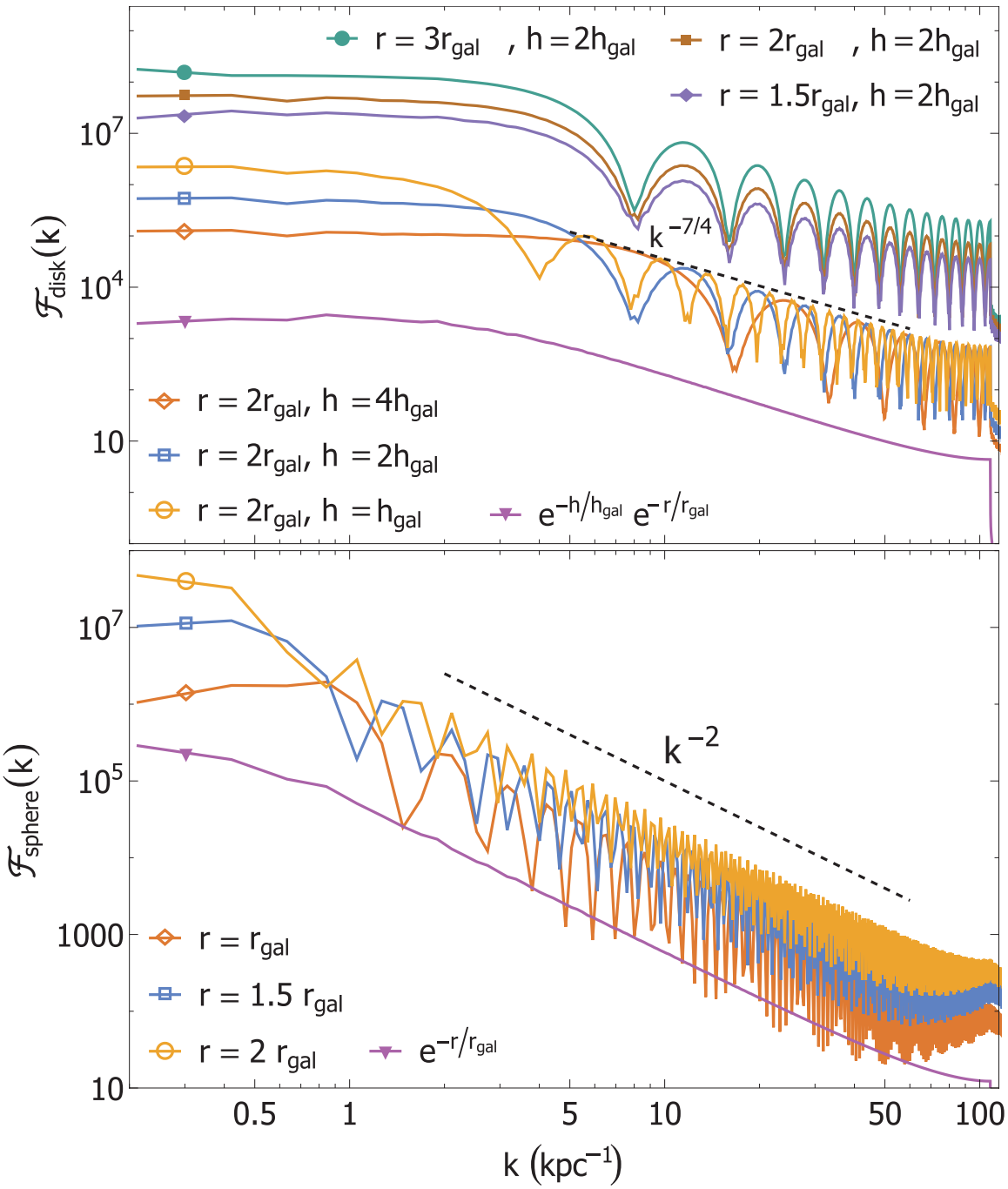

Figure A.1: Spectra for fiducial shapes of a galaxy. The impact of the shape parameters is assessed by plotting different thicknesses and radii for a disk (top) and a sphere (bottom). The three top lines for a disk have been shifted a factor $\times 1000$ for the sake of clarity. Purple lines display the spectrum corresponding to an exponential density profile rather than a uniform one, as expected for a more realistic galaxy. The dashed black lines display the exponent of the power-law decay: $\mathcal{F}_{\rm disk}(k) \propto k^{-7/4}$ for a disk and $\mathcal{F}_{\rm sphere}(k) \propto k^{-2}$ for a sphere.

spectrum. The strong oscillations seen in the spectrum are caused by the disk being implemented as a Heaviside-like window function. The thickness of the disk affects the scale of the first minimum, $k = \frac{\pi}{h}$ (i.e. the beginning of the decline). On the other hand, the radius of the disk affects how sharp the decay to the minimum is and the amount of power contained in the largest scales, as well as the mean value at $k = 0$. As the radius becomes larger, the spectrum gains power on scales $k < 3k_{\mathrm{min}}$. Conversely, smaller radii lead to a lowering at $k < 3k_{\mathrm{min}}$. As expected, the normalisation of the curves is proportional to the size of the disk, affected by both parameters (α, β). Finally, the decay followed by all disk spectra is fitted by $\mathcal{F}(k) \propto k^{-7/4}$ (black dashed line, Figure A.1).

A spherical galaxy shape on the other hand, leads to a more simple spectrum. It contains roughly constant power on the largest scales and starts decaying at the scale of the sphere radius. In Figure A.1, the spectra of a uniform density sphere of radii $r = \alpha r_{\mathrm{gal}}$ for various α are displayed. The decay of the spectrum for the sphere follows $\mathcal{F}(k) \propto k^{-1.92} \sim k^{-2}$. Changing the radius of the solid sphere exclusively affects the normalisation and once the radius becomes small enough, causes a decay at scales larger than the radius scale due to periodicity effects disappearing.

Finally, to present a more realistic case, both the disk and the sphere are implemented decreasing exponential density profiles

$$v_{\mathrm{cyl}}(r_{\mathrm{polar}}, h) = \exp\left(-r_{\mathrm{polar}}/r_{\mathrm{gal}}\right) \cdot \exp\left(-h/h_{\mathrm{gal}}\right), \tag{A.1}$$

$$v_{\mathrm{sp}}(r) = \exp\left(-r/r_{\mathrm{gal}}\right). \tag{A.2}$$

Their spectra transform in the same way as their uniform counterparts, but no longer present oscillations.

The measured disk decay $\mathcal{F}(k) \propto k^{-7/4}$ occurs on the smallest scales whenever a disk is present in the simulations. As an illustration, Fig. A.2 displays the magnetic

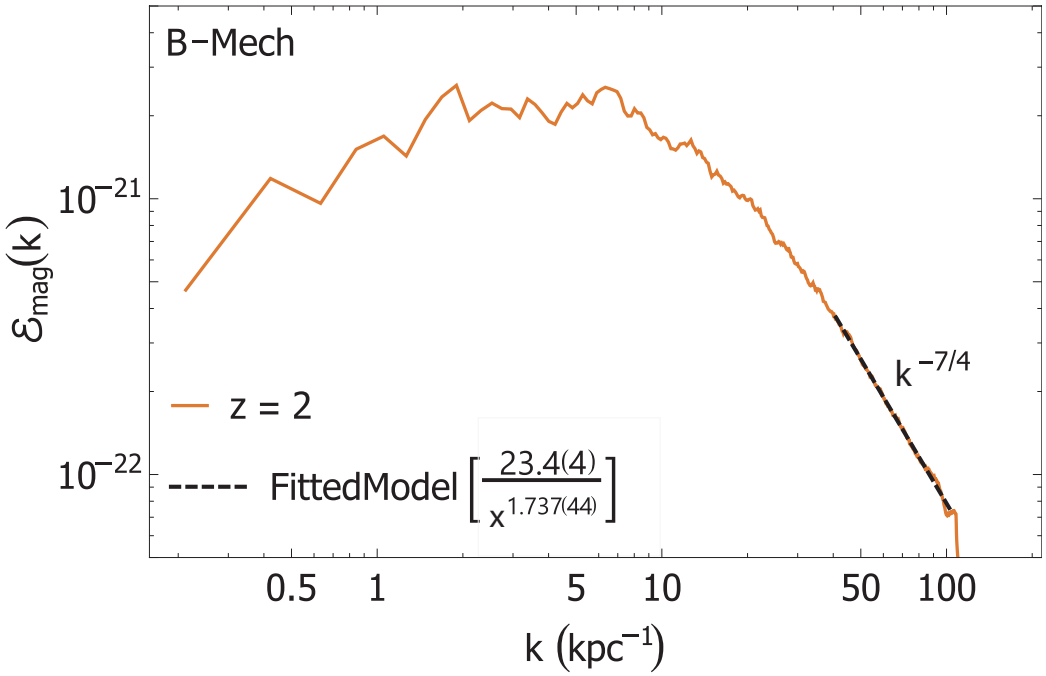

Figure A.2: B-Mech magnetic energy spectrum at $z = 2$ calculated as indicated in section 4.3.2. The black dashed lines represent a power-law fit to the spectrum in the corresponding k region, with the result of the fit shown on the figure ($1\,\sigma$ errors shown in brackets). After $k \sim 10$ kpc^{-1}, the spectrum progressively converges to the $\mathcal{E}_{\rm mag} \propto k^{-7/4}$ regime expected for an exponential disk (see text for detail). This shape-domination of the spectra is observed for studied spectra whenever magnetic fields are well confined to the galaxy.

energy spectrum for B-Mech at $z = 2$. The decay on small scales starts to be dominated by the shape of the galaxy around $k \sim 10$ kpc^{-1} and eventually follows the aforementioned $\mathcal{E}_{\rm mag} \propto k^{-7/4}$, as indicated by the dashed black line.

A.2 Morphological parameters calculation

In Section 6.4.1 we employ the radial scale R_s and height scale h_s of our galaxies to study their morphology. To compute these quantities R_s is extracted from the radial profile of a cylinder with its height component aligned along the angular momentum of the galaxy. This cylinder has a half-thickness of 0.05 $r_{\rm DM}$, and radially extends out to 0.7 $r_{\rm DM}$. For h_s, we maintain the orientation of the cylinder, but now employ

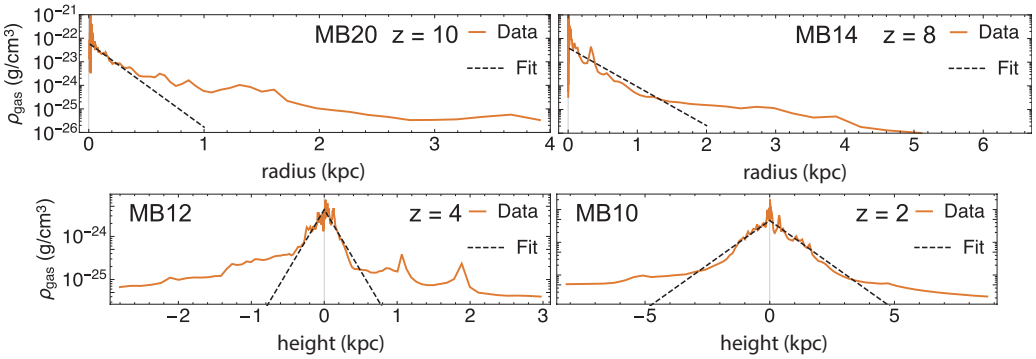

Figure A.3: Generic examples of radial (top row) and vertical (bottom row) exponential fits (black dashed lines) to the gas density profiles (orange solid lines) extracted for various outputs of our simulations.

a radial extent of 0.2 $r_{\rm DM}$ and a half-thickness 0.1 $r_{\rm DM}$, separating the upward and downward halfs of the profile. To the resulting density profiles we fit an exponential function of the form $f(x) = a \exp(x/b)$ with $(a,\, b)$ as free parameters. We identify $b \to R_s$ and $b \to h_s$ for the radial and vertical profiles respectively. We display some generic examples of various fits in Fig. A.3.

Bibliography

Aartsen, M. G., Abbasi, R., Ackermann, M., et al. 2014, European Physical Journal C, 74, 1

Aartsen, M. G., Abraham, K., Ackermann, M., et al. 2016, European Physical Journal C, 76, 133

Ade, P. A. R., Aghanim, N., Arnaud, M., et al. 2016, Astronomy & Astrophysics, 594, A13

Agertz, O., Lake, G., Teyssier, R., et al. 2009a, Monthly Notices of the Royal Astronomical Society, 392, 294

Agertz, O., Teyssier, R., & Moore, B. 2009b, Disc formation and the origin of clumpy galaxies at high redshift

Alves Batista, R., Shin, M. S., Devriendt, J., Semikoz, D., & Sigl, G. 2017, Physical Review D, 96, 023010

Anderson, J. D. 1995, Computational Fluid Dynamics: The Basics with Applications

Arshakian, T. G., Beck, R., Krause, M., & Sokoloff, D. 2009, Astronomy & Astrophysics, 494, 21

Aubert, D., Pichon, C., & Colombi, S. 2004, Monthly Notices of the Royal Astronomical Society, 352, 376

Bagchi, J., Enßlin, T. A., Miniati, F., et al. 2002, New Astronomy, 7, 249

Balsara, D. S. & Kim, J. 2004, The Astrophysical Journal, 602, 1079

Bambic, C. J., Morsony, B. J., & Reynolds, C. S. 2018, The Astrophysical Journal, 857, 84

Barrow, J. D. & Tsagas, C. G. 2011, Monthly Notices of the Royal Astronomical Society, 414, 512

Barteldrees, A. & Dettmar, R.-J. 1994, Astronomy and Astrophysics, 24, 337

Beck, A. M., Dolag, K., Lesch, H., & Kronberg, P. P. 2013, Monthly Notices of the Royal Astronomical Society, 435, 3575

Beck, R. 2015, Astronomy & Astrophysics, 578, A93

Beck, R., Fletcher, A., Shukurov, A., et al. 2005, Astronomy & Astrophysics, 444, 739

Beck, R. & Wielebinski, R. 2013, in Planets, Stars and Stellar Systems (Dordrecht: Springer Netherlands), 641–723

Behroozi, P. S., Wechsler, R. H., & Conroy, C. 2013, Astrophysical Journal, 770, 57

Bernet, M. L., Miniati, F., Lilly, S. J., Kronberg, P. P., & Dessauges-Zavadsky, M. 2008, Nature, 454, 302

Bhat, P. & Subramanian, K. 2013in (Narnia), 400

Biermann, L. 1950, Zeitschrift Naturforschung Teil A, 5, 65

Birnboim, Y. & Dekel, A. 2003, Monthly Notices of the Royal Astronomical Society, 345, 349

Blanton, M. R., Dalcanton, J., Eisenstein, D., et al. 2001, The Astronomical Journal, 121, 2358

Bolton, J. S. & Haehnelt, M. G. 2007, Monthly Notices of the Royal Astronomical Society, 382, 325

Bond, J. R., Kofman, L., & Pogosyan, D. 1996, Nature, 380, 603

Borve, S., Omang, M., & Trulsen, J. 2001, The Astrophysical Journal, 561, 82

Brandenburg, A. & Dobler, W. 2002, Computer Physics Communications, 147, 471

Brandenburg, A. & Subramanian, K. 2005, Astrophysical magnetic fields and nonlinear dynamo theory

Bray, J. D. & Scaife, A. M. M. 2018, The Astrophysical Journal, 861, 3

Broderick, A. E., Chang, P., & Pfrommer, C. 2012, The Astrophysical Journal, 752, 22

Broderick, A. E., Tiede, P., Chang, P., et al. 2018, The Astrophysical Journal, 868, 87

Bruzual, G. & Charlot, S. 2003, Monthly Notices of the Royal Astronomical Society, 344, 1000

Bryan, G. L., Norman, M. L., O'Shea, B. W., et al. 2014, Astrophysical Journal, Supplement Series, 211, 19

Bullock, J. S., Dekel, A., Kolatt, T. S., et al. 2000, The Astrophysical Journal, 555, 240

Butsky, I., Zrake, J., Kim, J.-h., Yang, H.-I., & Abel, T. 2017, The Astrophysical Journal, 843, 113

Cacciato, M., Dekel, A., & Genel, S. 2012, Monthly Notices of the Royal Astronomical Society, 421, 818

Calverley, A. P., Becker, G. D., Haehnelt, M. G., & Bolton, J. S. 2011, Monthly Notices of the Royal Astronomical Society, 412, 2543

Chamandy, L., Shukurov, A., & Subramanian, K. 2014, Monthly Notices of the Royal Astronomical Society: Letters, 446, L6

Cheera, V. & Nigam, R. 2018, Astrophysics and Space Science, 363, 93

Chen, Z., Jiang, Z., Tamura, M., Kwon, J., & Roman-Lopes, A. 2017, The Astrophysical Journal, 838, 80

Chisari, N. E., Richardson, M. L. A., Devriendt, J., et al. 2018, Monthly Notices of the Royal Astronomical Society, 480, 3962

Chyży, K. T. 2008, Astronomy & Astrophysics, 482, 755

Clarke, T. E. 2004 [eprint[arXiv]0412268]

Coc, A., Uzan, J. P., & Vangioni, E. 2014, Journal of Cosmology and Astroparticle Physics, 2014, 050

Coutinho, B. C., Hong, S., Albrecht, K., et al. 2016 [eprint[arXiv]1604.03236]

Cresci, G., Hicks, E. K. S., Genzel, R., et al. 2009, The Astrophysical Journal, 697, 115

Dahlem, M., Petr, M. G., Lehnert, M. D., Heckman, T. M., & Ehle, M. 1997, Astronomy and Astrophysics, 320, 731

Dedner, A., Kemm, F., Kröner, D., et al. 2002, Journal of Computational Physics, 175, 645

Dekel, A. & Birnboim, Y. 2006, Monthly Notices of the Royal Astronomical Society, 368, 2

Devriendt, J. E. G., Guiderdoni, B., & Sadat, R. 1999, Astronomy and Astrophysics, 350, 381

Doi, K. & Susa, H. 2011, Astrophysical Journal, 741, 93

Dolag, K., Grasso, D., Springel, V., & Tkachev, I. 2005a, Journal of Cosmology and Astroparticle Physics, 2005, 113

Dolag, K. & Stasyszyn, F. 2009, Monthly Notices of the Royal Astronomical Society, 398, 1678

Dolag, K., Vogt, C., & Enßlin, T. A. 2005b, Monthly Notices of the Royal Astronomical Society, 358, 726

Donnert, J., Dolag, K., Lesch, H., & Müller, E. 2009, Monthly Notices of the Royal Astronomical Society, 392, 1008

Draine, B. T. & Li, A. 2006, The Astrophysical Journal, 657, 810

Dubois, Y. & Commerçon, B. 2015, Astronomy & Astrophysics, 585, A138

Dubois, Y. & Teyssier, R. 2008, Astronomy & Astrophysics, 482, L13

Dubois, Y. & Teyssier, R. 2010, Astronomy & Astrophysics, 523, A72

Dunkley, J., Komatsu, E., Nolta, M. R., et al. 2009, Astrophysical Journal, Supplement Series, 180, 306

Durrive, J. B. & Langer, M. 2015, Monthly Notices of the Royal Astronomical Society, 453, 345

Durrive, J. B., Tashiro, H., Langer, M., & Sugiyama, N. 2017, Proceedings of the International Astronomical Union, 12, 60

Eisenstein, D. J. & Hu, W. 1997, The Astrophysical Journal, 496, 605

Elmegreen, B. G. & Burkert, A. 2010, Astrophysical Journal, 712, 294

Elmegreen, B. G., Elmegreen, D. M., Fernandez, M. X., & Lemonias, J. J. 2009a, Astrophysical Journal, 692, 12

Elmegreen, D. M., Elmegreen, B. G., Marcus, M. T., et al. 2009b, Astrophysical Journal, 701, 306

Erb, D. K., Steidel, C. C., Shapley, A. E., Adelberger, K. L., & Pettini, M. 2004, The Astrophysical Journal, 612, 122

Evans, C. R. & Hawley, J. F. 1988, The Astrophysical Journal, 332, 659

Evirgen, C. C., Gent, F. A., Shukurov, A., Fletcher, A., & Bushby, P. 2017, Monthly Notices of the Royal Astronomical Society: Letters, 464, L105

Federrath, C. 2016, Journal of Plasma Physics, 82, 535820601

Federrath, C. & Klessen, R. S. 2012, Astrophysical Journal, 761, 156

Federrath, C., Roman-Duval, J., Klessen, R., Schmidt, W., & Mac Low, M. M. 2010, Astronomy and Astrophysics, 512, A81

Federrath, C., Schober, J., Bovino, S., & Schleicher, D. R. 2014, Astrophysical Journal Letters, 797, L19

Federrath, C., Sur, S., Schleicher, D. R., Banerjee, R., & Klessen, R. S. 2011a, Astrophysical Journal, 731, 62

Federrath, C., Sur, S., Schleicher, D. R., Banerjee, R., & Klessen, R. S. 2011b, Astrophysical Journal, 731, 62

Field, G. B., Goldsmith, D. W., & Habing, H. J. 1969, Cosmic-ray heating of the interstellar gas, Tech. rep.

Fontanot, F., La Barbera, F., De Lucia, G., Pasquali, A., & Vazdekis, A. 2018, Monthly Notices of the Royal Astronomical Society, 479, 5678

Forbes, J. C., Krumholz, M. R., Goldbaum, N. J., & Dekel, A. 2016, Nature, 535, 523

Fromang, S., Hennebelle, P., & Teyssier, R. 2006, Astronomy & Astrophysics, 457, 371

Fujisawa, K., Okawa, H., Yamamoto, Y., & Yamada, S. 2018, The Astrophysical Journal, 872, 155

Gaensler, B., Beck, R., & Feretti, L. 2004, New Astronomy Reviews, 48, 1003

Genel, S., Dekel, A., & Cacciato, M. 2012, Monthly Notices of the Royal Astronomical Society, 425, 788

Geng, A., Kotarba, H., Bürzle, F., et al. 2012, Monthly Notices of the Royal Astronomical Society, 419, 3571

Gent, F. 2014, Ph.D. Thesis, 153

Genzel, R., Schreiber, N. M., Übler, H., et al. 2017, Nature, 543, 397

Gheller, C., Vazza, F., Brüggen, M., et al. 2016, Monthly Notices of the Royal Astronomical Society, 462, 448

Gill, S. P., Kneb, A., & Gibson, B. K. 2004, Monthly Notices of the Royal Astronomical Society, 351, 399

Girichidis, P., Naab, T., Walch, S., et al. 2016, The Astrophysical Journal, 816, L19

Gnedin, N. Y., Ferrara, A., & Zweibel, E. G. 2000, The Astrophysical Journal, 539, 505

Gomez, G. C., Vazquez-Semadeni, E., & Zamora-Aviles, M. 2018, Monthly Notices of the Royal Astronomical Society, 480, 2939

Gómez-Guijarro, C., Toft, S., Karim, A., et al. 2018, The Astrophysical Journal, 856, 121

Grasso, D. & Rubinstein, H. R. 1996, Physics Letters, Section B: Nuclear, Elementary Particle and High-Energy Physics, 379, 73

Gressel, O., Elstner, D., & Ziegler, U. 2013, Astronomy & Astrophysics, 560, A93

Gressel, O., Elstner, D., Ziegler, U., & Rüdiger, G. 2008, Astronomy & Astrophysics, 486, L35

Grisdale, K., Agertz, O., Renaud, F., et al. 2019 [eprint[arXiv]1902.00518]

Grisdale, K., Agertz, O., Romeo, A. B., Renaud, F., & Read, J. I. 2017, Monthly Notices of the Royal Astronomical Society, 466, 1093

Guillet, T. & Teyssier, R. 2011, Journal of Computational Physics, 230, 4756

Haardt, F. & Madau, P. 1996, The Astrophysical Journal, 461, 20

Hahn, O. & Abel, T. 2011, Monthly Notices of the Royal Astronomical Society, 415, 2101

Han, J. 2017, Annual Review of Astronomy and Astrophysics, 55, 111

Hatfield, P. W., Lindsay, S. N., Jarvis, M. J., et al. 2016, Monthly Notices of the Royal Astronomical Society, 459, 2618

Haugen, N. E. L., Brandenburg, A., & Dobler, W. 2004a, Physical Review E - Statistical Physics, Plasmas, Fluids, and Related Interdisciplinary Topics, 70, 14

Haugen, N. E. L., Brandenburg, A., & Mee, A. J. 2004b, Monthly Notices of the Royal Astronomical Society, 353, 947

Hayward, C. C. & Hopkins, P. F. 2017, Monthly Notices of the Royal Astronomical Society, 465, 1682

Henden, N. A., Puchwein, E., Shen, S., & Sijacki, D. 2018, Monthly Notices of the Royal Astronomical Society, 479, 5385

Hennebelle, P. & Chabrier, G. 2011, Astrophysical Journal Letters, 743, L29

Hennebelle, P. & Iffrig, O. 2014, Astronomy & Astrophysics, 570, A81

Hennebelle, P. & Inutsuka, S.-I. 2019 [eprint[arXiv]1902.00798]

Hinshaw, G., Larson, D., Komatsu, E., et al. 2013, Astrophysical Journal, Supplement Series, 208, 19

Hogan, C. J. 1983, Physical Review Letters, 51, 1488

Hollenstein, L., Caprini, C., Crittenden, R., & Maartens, R. 2008, Physical Review D - Particles, Fields, Gravitation and Cosmology, 77, 063517

Hopkins, P. F. 2016, Monthly Notices of the Royal Astronomical Society, 462, 576

Hopkins, P. F. 2017 [eprint[arXiv]1712.01294]

Hopkins, P. F., Kereš, D., & Murray, N. 2013, Monthly Notices of the Royal Astronomical Society, 432, 2639

Hopkins, P. F., Kereš, D., Oñorbe, J., et al. 2014, Monthly Notices of the Royal Astronomical Society, 445, 581

Hopkins, P. F., Quataert, E., & Murray, N. 2012, Monthly Notices of the Royal Astronomical Society, 421, 3522

Hopkins, P. F. & Squire, J. 2018, Monthly Notices of the Royal Astronomical Society, 479, 4681

Hull, C. L. H., Mocz, P., Burkhart, B., et al. 2017, The Astrophysical Journal, 842, L9

Iffrig, O. & Hennebelle, P. 2017, Astronomy & Astrophysics, 604, A70

Ikarashi, S., Ivison, R. J., Caputi, K. I., et al. 2015, Astrophysical Journal, 810, 133

Inoue, S. & Yoshida, N. 2019, Monthly Notices of the Royal Astronomical Society, 485, 3024

Jana, R. & Nath, B. B. 2018, Monthly Notices of the Royal Astronomical Society, 479, 153

Ji, S., Oh, O. P., & McCourt, M. 2018, Monthly Notices of the Royal Astronomical Society, 476, 852

Ji, S., Peng Oh, S., Ruszkowski, M., & Markevitch, M. 2016, Monthly Notices of the Royal Astronomical Society, 463, 3989

Johnston-Hollitt, M., Govoni, F., Beck, R., et al. 2015, in Advancing Astrophysics with the Square Kilometre Array (AASKA14), 92

Kandus, A., Kunze, K. E., & Tsagas, C. G. 2011, Primordial magnetogenesis

Katz, N. 1992, The Astrophysical Journal, 391, 502

Kauffmann, J., Pillai, T., & Goldsmith, P. F. 2013, Astrophysical Journal, 779, 185

Kaviraj, S., Laigle, C., Kimm, T., et al. 2016, Monthly Notices of the Royal Astronomical Society, 467, stx126

Kazantsev, A. P. 1968, Soviet Physics JETP, 26, 1031

Kennicutt, R. C. & Evans, N. J. 2012, Annual Review of Astronomy and Astrophysics, 50, 531

Kennicutt, Jr., R. C. 1998, The Astrophysical Journal, 498, 541

Kereš, D., Katz, N., Weinberg, D. H., & Davé, R. 2005, Monthly Notices of the Royal Astronomical Society, 363, 2

Khochfar, S. & Silk, J. 2009, Monthly Notices of the Royal Astronomical Society, 397, 506

Kim, E.-j., Olinto, A. V., & Rosner, R. 1996, The Astrophysical Journal, 468, 28

Kim, K. S., Lilly, S. J., Miniati, F., et al. 2016, The Astrophysical Journal, 829, 133

Kimm, T. & Cen, R. 2014, Astrophysical Journal, 788, 121

Kimm, T., Cen, R., Devriendt, J., Dubois, Y., & Slyz, A. 2015, Monthly Notices of the Royal Astronomical Society, 451, 2900

Kimm, T., Devriendt, J., Slyz, A., et al. 2011 [eprint[arXiv]1106.0538]

Kimm, T., Katz, H., Haehnelt, M., et al. 2017, Monthly Notices of the Royal Astronomical Society, 466, stx052

Kinney, R. M., Chandran, B., Cowley, S., & McWilliams, J. C. 2002, The Astrophysical Journal, 545, 907

Kitchatinov, L. L. & Rüdiger, G. 2004, Astronomy & Astrophysics, 424, 565

Klessen, R. S. & Hennebelle, P. 2010, Astronomy and Astrophysics, 520, A17

Knollmann, S. R. & Knebe, A. 2009, Astrophysical Journal, Supplement Series, 182, 608

Kolatt, T. 2002, The Astrophysical Journal, 495, 564

Kolb, E. & Turner, M. 1990, The Early Universe, Vol. 80, xxii + 547

Kolmogorov, A. 1941, Akademiia Nauk SSSR Doklady, 30, 301

Korpi, M. J., Brandenburg, A., Shukurov, A., Tuominen, I., & Nordlund, Å. 1999, The Astrophysical Journal, 514, L99

Kotarba, H., Lesch, H., Dolag, K., et al. 2011, Monthly Notices of the Royal Astronomical Society, 415, 3189

Kroupa, P. 2001, Monthly Notices of the Royal Astronomical Society, 322, 231

Krumholz, M. R. & Burkhart, B. 2016, Monthly Notices of the Royal Astronomical Society, 458, 1671

Krumholz, M. R. & McKee, C. F. 2005, The Astrophysical Journal, 630, 250

Kulsrud, R. M. & Zweibel, E. G. 2008, Reports on Progress in Physics, 71, 046901

Langer, M., Puget, J. L., & Aghanim, N. 2003, Physical Review D - Particles, Fields, Gravitation and Cosmology, 67, 043505

Lesch, H. & Chiba, M. 1995, Astronomy and Astrophysics, 297, 305

Linde, A. D. 1982, Physics Letters B, 116, 335

Machida, M., Nakamura, K. E., Kudoh, T., et al. 2013, Astrophysical Journal, 764, 81

Madau, P. & Dickinson, M. 2014, Annual Review of Astronomy and Astrophysics, 52, 415

Mandelker, N., van Dokkum, P. G., Brodie, J. P., van den Bosch, F. C., & Ceverino, D. 2017, The Astrophysical Journal, 861, 148

Mao, S. A., Carilli, C., Gaensler, B. M., et al. 2017, Nature Astronomy, 1, 621

Mao, S. A., Gaensler, B. M., Stanimirović, S., et al. 2008, The Astrophysical Journal, 688, 1029

Marinacci, F. & Vogelsberger, M. 2016, Monthly Notices of the Royal Astronomical Society: Letters, 456, L69

Marinacci, F., Vogelsberger, M., Mocz, P., & Pakmor, R. 2015, Monthly Notices of the Royal Astronomical Society, 453, 3999

Marinacci, F., Vogelsberger, M., Pakmor, R., et al. 2017, Monthly Notices of the Royal Astronomical Society, 480, 5113

Marri, S. & White, S. D. M. 2003, Monthly Notices of the Royal Astronomical Society, 345, 561

Martel, H. & Shapiro, P. R. 1998, Monthly Notices of the Royal Astronomical Society, 297, 467

Mee, A. J. & Brandenburg, A. 2006, Monthly Notices of the Royal Astronomical Society, 370, 415

Mitchell, P. D., Blaizot, J., Devriendt, J., et al. 2018, Monthly Notices of the Royal Astronomical Society, 474, 4279

Miyoshi, T. & Kusano, K. 2005, Journal of Computational Physics, 208, 315

Mo, H. J., Mao, S., & White, S. D. 1998, Monthly Notices of the Royal Astronomical Society, 295, 319

Mocz, P., Pakmor, R., Springel, V., et al. 2016, Monthly Notices of the Royal Astronomical Society, 463, 477

Moss, D., Shukurov, A., & Sokoloff, D. 2000, Accretion and galactic dynamos, Tech. rep.

Moss, D., Snodin, A. P., Englmaier, P., et al. 2007, Astronomy & Astrophysics, 465, 157

Moster, B. P., Naab, T., & White, S. D. 2013, Monthly Notices of the Royal Astronomical Society, 428, 3121

Mulcahy, D. D., Beck, R., & Heald, G. H. 2017, Astronomy & Astrophysics, 600, A6

Mulcahy, D. D., Horneffer, A., Beck, R., et al. 2014, Astronomy & Astrophysics, 568, A74

Murray, N., Quataert, E., & Thompson, T. A. 2010, Astrophysical Journal, 709, 191

Neronov, A. & Vovk, L. 2010, Science, 328, 73

Ntormousi, E., Dawson, J. R., Hennebelle, P., & Fierlinger, K. 2017, Astronomy & Astrophysics, 599, A94

Ocvirk, P., Pichon, C., & Teyssier, R. 2008, Monthly Notices of the Royal Astronomical Society, 390, 1326

Oteo, I., Ivison, R. J., Negrello, M., et al. 2017 [eprint[arXiv]1709.04191]

Padoan, P. & Nordlund, Å. 2011, Astrophysical Journal, 730, 40

Pakmor, R., Bauer, A., & Springel, V. 2011, Monthly Notices of the Royal Astronomical Society, 418, 1392

Pakmor, R., Gómez, F. A., Grand, R. J. J., et al. 2017, Monthly Notices of the Royal Astronomical Society, 469, 3185

Pakmor, R., Guillet, T., Pfrommer, C., et al. 2018, Monthly Notices of the Royal Astronomical Society, 481, 4410

Pakmor, R., Marinacci, F., & Springel, V. 2014, Astrophysical Journal Letters, 783, L20

Pakmor, R. & Springel, V. 2013, Monthly Notices of the Royal Astronomical Society, 432, 176

Pandey, K. L., Sethi, S. K., & Ratra, B. 2019, arXiv Astrophysics [eprint[arXiv]1901.01434]

Panessa, F., Baldi, R. D., Laor, A., et al. 2019 [eprint[arXiv]arXiv:1902.05917v1]

Patel, S. G., Holden, B. P., Kelson, D. D., et al. 2012, The Astrophysical Journal, 748, L27

Pawlik, A. H., Schaye, J., & van Scherpenzeel, E. 2009, Monthly Notices of the Royal Astronomical Society, 394, 1812

Peebles, P. J. E. 1994, The Astrophysical Journal, 429, 43

Pfrommer, C., Pakmor, R., Schaal, K., Simpson, C. M., & Springel, V. 2017, Monthly Notices of the Royal Astronomical Society, 465, 4500

Pillepich, A., Springel, V., Nelson, D., et al. 2018, Monthly Notices of the Royal Astronomical Society, 473, 4077

Pineda, J. L., Goldsmith, P. F., Chapman, N., et al. 2010, Astrophysical Journal, 721, 686

Planck Collaboration. 2015, Astronomy & Astrophysics, 594, A19

Planck Collaboration, P., Aghanim, N., Akrami, Y., et al. 2018 [eprint[arXiv]1807.06209]

Pogosian, L. & Zucca, A. 2018, Searching for primordial magnetic fields with CMB B-modes

Powell, K. G., Roe, P. L., Linde, T. J., Gombosi, T. I., & De Zeeuw, D. L. 1999, Journal of Computational Physics, 154, 284

Powell, L. C., Slyz, A., & Devriendt, J. 2011, Monthly Notices of the Royal Astronomical Society, 414, 3671

Power, C., Navarro, J. F., Jenkins, A., et al. 2003, Monthly Notices of the Royal Astronomical Society, 338, 14

Press, W. H. & Schechter, P. 1974, Formation of galaxies and clusters of galaxies by self-similar gravitational condensation, Tech. rep.

Pudritz, R. E. & Silk, J. 2002, The Astrophysical Journal, 342, 650

Ramos-Martínez, M., Gómez, G. C., & Pérez-Villegas, Á. 2018, Monthly Notices of the Royal Astronomical Society, 476, 3781

Rasera, Y. & Teyssier, R. 2006, Astronomy & Astrophysics, 445, 1

Ratra, B. 1992, Cosmological seed magnetic field from Inflation, Tech. rep.

Rees, M. J. 1987, Quarterly Journal of the Royal Astronomical Society, 28, 197

Rembiasz, T., Obergaulinger, M., Cerdá-Durán, P., Aloy, M.-Á., & Müller, E. 2016, The Astrophysical Journal Supplement Series, 230, 18

Reynolds, S. P., Gaensler, B. M., & Bocchino, F. 2012, Space Science Reviews, 166, 231

Ricciardelli, E., Quilis, V., & Planelles, S. 2013, Monthly Notices of the Royal Astronomical Society, 434, 1192

Ricciardelli, E., Quilis, V., & Varela, J. 2014in (Oxford University Press), 601–609

Rieder, M. & Teyssier, R. 2016, Monthly Notices of the Royal Astronomical Society, 457, 1722

Rieder, M. & Teyssier, R. 2017a, Monthly Notices of the Royal Astronomical Society, 471, 2674

Rieder, M. & Teyssier, R. 2017b, Monthly Notices of the Royal Astronomical Society, 472, 4368

Robishaw, T., Quataert, E., & Heiles, C. 2008, The Astrophysical Journal, 680, 981

Roche, P. F., Lopez-Rodriguez, E., Telesco, C. M., Schodel, R., & Packham, C. 2018 [eprint[arXiv]1807.11744]

Roettiger, K., Stone, J. M., & Burns, J. O. 2002, The Astrophysical Journal, 518, 594

Rosdahl, J., Katz, H., Blaizot, J., et al. 2018, Monthly Notices of the Royal Astronomical Society, 479, 994

Rosdahl, J., Schaye, J., Dubois, Y., Kimm, T., & Teyssier, R. 2017, Monthly Notices of the Royal Astronomical Society, 466, 11

Rosdahl, J. & Teyssier, R. 2015, Monthly Notices of the Royal Astronomical Society, 449, 4380

Rosen, A. & Bregman, J. N. 1995, The Astrophysical Journal, 440, 634

Roškar, R., Teyssier, R., Agertz, O., Wetzstein, M., & Moore, B. 2014, Monthly Notices of the Royal Astronomical Society, 444, 2837

Ruiz-Granados, B., Rubiño-Martín, J. A., Florido, E., & Battaner, E. 2010, Astrophysical Journal Letters, 723, L44

Ryu, D., Kang, H., Cho, J., & Das, S. 2008, Science, 320, 909

Safarzadeh, M. & Loeb, A. 2019 [eprint[arXiv]1901.03341]

Salem, M. & Bryan, G. L. 2014, Monthly Notices of the Royal Astronomical Society, 437, 3312

Samui, S., Subramanian, K., & Srianand, R. 2018, Monthly Notices of the Royal Astronomical Society, 476, 1680

Sanchez Almeida, J. 2017 [eprint[arXiv]1612.00776]

Schekochihin, A. A., Cowley, S. C., Hammett, G. W., Maron, J. L., & McWilliams, J. C. 2002, New Journal of Physics, 4, 84

Schekochihin, A. A., Cowley, S. C., Taylor, S. F., Maron, J. L., & McWilliams, J. C. 2004, The Astrophysical Journal, 612, 276

Schlickeiser, R. 2012, Physical Review Letters, 109, 261101

Schmidt, M. 1959, The Astrophysical Journal, 129, 243

Schober, J., Rogachevskii, I., Brandenburg, A., et al. 2017, The Astrophysical Journal, 858, 124

Schober, J., Schleicher, D. R., Federrath, C., Bovino, S., & Klessen, R. S. 2015, Physical Review E - Statistical, Nonlinear, and Soft Matter Physics, 92, 023010

Seifried, D., Pudritz, R. E., Banerjee, R., Duffin, D., & Klessen, R. S. 2012, Monthly Notices of the Royal Astronomical Society, 422, 347

Semenov, D., Henning, T., Helling, C., Ilgner, M., & Sedlmayr, E. 2003, Astronomy & Astrophysics, 410, 611

Sethi, S., Haiman, Z., & Pandey, K. 2010, Astrophysical Journal, 721, 615

Sharma, R., Subramanian, K., & Seshadri, T. R. 2018, Physical Review D, 97, 1

Shin, M. S. & Ruszkowski, M. 2013, Monthly Notices of the Royal Astronomical Society, 428, 804

Smoot, G. F., Bennett, C. L., Kogut, A., et al. 1992, The Astrophysical Journal, 396, L1

Sobey, C., Bilous, A. V., Grießmeier, J.-M., et al. 2019, Monthly Notices of the Royal Astronomical Society, 484, 3646

Sofue, Y. & Rubin, V. 2001, Annual Review of Astronomy and Astrophysics, 39, 137

Sparke, L. S. 1982, The Astrophysical Journal, 260, 104

Spergel, D. N., Bean, R., Dore, O., et al. 2007, The Astrophysical Journal Supplement Series, 170, 377

Springel, V. 2010, Monthly Notices of the Royal Astronomical Society, 401, 791

Springel, V. & Hernquist, L. 2002, Monthly Notices of the Royal Astronomical Society, 339, 289

Springel, V., Yoshida, N., & White, S. D. M. 2001, GADGET: a code for collisionless and gasdynamical cosmological simulations, Tech. rep.

Stinson, G., Seth, A., Katz, N., et al. 2006, Monthly Notices of the Royal Astronomical Society, 373, 1074

Stone, J. M., Gardiner, T. A., Teuben, P., Hawley, J. F., & Simon, J. B. 2008, The Astrophysical Journal Supplement Series, 178, 137

Su, K. Y., Hopkins, P. F., Hayward, C. C., et al. 2017, Monthly Notices of the Royal Astronomical Society, 471, 144

Subramanian, K. 2016, The origin, evolution and signatures of primordial magnetic fields

Sur, S., Federrath, C., Schleicher, D. R. G., Banerjee, R., & Klessen, R. S. 2012, Monthly Notices of the Royal Astronomical Society, 423, 3148

Sutherland, R. S. & Dopita, M. A. 1993, The Astrophysical Journal Supplement Series, 88, 253

Swaters, R. A., Sancisi, R., van Albada, T. S., & van der Hulst, J. M. 2009, Astronomy & Astrophysics, 493, 871

Tahani, M., Plume, R., Brown, J. C., & Kainulainen, J. 2018, Astronomy & Astrophysics, 614, A100

Taylor, A. M., Vovk, I., & Neronov, A. 2011, Astronomy & Astrophysics, 529, A144

Taylor, A. R., Agudo, I., Akahori, T., et al. 2015, in Proceedings of Science, Vol. 9-13-June-, 113

Teyssier, R. 2002, Astronomy & Astrophysics, 385, 337

Teyssier, R., Fromang, S., & Dormy, E. 2006, Journal of Computational Physics, 218, 44

Teyssier, R., Pontzen, A., Dubois, Y., & Read, J. I. 2013, Monthly Notices of the Royal Astronomical Society, 429, 3068

Tillson, H., Devriendt, J., Slyz, A., Miller, L., & Pichon, C. 2015, Monthly Notices of the Royal Astronomical Society, 449, 4363

Toft, S., Smolčić, V., Magnelli, B., et al. 2014, Astrophysical Journal, 782, 68

Toro, E. F., Spruce, M., & Speares, W. 1994, Shock Waves, 4, 25

Trivedi, P., Reppin, J., Chluba, J., & Banerjee, R. 2018, Monthly Notices of the Royal Astronomical Society, 481, 3401

Tsagas, C. G. & Maartens, R. 2000, Physical Review D - Particles, Fields, Gravitation and Cosmology, 61 [eprint[arXiv]9904390]

Turner, M. S. & Widrow, L. M. 1988, Physical Review D, 37, 2743

Tweed, D., Devriendt, J., Blaizot, J., Colombi, S., & Slyz, A. 2009, Astronomy & Astrophysics, 506, 647

Vafin, S., Deka, P. J., Pohl, M., & Bohdan, A. 2019 [eprint[arXiv]1901.09640]

van Daalen, M. P., Schaye, J., Booth, C. M., & Dalla Vecchia, C. 2011, Monthly Notices of the Royal Astronomical Society, 415, 3649

Varalakshmi, C. & Nigam, R. 2017, Astrophysics and Space Science, 362, 16

Vázquez-Semadeni, E., Banerjee, R., Gómez, G. C., et al. 2011, Monthly Notices of the Royal Astronomical Society, 414, 2511

Vazza, F., Brüggen, M., Gheller, C., et al. 2017, Classical and Quantum Gravity, 34, 234001

Vazza, F., Brüggen, M., Gheller, C., & Wang, P. 2014, Monthly Notices of the Royal Astronomical Society, 445, 3706

Vazza, F., Brunetti, G., Brüggen, M., & Bonafede, A. 2018, Monthly Notices of the Royal Astronomical Society, 474, 1672

Vazza, F., Ferrari, C., Brüggen, M., et al. 2015, Astronomy & Astrophysics, 580, A119

Villagran, M. A. & Gazol, A. 2018, Monthly Notices of the Royal Astronomical Society, 476, 4932

Wang, B. & Silk, J. 1994, The Astrophysical Journal, 427, 759

Wang, P. & Abel, T. 2009, The Astrophysical Journal, 696, 96

Wareing, C. J., Pittard, J. M., Wright, N. J., & Falle, S. A. 2018, Monthly Notices of the Royal Astronomical Society, 475, 3598

West, J. L., Jaffe, T., Ferrand, G., Safi-Harb, S., & Gaensler, B. M. 2017, The Astrophysical Journal, 849, L22

Westfall, K. B., Andersen, D. R., Bershady, M. A., et al. 2014, Astrophysical Journal, 785, 43

White, S. D. M. & Frenk, C. S. 1991, The Astrophysical Journal, 379, 52

Widrow, L. M. 2002, Origin of galactic and extragalactic magnetic fields

Wilcots, E. 2004, New Astronomy Reviews, 48, 1281

Wild, V., Almaini, O., Cirasuolo, M., et al. 2014, Monthly Notices of the Royal Astronomical Society, 440, 1880

Wilkinson, C. L., Pimbblet, K. A., & Stott, J. P. 2017, Monthly Notices of the Royal Astronomical Society, 472, 1447

Wise, J. H., Turk, M. J., Norman, M. L., & Abel, T. 2012, Astrophysical Journal, 745, 50

Wittor, D., Vazza, F., & Brüggen, M. 2017, Monthly Notices of the Royal Astronomical Society, 464, 4448

Wolfe, A. M., Lanzetta, K. M., & Oren, A. L. 1992, The Astrophysical Journal, 388, 17

Wurster, J., Bate, M. R., & Price, D. J. 2018, Monthly Notices of the Royal Astronomical Society, 480, 4434

Wyithe, J. S. B. & Bolton, J. S. 2011, Monthly Notices of the Royal Astronomical Society, 412, 1926

Yan, D., Zhou, J., Zhang, P., Zhu, Q., & Wang, J. 2018, The Astrophysical Journal, 870, 17

Yang, H. Y. K. & Reynolds, C. S. 2015, The Astrophysical Journal, 818, 181

Zamora-Avilés, M., Vázquez-Semadeni, E., Körtgen, B., Banerjee, R., & Hartmann, L. 2018, Monthly Notices of the Royal Astronomical Society, 474, 4824

Zeldovich, Y. B. 1983, The Fluid Mechanics of Astrophysics and Geophysics

Zhang, H., Gao, Y., & Law, C. K. 2018, The Astrophysical Journal, 864, 167

Zhuravleva, I., Churazov, E., Schekochihin, A. A., et al. 2014, Nature, 515, 85

Zweibel, E. G. 2013, Physics of Plasmas, 20, 055501